

# Dissertation

submitted to  
the Combined Faculties of the Natural Sciences and Mathematics  
of the Ruperto-Carola-University of Heidelberg, Germany  
for the degree of Doctor of Natural Sciences

Put forward by  
Marc Weber  
born in Saarlouis

Oral examination on 19th June 2013



# **Gentle Neutron Signals and Noble Background in the XENON100 Dark Matter Search Experiment**

Referees:

Prof. Dr. Wolfgang Hampel

Prof. Dr. André Schöning



---

**Abstract** This thesis is brought forward to improve the understanding of peculiar aspects concerning signal and background in the XENON100 experiment, which aims at the direct detection of weakly interacting massive particles (WIMPs). These yet undiscovered particles provide a well-motivated solution to the quest for dark matter in our Universe. Within three years of operation, the XENON100 detector has evolved to become the most sensitive instrument to probe spin-independent WIMP-nucleon cross-sections down to  $2.0 \times 10^{-45} \text{ cm}^2$  for WIMP masses in the range of  $55 \text{ GeV}/c^2$ .

We first present an introduction to the detection principle underlying the application of liquid xenon as a target medium for rare event searches. In the following, we summarize our contributions to the suppression of anomalous radiation backgrounds, appearing in the context of reported data analysis for the dark matter searches. We devote the subsequent chapter to the investigation of naturally decaying radon as one of the most dominant sources of internal background. Conclusions drawn are relevant not only for the interpretation of the current background level in XENON100 but also for future detector generations. Finally, we aim at a coherent understanding of nuclear recoil interactions, as mediated by neutrons or potential WIMPs, in the XENON100 detector. Through comparison of neutron calibration data to a dedicated simulation of the entire detector signal response, we derive a measurement of the charge yield and light quenching in liquid xenon, both functions of recoil energy. By achieving absolute and spectral agreement in both accessible signal channels between data and simulation we further provide proof of the correctness and robustness of the interpretation of dark matter results put forward by the XENON100 experiment.

**Kurzfassung** Die vorliegende Arbeit befasst sich mit verschiedenen Erscheinungsformen von Signal und Untergrund, die für das Experiment XENON100 mit dem Ziel des direkten Nachweises von massiven, schwach wechselwirkenden Teilchen (engl. abgekürzt „WIMPs“) von Bedeutung sind. Man geht davon aus, dass diese Teilchen eine Erklärung für das Vorhandensein von sogenannter dunkler Materie im Universum liefern können. Innerhalb von drei Jahren nach der ersten Inbetriebnahme gelang es mit dem genannten Detektor, XENON100, die bislang weitreichendste Messung des spin-unabhängigen Wechselwirkungsquerschnittes von WIMPs mit gewöhnlicher Materie durchzuführen und diesen bis zu einem Wert von  $2.0 \times 10^{-45} \text{ cm}^2$ , bei angenommener WIMP-Masse von  $55 \text{ GeV}/c^2$ , auszuschließen.

Wir geben zunächst einen kurzen Einblick in das Funktionsprinzip des mit flüssigem Xenon betriebenen Detektoraufbaus, der speziell für die Suche nach seltenen Ereignissen ausgelegt ist. Anschließend fassen wir den eigenen Beitrag zur Reduzierung des sogenannten anomalen Untergrundes zusammen, der in die Auswertung der Dunkle-Materie-Daten eingeht. Das darauf folgende Kapitel untersucht die Erscheinung und die Auswirkungen des Zerfalls von Radon im Inneren des Experiments. Das radioaktive Edelgas und seine Zerfallstöchter stellen mitunter ein Hindernis für das Ziel bestmöglicher Unterdrückung von natürlicher Strahlung im relevanten Energiebereich für die Suche nach Dunkler-Materie-Wechselwirkung dar. Schließlich richtet sich der Schwerpunkt im letzten Kapitel auf das Verständnis von elastischen Rückstößen zwischen Neutronen (oder möglicherweise WIMPs) und Xenonkernen in verflüssigter Umgebung. Dabei werden zunächst Ladungsausbeute und Szintillationslichteffizienz durch einen Abgleich von Neutronenkalibrationsdaten mit einer eigens entwickelten Simulation der Detektorantwort als Funktionen der Energie bestimmt. Mittels der letztlich erzielten spektralen und absoluten Übereinstimmung von Daten und Modell beider zugänglicher Signalarten des Detektors kann bestätigt werden, dass bisherige Ergebnisse zur Dunkle-Materie-Suche im XENON100 Experiment auf korrekte Weise interpretiert wurden.

---

# Contents

<b>1</b>	<b>The Quest for Dark Matter</b>	<b>3</b>
1.1	Astrophysical observations . . . . .	3
1.2	Particle candidates . . . . .	6
1.3	The WIMP coincidence . . . . .	6
1.4	Detection techniques . . . . .	8
1.5	WIMP recoil rates in direct search experiments . . . . .	9
1.6	Direct detection experiments . . . . .	13
<b>2</b>	<b>The XENON100 Experiment</b>	<b>15</b>
2.1	Detection principle of a two-phase xenon TPC . . . . .	15
2.1.1	Scintillation and ionization in liquid xenon . . . . .	16
2.1.2	Primary scintillation light (S1) . . . . .	17
2.1.3	Secondary scintillation light (S2) . . . . .	19
2.1.4	Position reconstruction and signal correction . . . . .	20
2.2	Detector setup and shield . . . . .	23
2.3	Data acquisition and processing . . . . .	26
2.4	Event selection and data analysis . . . . .	27
2.4.1	Event selection . . . . .	28
2.4.2	Recoil discrimination . . . . .	31
2.4.3	Recoil energy scale . . . . .	32
2.5	Scientific results on dark matter search . . . . .	34
<b>3</b>	<b>Reduction of Anomalous Background</b>	<b>39</b>
3.1	Composition of electronic recoil background . . . . .	39
3.2	Origin of anomalous leakage events . . . . .	40
3.3	The S1 pattern likelihood cut . . . . .	41
3.4	Optimization of the PL cut performance . . . . .	44
3.5	Impact on the 225 live days dark matter result . . . . .	47
<b>4</b>	<b>Radon Background</b>	<b>49</b>
4.1	Origin and decay of radon . . . . .	49
4.2	Radon as potential background source . . . . .	50
4.3	Data collection . . . . .	53
4.4	Radon decay identification . . . . .	53
4.4.1	Alpha spectroscopy . . . . .	54
4.4.2	BiPo tagging and event reconstruction . . . . .	58
4.5	Radon decay energy distributions . . . . .	65
4.5.1	Light and charge yield for alpha decays . . . . .	65

4.5.2	Beta and alpha spectra from BiPo coincidence . . . . .	69
4.6	Spatial distributions . . . . .	72
4.6.1	Position reconstruction . . . . .	72
4.6.2	Spatial distribution of alpha decays . . . . .	72
4.6.3	Spatial distribution of BiPo decays . . . . .	73
4.6.4	Modeling $^{212}\text{Bi}^+$ ion drift . . . . .	75
4.6.5	BiPo at zero drift field . . . . .	77
4.6.6	Summary of spatial distributions . . . . .	79
4.7	Radon rate evolution . . . . .	80
4.8	Impact of radon on low energy background . . . . .	86
4.9	Summary of radon analysis . . . . .	88
<b>5</b>	<b>Light and Charge From Nuclear Recoils</b>	<b>91</b>
5.1	Nuclear recoil energy scale . . . . .	91
5.2	Neutron calibration data . . . . .	94
5.2.1	Neutron source . . . . .	94
5.2.2	Data acquisition . . . . .	95
5.2.3	Event selection . . . . .	95
5.3	Monte-Carlo simulation of neutron calibration . . . . .	98
5.3.1	Neutron track simulation with GEANT4 . . . . .	98
5.3.2	Simulation of observable S1 and S2 . . . . .	101
5.4	Fitting simulation to data . . . . .	105
5.4.1	Fitting S2 and determining $Q_y$ . . . . .	107
5.4.2	Fitting S1 and determining $\mathcal{L}_{eff}$ . . . . .	112
5.4.3	Data matching using combined best fit $\mathcal{L}_{eff}$ and $Q_y$ . . . . .	114
5.5	Reproducing combined S1/S2 nuclear recoil distributions . . . . .	115
5.6	Simulation of WIMP recoils . . . . .	121
5.7	Summary of the nuclear recoil response study . . . . .	125

---

# List of Figures

1.1	Rotation curves of spiral galaxies . . . . .	4
1.2	Rotation curve and predictions of different mass contributions . . . . .	4
1.3	Mass distribution and x-ray emission from bullet cluster collision . . . . .	5
1.4	Angular power spectrum of the <i>Planck</i> 2013 CMB survey . . . . .	5
1.5	Evolution of WIMP number density . . . . .	7
1.6	WIMP interaction scheme . . . . .	8
1.7	Comparison of expected differential WIMP rates for various target materials . . . . .	12
2.1	Detection principle of a time projection chamber (TPC) . . . . .	16
2.2	Example of S1 pulse shape . . . . .	19
2.3	Example of S2 pulse shape . . . . .	19
2.4	Drifttime determination . . . . .	20
2.5	(x,y) event position reconstruction . . . . .	21
2.6	S1 light collection efficiency map . . . . .	22
2.7	Determination of the electron lifetime attenuation . . . . .	22
2.8	Passive shield construction of the XENON100 setup . . . . .	24
2.9	Scheme of the XENON100 detector . . . . .	24
2.10	Pictures of the XENON100 TPC . . . . .	25
2.11	The XENON100 DAQ system . . . . .	26
2.12	Comparison of different hardware trigger configurations . . . . .	26
2.13	Illustration of the S2 width cut . . . . .	28
2.14	Definition of single scatter selection . . . . .	29
2.15	Distribution of second largest S2 . . . . .	29
2.16	Spatial distribution of electronic recoil events . . . . .	31
2.17	Discrimination between electronic and nuclear recoils . . . . .	32
2.18	S1-S2 correlation in $^{137}\text{Cs}$ calibration . . . . .	33
2.19	Combined cut acceptance for the 225 live days analysis . . . . .	35
2.20	Event distribution in discrimination space after 225 live days dark matter search . . . . .	36
2.21	Spatial event distribution after 225 live days . . . . .	36
3.1	Electronic recoil band from $^{60}\text{Co}$ calibration . . . . .	40
3.2	Projection of the electronic recoil band on the discrimination parameter axis . . . . .	40
3.3	Example of exceptional PMT hit pattern . . . . .	42
3.4	Definition of the S1 pattern likelihood cut . . . . .	43
3.5	Spatial distribution of events rejected by the S1 pattern likelihood cut . . . . .	44
3.6	Leakage rejection performance of several pattern likelihood cut definitions . . . . .	45
3.7	Definition of the pattern likelihood acceptance for nuclear recoils . . . . .	47
3.8	PL <sup>97%</sup> cut acceptance as a function of S1 . . . . .	47

3.9	Impact of the PL cut on the 225 live days dark matter result . . . . .	48
4.1	Radon decay chains . . . . .	50
4.2	Predicted background rate as a function of radon concentration . . . . .	52
4.3	Electronic recoil background composition . . . . .	53
4.4	Waveform example for $\alpha$ event . . . . .	55
4.5	Second largest S1 signal distribution for $\alpha$ events . . . . .	55
4.6	Standard corrected S1 as function of z position . . . . .	56
4.7	S1 corrected by the alpha light map as function of z position . . . . .	56
4.8	S1 light correction map for $\alpha$ events . . . . .	57
4.9	Construction examples for spatial correction map . . . . .	57
4.10	Improved S1 resolution using the alpha light map . . . . .	58
4.11	BiPo event topologies . . . . .	60
4.12	Waveform examples of BiPo decays . . . . .	62
4.13	Lifetime distribution of $^{212}\text{Po}$ . . . . .	63
4.14	Lifetime distribution of $^{214}\text{Po}$ . . . . .	63
4.15	S1 spectra of various $\alpha$ decays . . . . .	66
4.16	Alpha peak separation in S2 vs. S1 space . . . . .	68
4.17	Fits to S2 distributions from $^{222}\text{Rn}$ and $^{218}\text{Po}$ decays . . . . .	69
4.18	S1 $_{\alpha}$ signal correlation with z position . . . . .	70
4.19	Summed S2 signal of selected $^{214}\text{BiPo}$ events . . . . .	70
4.20	Measured S1 $\beta$ spectra of $^{212}\text{Bi}$ and $^{214}\text{Bi}$ . . . . .	71
4.21	Spatial distribution of $\alpha$ decays . . . . .	73
4.22	Spatial distribution of BiPo decay coincidences . . . . .	74
4.23	Fit to z distribution of $^{212}\text{BiPo}$ events . . . . .	76
4.24	Calibration of the S1 asymmetry parameter (I) . . . . .	78
4.25	Calibration of the S1 asymmetry parameter (II) . . . . .	78
4.26	Comparison of S1 asymmetry distributions at different electric fields . . . . .	79
4.27	Vertical position distribution of different radon chain components . . . . .	80
4.28	Time evolution of radon rate during air leak . . . . .	81
4.29	Time evolution of radon rate during 225 live days . . . . .	83
4.31	Test of time-correlation between the internal radon evolution and concentration in ambient air . . . . .	85
5.1	$\mathcal{L}_{eff}$ results from direct measurements . . . . .	94
5.2	$Q_y$ results from direct and indirect measurements . . . . .	94
5.3	Spatial distribution of single scattering neutrons . . . . .	96
5.4	Nuclear recoil band and activated xenon lines . . . . .	96
5.5	Nuclear recoil event selection . . . . .	97
5.6	GEANT4 detector and shield geometry . . . . .	99
5.7	GEANT4 detector model and event display . . . . .	99
5.8	Comparison of $^{241}\text{AmBe}$ neutron emission spectra . . . . .	100
5.9	Simulated nuclear recoil energy deposition for different neutron emission spectra . . . . .	100
5.10	Flow chart of detector response simulation . . . . .	102
5.11	Distance of neighbouring S2 peaks along the drift axis . . . . .	104
5.12	S2 Peak distance normalized to the measured S2 width . . . . .	104
5.13	Nuclear recoil cut acceptance as a function of S1 . . . . .	105

---

5.14	Data/MC comparison of the S1 spectrum using the global $\mathcal{L}_{eff}$ description . . . . .	106
5.15	Data/MC comparison of the S2 spectrum using the interpolation of Manzur $Q_y$ . . . . .	106
5.16	Best fit of the simulated S2 spectrum to data . . . . .	109
5.17	$Q_y$ solution to the best fit S2 matching . . . . .	109
5.18	Definition of global $\mathcal{L}_{eff}$ fit and uncertainties . . . . .	110
5.19	Nuclear recoil cut acceptance as a function of S1 . . . . .	110
5.20	Decomposition of the best-fit $Q_y$ uncertainty . . . . .	111
5.21	Best fit of the simulated S1 spectrum to data . . . . .	113
5.22	$\mathcal{L}_{eff}$ solution to yield best spectral matching . . . . .	113
5.23	S1 Data/MC comparison using fitted $\mathcal{L}_{eff}$ and $Q_y$ . . . . .	114
5.24	S2 Data/MC comparison using fitted $\mathcal{L}_{eff}$ and $Q_y$ . . . . .	114
5.25	Data/MC Comparison of spatial event distribution (I) . . . . .	115
5.26	Data/MC Comparison of spatial event distribution (II) . . . . .	115
5.27	Comparison of S1-S2 signal correlation. . . . .	117
5.28	S1-S2 band shape comparison . . . . .	117
5.29	Comparison of nuclear recoil bands . . . . .	118
5.30	Nuclear recoil band shape comparison . . . . .	118
5.31	Sliced projections of the nuclear recoil band . . . . .	119
5.32	2-D decomposition of the nuclear recoil band . . . . .	120
5.33	1-D Decomposition of the nuclear recoil band . . . . .	120
5.34	Energy reconstruction via S1 and S2 . . . . .	120
5.35	Integrated recoil spectra for 8 and 25 GeV/c <sup>2</sup> WIMPs . . . . .	122
5.36	Simulation of potential WIMP signature . . . . .	123
5.37	$\mathcal{L}_{eff}$ result in comparison with other measurements . . . . .	126
5.38	$Q_y$ result in comparison with other measurements . . . . .	126

---

# Introduction

For many decades people have been following the idea of dark matter to explain the invisible matter component of our Universe. While no experiment has been likely to detect it yet, there are many signs pointing at its existence and they have encouraged scientists all the more to develop novel detection techniques in various fields of physics. Among many operating experiments is XENON100, aiming at direct observation of weakly interacting massive particles. It will provide the framework of this thesis.

Due to the proposed nature of dark matter particles it is expected that they will at most undergo feeble interactions with ordinary matter. Consequently, whatever technology is applied by certain detector experiments, all have in common to search for extremely rare events. Hence, it is crucial to suppress any background contribution from natural radioactivity or cosmic rays in order to be sensitive for a tiny excess of events, possibly caused by the unknown particle. At the same time, one has to develop a decent understanding of how a potential signal in the detector would eventually appear. Subjects concerning both needs – the suppression of background and footprints of potential signals – are addressed in the present work.

After a general introduction to the field of dark matter searches in Chapter 1 we continue in Chapter 2 with a description of the XENON100 experimental setup, principles of data evaluation and a short summary of achieved scientific results.

The following Chapter 3 is devoted to the optimization of a particular event criterion, applied to reduce the non-gaussian (“anomalous”) background contribution from external radiation which has the potential to mimick the signature of dark matter particles inside the XENON100 detector.

The focus of the subsequent Chapter 4 is an intense evaluation of the radioactive noble gas radon and its subsequent decay products inside the active xenon detection chamber. The understanding of the decay chain signature in a noble liquid detector is of particular interest because radon provides a source of intrinsic background. Opposite to external radiation it cannot be simply reduced by increasing the target mass and hence poses a potential threat to reach ultimate radio-purity in the central volume of XENON100 or future detector generations.

In the final Chapter 5 we turn from the study of background to the interpretation of eventual signals. For this purpose we aim at a coherent model of the nuclear recoil event signature in XENON100, based on the comparison between measurement and simulation of a regular neutron calibration of the detector. By persuing both absolute and spectral agreement between data and simulation we will thereby deduce the energy dependent charge yield and light quenching function of nuclear interactions in a liquid xenon medium. Applying our gained knowledge, we conclude our analysis by predicting the XENON100 response to possible interactions with dark matter particles.



## The Quest for Dark Matter

“(..) würde sich also das überraschende Resultat ergeben, dass dunkle Materie in sehr viel grösserer Dichte vorhanden ist als leuchtende Materie.”

*Fritz Zwicky, 1933  
Helvetica Physica Acta, Vol. 6, p. 125*

It is one of today’s most outstanding quests of science to explain the compounds and the history of our Universe since the Big Bang. Achievements from many fields of physics have already tremendously helped to understand parts of Nature’s great puzzle only to reveal that we know almost nothing about its major ingredients, called “dark energy” and “dark matter”. All what is left, the sum of countless galaxies, hydrogen clouds, stars and planets form merely 5% of what the Universe is in total made of.

This partition is nowadays derived from the standard model of cosmology, called  $\Lambda$ CDM. The name already incorporates its major constituents: the infamous cosmological constant  $\Lambda$  and some weakly specified type of cold (i.e. non-relativistic) dark matter (CDM). The constant appears from Einstein’s equations of general relativity which is considered to govern the dynamics of our essentially flat and expanding Universe and is today attributed to dark energy. The other ingredient, dark matter, represents the utmost motivation of the present thesis, which explains why we want to discuss its origin, impact and potential structure with some more details in the following sections.

### 1.1 Astrophysical observations

In 1933 Zwicky made the puzzling observation that the velocity dispersion of individual nebulae in the large Coma galaxy cluster contradicts the expectation of the virial theorem<sup>1</sup> if estimating the total mass solely from the visible matter content [1]. Although he provided a few alternative explanations for the obvious mass discrepancy, his favoured guess pointed towards an abundance of “dark” matter much larger than luminous one. This conclusion remarked a starting point for an enduring series of astrophysical observations, today giving compelling indirect evidence for the existence of an additional non-luminous type of matter.

The next remarkable discovery was brought forward by the measurement of extended rotation curves of stars in spiral galaxies. From Newtonian motion one would expect that the rotation velocity of objects in a gravitational potential is described by  $v(r) = \sqrt{GM(r)/r}$ . As long as the body is inside the core of the radial mass distribution  $M(r)$  the speed is supposed to increase linearly with radius  $r$  until a turning point is reached. From then, the centre of the galaxy appears more and more

---

<sup>1</sup>The virial theorem relates the average potential energy density  $\bar{\epsilon}_P$  of a stationary gravitationally bound system to its mean kinetic energy density  $\bar{\epsilon}_K$ , which is proportional to the velocity dispersion, according to  $\bar{\epsilon}_K = -\frac{1}{2}\bar{\epsilon}_P$ .

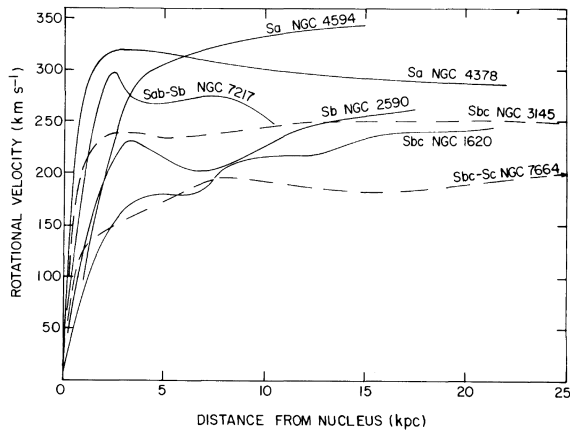


**Figure 1.1:** Rotational velocity of stars as a function of distance from their galactic centre. Shown are 7 curves of high luminous galaxies. After the expected linear increase at small radii, there is no decline observed afterwards. Instead, the constant continuation can be explained by the presence of a dark halo surrounding the visible mass in the centre. Figure from Rubin et al. [2].

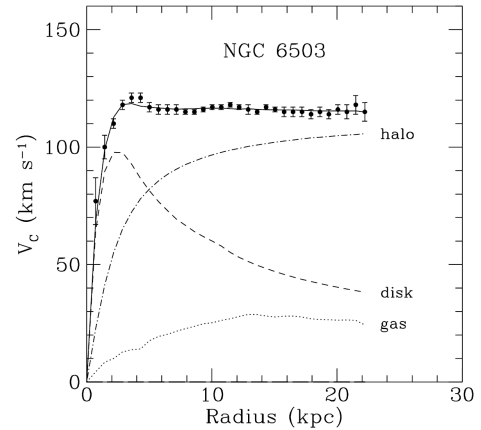


**Figure 1.2:** Measurement of rotation curve (data points) and expected contributions from different mass components: Visible matter content only (dashed line), galactic gas (dotted) and dark matter halo (dashed dotted). Figure adopted from [3].

point-like, leading to a decline  $\propto r^{-1/2}$  of the velocity with growing distance. In a remarkable analysis of 10 high-luminosity spiral galaxies Rubin, Ford and Thonnard could demonstrate that this is not necessarily the case [2]. Instead they found that the so-called rotation curves  $v(r)$  flatten out or slightly rise towards the remote edges of the galaxies. Their results for seven particular galaxies are shown in Fig. 1.1. Therein, the velocity of stars, determined from the redshift in the  $H\alpha$  optical and 21 cm radio-wavelength transition line of stellar hydrogen, is drawn on the y-axis as a function of distance from the galactic centre. The assumption of an additional matter component, a “dark halo”, surrounding the luminous core can account for the observed trend. This is well illustrated in another diagram from [3], provided in Fig. 1.2. It shows convincingly the partition of a measured rotation curve into three major components: The luminous matter, gas component and a dark halo. It must be mentioned that dark matter does not provide an unique model to explain the constant behavior. An alternative approach is to assume a modified theory of gravity (MOND) acting differently from Newton’s mechanics on large galactic scales [4]. However, while it also implies the flattening of rotation curves it widely fails to describe other striking phenomena related to the missing mass problem, as mentioned in the following.

One of the further pieces of evidence comes from gravitational lensing [5, 6]. The effect describes the distortion of light from far distant galaxies due to the presence of a large gravitational potential placed in the line of sight between its source and an earthbound observer. By measuring the degree of light deflection it is possible to infer the amount of mass inducing the light disturbance, supposed that the involved lens distances are known from redshift determinations. This value can be compared to the mass estimate from the sum of all luminous objects confined by the lens and one finds again a discrepancy to be overcome best by the existence of some type of invisible matter component.

Results from lensing effects can be combined with x-ray measurements of the Chandra space telescope to produce the famous picture of the so-called “Bullet-Cluster”, shown in Fig. 1.3. It illustrates

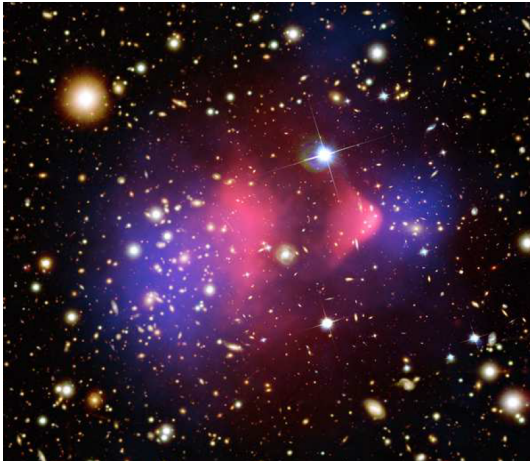
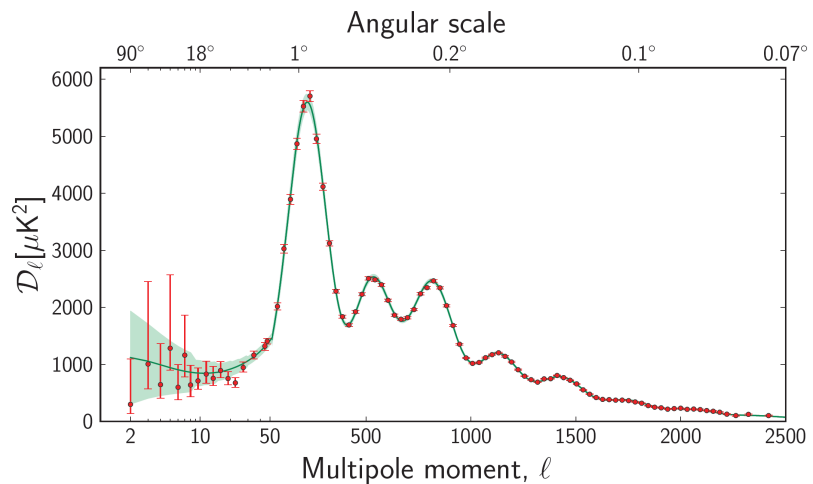


**Figure 1.3:** Collision of two galaxy clusters (“Bullet Cluster” 1E0657-56) viewed from three perspectives: optical image (credit: NASA/STScI; Magellan/U.Arizona/D.Clowe et al.), x-ray map (NASA/CXC/CfA/M.Markevitch et al.) and mass distribution from gravitational lensing (NASA/STScI; ESO WFI; Magellan/U.Arizona/D.Clowe et al.). The major mass constituents, dominated by pervading dark matter (marked in blue), are separated from colliding and interacting intergalactic medium (red colour). Find more explanation in text.

**Figure 1.4:** Angular power spectrum of temperature anisotropies on the CMB sky map measured by the *Planck* satellite experiment [7]. From a global fit of the 6-parametric  $\Lambda$ CDM cosmologic model to the position and relative height of the angular resonances, the dark matter density as of today can be inferred amongst others.



remarkably the collision of two galaxy clusters and how the mass composition splits into two components: While the two mass centres, reconstructed from gravitational lensing (coloured blue), have pervaded apparently unaffected, a bright emission in the x-rays from crashing intergalactical gas clouds is observed at the same time (red hue). It is interpreted such that ordinary matter with its implied charge interactions has been separated from almost collisionless particles, which incorporate the bulk of the total mass distribution. This stringently adds to the already established notion that dark matter interacts gravitationally, maybe weakly but certainly not electromagnetically, including the emission of detectable photons.

Besides evident indications for the general existence of some dark matter component there had been missing for long an universal quantification of its density in comparison to ordinary matter. Like hardly any other has the discovery of the cosmic microwave background (CMB) radiation by Penzias and Wilson in 1965 prepared the ground for cosmology to promote from a fairly qualitative to an “exact” field of science. It turned out that the map of temperature fluctuations in the relic radiation – nothing but a photograph of the universe when it became transparent for optical wavelengths about 400 000 years after the Big Bang – encodes the matter filaments of the earliest times. With the expansion of space since then, the radiation has thermally cooled down to 2.725 K today and it became

possible to extract a high-resolution map of anisotropies of this temperature on the level of few  $\mu\text{K}$  in all directions of the sky. Beginning from the primordial matter distribution, the formation of structure, as observed now in form of galaxies and clusters, has evolved. By evaluating the power spectrum of fluctuations (essentially a decomposition of the temperature map into spherical harmonics) one is sensitive for example to the current baryonic ( $\Omega_b h^2$ ), dark matter ( $\Omega_c h^2$ ) and dark energy ( $\Omega_\Lambda$ ) densities. The first precision measurement was provided by the COBE satellite experiment [8] but was excelled in resolution some years later by the results from WMAP [9]. And just at the time of writing, the most recent *Planck* experiment has published first results of its sky survey with unprecedented precision. Mainly these CMB measurements (supported among others by results from the study of Big Bang nucleosynthesis (BBN) or baryon acoustic oscillation) allow for a precise quoting of the most dominant ingredients of our Universe today (data from *Planck* 2013 [7]):

$$\Omega_b h^2 = 0.02207 \pm 0.00033, \quad \Omega_c h^2 = 0.1196 \pm 0.0031, \quad \Omega_\Lambda = 0.686 \pm 0.020 .$$

The first two quantities are thereby normalized to the Hubble constant via  $H_0 = 100 h \text{ km s}^{-1} \text{ Mpc}^{-1}$ . According to this, the total energy density of an assumingly flat Universe comprises  $\sim 70\%$  dark energy,  $\sim 25\%$  dark matter and only  $\sim 5\%$  of ordinary matter. The amount of radiation energy density has meanwhile dropped to an almost insignificant level after it dominated the early stage of the universe expansion. This realization raises a major question: what are these unknown components made of and how could we ever prove their existence directly? We are seeking for partial answers in the following subsections, referring only to the dark matter case.

## 1.2 Particle candidates

The astrophysical observations already set important constraints for potential dark matter candidates. We saw that they must be prone to gravitation and at most weakly self-interacting because otherwise phenomena like the bullet cluster could hardly be understood. Baryons do not provide a sufficient answer because their amount is restricted by the existing model of nucleosynthesis and the measured abundances of light elements in space, as well as from the mentioned CMB results. Besides we can assume that dark matter couples to photons only extremely weakly since otherwise light absorption or electromagnetic interaction with the hot interstellar medium would be seen.

These arguments would point immediately to a long known particle candidate, the neutrino, were its abundance not tightly constraint to far lower density from CMB data. Even when neglecting this argument for a while, neutrinos cannot provide an explanation of observed structure formation on the galactic and intergalactic scales. This statement is supported by N-body computer simulations, trying to understand galaxy cluster formation on very large scales, such as the Millenium [10] or Via Lactea [11] simulation. They require dark matter to be massive and non-relativistic in order to reproduce the astronomically observed clumps and filaments of the visible matter in the Universe.

## 1.3 The WIMP coincidence

It seems necessary to extent the group of candidates beyond the Standard Model (SM) of physics. What is ideally needed is a non-baryonic particle, which is stable over the age of the Universe, and yields the right abundance starting from thermal reactions in the early stage of space and time. A possible way to generate a fixed amount of a specific matter density is given by the concept of freeze-out, which is already successful at explaining the photon decoupling (today observed in CMB radiation)

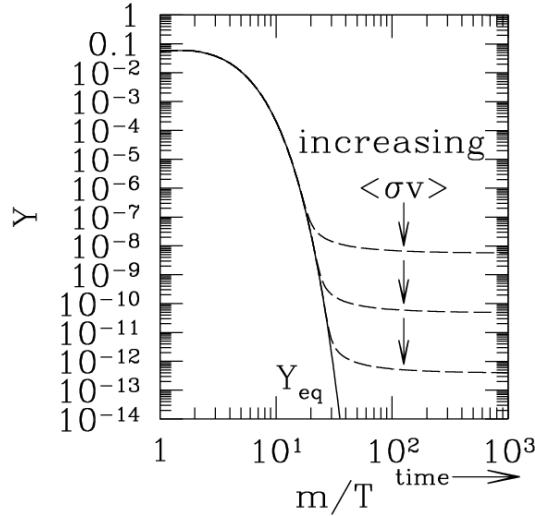


**Figure 1.5:** Evolution of the dark matter number density (here normalized by the entropy density  $s$  via  $Y = n/s$ ) as a function of mass over temperature in the universe (proportional to increasing time after the Big Bang). Different assumed annihilation cross-sections  $\langle \sigma_{ann} v \rangle$  lead to differing relic dark matter number densities. Figure from [12].

and the production of nuclei (now traced from the abundance of light elements). At times when the Universe was in a hot dense plasma state, the temperature and energy density were high enough to enable a chemical equilibrium between creation and annihilation reactions between various particle and radiation species. For example, a dark matter particle  $\chi$  could transform into other fermions or bosons of the Standard Model by colliding with its anti-partner and be produced vice versa [12],

$$\chi\bar{\chi} \leftrightarrow f\bar{f}, W^+W^-, HH, \dots \quad (1.1)$$

The annihilation rate  $R_{ann} = \langle \sigma_{ann} v \rangle n$  is thereby determined by the thermal average over the self-interaction cross-section  $\sigma_{ann}$  and the relative velocity  $v$  of dark matter particles, as well as their number density  $n$ . For the opposite reaction it is necessary that the available kinetic energy of colliding particles is large enough to exceed the mass threshold of generating a  $\chi\bar{\chi}$  pair in the final state. During the equilibrium, the energy distribution is assumed to follow the Boltzmann factor  $e^{-E/k_B T}$  and thus, only events in the high tail stay able to participate while the temperature  $T$  drops. Finally, when the universal expansion rate becomes larger than the annihilation rate, the remaining dark matter particles freeze out simply because it becomes so unlikely for two candidates to meet and annihilate. This moment defines the persisting particle number inside a comoving volume. The evolution is illustrated in Fig. 1.5, where the number density is drawn as a function of  $1/T$ , proportional to the time passed after perfect equilibrium. From the detailed calculation of the abundance evolution, the freeze out temperature (in units of energy or mass) is expected around  $T_f \approx m_\chi/20$ , as shown in the plot. The remaining number density  $n$  after this moment depends critically on the annihilation rate before the freeze-out and comes out smaller for increasing  $\langle \sigma_{ann} v \rangle$ . Considering the further time evolution of the Universe according to the successful  $\Lambda$ CDM model, the relic dark matter density as of today,  $\Omega_\chi h^2$  can be inferred and the underlying calculations simplify to [12, 13]

$$\Omega_\chi h^2 \approx \frac{3 \times 10^{-27} \text{ cm}^3 \text{ s}^{-1}}{\langle \sigma_{ann} v \rangle} \quad (1.2)$$

It can be considered a great coincidence that this equation yields the right order of magnitude for the relic dark matter abundance if one assumes a particle with mass  $m_\chi$  and annihilation cross-section

$\langle\sigma_{ann}v\rangle$  typical for the electroweak scale. This circumstance has born the generic idea of a weakly interacting massive particle, the WIMP [14, 13], which has become one of the most favoured dark matter candidates. One must admit, however, that Eq. (1.2) is based on the assumption that our understanding of the Universe expansion can be extrapolated to the time before BBN had happened.

Not only on the cosmological side of physics a certain interest on the WIMP has aroused as a consequence. Also on the other side, high energy physicists are seeking for signs of new particles at or above the electroweak scale. The question has thus to be answered how the WIMP can be implemented into extensions of the Standard Model. Among many potential solutions, Supersymmetry (SUSY), which attributes each fermion of the SM a supersymmetric boson and vice versa, is still considered one of the most natural proposals. In its minimal symmetric formulation, named MSSM, it requires a certain parity to be conserved at interaction vertices. This constraint permits the decay of a supersymmetric particle solely into SM constituents, and implies the existence of a lightest SUSY particle (LSP), which defies disintegration and can remain stable over time. Among few alternatives, the most prominent LSP is the lightest neutralino, which is uncharged under electromagnetic or strong interaction. It defines the standard WIMP realization that many particle and astro-particle physicists hope to discover one day.

It must be emphasized that WIMPs are by far not the only considered candidates. The fact that the appearance of other MSSM particles at collider searches like the LHC can so far only be excluded and that there are still large uncertainties in the cosmological arguments mentioned before, makes people conscious of alternatives. Among them are ideas about Axions, Kaluza-Klein dark matter or sterile neutrinos (reviewed e.g. in [15]). For the scope of this thesis they only play a minor role and we continue with an outline of detection techniques for WIMP search.

## 1.4 Detection techniques

There are three generic WIMP coupling channels to ordinary matter, illustrated in Fig. 1.6, and each is connected to a different detection techniques, dependent on the direction in which the graph is read.

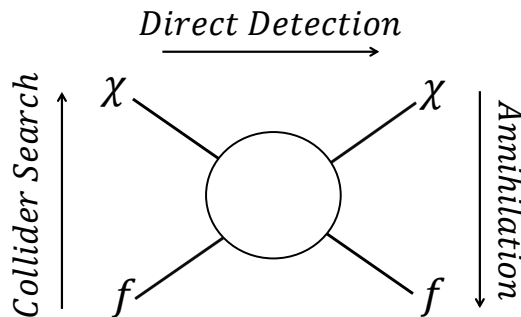


**Figure 1.6:** Scheme of potential WIMP ( $\chi$ ) interactions with fermionic particles ( $f$ ).

For example considering the upward direction of Fig. 1.6, WIMPs could be produced by the energetic collision of two fermions, such as  $q\bar{q}$  pairs at the Large Hadron Collider (LHC). In this process, heavy SUSY particles could be produced and subsequently decay via cascades into the LSP. The signature left to the detector would consist of many quark jets, leptons and – most importantly – missing transverse momentum which is carried away by the untraceable neutralino. So far, no evidence

for such a decay scheme was found but exclusion limits were placed on potential WIMP topologies [16, 17]. Even if successful, collider experiments alone can never prove the stability of the disappearing particle beyond the traveling time through the detector. This would leave the question open if the particle is the same which has survived in our Universe since the beginning – a crucial criterion for the characterization of a dark matter WIMP.

Another way to read the given diagram is in downward direction and to search for an annihilation signal. Among potential final state scenarios is the production of two  $\gamma$  ray photons, mediated by a one-loop process, at the energy of the dark matter particle’s rest mass. The observation of a distinct  $\gamma$  line on top of the otherwise featureless spectrum would yield smoking-gun evidence for the annihilation of dark matter in our Galaxy. Recent evaluation of data [18] from the *Fermi* satellite experiment, a  $\gamma$  ray space telescope in the Earth’s orbit, spotted indeed hints at the appearance of such a line when directing the telescope towards our galactic centre, where the bulk of dark matter distribution would be expected. However, the global significance is still insufficient to speak about a signal and also more cross-checks are needed to exclude detector related artifacts which could pretend to give a  $\gamma$ -like feature.

The third method is measuring the WIMP scattering off an atomic nucleus. The discovery of a recoil signal would prove and probe the direct coupling to constituents of the ordinary matter. Since the dark matter is believed to be heavy and travel at non-relativistic speed, the expected recoil energies are only on the scale of few to tens of keV, depending also on the mass of the target atoms. This makes it challenging to fight against natural sources of background and – even in case of success – extract precise information about the WIMP particle mass.

As often, the entire picture of the WIMP hypothesis and its various parameters can be revealed best by the combination of all three techniques and making use of their complementarity. So far, none of the mentioned routes have yielded an unambiguous answer to the WIMP question. Since the direct detection is clearly in the focus of the present work we continue with the discussion of how a WIMP signature is supposed to look like when scattering off well-known matter and at which frequency such an interaction could be expected.

## 1.5 WIMP recoil rates in direct search experiments

The principle behind direct dark matter search is as old as scattering experiments in general but it comes with a certain clue. About 100 years ago it was Rutherford to conduct a seminal experiment in order to infer information about the structure of ordinary matter by studying the scattering of “known”  $\alpha$  particles. Since then our knowledge about the nuclear composition of matter has grown enough to be ready to turn the argument and investigate properties of “unknown” projectiles through their scattering off a well-understood target.

The hypothesis that WIMPs are massive and move non-relativistic keeps the calculation of interaction rates relatively simple. We start from the generic formula which connects the observed event rate  $dN/dt$  in any detector with the probability for an interaction between two scattering particles  $\sigma$ , mediated by the so-called luminosity  $L$ ,

$$\frac{dN}{dt} = \sigma \cdot L . \quad (1.3)$$

The right hand side is factorized into two parts: The cross-section  $\sigma$  encodes the *particle physics* description of interactions between target and projectile. The luminosity  $L$  is determined by the kinematics of the scattering particles, which is influenced by *astrophysical* assumptions in case of WIMPs.

In our context,  $L$  is the product of fixed target atoms  $N_T$  and the flux  $F_\chi = n_\chi \langle v \rangle$  of WIMPs passing through the detector with particle density  $n_\chi = \rho_0/m_\chi$  and mean velocity  $\langle v \rangle$ . Thereby,  $m_\chi$  is the WIMP mass and  $\rho_0$  is the assumed dark matter density at the Earth's local position in the Milky Way. The latter is usually inferred from combining halo model assumptions and galactic N-body simulations with actual measurements of the rotation curve [19]. The predicted value depends, among others, on the assumed dark matter profile. To allow for comparison between results from different experiments, a common value  $\rho_0 = 0.3 \text{ GeV/cm}^3$  is assumed because it has been found a reasonable choice under spherical halo distribution assumptions (e.g. [20]). The remaining, relatively large uncertainties linearly translate into the predicted recoil rate.

Typically one is interested in the dependence on the transferred nuclear recoil energy  $E_{nr}$  and normalizes the rate to the total mass of the target  $M_T$  to allow for inter-comparison of different experiments. We call the arising quantity the differential event rate  $dR/dE_{nr}$  and note that it is usually quoted in units of  $\text{kg}^{-1}\text{keV}^{-1}\text{day}^{-1}$ . This enables us to continue from Eq. (1.3) as follows:

$$\frac{dR}{dE_{nr}} \equiv \frac{1}{M_T} \frac{d^2 N}{dE_{nr} dt} \approx \frac{d\sigma(E_{nr}, v)}{dE_{nr}} \cdot \frac{\rho_0}{m_N m_\chi} \langle v \rangle, \quad (1.4)$$

where the new variable  $m_N$  denotes the mass of a single target nucleus. We generally expect the cross-section to be both a function recoil energy  $E_{nr}$  and the incoming particle velocity  $v$ . We must further consider that  $v$  follows a certain probability distribution  $f(v)$  and therefore have to write Eq. (1.4) in its correct notation,

$$\frac{dR}{dE_{nr}} = \frac{\rho_0}{m_N m_\chi} \cdot \int_{v_{\min}(E_{nr})}^{v_{\text{esc}}} v f(v) \cdot \frac{d\sigma(E_{nr}, v)}{dE_{nr}} dv. \quad (1.5)$$

The speed distribution  $f(v)$  in the standard dark matter halo model is parameterized by a Maxwellian function with a mean velocity dispersion of  $v_0 = (220 \pm 20) \text{ km/s}$  [21] which is appropriate for an isothermal sphere, centered in the rest frame of our Galaxy. It has to be transferred into the local coordinate system of earthbound experiments, considering the motion of our solar system and the Earth's orbit therein. The latter is responsible for the expected WIMP rate to be sinusoidally modulated within the period of one year but its amplitude limited by the ratio of the maximum Earth velocity  $v_E \approx \pm 30 \text{ km/s}$  with respect to the solar system motion at  $\sim 220 \text{ km/s}$  [21] around the galactic centre.

The integral boundaries are non-trivial because of the following reasons: the lower limit  $v_{\min}(E_{nr})$  is the minimal velocity of the incoming WIMP particle to cause an energy transfer of  $E_{nr}$  via  $180^\circ$  back-scattering off the target nucleus and can be classically calculated as

$$v_{\min}(E_{nr}) = \sqrt{\frac{m_N E_{nr}}{2\mu^2}}, \quad (1.6)$$

where we have used the reduced mass notation  $\mu = m_N m_\chi / (m_N + m_\chi)$  for simplification. The upper bound is set by the maximum velocity at which WIMPs are still gravitationally bound inside the galactic halo, i.e. the escape velocity. Its value is commonly assumed  $v_{\text{esc}} = 544 \text{ km/s}$  [22]. These combined are often referred to as astrophysical standard assumptions but it is important to note that they are not set in stone. Many model deviations are under current discussion [23] and can eventually impact the interpretation of direct detection sensitivity or signal claims.

Beside the astrophysical aspects we want to briefly discuss the particle physics content, subsumed by the differential interaction cross-section  $d\sigma/dE_{nr}$ . It ultimately arises from the WIMP coupling to quarks, the constituents of protons and neutrons which form the target nucleus. Depending on whether one assumes an axial current mediation or an scalar-scalar coupling of the participating quantum fields, one ends up with a spin-dependent (SD) or spin-independent (SI) description of the cross-section. For the context of the present work we want to focus on the spin-independent case. By accounting for the coherent effect of the single nucleons making up to the entire nucleus by means of a nuclear form factor  $F(E_{nr})$  one can write the differential SI cross-section as [19]

$$\frac{d\sigma_{SI}}{dE_{nr}} = \frac{m_N}{2\mu^2 v^2} F^2(E_{nr}) \sigma_0 . \quad (1.7)$$

The form factor, essentially the Fourier transform of the nucleon density, is given as a function of the momentum transfer  $q$  and therefore implicitly dependent on  $E_{nr}$ . Typical parameterizations are developed e.g. in [24] and reviewed in [25]. What remains to discuss is the coupling to the individual nuclear constituents, i.e. protons and neutrons. Concerning the scalar interaction, it can be expressed by [26]

$$\sigma_0 = \frac{[Zf^p + (A - Z)f^n]^2 \mu^2}{(f^p)^2 \mu_p^2} \sigma_p^{SI} , \quad (1.8)$$

with neutron number  $(A - Z)$  and proton number  $Z$ , connected to their respective parton density functions  $f^n$  and  $f^p$ , which sum over the contained quark contributions. The factor  $\mu_p$  is the reduced mass in the WIMP-proton system and  $\sigma_p^{SI}$  appears decoupled as the WIMP-proton cross-section. One can approximately assume equal sharing between protons and neutrons,  $f^n \approx f^p$ , and therefore summarize

$$\frac{d\sigma_{SI}}{dE_{nr}} = \frac{m_N A^2}{2\mu_p^2 v^2} F^2(E_{nr}) \sigma_p^{SI} . \quad (1.9)$$

An immediate conclusion is that the SI interaction probability scales with the square of the atomic mass number  $A$  and the expected detection rate is therefore enhanced quadratically by the use of heavy target elements – a fact that is fortunate for the choice of xenon for example ( $A \approx 131$ ).

We summarize the final result by plugging Eq. (1.9) into Eq. (1.5). Under the assumptions made, the cross-section does no longer depend on the velocity  $v$  and can be pulled in front of the integral, leading to the simplified expression from [27]

$$\frac{dR}{dE_{nr}} = \frac{\rho_0 A^2}{2\mu_p^2 m_\chi} F^2(E_{nr}) \sigma_p^{SI} \int_{v_{\min}(E_{nr})}^{v_{\text{esc}}} \frac{f(v)}{v} dv . \quad (1.10)$$

The differential rate as a function of recoil energy, on the left hand side, can be measured in direct detection experiments and tested against the model contained on the right. Typically, one defines an energy region  $[E_{\min}, E_{\max}]$  and counts the observed signal events within a certain measurement time  $T$  by employing a total target mass  $M$ . The expected number of events  $N$  is thus

$$N(m_\chi, \sigma_p^{SI}) = T M \int_{E_{\min}}^{E_{\max}} \frac{dR}{dE_{nr}} dE_{nr} . \quad (1.11)$$

and solely parameterized by the assumed WIMP mass  $m_\chi$  and the WIMP-nucleon interaction cross-section (the coupling to protons and neutrons is considered equal in this calculation). This is why the typical parameter space, in which direct experiments report their results, is spanned by these two

quantities. If no significant signal excess over background is observed, the same formula enters the calculation of exclusion limits, which are then implicit functions of  $\sigma_{\chi N}^{SI}$  and  $m_\chi$ .

In Fig. 1.7 we present a comparison of expected differential rates for various target materials, assuming a WIMP mass of  $m_\chi = 100 \text{ GeV}/c^2$  and  $\sigma_{\chi N}^{SI} = 1 \times 10^{-44} \text{ cm}^2$ . All spectra have in common

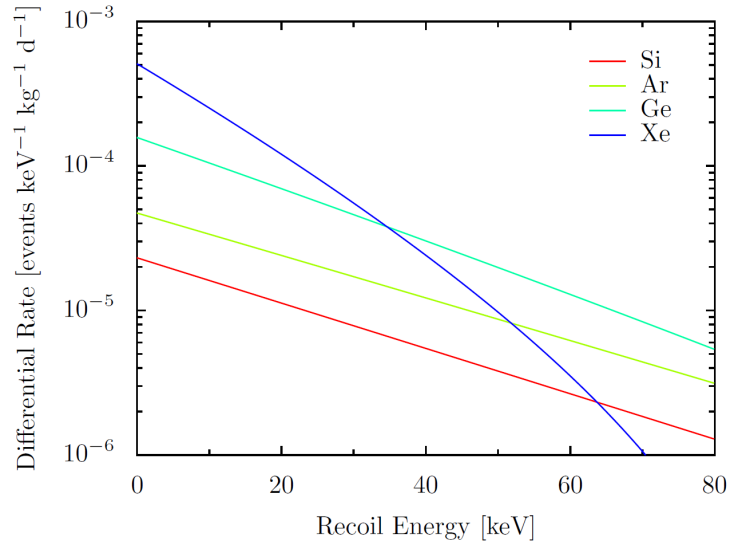


**Figure 1.7:** Comparison of predicted differential event rates for various target materials, assuming  $m_\chi = 100 \text{ GeV}/c^2$  and  $\sigma_{\chi N}^{SI} = 10^{-44} \text{ cm}^2$ . The overall event number scales with  $A^2$  and favors heavy target elements over lighter ones. Besides, the shape of the nuclear form factor can additionally influence the rate expectation – obvious in the case of Xe. Figure adopted from [28].

that the predicted event number is roughly exponentially falling with increasing deposited recoil energy – a consequence of the form factor contribution  $F(E_{nr})$  and the fact that only WIMPs in the high energy tail of the velocity distribution  $f(v)$  can induce a large energy transfer. As expected, the rate generally scales with  $A^2$ , which explains the enhancement of using xenon over other target materials for energies up to  $\sim 40 \text{ keV}$ . Towards higher energies, the nuclear coherence effects,  $F(E_{nr})$ , lead to a faster decline in case of xenon.

The differential rate equation (1.10) will be used in Sec. 5.6 when we simulate the response of the XENON100 detector to WIMP induced nuclear recoils. It is also applied in the general interpretation of SI results from the XENON100 dark matter search, as briefly summarized in Sec. 2.5.

## 1.6 Direct detection experiments

Having presented the basic concept of WIMP detection in a fixed target experiment we conclude with a short outline of existing experimental realizations and comment on their advantages and drawbacks. There are several generic possibilities to measure energy depositions down to the range of few keV – defined by their applied signal read-out channel(s): heat (phonons), charge (electron-hole pairs) or scintillation light (photons).

The fraction of recoil energy expended into heat can be determined by cryogenic phonon sensors, which translate tiny changes of temperature into an electronic signal. Due to the small excitation level, a large number of information carriers is produced per amount of energy and, consequently, a very high resolution can be reached.

In different approaches, electronic excitations can be used to extract an ionization and scintillation signal proportional to the underlying energy release. Typically few or tens of eV must be expended to create one electron-hole pair or a single scintillation photon, respectively. The achievable energy resolution is therefore somewhat worse in the ionization channel and considerably reduced in the light signal. The negative effect for the latter is increased by the finite collection and quantum efficiency appearing in context with photon counting.

Only sufficient energy resolution is not the single key for dark matter search. At least equally important is the ability to separate natural background radiation, caused for example by radioactive decay or cosmic rays, from potential WIMP signal events. It was found very advantageous to combine at least two of the above mentioned techniques in the same detector in order to make use of the discrimination power given by the ratio of the signal channels: since the stopping mechanism of recoiling nuclei, as implied by neutral particles like WIMPs, is generally distinct from energy loss through direct electronic excitation, the ratio is expected to be different for both major classes of signal and electromagnetic background. Today, there are many experiments adopting possible two-fold combinations of read-out channels:

Among the ionization-phonon detectors is the CDMS experiment [29] operating high purity germanium crystals at cryogenic temperature. The method provides excellent discrimination between electronic recoil background and potential WIMP signals, only little disturbed by possible leakage of surface events due to incomplete charge carrier collection at the edges of the crystals. The experiment has for long led the field of SI WIMP search. The direct competitor is the EDELWEISS experiment [30], employing a very similar method.

A multi-target approach is taken by the CRESST experiment [31], which measures both phonon and scintillation signals arising from excitations in a  $\text{CaWO}_4$  crystal. Since different elements are involved in the detector material, distinct nuclear recoil signatures unfold depending on whether a WIMP scatters on calcium, tungsten or oxygen. Once a discovery was made, this variety would allow for more accurate constraints on the relevant WIMP parameters  $m_\chi$  and  $\sigma_{\chi N}^{SI}$ . In 2012 the CRESST collaboration has reported a significant excess of events in the so-called tungsten band, which in principle allows for a positive dark matter interpretation [32]. However, serious doubts remain if the excess signature could also be caused by underestimation of the expected background rate, for example related to  $\alpha$  events at the crystal surface.

Simultaneous measurement of scintillation light and ionization charge is particularly employed by liquid noble gas detectors, such as the XENON100 [33], ZEPPLIN-III [34] or LUX [35] experiments. One of their greatest advantages is the scalability towards large detector volumes combined with a high density of the target material. It directly enters the detector exposure, the product of measuring

time  $T$  and active detector mass  $M$ , and enhances linearly the number of total WIMP expectation, as given by Eq. (1.11). Especially in case of using xenon, the high stopping power (implied by the large charge number  $Z$  and high liquid density of  $\rho \approx 3 \text{ g/cm}^3$ ) allows for efficient self-shielding against external radiation and provides a very clean inner detector volume. At the same time, xenon is composed solely of naturally stable isotopes, except for the rare double-beta decay of  $^{136}\text{Xe}$ . Among other noble liquid candidates it also provides the best charge and light yield per given energy absorption [36]. However, the technique as a whole suffers from a worse recoil discrimination power as opposed to ionization-phonon or scintillation-phonon detectors. By using liquid argon, like in the WArP [37] or future DarkSide [38] detectors, this drawback can be partly compensated by applying pulse shape analysis on the prompt scintillation signal in order to distinguish between electronic and nuclear recoils.

It may be a coincidence or not that the most prominent signal claims for WIMP interaction are placed by experiments which exploit only one single ionization read-out channel and have no generic means for recoil distinction. In both cases the WIMP hypothesis is derived from an annual modulation on top of the measured background rate. As briefly mentioned before, the relative motion of the Earth around the Sun leads to a  $\sim 15\%$  boost of the mean relative WIMP velocity in summer and respective decrease in winter. The certain background modulation has been recorded in the NaI detectors of the DAMA/LIBRA experiment [39] during many years of operation. A similar - though not entirely consistent - one-year variation was recently reported from the CoGeNT collaboration [40], which operates a p-type point-contact germanium detector with very low energy threshold. Both their results remain in contradiction with the null-observation of other experiments, like CDMS-II [41] or XENON100 [42].

Equally designed as single channel detectors are those experiments probing in particular the spin-dependent WIMP-nucleon scattering, such as PICASSO [43] or COUPP [44]. They employ target materials with high nuclear spin momentum, like fluorine, and are operated as superheated acoustical or optical bubble chambers. The creation of observable bubbles requires a large ionization density as only sufficiently caused by nuclear recoil interaction and turns out as an effective tool against radiation backgrounds.

As illustrated only with the above examples, a broad experimental field of science has evolved, including partly complementary or competing detection technologies. They all have in common to search for extremely rare events and struggle against all sorts of natural background radiation. With the current generation of experiments, however, it has become possible for the first time to probe those parameter regions favoured by native ideas of a WIMP at the electroweak scale and to find out whether it can provide a convincing answer to the quest of dark matter in the universe.

One particular experiment searching for direct evidence of WIMP interactions is called XENON100. We continue from here with a more detailed introduction to its detection principle and reported results because it provides the overall framework to the main part of this thesis.

# The XENON100 Experiment

Starting from the first proposal [45] of making use of a dual phase time-projection chamber (TPC) for dark matter detection in 1989, the technology applied in the currently operated XENON100 detector has developed over already more than 20 years. The current experiment is the successor of the prototype XENON10 detector [46], which was installed at the same place in the Gran Sasso underground facility (LNGS), Italy, and at that time the first noble liquid detector to compete with the sensitivity of the ionization-phonon technology in the search for dark matter [28]. Thanks to the achievement to scale the proven detection technique from 10 kg to  $\sim 100$  kg of target mass within only few years, the XENON100 experiment has set the benchmark sensitivity for standard assumption WIMPs at the time of writing [47, 42].

In this chapter we provide a brief introduction to the radiation detection principles of dual-phase noble gas chambers and the creation of detectable signals therein. We continue with a description of the XENON100 experimental setup, data acquisition and detector calibration. The following section is supposed to generally introduce tools of data analysis essential for the understanding of the main parts of the present thesis. They are also needed for the summary of recent scientific results on dark matter search by the XENON100 collaboration, presented in the last section of this chapter.

## 2.1 Detection principle of a two-phase xenon TPC

Liquefied xenon (LXe) is a suitable radiation detection material because it has the ability to scintillate and become ionized by interactions with charged particles or  $\gamma$  rays. This property can be optimally utilized in a setup as shown in Fig. 2.1. An inner cylindrical chamber is thereby immersed into a cryogenic vessel, equally filled with LXe, and closed on top with a diving bell structure [33]. This allows to maintain a liquid/gas interface in the upper part of the inner cage. Therein, two electric fields of different strength are applied: One is the moderate drift field of  $\sim 1$  kV/cm across the liquid phase between cathode and ground mesh (gate grid), and another is the extraction field  $\gtrsim 10$  kV/cm across only few mm distance in the gaseous xenon (GXe), between ground mesh and anode grid. Two arrays of photomultiplier tubes (PMT) are employed inside the LXe and above the anode mesh in the gaseous phase, in order to monitor the inner target volume from two sides – top and bottom – of the inner chamber.

After any interaction in the LXe target two distinct signal types are created. Direct scintillation light (S1) at vacuum-ultraviolet (VUV) wavelength is promptly emitted after few nanoseconds and is detected by the photo-sensors after traveling through the enclosed chamber surrounded by VUV reflective polytetrafluoroethylene (PTFE, trademark Teflon<sup>®</sup>) walls. At the same time, ionization electrons are drifted from the initial vertex opposite to the direction of the applied external field towards the phase boundary. Arriving at the grounded gate grid they are extracted into the gas phase by the much stronger anode field. Its strength in the GXe is adjusted such that the electrons are re-accelerated between recoils with the xenon atoms and create proportional scintillation light along excitation/ion-

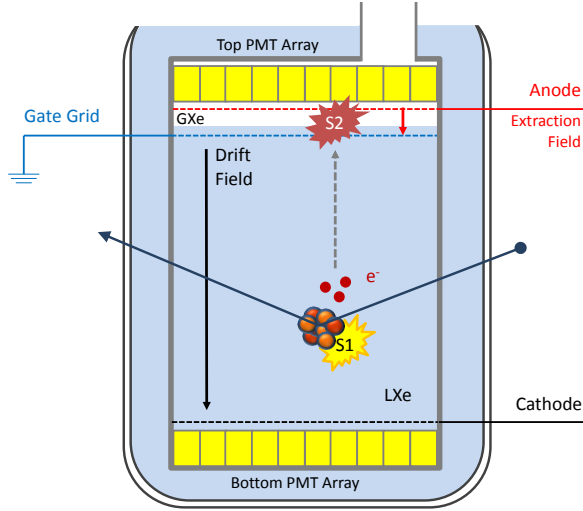


**Figure 2.1:** Detection principle of a two-phase time projection chamber (TPC). Interactions in the liquid xenon volume (LXe) create both prompt scintillation light (S1) and ionization electrons. In the applied electrical field the electrons are drifted parallel to the field lines until they reach the liquid/gas interface. Extracted into the gaseous xenon (GXe) by a much stronger field they generate secondary amplified scintillation signal (S2). The time difference between S1 and S2 can be mapped to the height of the vertical event position.

ization tracks through the gas gap. This provides a secondary, amplified signal (S2) which enables to reconstruct the original event location along the vertical direction by measuring the time difference  $dt$  between S1 and S2 signals. It can be translated into a physical drift length of electrons parallel to the electric field lines from the interaction vertex to the liquid surface. This justifies labeling the inner structure, enclosed by the PTFE walls and the PMT arrays, a time projection chamber (TPC) because the time gap  $dt$  is mapped to a spatial coordinate. In addition, the position in the perpendicular plane can be derived from the S2 hit pattern on the top PMT array, as explained in more detail in Sec. 2.1.4.

We continue first with a more detailed discussion of the signal creation processes in LXe and return afterwards to the realization of the TPC principle in the XENON100 detector design.

### 2.1.1 Scintillation and ionization in liquid xenon

Featuring an electronic band structure, liquid xenon and other liquefied rare gases share some electrical properties with semi-conductors due to the large gap between their valence and conduction band [48, 49]. Incoming radiation or particles produce ionized and excited atoms (so called excitons) along their track. The excitons  $\text{Xe}^*$  can subsequently collide with surrounding xenon atoms and form excited molecular states  $\text{Xe}_2^*$ , named excited dimers or excimers. When they decay to the ground level, vacuum ultraviolet (VUV) scintillation light is emitted at a mean wavelength of 178 nm [50, 51, 36]:



Emitted electrons from the ionization process can either recombine with surrounding ions or escape. This effect is balanced by the presence of an externally applied electric field and also depends on the geometrical track structure of different types of ionizing particles [36]. Recombination provides another possibility to produce excitons apart from direct excitation:



After  $\text{Xe}^*$  has been formed in this way it adds to the creation of scintillation light according to Eq. (2.2). Regardless of the production mode, the light emission occurs very fast on the timescale of few to tens of nanoseconds, depending on whether the excimers occupy a singlet or triplet state [36]. For  $\alpha$  particles two decay time components were measured to be 4.2 ns and 22 ns, respectively [52]. Slight deviations are observed for relativistic electrons [50] and it is also found that the applied electric field affects the partition of excitation states and thus the effective relaxation time [52]. However opposite to liquid argon scintillators, the difference in time constants is not pronounced enough to allow for particle identification by means of pulse-shape analysis [52].

The partition into charge and light carriers is controlled by the recombination probability of emitted electrons. In principle the number  $N_{ex}$  of excimers available to cause scintillation can be expressed as [53]

$$N_{ex} = N'_{ex} + r N_i, \quad (2.6)$$

where  $N'_{ex}$  is the number of immediately produced excited states,  $N_i$  the number of electron-ion pairs and  $r \in [0, 1]$  the probability for an electron to recombine and add another excited state. It is further assumed [53] that the efficiency of emitting a scintillation photon by an excited state – irrespective of whether formed directly or after recombination – is approximately 100 % and therefore allows the number of produced scintillation photons to be written  $N_{ph} = N_{ex}$ .

Complementary, the number of charge carriers  $N_q$  which are drifted away from the point of interaction by an external electric field is given by the fraction of electrons that escape recombination:

$$N_q = (1 - r) N_i. \quad (2.7)$$

While the ratio of  $N'_{ex}/N_i$  is expected to be constant over a wide range of recoil energies [54] the escape fraction  $(1 - r)$  depends on energy transfer and the ionization track structure. Alpha particles, as explicitly studied in Chapter 4, lose their energy in almost point-like interactions, leaving electrons behind in a dense concentration, and imply high recombination rates even in strong extraction fields [55]. In contrast,  $\gamma$  radiation undergoes Compton scattering with multiple steps at different interaction sites, thereby enhancing the effective charge yield.

Obviously, the more the ratio of  $N'_{ex}/N_i$  is shifted in favour of produced electron-ion pairs  $N_i$  the stronger appears the interplay – or more precisely, the anti-correlation – of charge and light signals. For ionizing radiation the number of ions typically exceeds the number of excited states by far:  $N'_{ex}/N_i \approx 0.06$  [54]. Consequently, one observes a dominant anti-correlation in the measured amount of light and charge for electron or  $\gamma$  absorption in LXe. For nuclear recoils, as induced by neutrons, this effect is much less pronounced, finding the same ratio to be  $\approx 1.09$  [56] and thus the two modes, direct excitation and recombination-driven scintillation, are almost equally balanced.

Up to this point we have only explained how the transferred energy of ionizing radiation is expended into photons and electrons but not yet defined how they translate into the observable quantities S1 and S2. We want to catch this up swiftly in the next section.

### 2.1.2 Primary scintillation light (S1)

Not all of the scintillation photons emitted inside the LXe TPC contribute to the observed signal S1. Various effects are responsible for finally detecting only a few percent of the original amount of light. From the initial point of interaction, the photons travel through the liquid and gaseous xenon target, sometimes being repeatedly reflected at the cylindrical PTFE surrounding walls until they hit the photocathode of one of the PMTs or become absorbed otherwise. The latter effect comprises signal loss

due to the finite attenuation length in LXe and limited reflectivity for VUV photons at the walls and the liquid/gaseous interface. The attenuation depends mostly on the impurity concentration of those trace elements whose absorption bands overlap with the VUV spectrum, e.g. water vapor and oxygen [36]. During the detector operation those contaminants are constantly removed by a high temperature zirconium getter [33] inside a purification loop to guarantee both minimum scintillation opacity and maximum electron drift length needed to create a sufficient secondary signal. The combination of the mentioned effects defines the so-called light collection efficiency (LCE), which states the fraction of emitted light reaching the active windows of the photocathodes and depends on the emission position inside the TPC.

Besides geometrically implied light suppression, the quantum efficiency (QE) – i.e. the probability of converting incoming photons into photoelectrons – of the individual PMTs plays an important role. The light sensors applied in XENON100 show an average QE of 32% (24%) for the bottom (top) PMTs with a spread of few percent [33]. Those PMTs with highest efficiency are placed in the bottom array because the high refraction index of LXe implies most of the light to stay inside the liquid phase.

The signal resolution is dominated by the collection rather than initial production of the signal, given that the combined probability  $p = LCE \times QE$  for one photon to be detected out of  $N_{ph}$  emitted is only of order of a few percent. Consequently, the distribution of observed photo-electrons  $N_{S1}$  is expected to follow a Bernoulli trial  $\mathcal{B}(N_{S1}; N_{ph}, p)$ . In the limit of  $p$  being only a few percent and  $N_{ph}$  large compared to mean number of detected photons  $\mu_{S1} = pN_{ph}$ , one can approximate the distribution by a Poissonian, solely parameterized by its mean  $\mu_{S1}$ :

$$\mathcal{P}(N_{S1}; \mu_{S1}) = \frac{\mu_{S1}^{N_{S1}}}{N_{S1}!} e^{-\mu_{S1}}. \quad (2.8)$$

Finally, the produced photo-electrons are amplified by creating secondary avalanche electrons inside the PMTs. The so produced signal, summed over all contributing PMT channels, is defined as the observed  $S1^{obs}$ . In detail, this multiplication step is sufficiently described by a Gaussian approximation, treating the acceleration of photo-electrons by the PMTs as uncorrelated processes:

$$p_{S1}(S1^{obs}; N_{S1}, \sigma_{S1}) = \frac{1}{\sqrt{2\pi}\sigma_{S1}} \cdot \exp\left(-\frac{(S1^{obs} - N_{S1})^2}{2\sigma_{S1}^2}\right). \quad (2.9)$$

Thereby, the width  $\sigma_{S1}$  is connected to the single photoelectron PMT resolution  $\Delta_{PMT}$  via the square root of number of photoelectrons, i.e.  $\sigma_{S1} = \Delta_{PMT} \sqrt{N_{S1}}$ . From regular LED calibration measurements of the XENON100 PMTs, the average single photoelectron resolution is known to be  $\Delta_{PMT} \approx 0.5$  PE [57].

We have noted the mathematical description of S1 signal fluctuations in Eq. (2.8) and (2.9) explicitly because it will become relevant for the simulation of nuclear recoils in Chapter 5.

Because of the prompt scintillation decay time and the fast response of the PMTs, the S1 signal is confined within a narrow time window of typically few tens of nanoseconds. A typical waveform example is given in Fig. 2.2.

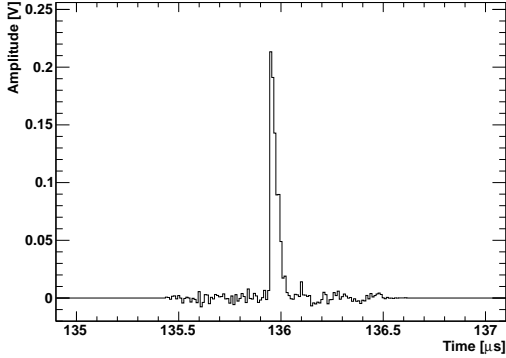


**Figure 2.2:** Example of an S1 pulse shape. Prompt scintillation and fast PMT response imply a narrow peak with an exponential decay slope of only few tens of ns. The pulse contains an integral amount of 53 PE.

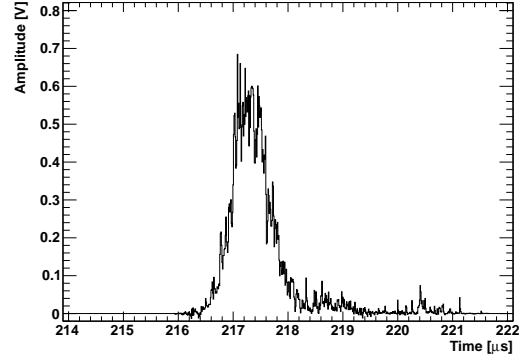


**Figure 2.3:** The S2 pulse shape features a much broader width due to electron cloud diffusion and secondary scintillation conversion. The example belongs to the same S1 shown in Fig. 2.2. The reconstructed S2 size corresponds to 2900 PE.

### 2.1.3 Secondary scintillation light (S2)

To infer information about the charge signal, the produced electrons have to be drifted away from the point of interaction towards the liquid surface where they are extracted into the gaseous phase and produce the proportional scintillation signal S2. On their track along the electrical field lines, some of them preferably attach to electronegative impurities, such as  $O_2$ ,  $SF_6$  or  $N_2O$ , and thus fail to contribute to the collective signal. The decrease of free electrons as function of time is proportional to the present electron number and the concentration of impurities dissolved in the LXe. Therefore, the time variation is exponentially falling and the amount of electrons  $N_q$  reaching the gas phase after drifting for the time interval  $dt$  [36] is

$$N_q(dt) = N_q(0) e^{-dt/\tau} . \quad (2.10)$$

The exponential constant  $\tau \equiv (k_s S)^{-1}$  is called *electron lifetime* and comprises the attachment rate  $k_s$  and impurity concentration  $S$ , assumed to be homogeneous in the LXe volume. In the constant electric field of the XENON100 detector the drift time  $dt$  is directly translated into the vertical  $z$  coordinate of the interaction vertex using the constant electron drift velocity  $v_d$ ,

$$z = v_d dt. \quad (2.11)$$

Therefore, the further the distance  $z$  from the liquid surface the more suppressed appears the number  $N_q$  of detectable electrons.

Once extracted into the GXe phase, it is well understood that at field strengths of several kV/cm, so-called proportional scintillation occurs [58]. The strongly accelerated electrons induce multiple scintillation photon emission along their way through the gas gap. Consequently, the total signal depends proportionally on the electron track length, the field strength and the vapor pressure [58, 59]. This effect must not be mistaken for actual electron-multiplication (avalanche signal) present only at even far stronger fields of  $\mathcal{O}(10^3 \text{ kV/cm})$ .

Continuing in the proportional regime, the observed secondary scintillation signal  $S2^{obs}$  is defined by the sum of collected photoelectrons from all PMT channels. The quantity is linearly related to the

number of extracted electrons via the gain factor  $g_{S2}$

$$S2^{obs} = g_{S2} N_q(dt) . \quad (2.12)$$

The gain factor  $g_{S2}$  describes the amplification through photons in the gas phase and depends on parameters describing the secondary amplification stage, e.g. size of the acceleration gap, anode voltage or GXe vapor pressure above the liquid phase. It encodes furthermore the collection and quantum efficiency of those PMTs converting the proportional scintillation light into photoelectrons. Typical values achieved in XENON100 are  $g_{S2} \approx 20 \text{ PE}/e^-$  depending on the specific xenon gas configuration and can be determined from in-situ measurements of the single electron S2 distribution [60].

For later use in Chapter 5 it is necessary to discuss how the  $S2^{obs}$  signal fluctuates. The large number of secondary photons implies that the accumulated signal distribution  $p_{S2}$  can be well approximated by Gaussian statistics, making the reasonable assumption that the total amplification is the direct sum of independent single electron contributions:

$$p_{S2}(S2^{obs}; g_{S2}N_q, \sigma_{S2}) = \frac{1}{\sqrt{2\pi}\sigma_{S2}} \cdot \exp\left(-\frac{(S2^{obs} - g_{S2}N_q)^2}{2\sigma_{S2}^2}\right) . \quad (2.13)$$

By definition,  $g_{S2}N_q$  is the expected mean value and the  $1\sigma$  width is proportional to the spread  $\Delta g_{S2}$  of the single electron S2 distribution and the square root of amplified electrons  $N_q$ , thus  $\sigma_{S2} = \Delta g_{S2} \sqrt{N_q}$ .

Diffusion of the drifting electron cloud and secondary amplification in the gas phase imply a much broader time spread of the S2 signals with respect to the narrow S1 pulses. Waveforms typically feature a Gaussian shape, like the example depicted in Fig. 2.3, and extend over 1–2 microseconds. In this way they can be well separated from S1 candidates by peak shape analysis of digitized waveforms.

### 2.1.4 Position reconstruction and signal correction

One of the major advantages of a two-phase detector is provided by the ability to determine particle interaction vertices in all three spatial dimensions with high accuracy. It is crucial for the selection of inner partial volumes (often called *fiducial volumes*, FV) and the consequent rejection of background radiation from surrounding detector materials and surfaces.

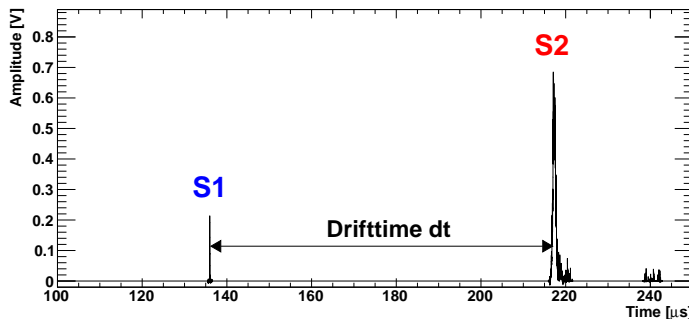
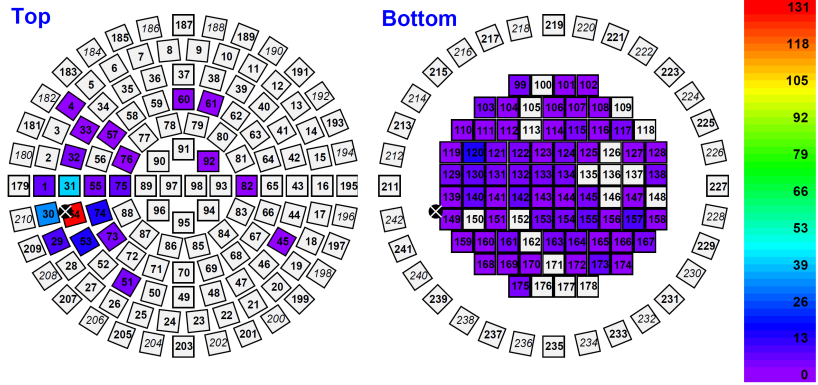


**Figure 2.4:** Determination of the electron drift time for translation into the  $z$  event coordinate. Therefore, it is necessary to measure the time distance between the delayed S2 and prompt S1 signals in the recorded waveforms of the XENON100 detector.

The coordinate system of the XENON100 detector is spanned by a vertical  $z$  axis and an orthogonal  $(x,y)$  plane. The  $z$  axis is defined along the centre line of the cylindrical TPC and points in upward direction, anti-parallel to the electric drift field lines. Its origin is set at the liquid/gas interface such that

**Figure 2.5:** S2 light pattern distribution on the top and bottom PMT arrays for a low recoil energy event inside the TPC. The perpendicular  $(x,y)$  event coordinate is reconstructed from the specific illumination pattern of PMTs on top. The color axis is proportional to the number of photoelectrons per PMT. The extracted position is indicated by a black dot. Figure adopted from [33].



positions inside the liquid volume obtain negative values. For symmetry reasons it is often sufficient to consider radial positions  $r = \sqrt{x^2 + y^2}$  in the perpendicular  $(x,y)$  space.

The absolute time difference  $dt = t_{S2} - t_{S1}$  between S1 and S2 signal is used to infer the drift length  $l$  of electrons, which is transformed into the  $z$  coordinate by a negative sign,

$$z \equiv -l = -v_d dt. \quad (2.14)$$

The electron drift velocity  $v_d$  is found linear dependent on the electric field of moderate strength, typically applied to noble liquid ionization chambers. The proportional constant is then given by the electron mobility  $\mu$  [36]. At the nominal drift field of  $E = 530$  V/cm applied to the XENON100 TPC the value is  $v_d = 1.73$  mm/ $\mu$ s [33]. The accuracy in  $z$  is limited by the uncertainty of the peak maximum position determination of the S2 signal and yields a  $1\sigma$  resolution of 0.3 mm, experimentally confirmed by measuring events with precise position information [33]. This must not be mistaken as the ability to separate two neighbouring scattering positions in  $z$  direction. It is limited by the total width of involved S2 pulse shapes and distinction becomes possible when the mean peak positions are more than 3 mm apart.

A different method is used to infer the  $(x,y)$  event coordinates. Depending on the planar position where electrons cross the liquid/gas interface and create S2 light by secondary scintillation, only a confined area on the top PMT array is illuminated. This effect is shown in Fig. 2.5. S2 light is accumulated only by a sub-cluster of neighbouring PMTs on the top array but widely spread on the bottom. Three different computer algorithms are implemented in the XENON100 event processor to infer the most likely  $(x,y)$  position based on a  $\chi^2$ , neural network and support vector machine technique (refer to [33] and citations therein). In all three cases the general idea is to match the observed top PMT hit pattern with the expectation from a calibration/training sample of known vertex locations. The circular arrangement of photo sensors helps to improve the radial position accuracy. The performance of the algorithms is very similar and the  $1\sigma$  radial resolution achieved is  $< 3$  mm, as confirmed with a collimated  $^{57}\text{Co}$   $\gamma$  calibration source placed above the TPC at several radii [33].

The light spread on the bottom TPC is rather homogeneous and much less suited to extract spatial information because of the large solid angle and the large probability of multiple light reflection from remote emission spots. Nevertheless, we will point out in Chapter 3 how also the bottom pattern can be used to define a consistency criterion on single scatter event identification.

At the beginning of detector operation the electric field was found to be not perfectly homogeneous in the corner TPC regions at low  $z$  positions. The reason is bending of the field lines because they

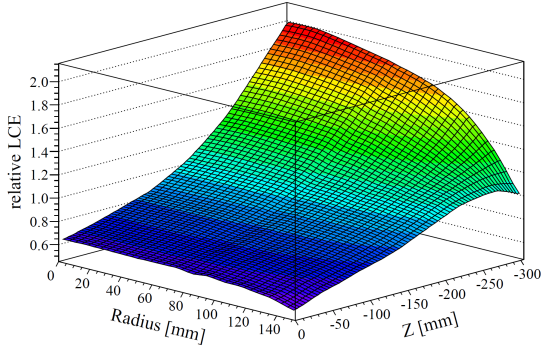


**Figure 2.6:** Relative S1 light yield correction map as a function of  $r$  and  $z$ . Light collection is largest towards the central bottom PMTs and decreases in the direction of larger radii and the liquid surface level. Figure courtesy of [33].

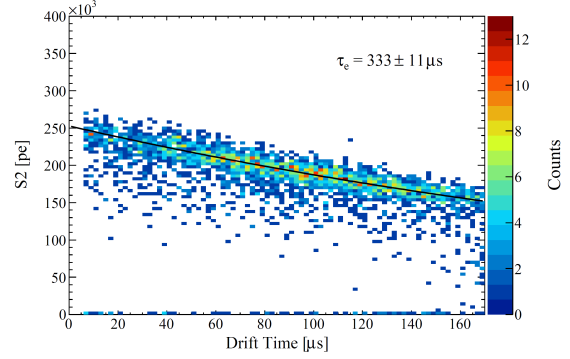


**Figure 2.7:** Determination of the electron lifetime attenuation  $\tau$  from the S2 dependency of the  $^{137}\text{Cs}$  662 keV full absorption line as a function of drift time. An exponential fit yields an inverse decay slope of  $\tau \approx 333 \mu\text{s}$  in this example. Figure adopted from [28].

leak partly through the pitches in the cathode mesh, employed to provide high light transparency. This slight defect for  $r > 120$  mm and  $z < -250$  mm is corrected for by finite element computation of the field configuration [61, 33] and confirmation of the result on  $\gamma$  line calibration from homogeneously distributed metastable xenon isotopes after neutron irradiation.

With precise information about the spatial interaction vertex, both S1 and S2 channels can be corrected for space dependent light collection inhomogeneities (as already mentioned in the previous sections). To compensate local variations in the S1 yield, a relative light collection map is constructed from the 40 keV and 164 keV  $\gamma$  lines from  $^{129}\text{Xe}$  and  $^{131m}\text{Xe}$ , both excited by inelastic neutron scattering. They provide an ideal calibration sample because of their homogeneous distribution within the TPC due to the large penetration length of neutrons. For cross-checks, another calibration is based on the 662 keV  $^{137}\text{Cs}$  line absorption. Fig. 2.6 presents the relative light yield variation as a function of  $(r,z)$  positions in the XENON100 TPC. The map was later augmented to all three spatial coordinates  $(x,y,z)$  to account for sub-percent deviations from the radial symmetry. The light yield is highest near the bottom PMTs and decreases with rising  $z$  positions. Applying the relative map  $\mathcal{M}_{\text{S1}}(x, y, z)$  the corrected S1 signal is defined as

$$\text{S1}^{\text{corr}} = \mathcal{M}_{\text{S1}}(x, y, z) \text{S1}^{\text{obs}} . \quad (2.15)$$

For the upcoming parts of this thesis, we will always use the short notation S1 for the corrected signal and explicitly mention when talking about the observed quantity, thus

$$\text{S1} \equiv \text{S1}^{\text{corr}} . \quad (2.16)$$

Concerning the charge proportional S2 the most important correction is to balance the signal loss due to the finite electron lifetime  $\tau$  (see Sec. 2.1.3). It can be inferred experimentally by measuring the slope of the  $\text{S2}^{\text{obs}}$  distribution as a function of the reconstructed drift time  $dt$  (refer to Fig. 2.7). The measurement is regularly repeated during detector operation because  $\tau$  depends directly on the electronegative impurity concentration which is constantly improved by the hot getter purification and varies over the timescale of days [33]. Additionally, second order deviations in the S2 response appear at large radial positions due to varying light collection efficiency for some PMTs in the top array. It is

equalized by a  $(x,y)$  dependent S2 map  $\mathcal{M}_{S2}$  created from the same calibration samples as  $\mathcal{M}_{S1}$ . This leads to a total correction of the S2 signal according to

$$S2^{corr} = e^{dt/\tau} \mathcal{M}_{S2}(x,y) S2^{obs} . \quad (2.17)$$

Equivalent to S1 we apply the short notation

$$S2 \equiv S2^{corr} \quad (2.18)$$

in the successive parts of this work.

## 2.2 Detector setup and shield

The XENON100 detector is installed underground at the Laboratori Nazionali del Gran Sasso (LNGS), Italy. It is protected by average  $\sim 1400$  m overburden to suppress the atmospheric muon flux by roughly 6 orders of magnitude. In order to shield environmental radiation and ambient neutrons, additional layers of lead, polyethylene, and ultra-pure copper surround the inner detector vessel. A detailed scheme of the shield construction is depicted in Fig. 2.8.

The enclosing water containers and hydrogen-rich polyethylene (PE) layers are supposed to thermalize and eventually stop fast neutrons induced by muon interactions in the surrounding rock cavern or in the shield materials (for detailed discussion about neutron origin and propagation refer to [62]). Natural  $\gamma$  rays from radioactive decays, such as the high energetic 2.6 MeV line from  $^{208}\text{Tl}$ , are sufficiently attenuated from all directions by 25 cm of high stopping power material, divided into 20 cm of lead plus 5 cm of electro-purified copper. The inner lead layer is composed of special low radioactive  $^{210}\text{Pb}$  concentration and the housing is constantly flushed with boil-off nitrogen to suppress ambient air with its comparably high concentration of environmental radioactive radon [33].

Figure 2.9 depicts a drawing of the XENON100 detector placed inside the passive shield. Photographs of inner assembly parts are shown in Fig. 2.10. The double-wall stainless steel cryogenic vessel contains a total mass of 161 kg LXe. The actual TPC is made of 24 interlocking PTFE panels which form an almost cylindrical volume and provide light reflectivity in the ultra-violet wavelength range. It is confined by two PTFE arrays at the top and bottom which encase a total amount of 242 1 square inch Hamamatsu R8520-06-A1 photomultipliers. The arrangement of PMTs is different on the two arrays: a concentric circular pattern on top improves the achievable spatial vertex resolution (refer to Sec. 2.1.4) and rectangular placement on the bottom yields optimal coverage for a high light collection efficiency.

The TPC structure sub-divides the cryostat volume into two optically separated parts: a light-tight inner 62 kg active target and another 99 kg surrounding veto volume. The diving bell construction allows for few cm LXe coverage in all directions, including the volume above the TPC. This acts as an efficient shield against radioactivity from the outer mounting components. The veto volume is watched by 64 out of the 242 PMTs to further provide active external background suppression.

The electric field configuration is established by a set of thin metal meshes, optimized for high optical transparency because the meshes are mounted between the photo-sensors and the active target. A solution is provided by employing a hexagonal grid pattern. Additionally, 40 equidistant field shaping electrodes, made of thin copper wires, are placed in rings along the vertical axis to form a field cage. The cathode is mounted  $\sim 17$  mm above the bottom PMT windows and applied to  $-16$  kV high voltage. An additional screening mesh shields the photo-tubes from strong leaking fields. Approximately at the level of the liquid surface the field cage is closed by two ground meshes with 5 mm

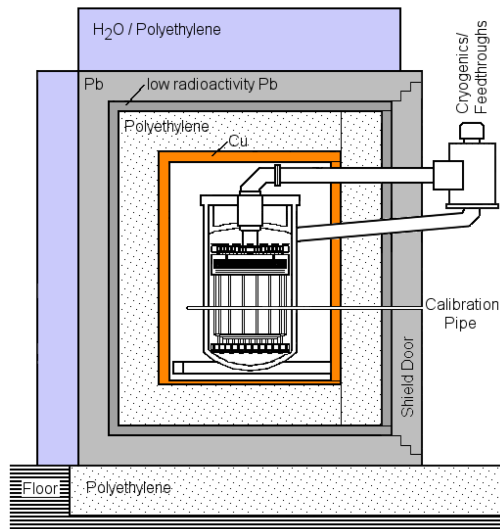


**Figure 2.8:** Shield design and inner cryogenic vessel of the XENON100 detector. Heavy layers of lead and electro-purified copper act against environmental  $\gamma$  radiation while light materials, such as water and polyethylene, are placed to moderate and thermalize ambient neutrons arising from spontaneous fission and muon spallation in the cavern rock or shield materials. Figure adopted from [33].

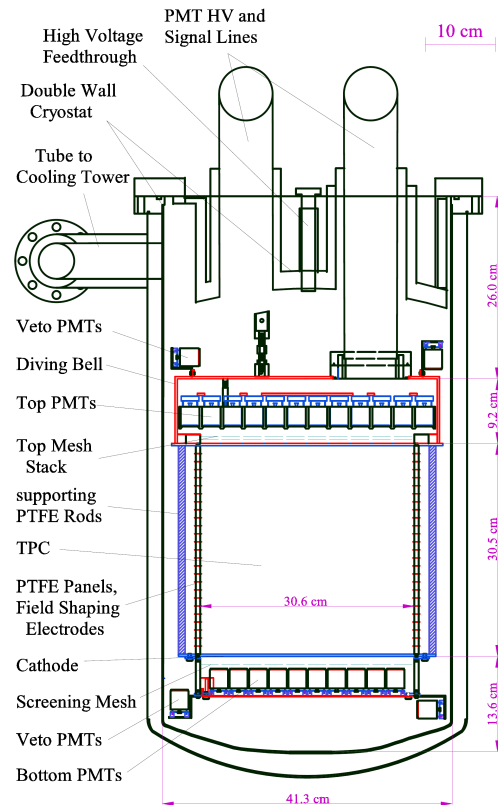


**Figure 2.9:** Scheme of the XENON100 detector. The total 161 kg LXe are divided into 62 kg inner TPC target mass and 99 kg in the surrounding active veto volume. Figure from [33].

distance. In between, the anode grid is placed and set to +4.5 kV to provide the strong extraction field of  $\sim 12$  kV/cm needed to create secondary scintillation light proportional to the number of extracted electrons. The topmost ground grid is used to protect the upper PMTs from the high electric field. The active field cage dimensions are 306 mm in vertical length and horizontal diameter. The inner drift field is almost homogeneous (see explanation of small deviations in Sec. 2.1.4) with a strength of 530 V/cm and points vertically from anode to cathode level.

The cooling power to liquefy xenon and keep it at operation temperature of  $-91^\circ\text{C}$  at 2.2 atm pressure in the gaseous phase is provided by a pulse tube refrigerator (PTR) mounted outside the passive shield and connected through an insulated pipe to the inner cryostat. Connected to the PTR there is a cold-finger to enable xenon gas condensation and re-entering to the cryostat via a funnel ending at the inner veto volume. The presence of a gaseous phase below the diving bell and the actual height of the liquid level are maintained by the constant recirculation of xenon: taken from the liquid, xenon is evaporated and pumped through a hot zirconium getter to be purified from electronegative components which adversely affect the electron lifetime and light attenuation inside the detector. The cleaned gas re-enters the diving bell from the top and thereby adjusts the liquid/gas equilibrium depending on the exact circulation flow velocity of typically  $\sim 5$  slpm<sup>1</sup>. Liquid level meters and additional temperature

<sup>1</sup>Standard liters per minute (slpm): Volume flux of gas at standard temperature and pressure.

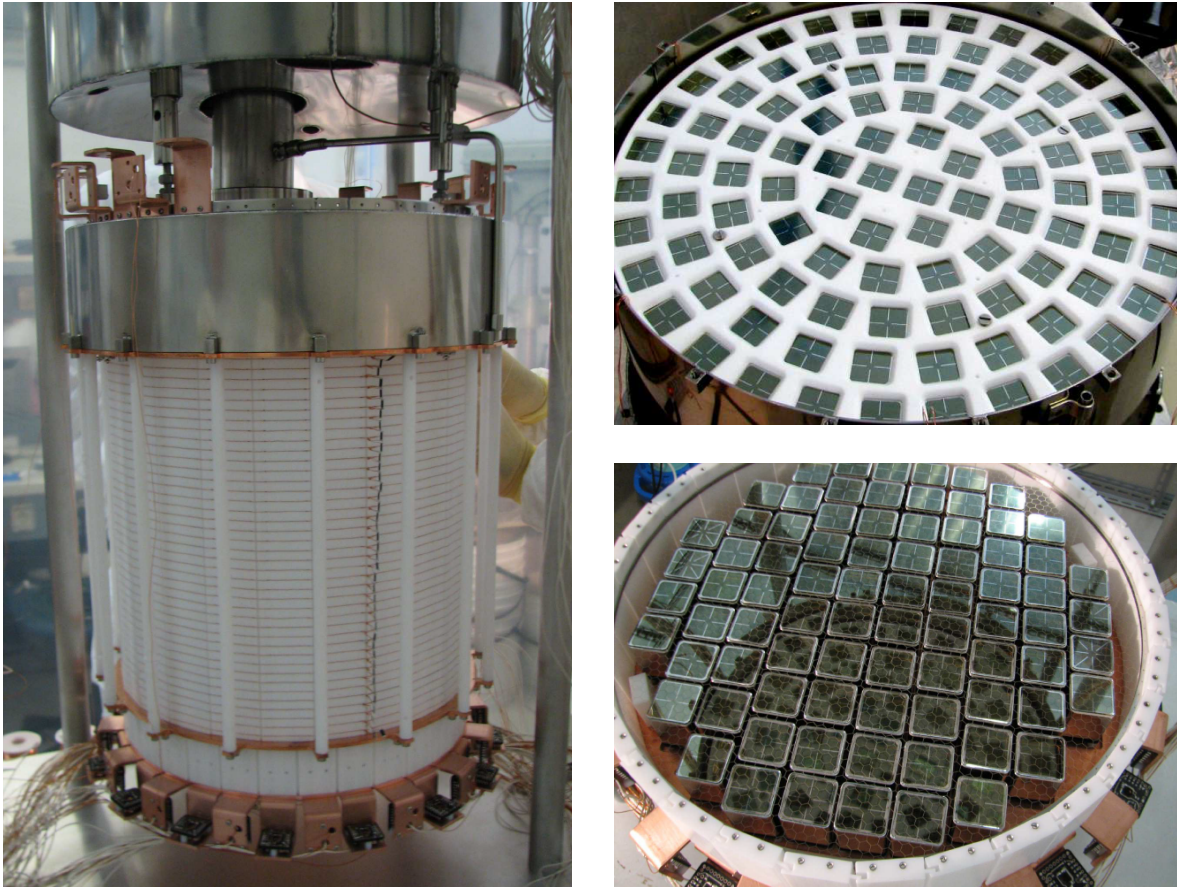


**Figure 2.10:** Pictures of the TPC assembly, courtesy of XENON100. (Left) Mounted TPC with diving bell and cylindrical PTFE panel structure. PMTs placed at the outer bottom face the optically separated active veto part. (Top right) Arrangement of PMTs in the upper panel, encased by PTFE. (Bottom right) Bottom PMT array optimized for maximum scintillation light collection.

sensors help to regulate the liquid level at the desired distance between ground and anode mesh.

Almost all numbers in this section are quoted from a recent summary of the XENON100 experiment [33]. Therein, more detailed information about the cryogenic system and inner detector design is provided.

It is important to mention that all materials in relevant distance to the centre target volume, in particular mounting parts of the TPC, PMTs, electric feed-through cables and samples of the stainless steel cryostat, were extensively screened for their natural radioactivity concentration by means of ultra-low background germanium spectroscopy [63] and selected accordingly.

The employed xenon itself is purified from residual concentration of natural krypton, abundant from the commercial gas facilitation and contact to ambient air. The radioactive  $\beta$  isotope  $^{85}\text{Kr}$  is produced mainly as a fission product of uranium from nuclear reprocessing plants. It decays with a half-life of 10.76 a and poses a threat to the XENON100 sensitivity because of the low energy end of its  $\beta$  decay spectrum ( $E_{\beta}^{\text{max}} = 687 \text{ keV}$ ). Commercially available xenon has usually a  $^{nat}\text{Kr}$  contamination of few parts per million (ppm), far above the tolerable level. Therefore, a cryogenic distillation column was installed next to the experimental site to process the xenon immediately before detector filling [33].

By exploiting different boiling temperatures of krypton (120 K at 1 bar pressure) and xenon (165 K) a physical separation to the remaining level of few ppt (parts per trillion) could be eventually achieved and confirmed by independent measurements [64] for the most recent WIMP search run [42]. We will mention the krypton topic again in the context of the other noble gas radon, treated in Chapter 4.

## 2.3 Data acquisition and processing

After the detector construction had been accomplished in 2008 and 2009 (a detailed description of the mounting period is given in [28]) the detector was ready for operation and data acquisition (DAQ). A simplified scheme of the XENON100 DAQ system is shown in Fig. 2.11. The analog signals from all 242 PMT channels are first amplified by a factor 10 using Phillips 776 NIM modules and afterwards individually digitized by VME Flash ADCs (analog-digital-converters) with 100 MHz sampling rate and 14 bit digital resolution. The ADCs operate without mentionable dead time loss at the typical background event trigger rate of  $\sim 1$  Hz thanks to an integrated circular buffer in each channel.

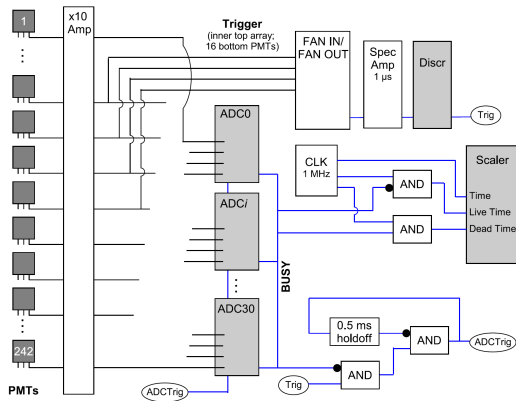


**Figure 2.11:** Scheme of the XENON100 DAQ system. All 242 PMT channels are individually digitized by Flash ADCs. The hardware trigger setup is displayed in the configuration of the 100 live days dark matter search [47] based on the integrated analog signals from a subset of central PMTs. Figure from [33].

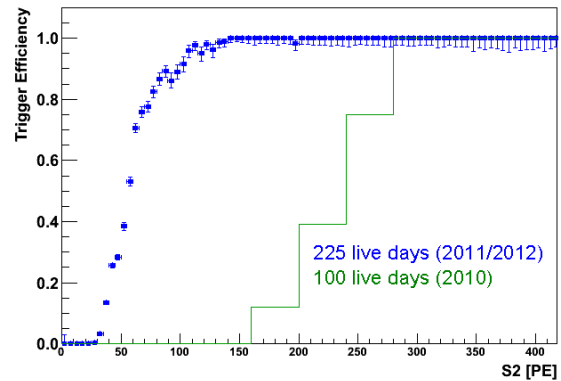


**Figure 2.12:** Comparison of two different hardware trigger configurations as described in text. It was possible to significantly lower the S2 threshold to  $\sim 150$  PE while maintaining  $> 99\%$  trigger probability in the second major dark matter search of 2011/2012 [42]. Figure courtesy of XENON100.

A trigger is necessary to read out all individually recorded PMT waveforms at once from the Flash ADC panels and store them to disk in a custom made file format. Two different trigger configurations were applied for the two main dark matter searches reported in [47, 42]. In the first case, the analog signals of a subset of central top and bottom PMTs were combined in a linear FAN In/FAN Out, their sum amplified, shaped and discriminated. By this, an effective trigger probability of  $> 99\%$  for events with S2 size  $> 300$  PE could be achieved. This condition was significantly improved for the second science run by effectively defining a hardware majority condition on the number of PMTs exceeding an adjusted threshold of each  $\sim 0.5$  PE. Fig. 2.12 shows a comparison between the two mentioned trigger conditions. The two acceptance curves are determined directly from the experiment by digitizing the trigger signal simultaneously to the standard waveform acquisition. In off-line analysis of the data it was counted how often S2 peaks at a given size could cause a trigger. Under obviously improved conditions the  $> 99\%$  trigger probability threshold is established for S2 signals equivalent to  $> 150$  PE size.

The window length of an recorded event is set to  $\sim 400\mu\text{s}$  with the triggering pulse placed in the center. This covers in total more than twice the maximum drift length of  $\sim 178\mu\text{s}$  defined by the vertical boundaries of the TPC. It is necessary to store every relevant information in the time between the occurrence of the prompt S1 and delayed S2 after electron drift, regardless if the trigger was created by the primary or secondary scintillation light (the partition into these two classes happens at a later stage). Followed by every event is a  $500\mu\text{s}$  trigger hold-off to avoid overlapping.

The information contained in all individual PMT traces is compressed using a zero-length encoding technique implemented in on-board FPGAs<sup>2</sup> [28] which reduces those parts of the PMT waveform that consist solely of baseline fluctuations but carry no signal. Starting from the remaining data, which is then written to hard disks, the XENON100 raw data processor extracts all relevant information from both the individual and summed PMT traces and implements dedicated peak identification algorithms to find and classify waveform pulses according to S1 and S2 [28, 33]. Not only information about the accurate timing position within the waveform and involved peak integrals but also an entire collection about peak width, PMT coincidence level, reconstructed 3-D spatial position for every identified S2, etc. are extracted and made accessible for off-line analysis in a common ROOT [65, 66] tree format. Analyses presented in the main chapters of this work are usually based on this stage of the data processing chain. However, sometimes it turned out useful to study raw waveforms by eye in order to gain in understanding from the originally underlying traces and also to check the performance/correctness of the computer algorithms. For further reading on the details of data processing we recommend the work of [28].

We close this section with several definitions. In the context of data analysis we call an *event* the set of information retrieved from the occurrence of a hardware trigger signal. Every event is described by the  $400\mu\text{s}$  waveform which is meant to subsume one or several sub-waveforms consisting of S1 or S2 pulses. Sometimes, we use the short notation of “S1 (S2) waveform” when strictly meaning only the part of the total waveform that confines one single S1 (S2) pulse. A collection of events is called *dataset*. Typically the acquisition is stopped after some time for collective processing of the taken raw data. The measuring time can vary between hours (calibration measurements) and one or few days (low background data taking). A time period of many up to hundreds of days in which the detector was operated under stable conditions is named *run*. Two extended [47, 42] and one first operation [67] dark matter search run were reported by the XENON100 experiment until the time of writing.

## 2.4 Event selection and data analysis

It was introduced before how events in the XENON100 detector are recorded and processed but obviously not all of them represent suitable candidates for calibration or dark matter analyses and some of them may not even be induced by true physical interactions in the LXe TPC. Therefore it is necessary to develop criteria which are useful to separate signal from noise events and classify the signals according to their physical properties.

In this section we want to give a short introduction into tools of event selection and analysis techniques, both reappearing in the main chapters in this thesis. We also want to prepare the ground for a summary of the XENON100 scientific results from dark matter search at the end of this chapter.

---

<sup>2</sup>Field Programmable Gate Arrays

## 2.4.1 Event selection

Selection criteria are usually defined on the available variables stored in the ROOT parameter tree which contains a set of events. With the help of these, one can place a condition which events have to obey in order to be selected or otherwise rejected. Adopting the language of high energy physics the condition is sometimes called a *cut*. Without mentioning too many technical details we want to provide a short overview of all cuts relevant for the dark matter analysis. Some of the information is also contained in [57] and we refer to it for additional reading.

**Basic data quality** It is important to reject events which are obviously triggered by electronic noise or artifacts in the data acquisition. Since the hardware trigger threshold of the XENON100 detector is as low as to enable sensitivity down to the few to single drift electron level, baseline fluctuations in the waveform or accumulated electronic noise can sometimes be mistaken for a real trigger or appear at random positions within the waveform of a proper event. A cut based on the signal-to-noise ratio is used to effectively suppress those events. It requires that a sufficiently large proportion of the waveform integral is contained in the largest S1 and S2 peaks identified in the trace.

Additional reduction of the noise level is achieved by applying a set of conditions using the width and the information entropy level in single PMT traces of the S1 peaks in order to quantify the consistency with an expected good waveform shape. These criteria – originally designed to remove only a few noise events out of several tens of live days – are usually of minor impact for calibration source measurements taken over short periods only.

Continuing with the rejection of noise events, a cut on the PMT coincidence level of the S1 signal is placed. It is necessary that at least one S1 peak is composed of at least 2 individual PMT contributions within a 20 ns time window defined around the peak maximum. To add one to the coincidence level, the individual PMT traces must pass a noise threshold equivalent to 0.35 PE. By this means the number of S1 pulses caused by PMT dark current is significantly reduced. It must be taken into account, however, that some true signals will be rejected because the detected photons are coming from the tail of the exponential decay time distribution.

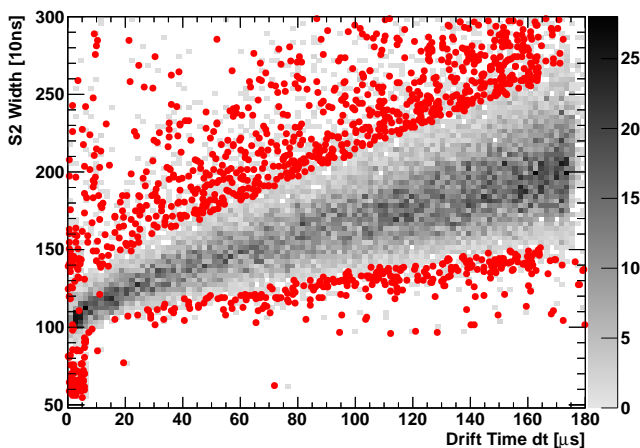


**Figure 2.13:** Illustration of the S2 width cut. Red dotted events are rejected as being outliers of the expected S2 peak width distribution as a function of electron drift time dt.

Further remaining events must satisfy a requirement on the width of the largest S2 peak. Only if this shape property of the S2 waveform is consistent with the expectation of a diffusing electron cloud as a function of drifttime, it can be assured that interaction took place inside the liquid xenon. Otherwise, it is likely that the event was created somewhere in the gas phase and the resulting S2 is

arbitrarily connected with a randomly coincident S1. If that was the case the event might be falsely reconstructed inside the fiducial volume. Fig. 2.13 illustrates this cut condition. Only those events in the bulk population are accepted because they largely follow a square root drift time dependency as expected for electron cloud diffusion as a function of path length. Outliers to this expectation are rejected and marked red in the plot.

**Single scatter events** Many analyses – among WIMP searches and neutron calibration presented in Chapter 5 – rely on the selection of single-fold physical interactions in the TPC because it provides an efficient means to distinguish between background radiation (mainly multiple scattering events) and expected WIMP signals (single scattering events). An obvious precondition is to reject all events which show two or more confirmed S1 signals within the  $400\ \mu\text{s}$  time window. This signature would indicate that there happened two or more distinct processes, for example the subsequent decays of natural  $^{214}\text{Bi}$  and  $^{214}\text{Po}$ , discussed in Chapter 4, or random correlation of incoming radiation.

The next important step is to cut on single scatter events according to the number of registered S2 peaks. Two or more S2 above a certain noise threshold point at multiple scatter vertices along the track of a particle or  $\gamma$  ray. Note that this is independent from the single-fold condition on the S1 because the prompt light emitted from various positions is anyway collected within the given time resolution of tens of ns. To guarantee the single-site criterion, however, it is not appropriate to simply ask the number of observed S2 peaks to equal one. This would act too strict since there is a considerable distribution of single electron signals which appear unrelated to the actual scattering event. The occurrence of delayed single to few electrons is well known and the explanation is that some of the drifting particles become trapped at the liquid/gaseous interface until they are finally extracted into the gas phase by the high anode field. Another reason is the appearance of small S2 pulses due to photo-ionization of impurities or metallic parts in the TPC through the emitted ultra-violet scintillation photons [60]. What is consequently observed in any case is a tail of very small S2 which follow the main peak. We therefore need a somewhat relaxed cut condition to identify as many as possible true single scatters.

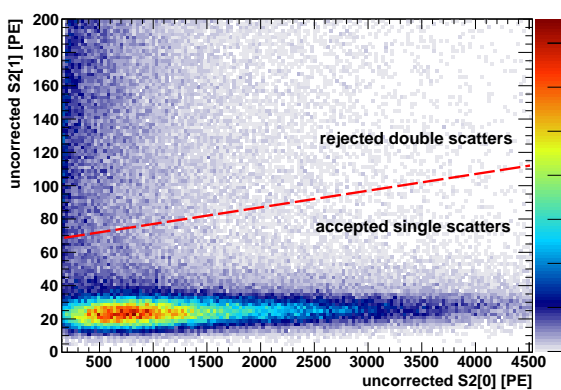


**Figure 2.14:** Selection of single scatter interactions according to the size of the second largest S2 as a function of the largest one. Events below the red dashed line are considered as single site events because their second largest S2 is mostly made of signals from unrelated single escape electrons. Events above the line are almost entirely composed of true second interactions and are supposed to be rejected.

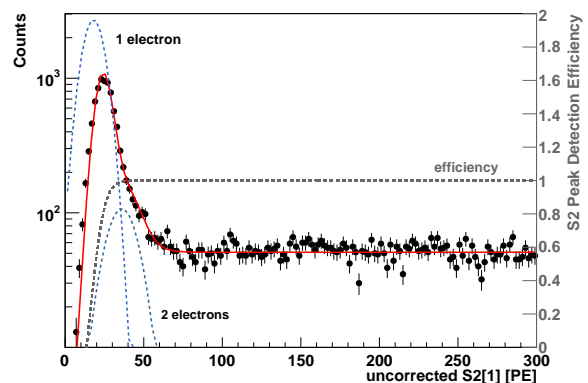


**Figure 2.15:** One dimensional projection of the second largest S2. Indicated with blue dashed lines are Gaussian contributions from single and double delayed electron signals. The gray dashed line and right scale show the assumed efficiency loss of the data processor in identifying tiny S2 peaks.

The applied method is illustrated in Fig. 2.14 and 2.15. The first one shows the distribution of the uncorrected<sup>3</sup> S2 from second largest scatter (“S2[1]”) in the waveform as function of the S2 from the largest one (“S2[0]”). The majority of events is concentrated in a horizontally elongated distribution correlated with delayed single electrons on the y axis and appears almost constant along the x scale, i.e. independent of the underlying energy deposition of the triggering S2[0]. Looking at the projection on S2[1] in Fig. 2.15 enables to decompose the overall rise at low values into single and double electron contributions. Note that in order to match the observed spectrum one must introduce an efficiency function for the finite peak detection efficiency of the data processor as an additional fit parameter. One can pose an upper threshold on the size of the second largest S2 at the point where the distribution of single electrons rolls off and is replaced by a flat continuation of supposedly real second interactions. For the analysis of scientific dark matter data and the later presented neutron studies this point was found at roughly 70 PE, only weakly increasing with the size of the largest S2[0]. The exact conditions reads

$$\text{uncorrected S2[1]} < (70 + (\text{S2[0]} - 300)/100) \text{ PE.} \quad (2.19)$$

Every second identified S2[1] above the set threshold is considered to come from another true energy recoil rather than from a randomly appearing delayed electron signal.

**Detector threshold condition** Another cut is set to compensate for the finite hardware trigger probability at very small S2 signals. As explained in section 2.3, an effective majority condition is put on the number of PMTs which have to exceed a specific dark current threshold. This translated into an effective trigger acceptance curve is shown in Fig. 2.12. In order to guarantee > 99% event pick-up probability, an S2 condition of > 300 PE and > 150 PE was placed for the analysis of the first [47] and second [42] main WIMP searches of the XENON100 detector, respectively.

**Fiducial volume** The ability of 3-D event reconstruction inside the TPC provides a powerful tool to reduce background radiation from outer materials by selecting a central fiducial volume. This effect is shown by Fig. 2.16 on background data from the 225 live days period reported in [42]. Highest event density is concentrated near the TPC walls and the PMT arrays closing the TPC from top and bottom. The high stopping power of the LXe attenuates effectively  $\gamma$  radiation coming from these regions. To optimize the signal-to-background ratio in dark matter searches it turned out advantageous to define super-elliptical volumes in the (r,z) space which render the distribution of background near the walls and edges. Two such volume examples are indicated by the red (48 kg) and black (34 kg) lines. They were used to restrict the WIMP recoil search area in the analysis of the 100 and 225 live days data, respectively. The peculiar shape is also recommendable to avoid certain reconstruction imperfections obvious in the outer areas of the (r,z) plane.

**Active veto** The outer LXe volume surrounding the TPC can be employed as active veto against external radiation. The veto signal from the outer PMTs is digitized in the same way as the inner channels, including precise timing information about the position in the waveform. If found in  $\pm 20$  ns coincidence with a S1 signal inside the inner volume, the event is usually rejected in the off-line data analysis. Due to decreased PMT coverage, worse light collection and strong position dependency in the outer veto volume the minimum energy threshold to detect interactions is significantly higher than in the main target and requires minimum energy deposits in the range of 10 – 450 keV, depending on the spatial location [33]. Depending on the type of data analysis, it can be advantageous to neglect the veto information or particularly select events with active veto coincidence.

<sup>3</sup>“Uncorrected” means that the spatially dependent signal corrections from Sec. 2.1.4 are not applied.

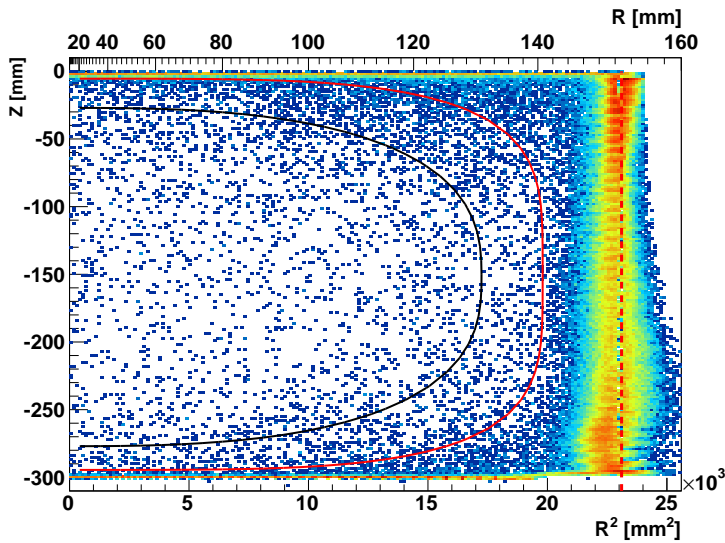


**Figure 2.16:** Spatial distribution of single scatter electronic recoil background events in the 225 live days dataset. The red and black lines define a 48 kg and 34 kg LXe fiducial volume, respectively. The vertical red dashed line marks the physical radial border of the TPC. The self-shielding capability of LXe enables to select a very clean inner detector region.

**Consistency cuts** Finally, cuts were developed to perform certain consistency checks on the event reconstruction quality. One condition sets a maximum discrepancy threshold between the three independent position algorithms implemented by the raw data processor. If their mutual agreement is insufficient the event is rejected because it is likely to have non-physical origin or it is a fake single scatter. The other consistency cut, called S1 pattern likelihood criterion, will be on focus of Chapter 3. Based on the illumination pattern of the PMT arrays it represents a powerful tool to remove a special class of background events that pretend to be single scatters but in fact have an additional interaction in fringe regions of the TPC.

## 2.4.2 Recoil discrimination

The two-channel approach allows for event type discrimination between electronic and nuclear recoils by the specific ratio of  $S2/S1$ . Electronic recoils (ER) denote particle or radiation interaction with the atomic shell electrons of the xenon target and typically create a large amount of ionization electrons along elongated tracks with multiple scattering sites. On the contrary, nuclear recoils (NR) are transferred by neutral massive particles that interact mainly with the atomic nucleus. Only a fraction of the expended energy is thereby turned into electronic excitation to create a detectable signal, and the rest is lost into heat. The recoiling atoms are also immediately stopped and the produced ionization electrons stay near the ions and have thus a larger recombination probability. The difference in signal response is shown in Fig. 2.17. Two single scatter event distributions, from  $^{60}\text{Co}$   $\gamma$  calibration (blue) and  $^{241}\text{AmBe}$  neutron sample data (red), are presented in the so called *flattened discrimination space*. On the y axis we draw  $\log_{10}(S2_b/S1)$ , subtracted by the mean of the electronic recoil population and using only the  $S2_b$  light collected on the bottom PMT array. On the x axis one usually refers to S1 as an estimator of the recoil energy. The  $\gamma$  ray sample is representative for the electronic recoils and implies a significantly larger  $S2/S1$  ratio than from nuclear recoils induced by the neutrons. For the dark matter search it is assumed that potential WIMP recoils share the same signature with neutron calibration while the background is dominated by electromagnetic interactions induced by natural radioactivity. This explains why the benchmark region for WIMP search (green dotted area) in this parameter space is chosen such that optimal rejection of background is achieved while simultaneously maintaining a large portion of the expected signal area.

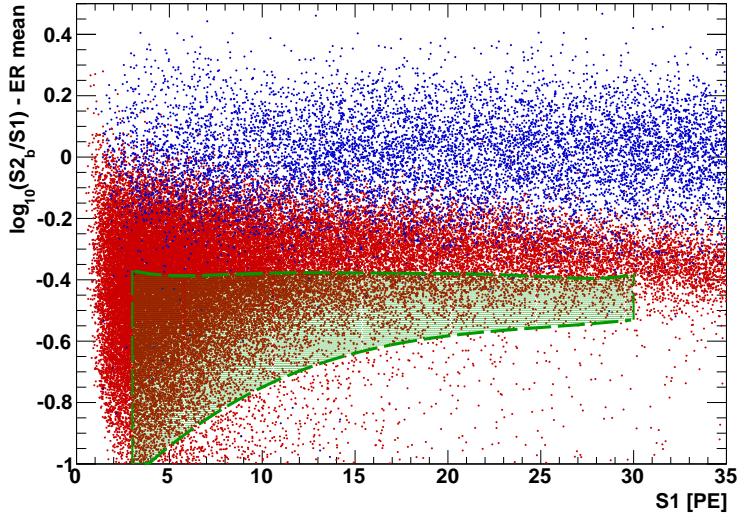


**Figure 2.17:** Comparison of electronic and nuclear recoil distributions in the flattened discrimination space. Blue data points are collected from  $^{60}\text{Co}$   $\gamma$  calibration and feature a larger ratio of S2/S1 than observed from  $^{241}\text{AmBe}$  neutron recoils (red). Both populations form so called recoil bands when drawn against the energy estimator S1. They are used to define the benchmark region of potential WIMP events and reject background radiation (green dotted area used in 225 live days dark matter search).

### 2.4.3 Recoil energy scale

When trying to reconstruct energy depositions from the observable S1 and S2 one has to distinguish carefully again between the two mentioned types of electronic and nuclear recoils.

**Electronic recoils** We have learned already that charged particles or energetic photons typically lose energy by direct ionization or excitation of the atomic shell electrons. For  $\beta$  and  $\alpha$  particles the energy transfer is described by the electronic stopping power in LXe while  $\gamma$  rays become photo-absorbed or undergo Compton-scattering (if they are energetic enough, pair production and subsequent energy loss can play a further role). For all natural sources the corresponding absorption lengths are on the order of a few  $\mu\text{m}$  ( $\alpha$ ), mm ( $\beta$ ) or cm ( $\gamma$  rays).

The energy released is either distributed into scintillation photons (due to direct excitation or recombining electrons) or ionization electrons, which in turn convert into S1 and S2, respectively. Consequently, the optimal energy scale makes use of the combination of both available signal channels,

$$E = a \cdot S1 + b \cdot S2, \quad (2.20)$$

where  $a$  and  $b$  can be determined from calibration measurements using the full absorption peaks of various well-known  $\gamma$  lines. The partition of energy into S1 and S2 is shown in Fig. 2.18 for  $^{137}\text{Cs}$  calibration of the detector. In a correlation plot of S2 against S1 one can observe the 662 keV full-absorption event accumulation. Elliptically elongated, the distribution of charge and light appears (anti-)correlated. Below the main absorption energy is the Compton spectrum of  $\gamma$  rays scattering once (or several times) and escaping the target.

Using the combined S1-S2 scale, the relative energy resolution achieved in the XENON100 experiment is less than 10 % for electronic interactions in the  $\gamma$  energy range of natural decay isotopes [33]. However, due to powerful shielding of external  $\gamma$  rays, the lowest accessible energies are from excited xenon states, not allowing for calibration points below 40 keV. To reach even further down in energy, dedicated low-electron recoil experiments become necessary [68].

Because of energy conservation, Eq. (2.20) is valid regardless of the actual sharing of energy transfer into light and charge. Even at a fixed applied drift field, any energy scale defined solely on S1 or

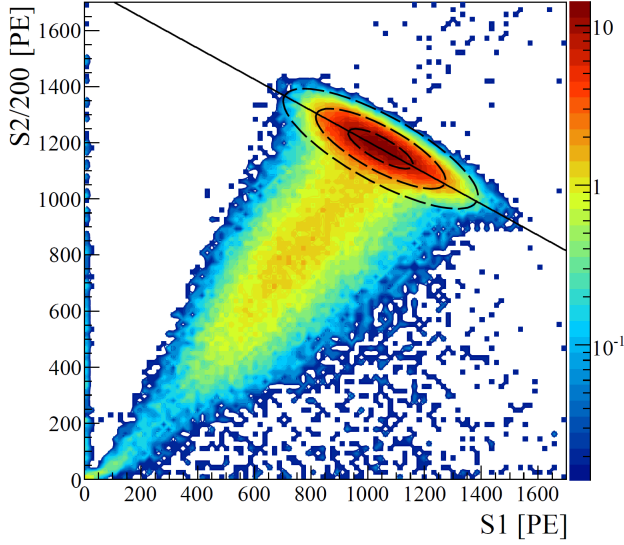


**Figure 2.18:** Detector calibration with a  $^{137}\text{Cs}$   $\gamma$  ray source. Shown is the (anti-)correlation between S2 and S1 obvious in the main absorption ellipse at 662 keV. Energy deposits below this line are single-fold Compton scatters where the  $\gamma$  escapes the active volume. Plot adopted from [33].

S2 cannot be linear over a wide range simply because the recombination fraction  $r$  and ion number  $N_i$  from eq. (2.7) are implicit functions of energy.

While an accurate calibration of electronic recoils is valuable for the understanding of the most prominent background sources it does not help in establishing an energy scale for what the detector is predominantly made for – searching for potential WIMP interactions, i.e. nuclear recoils.

**Nuclear recoils** The simple construction of an electronic recoil scale cannot be translated to nuclear reactions because a significant fraction of the expended energy is lost into heat and not accessible by the XENON100 detector. A well-established way to account for the quenching of the detectable signal is given by the effective scintillation yield function  $\mathcal{L}_{eff}$  which describes the amount of S1 light per unit energy from a nuclear recoil relative to the full-absorption yield of the 122 keV  $^{57}\text{Co}$   $\gamma$ -line. The true deposited energy  $E_{nr}$  from the nuclear recoil (nr) is then related to the measured S1 by the following formula:

$$E_{nr} = \frac{S1}{\mathcal{L}_{eff}(E_{nr}) \cdot L_y} \cdot \frac{S_e}{S_n}. \quad (2.21)$$

Therein,  $L_y$  is the specific light yield of 122 keV  $\gamma$  rays measured in the detector and the factors  $S_e$  and  $S_n$  contain the electric drift field dependency on this quantity for electronic and nuclear recoil interactions, respectively.  $\mathcal{L}_{eff}$  is a function of energy and has to be determined experimentally. For the analysis of XENON100 dark matter data the global  $\mathcal{L}_{eff}$  parameterization described in [47] was used. We will devote the entire Chapter 5 to the study of the nuclear recoil energy response and also provide a separate, indirect measurement of  $\mathcal{L}_{eff}$  therein. We refer also to a much more detailed discussion of the nuclear recoil energy conversion in this dedicated chapter.

After the introduction of the main analysis concepts we will conclude this chapter with a summary of the most recent scientific results of the XENON100 experiment.

## 2.5 Scientific results on dark matter search

After a first commission phase together with the publication of 11 live days of measurement [67] two major science runs of 100 and 225 live days have been recorded and evaluated by the XENON100 collaboration until the time of writing [47, 42]. The author of this thesis has actively participated in the detector operation (as scheduled shifter) and off-line data analysis, embedded in a collaborative effort to find direct evidence for WIMPs.

Although unsuccessful in discovery, within three years of operation between 2010 and 2012 the experiment has reached its designed sensitivity to search for spin-independent WIMP-nucleon cross-sections in the range of only few  $10^{-45}$  cm<sup>2</sup> for  $\sim 50$  GeV/c<sup>2</sup> WIMP masses. In this section we will focus mainly on the most recent results from the 225 live days run and mention previous results only when appropriate.

The data-taking period for the 225 live days measurement started in March 2011 and spanned over roughly one year. The xenon was first processed through the cryogenic distillation column to provide a low <sup>nat</sup>Kr concentration of  $(19 \pm 4)$  ppt to reduce the background contribution from  $\beta$  decaying <sup>85</sup>Kr. In the run before, the krypton level was measured about 20 times higher [64] and limited the final sensitivity for low recoil energy WIMP search [57]. The krypton had entered the detector through a tiny temporary air leak arising in the commission phase of late 2009, before the 100 live days run was started in early 2010. This limitation was overcome in the second long-term science run and the most dominant background components were given by external radioactivity and radon (Sec. 4.8).

Besides background data-taking singular and regular calibration measurements were performed. Neutron calibration data with a <sup>241</sup>AmBe ( $\alpha, n$ ) source could only be taken once per year due to regulations set by the underground laboratory LNGS. Two measurements were scheduled at the beginning and the end of the run. One of these is used for the studies presented in Chapter 5. Calibrations of the electronic recoil response were taken several times per week using a <sup>60</sup>Co, <sup>228</sup>Th and <sup>137</sup>Cs source, each time interrupting the background data recording for up to several hours. The low energy Compton scatters of the first two mentioned  $\gamma$  sources are necessary to determine precisely the position of the electronic recoil band and to finally place a background expectation. The <sup>137</sup>Cs source was used to regularly determine the development of the electron lifetime, needed to correct the S2 signal and monitor the electronegative purity concentration in the LXe. The lifetime increased during the run from initial  $374 \mu\text{s}$  to  $611 \mu\text{s}$  [42]. In order to monitor the response of the PMTs, weekly calibrations with a pulsed blue LED, guiding the light through optical fibers inside the TPC, were also taken.

It is important to mention that the expected WIMP signal region was inaccessible in recorded data until all event selection criteria had been decided, a precise benchmark region for WIMP scatters defined and a final background prediction stated (“blind analysis”). Therefore, the lower 10% of the electronic recoil band in the flattened discrimination parameter space between 3 – 100 PE in S1, remained blinded and only the complementary part acted as a control sample. This underlines the importance of external calibration data to fully characterize the expected electronic recoil event leakage into the pre-defined signal acceptance region (see also Chapter 3).

The availability of calibration data was also necessary to test the performance of the selection criteria introduced in Sec. 2.4 as well as identify classes of electronic noise to be removed from the recorded data. Two complementary quantities are important for the characterization of any cut condition: efficiency and acceptance.

The cut *efficiency* states the probability to reject a known background event, i.e. electromagnetic recoil or ambient neutron, from a sample of events consisting of both background and signal. In the

opposite direction, the cut *acceptance* declares how likely it is for a true signal event (i.e. WIMP recoil) to remain included in the selection sample after the cut condition was applied.

In an ideal world both quantities are desired to approach unity but in reality the distributions of signal and background overlap. In XENON100 the efficiency is determined mostly on electronic recoil calibration. The acceptance is mainly fixed on  $^{241}\text{AmBe}$  nuclear recoil data because the detector response to neutrons is assumed to be representative for WIMPs (more detailed discussion about this is presented in Sec. 5.6). Both quantities, efficiency and acceptance, have to be evaluated as a function of the nuclear recoil energy estimator S1 along which the WIMP search region of interest is defined between 3 – 30 PE ( $\cong 6.6 - 43.3$  keVnr). Figure 2.19 shows the result of the acceptance determination for the 225 live days run.

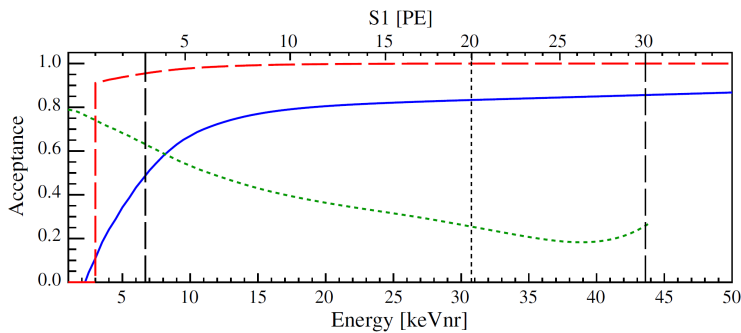


**Figure 2.19:** Components of the final WIMP signal acceptance as a function of the energy estimator S1 for the 225 live days analysis. The blue curve combines all data quality and single scatter criteria. The red line shows independently the translation of the S2 threshold cut into a function of S1. The green dashed line describes the acceptance of the hard 99.75% ER background rejection cut. Black vertical lines indicate the pre-defined S1 interval for the profile likelihood and maximum gap analysis. Figure from [42].

The blue curve is the combined acceptance function of all data quality and single scatter requirements in the chosen 34 kg fiducial volume. It falls off at very low recoil energies mainly because of the two-fold coincidence requirement on the S1 signal and continues with a small rising slope towards higher energies. Separate from all the other cuts, the acceptance of the S2 threshold cut (“S2 > 150 PE”) translated into a function of S1 is shown by the red curve. The roll-off of this function is to some extent dependent on the assumed WIMP mass. The reason is that according to the expected WIMP energy recoil spectrum (exponentially falling) the net effect of Poissonian fluctuations in the S1 channel is pronounced more or less. This must be taken into account when transferring the cut definition on S2 to the S1 based recoil energy scale [42]. Also shown as green dashed line is the acceptance of the background discrimination cut. For the cut-based analysis a fixed rejection probability level of 99.75% of the normally distributed electronic recoil band was chosen after a global sensitivity optimization, considering also the choice of the fiducial volume and the rejection level of dedicated cuts against anomalous leakage (see also Chapter 3). The resulting acceptance probability of all three curves combined directly enters the calculation of discovery or exclusion of the WIMP signal cross-section. An important result of Chapter 5 is therefore to prove that the acceptance determination for the evaluation of WIMP search was done correctly.

Two different statistical approaches of data analysis were applied simultaneously. The optimal sensitivity is reached by a profile likelihood (PL) ratio evaluation of the signal and background expectation. It was first proposed and explained for the XENON100 experiment in [69]. The concept behind is to benefit from taking into account the actual location of measured electronic recoil background and expected WIMP event signature in the discrimination parameter space. Besides adding taken calibration data as “control measurements”, it is further possible to incorporate systematic uncertainties of the

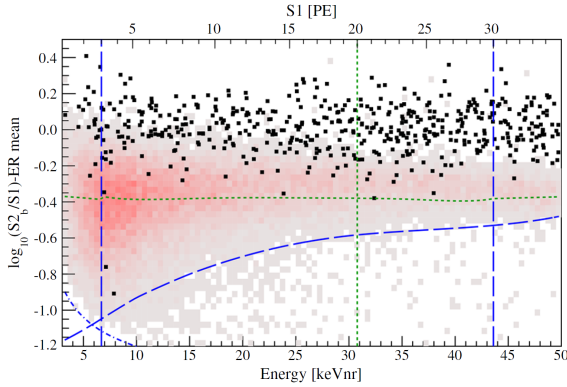


**Figure 2.20:** Measured event distribution in the discrimination space after 225 live days (black points). Underlying is the expected signal region calibrated by  $^{241}\text{AmBe}$  neutron recoils (light red histogram). Blue lines define the benchmark region for the PL analysis as described in text. The vertical green line limits the upper range for the maximum-gap evaluation. The green horizontal line corresponds to the 99.75% electronic leakage rejection probability. Figure adopted from [42].

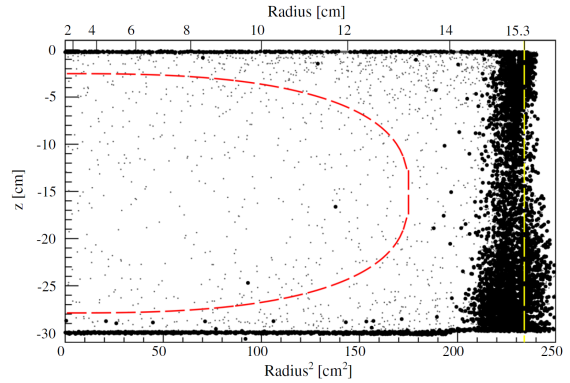


**Figure 2.21:** Spatial event distribution inside the TPC of the 225 live days dataset. Shown in black (grey) are all events below (above) the 99.75% rejection line. The pre-defined inner 34 kg fiducial volume is drawn with red dashed lines. The distribution does not show any unexpected feature including the two event positions inside the chosen volume. The background suppression in the inner parts from the xenon self-shielding is remarkable. Figure taken from [42].

assumed astrophysical and measured experimental parameters, such as  $\mathcal{L}_{eff}$ , which enter the computation of expected WIMP rate and recoil signature. The method also allows for a natural transition between a discovery claim and an exclusion limit, which is a deficit of other common approaches, like the maximum-gap method [70], suitable only for the extraction of limits. The maximum gap method is applied for the classical cut-based evaluation of data and was performed to cross-check the likelihood ratio method also because it provides a more intuitive way of interpretation. As mentioned above, the discrimination level of electronic background is fixed at 99.75% exclusion probability, constant over the predefined S1 interval between 3 – 20 PE. This window is somewhat restricted compared to the one in the profile likelihood method (3 – 30 PE) to yield the best signal-to-background ratio. The lower S1 threshold could be shifted towards a smaller value compared to the previous 100 live days run (at 4 PE) because of the improved hardware trigger condition (Sec. 2.3) and better control of the very small S1 electronic noise level. These boundaries, together with the lower  $3\sigma$  quantile of the nuclear recoil band, define the a priori benchmark region. The classical method neglects the shapes of the signal and background distribution and is solely based on a comparison between the background expectation and number of observed events. A total number of  $(1.0 \pm 0.2)$  background events was finally predicted in the cut-based benchmark region. The number is composed of two components. One is the number of predicted Gaussian and anomalous leakage from the electronic recoil band distribution and gives  $0.79 \pm 0.16$ . The complementary number of  $0.17^{+0.12}_{-0.07}$  is inferred from a Monte Carlo simulation of ambient neutron events [62, 71, 42], induced by spontaneous fission and muon spallation in the detector environment. These events cannot be discriminated by their ratio of S2/S1 since they would leave a nuclear recoil signature in the detector. After all data selection criteria had been fixed and an event expectation had been placed for the cut-based evaluation, 2 events were found in the pre-defined benchmark area after unblinding as shown in Fig. 2.20. They feature good waveform quality and are located at low values in the discrimination parameter near the detection threshold. The spatial location of events does not exhibit unexpected features, for both below and above the 99.75% rejection line, as presented in Fig. 2.21. The translation from the S1 photoelectron scale to deposited

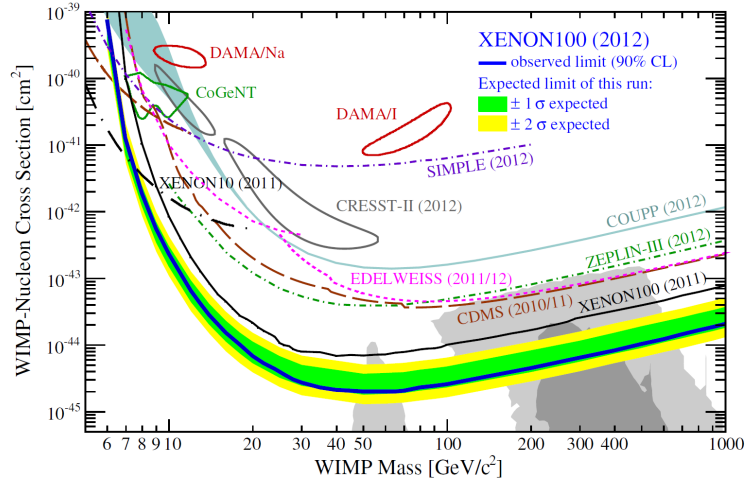


**Figure 2.22:** 90% confidence level exclusions limits on the spin-independent WIMP-nucleon cross-section placed by the XENON100 experiment after 100 live days (thin blue line, 2011) and 225 live days measurements (thick blue curve and coloured  $\pm 1, 2\sigma$  sensitivity bands, 2012). The allowed regions lie below the respective lines. Also shown are exclusion curves and signal claims of other direct search dark matter experiments. Grey shaded regions mark common theory predictions from constraint supersymmetric models. Figure taken from [42] and we refer to all citations therein.

recoil energy is mediated by Eq. 2.21 using the global  $\mathcal{L}_{eff}$  parameterization from [47].

The observation of only 2 candidate events is insignificant enough to reject the standard WIMP hypothesis, regardless of the assumed WIMP mass, with very high confidence. It is also obvious that the location of the two events is not in accordance with the bulk of the nuclear recoil region (light red distribution). Consequently, the profile likelihood method extracted an exclusion limit at 90% confidence level on the spin-independent WIMP-nucleon cross-section for all relevant WIMP masses up to 1 TeV/ $c^2$ . This final result is summarized in Fig. 2.22 together with the achievable sensitivity based on the background distribution in this run. The plot also includes the resulting exclusion limit determined from the previous 100 live days dark matter search. Standard astrophysical parameters, as introduced in Section 1.5, underlie the calculation. The evaluation sets most stringent limits on the interaction cross-section all over the parameter space of interest with a maximum sensitivity of  $2.0 \times 10^{-45} \text{ cm}^2$  at 55 GeV/ $c^2$  WIMP mass. The cross-check results obtained from the maximum-gap technique are in agreement within the systematic uncertainties.

We conclude at this point the general introduction to the XENON100 experiment and its achieved scientific reach. Beside the standard analysis of spin-independent dark matter models the collaboration has also studied alternative approaches of WIMP-matter coupling which to present is beyond the scope of this introduction. For interested readers we refer to the studies of the spin-dependent coupling [72] and implications for inelastic dark matter scattering [73].

Continuing with the main part of the present work, we focus on aspects of background and signal, relevant not only for the here presented dark matter results but also for the general understanding and interpretation of the XENON100 detector and other (future) detectors employing the LXe technique.



# Reduction of Anomalous Background

The sensitivity to detect a dark matter particle is determined by the ability to distinguish between background induced events and potential signals. In the XENON100 experiment this can be achieved by using the ratio  $S2/S1$  between the secondary and primary scintillation light as a discriminator between electronic and nuclear recoils. For the calculation of a detection limit or even a signal claim it is necessary to understand and quantify the distribution of background reaching into the expected region of interest. While the main background population in XENON100 is well described by Gaussian statistics there are additional sources of so-called anomalous background which are to be quantified or rejected in order not to be mistaken for real signals.

In this chapter we present how the optimization of a specific selection criterion, based on the  $S1$  light pattern on the PMT arrays, helps to significantly reduce the fraction of anomalous events for the evaluation of dark matter searches. We first give a short overview on origins and properties of anomalous tails in the distribution of the electronic recoil band and later quantify the achieved suppression in the latest dark matter analysis of 225 live days.

## 3.1 Composition of electronic recoil background

Interactions recorded within the active volume of the TPC can be classified according to the ratio of  $S2$  and  $S1$ . By relating this quantity to the deposited energy, two peculiar band structures will arise in a so-called discrimination space. This distinction has been introduced in Sec. 2.4.2 and is presented in Fig. 2.17 on calibration data. Therein, the mean ratio imposed by incoming ionizing radiation (blue scatter points) is several times larger compared to nuclear recoil interactions mediated by neutrons (red marked population). Accordingly we call the electronic recoil band (ER) representative for the electro-magnetic background distribution and use the nuclear recoil (NR) band to define the WIMP signal benchmark region.

During normal data recording the measured event rate is too low to provide an accurate characterization of the ER band using the accumulated statistics even from  $\sim 200$  days of measurement for the low energy region. Further the XENON100 collaboration has decided to take blinded background data for the dark matter searches. This means that the relevant part of the expected WIMP signal region (and simultaneously the lower tail of the ER background distribution) is not accessible before all event selection criteria are defined and the *a priori* signal expectation is placed. Therefore, it is necessary to rely on external calibration using single-site Compton scatters of far-penetrating  $\gamma$ -rays from  $^{60}\text{Co}$  and  $^{228}\text{Th}$  sources, placed outside the inner detector vessel. The representation of the actual detector background is only valid if the ER band is dominantly composed of  $\gamma$  radiation from surrounding detector materials. The 100 live days dark matter analysis [47] required modifications to this assumption since a little shift in the mean band description was caused by the increased level of internal  $^{85}\text{Kr}$  concentration after a tiny air leak during the preceding commission phase (more detailed information on the air leak are mentioned in Chapter 4). The reason for the observed deviation is the slightly altered band signature, implied by  $\beta$  decay of  $^{85}\text{Kr}$  as opposed to  $\gamma$  radiation. In the

succeeding analysis of the 225 live days dataset with far reduced krypton concentration [42], it was found instead that external band calibration provides a very accurate description of the ER band and could be reliably applied to predict the background expectation.

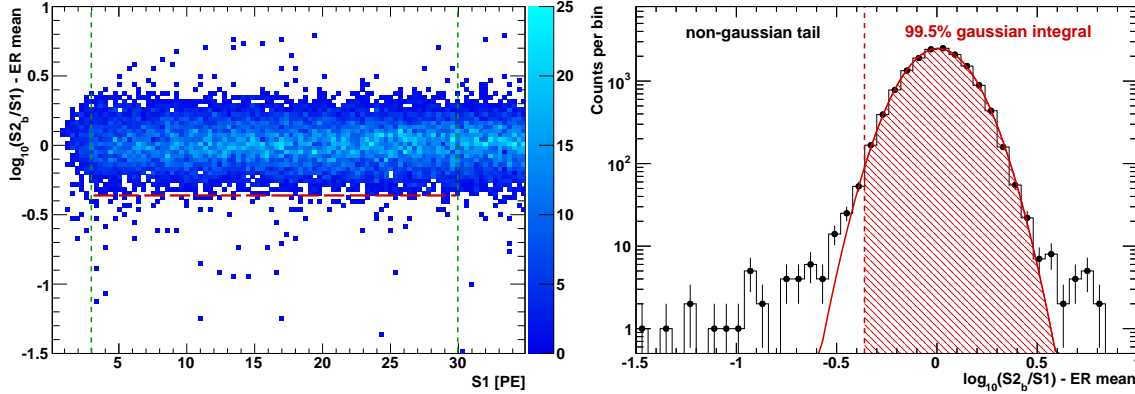


**Figure 3.1:** Electronic recoil band from  $^{60}\text{Co}$   $\gamma$ -calibration in the flattened discrimination parameter space for low recoil energies (refer to text). Selected single-scatter events obey all common data quality criteria in an inner 48 kg fiducial volume. The red dashed line indicates the 99.5% quantile of a Gaussian fit to the band projection shown in Fig. 3.2. Below this line, more events are observed than expected for a pure Gaussian distribution.

**Figure 3.2:** Projection on the y-axis of the electronic recoil band for the S1 interval between 3 and 30 PE (green vertical lines in Fig. 3.1). A Gaussian fit cannot sufficiently describe the anomalous tails in the observed distribution below the calculated 99.5% lower quantile indicated by the red vertical line.

Fig. 3.1 shows the ER band of  $^{60}\text{Co}$   $\gamma$ -rays, composed by single-site Compton scatters in the low energy regime above the WIMP region of interest (ROI). All available  $^{60}\text{Co}$  calibration data collected in parallel to the 225 live days dark matter run are combined for a total live time of  $\sim 21$  d. The population is drawn in the so-called flattened parameter space of  $\log_{10}(S2_b/S1)$ , where the energy dependence is compensated by subtracting the mean band position determined as a function of S1 and only the bottom PMT contribution is used (Sec. 2.5 and [57]). Events are selected according to all data quality criteria introduced for dark matter search in Sec. 2.4 except the S1 pattern likelihood (PL) cut, which is the one to be investigated in the following. An inner fiducial volume of 48 kg LXe is chosen for the present plot. Next to the 2-D representation is the projection on the discrimination axis for the benchmark region between 3 and 30 PE in S1. The central part is well described by a Gaussian distribution and the 99.5% lower quantile (red dashed line in both figures) is calculated from the fit integral as an example. Data shows that there are significantly more events left beyond this threshold than suggested by a mere Gaussian band shape projection. The excess is what we want to call anomalous leakage events because they reach down further in the discrimination variable than expected from the normal behavior. We note that non-gaussianity is to some extent present in the upper tail as well but not of major concern as acting in the opposite direction from the WIMP benchmark region. When we want to minimize the anomalous leakage into the potential WIMP region of interest we first have to think about possible origins.

### 3.2 Origin of anomalous leakage events

Events in the lower tail of the discrimination parameter share the property of showing an uncommonly low S2 signal with respect to the reconstructed S1. This class of events was first reported by [46, 34]

and is mainly referred to a phenomenon named gamma-X. It can occur when a  $\gamma$  particle scatters twice or more times inside the TPC but at least one interaction is located in a target region from where the electric field does not allow to drift electrons in the direction of the liquid/gas interface to create S2 light. Such regions are known to be covered by the  $\sim 17$  mm vertical space between the cathode mesh and bottom PMT array and include small gaps between individual photo-sensors. Also tiny spaces around the field shaping rings and the GXe volume above the liquid surface are potential regions of incomplete or missing charge collection. While the prompt S1 signal comprises scintillation light from all interaction sites, only the ionization electrons produced inside the homogeneous field cage can be reconstructed and S2 contributions from complementary scattering positions remain unrecognized. This explains why the apparent ratio of S2/S1 is shifted towards lower values. The effect is even enhanced by a high light collection efficiency for S1 emitted in those few millimeters close to the bottom PMTs. An extensive study of gamma-X origins and event signature for the XENON100 detector was performed and documented in the work of [74].

Since the  $\gamma$  rays must scatter at least once inside the charge insensitive region and once in the actual TPC in order to produce the effect, they have to originate from radioactive decay in external detector materials, most likely from the bottom construction parts. This was considered the main reason for the mentioned small mismatch between the ER band positions of science and calibration data in the 100 live days analysis since the dominant background contribution from  $^{85}\text{Kr}$  did not cause gamma-X signatures. Yet for the prediction of expected anomalous leakage, the  $^{60}\text{Co}$  calibration band was found applicable [47].

### 3.3 The S1 pattern likelihood cut

After discussing the dominant origin of anomalous events we focus now on means to reduce them. The design of a selection criterion to discriminate between gamma-X events and true single recoils has already evolved prior to the present thesis and the idea is as follows [75]:

For every recorded event one can compare the distribution of S1 photoelectrons on the top and bottom PMT arrays (so-called S1 hit pattern) to the one expected from a true single scatter sample provided for instance by full-absorption  $^{137}\text{Cs}$   $\gamma$  rays<sup>1</sup>. Since they share the property of depositing all of their energy at a single interaction vertex it can be excluded that they have undergone additional Compton scattering in gamma-X regions. Deviations from the expected pattern consequently indicate that the examined event is not conform to the single site hypothesis and may be rejected.

An illustrative example of a striking light pattern distribution is given by Fig. 3.3. The left plot shows the distribution of S2 light on the top array in the gaseous phase, used to determine the (x,y) coordinate of the event. It shows a well-confined spot as expected for the localized creation of S2 scintillation light from secondary amplification of the extracted electrons. On the contrary, the S1 pattern on the bottom array features more than only one cluster: One near the eventually reconstructed position but also other illuminated areas away from it. This hints at a potential second interaction vertex in a gamma-X region.

For the XENON100 experiment the algorithmic implementation and calibration was performed in the work of [61]. Therein, the TPC volume is first divided into a binned 3-D map. For every spatial bin the mean number  $\nu_i$  of photoelectrons counted by the  $i$ -th PMT is determined from the  $^{137}\text{Cs}$  calibration. Since  $\nu_i$  is usually a small number one expects it to be Poisson distributed. This leads to

<sup>1</sup>The control sample was later also calibrated using the 40 keV  $^{129}\text{Xe}$  de-excitation  $\gamma$  line after neutron irradiation but no significant difference was found.

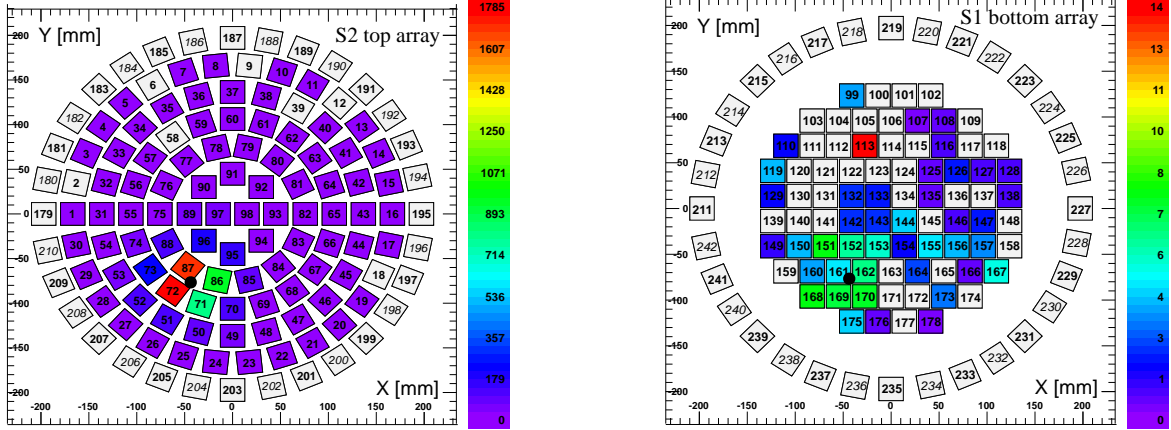


**Figure 3.3:** Example of an exceptional PMT hit pattern for an event rejected by the PL condition. (Left) S2 secondary scintillation light distribution on the top PMT array. The illuminated area is well confined due to spatial localization of the electron signal amplification in the gas phase. Only one interaction vertex in the x-y-plane can be spotted. (Right) S1 distribution on the bottom PMT array. Beside one area near the reconstructed S2 position (black point) other PMT regions are noticeably illuminated, indicating a second interaction vertex in a gamma-X volume. Figures are adopted from [57].

the construction of a likelihood function  $L$  [61],

$$L(n|\nu) = \prod_{i=1}^{N_{PMT}} \frac{\nu_i^{n_i}}{n_i!} e^{-\nu_i}, \quad (3.1)$$

corresponding to the probability to observe a partition of  $n = \sum n_i$  photoelectrons if  $\nu = \sum \nu_i$  is expected on average for events reconstructed in that particular vertex bin. One can show next [76] that the two-fold of the negative logarithm of the likelihood ratio

$$\lambda_P = \frac{L(n|\nu)}{L(n|n)} \quad (3.2)$$

follows a  $\chi^2$  distribution with  $N_{PMT}$  degrees of freedom (in the limit of every  $n_i$  being sufficiently large):

$$\chi_P^2 = -2 \log \lambda_P. \quad (3.3)$$

In the low energy region of interest,  $n$  is typically much smaller than  $\nu$  counted in case of  $^{137}\text{Cs}$  calibration at 662 keV. Therefore, the absolute numbers  $\nu_i$  are normalized according to  $\nu_i = \frac{n}{\nu} n_i$ .

The  $\chi_P^2$  value is now calculated for every event by the XENON100 raw data processor and made available for regular data analysis. As also documented in [61] the  $\chi_P^2$  is separately computed for the PMTs in the top and bottom arrays and so is  $\chi_{P,ratio}^2$  that considers the ratio of  $\lambda_P^{top} / \lambda_P^{bottom}$ . In preparation of the 225 live days analysis we have successively tested various combinations of these three variables within the present work,

$$\chi_P^2 = w_1 \cdot (\chi_{P,top}^2)^k + w_2 \cdot (\chi_{P,bottom}^2)^k + w_3 \cdot (\chi_{P,ratio}^2)^k. \quad (3.4)$$

We found that in fact best discrimination potential is achieved for a linear superposition (i.e. all weight factors  $w_i = 1$  and exponent  $k = 1$ ) as initially suggested by [61]. This particular choice will define what is called the S1 pattern likelihood parameter (sometimes abbreviated ‘‘PL’’) in the following.

It is straightforward to draw in Fig. 3.4 the PL parameter as a function of S1 for the already introduced collection of events from  $^{60}\text{Co}$  calibration. The more S1 photoelectrons are observed in total the more individual PMTs contribute to the signal sum and the higher is the involved  $N_{PMT}$ , representing the number of degrees of freedom. This explains why we find an increase of the PL band shape for growing S1. We also learn that the PL parameter does not provide a distinct separation between the two background classes of normal and anomalous ER events. It rather shows seamless upward tails, extending from an approximate Gaussian distribution for fixed S1 bins. In principle, however, higher PL values are supposed to disfavour the hypothesis of valid single-site events without gamma-X contribution.

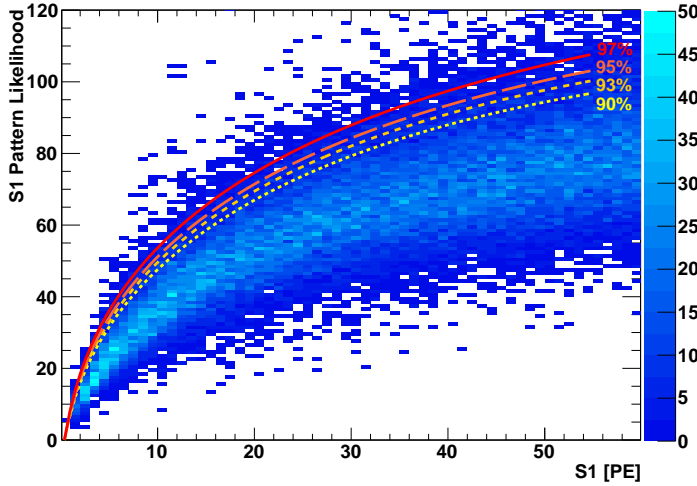


**Figure 3.4:** Distribution of the S1 pattern likelihood parameter as a function of S1 for  $^{60}\text{Co}$  events. For sufficiently large S1 the mean of the PL band approximates the number of PMTs contributing to the signal sum. Upper deviations correspond to large likelihood ratios and hint at anomalous PMT patterns. Different upper quantile levels are introduced and used for the definition of PL cut criteria (refer to text).

In our work, we define several pattern likelihood cuts with varying acceptance probabilities in the parameter space of Fig. 3.4 to later investigate their leakage removal potential. Therefore, we compute different upper quantile levels in the PL distribution for each 1 PE bin along the x-axis between 0 and 60 PE. The functional behavior of these quantile levels can be well approximated by a power law,

$$\text{PL}^q(\text{S1}) = a + b \cdot \text{S1}^{1/2} + c \cdot \text{S1} + d \cdot \text{S1}^{3/2}. \quad (3.5)$$

The parameters  $a, \dots, d$  are determined from a fit to each individual quantile level shown in Fig. 3.4, starting from 90% and ending at 97%. The definition of the pattern likelihood cut consequently depends on the chosen acceptance level, which we indicate by using the notation  $\text{PL}^{90\%}, \dots, \text{PL}^{97\%}$ . The cut condition is fulfilled if

$$\text{PL}(\text{S1}) < \text{PL}^q(\text{S1}), \quad q \in \{90\%, 93\%, 95\%, 97\%\}, \quad (3.6)$$

for any event with given S1. Otherwise, the event will be rejected as potential anomalous background.

In Fig. 3.5 we show the fraction of low energy ( $\text{S1} < 200 \text{ PE}$ )  $^{60}\text{Co}$  events that fail the  $\text{PL}^{97\%}$  selection criterion as a function of the reconstructed spatial position inside the TPC. It is evident that the cut rejection probability is largest in the bottom part at low  $z$  coordinates. This adds validity to the hypothesis that gamma-X events, which are expected to occur most likely in the vicinity of the charge-insensitive area below the cathode, can be identified by outliers in the PL distribution. However, we also observe a non-vanishing tagging efficiency in the rest of the TPC. Especially at high  $z$  it is unlikely that a  $\sim 1 \text{ MeV}$   $\gamma$  ray would scatter first below the cathode and afterwards travel a distance of 30 cm before interacting a second time. These events could either arise from a gamma-X region on top of the liquid phase or there are other mechanisms which can cause unusual S1 hit

patterns. It is important to note that the presented method is of course statistically limited by the small number of S1 photoelectrons in the dark matter benchmark region and it is hard to make a precise light pattern distinction when dealing with a total number of  $O(10)$  S1 photoelectrons or below. It has been tested that the spatial distribution of Fig. 3.5 is shifted the more towards the bottom the larger the S1 of rejected events.

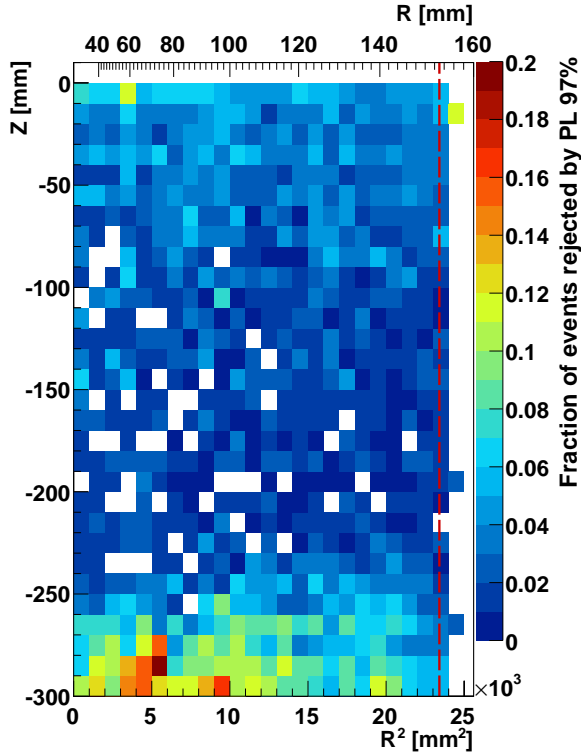


**Figure 3.5:** Fraction of low energy  $^{60}\text{Co}$  events ( $S1 < 200$  PE) which are rejected by the  $\text{PL}^{97\%}$  criterion as a function of the reconstructed radial (R) and z position inside the TPC. Identified events at the bottom are consistent with the expectation of gamma-X as possible explanation for anomalous PMT patterns.

### 3.4 Optimization of the PL cut performance

A prediction on the number of electronic recoil events leaking into the WIMP benchmark region had to be placed prior to the unblinding of the 225 live days dark matter run. The PL criterion, among a few other data quality cuts (Sec. 2.4), is supposed to minimize the share of anomalous leakage on that particular number in order to allow for a maximum discrimination between expected background and potential nuclear recoil signal. Two quantities must be balanced at the same time in order to provide best sensitivity towards a discovery or exclusion. First is the rejection efficiency of the PL cut, i.e. the probability to remove an actual background event from the region of interest. We will calculate this based on the rejection of  $^{60}\text{Co}$  electronic recoil events below the 99.75% Gaussian quantile line which was finally decided to define the discrimination level for the WIMP benchmark region [42]. Second is the acceptance of the PL cut, i.e. the probability for a true signal event to pass the set condition. This quantity will be estimated on a pure sample of  $^{241}\text{AmBe}$  neutron events which act as calibration of nuclear recoils.

The computation of the rejection efficiency is based on the sample of all available  $^{60}\text{Co}$  events, preselected by all other criteria which were applied to define a valid signal event for the WIMP search. The evaluation was done for both an 30 kg and 48 kg inner super-elliptical fiducial volume to enable a comparison between different volumes. It contributed to the final decision of using 34 kg LXe target

volume, based on overall optimization of the dark matter sensitivity [42]. From this data, we calculate the fraction  $f$  of events which are removed below the 99.75% Gaussian quantile line by a particular  $PL^q$  cut, labeled by its defining quantile level  $q$ . For the four examined choices of  $q$  and the 30 kg LXe inner volume we show the results in Fig. 3.6. Red marked events are those rejected by the cut selection and blue is the distribution of those passing. One can observe that the ability to identify anomalous leakage (below the red dashed 99.75% Gaussian rejection line) only slightly decreases with rising acceptance value  $q$  of the cut. The error on the fraction  $f$  is calculated from the binomial standard deviation  $\sigma = \sqrt{np(1-p)}$ , where  $n$  is the number of all events below the 99.75% discrimination line and  $p = \frac{n_{PL}}{n}$  is the ratio of PL rejected events over  $n$ . The numerical results are listed in the second and third column of Tab. 3.1.

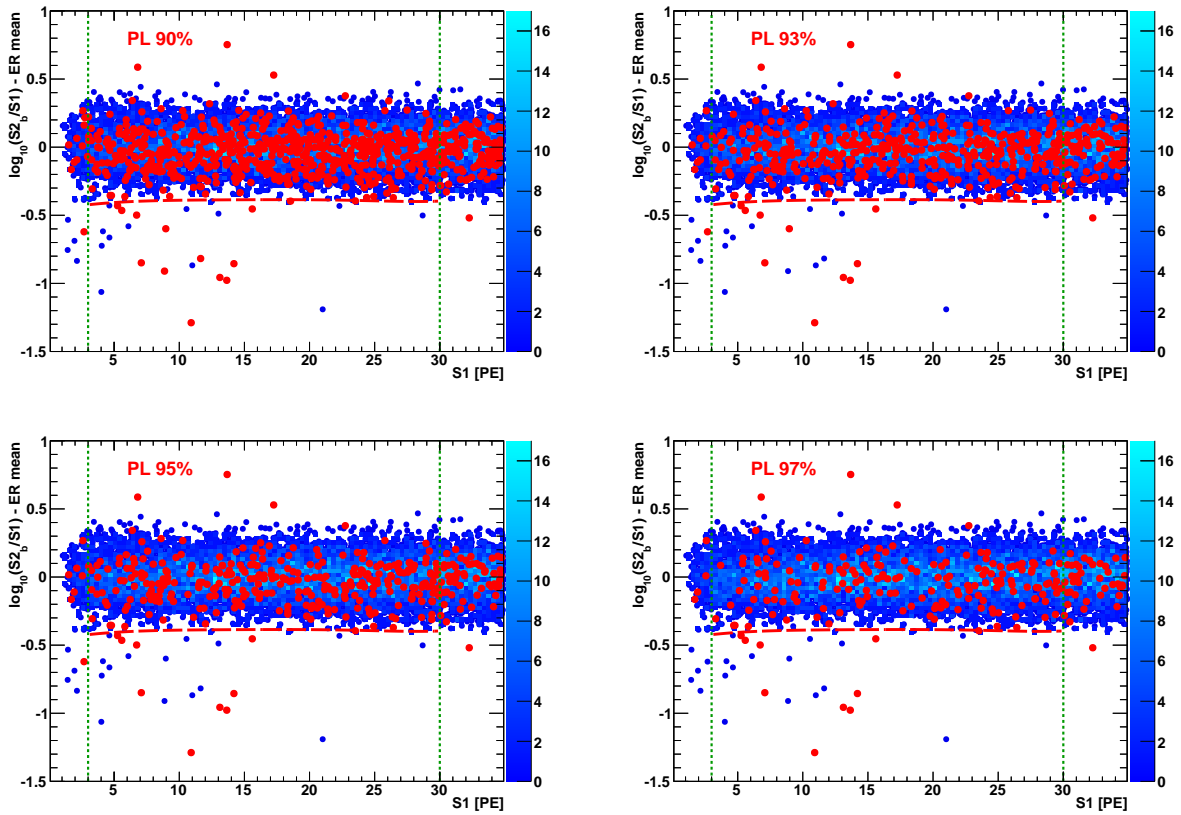


**Figure 3.6:** Rejection efficiencies of different quantile levels  $q$  of the PL cut in a 30 kg fiducial volume from  $^{60}\text{Co}$  calibration. Shown in red are events rejected by the PL criterion, while blue distributions complementary describe passing events. Relevant for quantitative analysis is only the WIMP benchmark region below the 99.75% Gaussian leakage rejection level (red horizontal line) and in between 3 – 30 PE (marked by green vertical lines).

Beside the removal fraction it is important to use the number of remaining events for a prediction of the total ER leakage in the taken background data after 225 days of measurement. This number is relevant to optimize the choice of fiducial volume, rejection level etc. in order to achieve the best signal-to-background discrimination. Therefore, we scale the number of leakage events passing a given  $PL^q$  cut in  $^{60}\text{Co}$  data to the measured background event rate known from the accessible (non-blinded) ER band region. The scaling factor  $S$  is simply given by the ratio of events in the taken 225

Cut level $q$	Anomalous BG rejection efficiency ( $^{60}\text{Co}$ )		Predicted ER events in ROI (225 live days)		Mean NR acceptance
	30 kg FV	48 kg FV	30 kg FV	48 kg FV	
PL 90%	(50±10)%	(59±5)%	0.5±0.2	2.0±0.3	91.0%
PL 93%	(40±10)%	(52±5)%	0.7±0.2	2.4±0.3	93.8%
PL 95%	(40±10)%	(47±5)%	0.7±0.2	2.6±0.4	95.4%
PL 97%	(40±10)%	(45±5)%	0.7±0.2	2.7±0.4	97.2%

**Table 3.1:** Results of the quantitative comparison of different PL acceptance levels  $q$ . Listed are rejection efficiencies determined on  $^{60}\text{Co}$  calibration data as well as event leakage prediction into the WIMP region for the 225 live days dark matter search. Low available statistics make distinctions difficult for the 30 kg target volume but trends are recognizable from the larger 48 kg sample. The last column provides the cut acceptance determined from the  $^{241}\text{AmBe}$  neutron calibration band. Statistical errors on this quantity are insignificant.

live days background band ( $N_{BG}$ ) and  $^{60}\text{Co}$  ( $N_{Co}$ ) ER calibration band for  $3 \text{ PE} < S1 < 30 \text{ PE}$ ,

$$S = \frac{N_{BG}}{N_{Co}}, \quad (3.7)$$

after the same blinding condition and all other selection criteria being equivalently applied to the calibration and dark matter dataset. The predicted number is then  $N_{Leakage} = S \cdot n_{PL}$ , with  $n_{PL}$  events passing the respective PL cut in  $^{60}\text{Co}$  data. Results are listed in the fourth and fifth column of Tab. 3.1.

To estimate the acceptance of a particular PL definition we count the number of passing events in the nuclear recoil band from the  $^{241}\text{AmBe}$  neutron calibration data taken in 2011. The same complete set of dark matter criteria as before is applied to provide a representative signal sample. In analogy to gamma-X, the neutron band is also slightly distorted by events that encompass additional unseen interactions in regions without a proper drift field (refer to Chapter 5.5 for more details). Knowing that WIMP particles would scatter once at most it is more accurate to consider only the central part of the NR band, like shown in Fig. 3.7. Therein, the  $\pm 1.5\sigma$  quantiles around the band median as a function of S1 define the upper/lower region of the acceptance test sample. The resulting acceptance probability for each cut representation averaged over the S1 interval 3 – 30 PE is likewise given in Tab. 3.1. The results differ only slightly from the original acceptance levels based on the definition of the PL cuts for ER events.

We interpret the results summarized in Tab. 3.1 as follows: In the 30 kg fiducial volume the rejection power is only weakly dependent on the chosen PL level  $q$  given the large counting uncertainties due to low statistics in that particular volume. It means that at the expense of signal acceptance not much is gained in leakage reduction when going from the 97% to the 90% acceptance level. For the 48 kg target one can recognize at least a trend in rejection gain from  $\sim 45\%$  to  $\sim 59\%$  in the same direction.

Contrary to the preceding 100 live days WIMP search the total ER background in the latest run was no more dominated by the intrinsic  $^{85}\text{Kr}$   $\beta$  decay but showed its largest contribution from external  $\gamma$  radiation. This finally motivated the choice of a smaller inner target volume of 34 kg as opposed to 48 kg because the surrounding LXe provides effective shielding against outside radioactivity. The significance of this effect can be read from the comparison of predicted leakage between the small and large fiducial volume in Tab. 3.1. Given the decision on the fiducial volume the best choice for the PL cut is the one which guarantees highest possible NR signal acceptance while providing almost equally good anomalous event suppression, thus PL<sup>97%</sup>.

Fig. 3.8 gives the PL<sup>97%</sup> cut acceptance determined for 1 PE binned slices in S1 by counting the number of passing events between the  $\pm 1.5\sigma$  boundaries of the nuclear recoil band (refer to Fig. 3.7). It is altogether constant with some minor bin-by-bin fluctuations beyond the mere statistical level. The

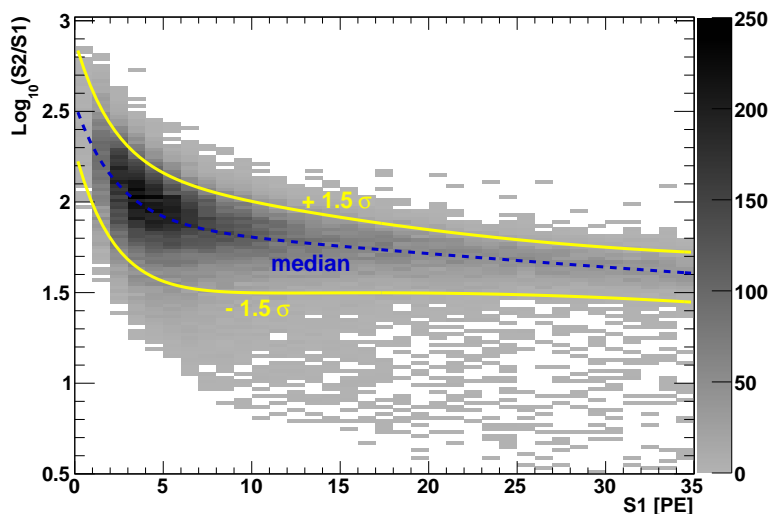


**Figure 3.7:** Definition of the PL acceptance test region on the nuclear recoil band from  $^{241}\text{AmBe}$  neutron calibration. To exclude neutron-X like event signatures and provide a pure single scatter sample only the inner central region, within the  $\pm 1.5\sigma$  quantile regions around the band shape median, is selected.

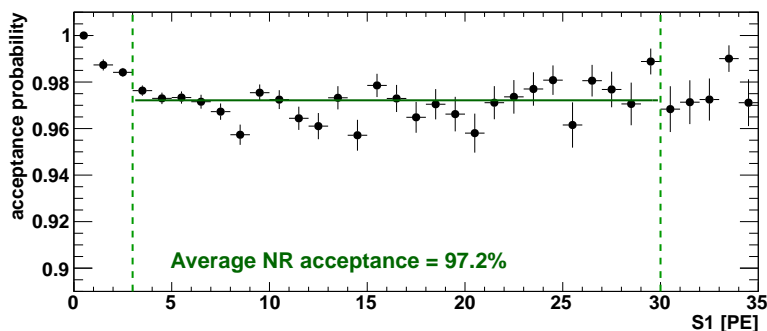


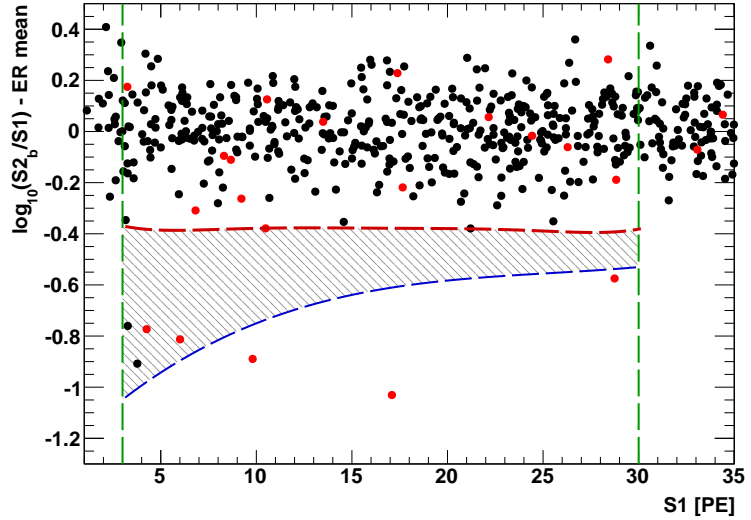
**Figure 3.8:** PL<sup>97%</sup> cut acceptance as a function of S1. The average (solid horizontal line) is determined within the S1 benchmark region between 3 – 30 PE (green vertical lines).

determined acceptance loss was considered in the evaluation of the latest WIMP search result, adding to the total S1 acceptance estimate from all other applied selection criteria.

### 3.5 Impact on the 225 live days dark matter result

We conclude this chapter by investigating the PL cut performance on the 225 live days dark matter search after unblinding the data in 2012 [42]. Fig. 3.9 provides the background summary plot already shown in Sec. 2.5 with one detail changed: Marked by red points are those events finally rejected by the PL<sup>97%</sup> condition after all other cuts applied. It is apparent that the cut keeps the high acceptance in the centre of the electronic recoil band (black point population around 0 in the flattened discrimination parameter) but helped efficiently at reducing the anomalous leakage far below the set 99.75% Gaussian rejection line (red horizontal curve). All but one of the red marked events between 3 – 30 PE are very

**Figure 3.9:** Measured event distribution in the flattened discrimination space from the 225 live days dark matter search (black data points, adopted from [42]). Marked red are those events rejected by  $PL^{97\%}$ . Also shown is the predefined WIMP benchmark region for the dark matter analysis (grey shaded area). The PL cut works efficient at reducing the amount of anomalous leakage into the signal region (and below).



close or even below the indicated lower  $3\sigma$  boundary of the nuclear recoil band (blue curve). This provides another strong confirmation that the  $PL^{97\%}$  cut has correctly removed anomalous leakage events rather than WIMP recoils. It is noteworthy that the two passing events in the benchmark region have very regular PL values in accordance with the main band population as a function of S1 (refer to Fig. 3.4) and thus would not have been rejected by any of the defined PL  $q$  levels in this analysis. It is also expected that the information value from the S1 PMT pattern is finally limited in approach of only a few photoelectrons. Therefore, studies about other possible background explanations of the two candidate events are further ongoing in the XENON100 collaboration even though the number is in good agreement with the total background expectation of  $1.0 \pm 0.2$  (electronic recoils plus neutron event prediction) determined before the unblinding inside the WIMP benchmark region [42].

# Radon Background

Among the most threatening sources of radiation background in noble liquid detectors are those of radioactive radon and krypton isotopes. Both belong to the group of noble elements and are difficult to separate by chemical or physical processes. Dispersed inside the whole liquid target their impact is inherently different from surface contamination and cannot be efficiently reduced by making use of the self-shielding capability of noble liquids. Thus, the understanding of so-called *intrinsic* contaminants is crucial not only for the background interpretation in current experiments, like XENON100, but will even gain in importance for future ton-scale detector generations, which strive for almost negligible surface effects.

In the present work we aim at a coherent picture about the disintegration and dynamic signature of radon and its subsequent decay products in the XENON100 detector. Some findings, like the light/charge yield of  $\alpha$  decays, represent general properties inherent to LXe as a radiation-sensitive material, while others, like evidence for the drift of charged radon daughter nuclides, turn out to become important for the eventual prediction of quantitative contribution to the integral low-energy background relevant for dark matter searches, such as reported in [42].

## 4.1 Origin and decay of radon

Radon is the heaviest element in the group of noble gases and the only one without stable isotopes. Its natural abundance thus arises from the  $\alpha$  decay of the long lived  $^{226}\text{Ra}$  and  $^{228}\text{Th}$ , which are themselves constantly produced within the decay chains of the primordial  $^{238}\text{U}$  and  $^{232}\text{Th}$ , respectively. The radon as part of the former chain,  $^{222}\text{Rn}$ , has a half-life of 3.8 days<sup>1</sup> and disintegrates via  $\alpha$  emission. The other important isotope,  $^{220}\text{Rn}$ , is sometimes called “thoron” because of its origin from the thorium chain. In contrast, it is very short-lived with only 55.6 s of half-life and decays under  $\alpha$  emission as well.

The further evolution in the decay chains of radon and thoron starts becoming more complex from this point. Fig. 4.1 provides a summary of decay sequences useful for the continuing discussion: The decay structure appears very similar in both chains. In each of them we find two high energetic  $\alpha$  decays with energies in the MeV range followed by two  $\beta$  disintegrations with typical energy endpoints of hundreds of keV to a few MeV. The prompt decays of  $^{212}\text{Po}$  and  $^{214}\text{Po}$  provide unique topologies for event identification. Their mean lifetimes are within the typical time-window of recorded waveforms by the XENON100 data acquisition and qualify for coincidence analysis as detailed in Sec. 4.4.2. While the thoron chain ends at the stable lead isotope  $^{208}\text{Pb}$ , the other isotope  $^{210}\text{Pb}$  is long-lived with a half-life of 22 years. It is a potential threat to many low background experiments that  $^{210}\text{Pb}$  survives even after many years of radon-reduced environment. The fact that one high-energy  $\beta$  decay follows on the way to the stable  $^{206}\text{Pb}$  turns it into one of only few disadvantages of using lead as

<sup>1</sup>All nuclear data quoted in this chapter, such as half-lives, decay energies, branching ratios etc. are collected from the recommended database provided on the website of the Laboratoire National Henri Becquerel [77].

a shielding material. Indicated in Fig. 4.1 are also those parts of the chains in secular equilibrium with the original amount of thorium and radium. Equilibrium is established if the lifetimes of the subsequent isotopes are much shorter in comparison to the mother nuclide and their production rates are essentially constant. Note also that the equilibrium chain with the primordial isotope of uranium can likely be broken and instead the amount of  $^{226}\text{Ra}$  may be enriched with respect to  $^{238}\text{U}$  or vice versa. Not shown in the figure is that almost all disintegrations feature prompt emission of  $\gamma$  quanta, among the most high-energetic natural  $\gamma$  line at 2.6 MeV from  $^{208}\text{Tl}$  decay.

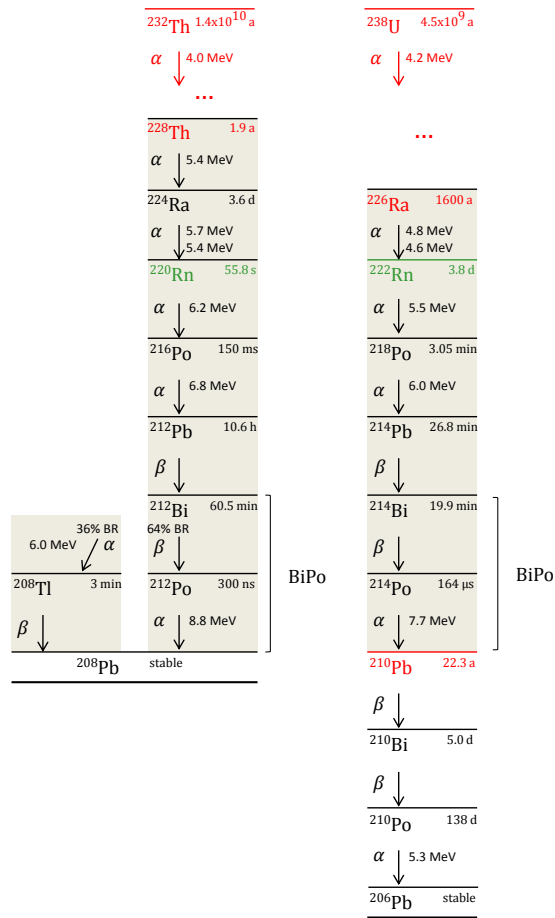


**Figure 4.1:** Parts of the decay chains of the primordial elements  $^{232}\text{Th}$  and  $^{238}\text{U}$ . Time constants are understood as half-lives. For  $\alpha$  emitters we report their energy release. Only relevant branches (branching ratio BR > 99%) are drawn. Both chains feature short-lived decays of  $^{212}\text{Po}$  and  $^{214}\text{Po}$ , useful for later BiPo coincidence analyses. Isotopes marked red are not necessarily in secular equilibrium with their mother nuclides. All nuclear decay data are collected from [77].

## 4.2 Radon as potential background source

The noble gas radon is practically inert to chemical reactions under regular conditions. Despite the large atomic radius it can easily diffuse through the air, many organic materials, tiny cracks in rock, etc. Typical activity concentrations in the environment range from a few to several hundreds of  $\text{Bq}/\text{m}^3$  in air, depending strongly on the composition of the earth soil, rock or concrete (in closed buildings) and on the ventilation. The mentioned properties pose a threat to all types of low-radioactivity background experiments facing the infiltration of radon into the detector and the successive decay inside or on the surface of the active volume. On the contrary, radon daughters behave chemically in a different way from noble gases, as they rather belong to the group of metals and, for example, more easily adhere to

surfaces. Many times in the past, extreme efforts have been taken by low-radioactivity experiments to avoid or reduce the radon concentration. Examples are the shield and cryostat design of the GERDA experiment [78, 79] or the manufacture of the BOREXINO inner vessel [80].

In the case of the XENON100 experiment the challenge is even the more peculiar as the employed target material consists of another heavy noble element, xenon. Active purification through chemical or physical separation – as done for electro-negative components (Sec. 2.2) or krypton – becomes thus very complicated. This is particularly true as the LXe is continuously circulated within the closed gas loop, in which some components, like the active getter or the circulation pump, add to the emanation of radon or allow for tiny leakage from the outside air. However, even in a perfectly leak tight system, radon can always emanate after the decay of radium, which is abundant in traces inside or at the surface of practically any detector component. This motivates material screening and selection of only the most radio-pure components, especially in terms of uranium and thorium, already before detector construction [63].

If a radium decay happens on the surface or within the uppermost layers of outer materials, the recoil induced by  $\alpha$  emission can be sufficiently energetic to repel the nucleus into the LXe volume and the particle can thus move somewhere else before disintegrating. This source of emanation is expected to be dominant for the  $^{222}\text{Rn}$  branch, as its half-life exceeds by far the one of thoron, which is likely to disintegrate shortly after repulsion. In contrast, the 3.8 days of half-life in case of  $^{222}\text{Rn}$  provide enough time for the atom to travel over large distances, such as through the xenon recirculation loop. Consequently, we would expect possible sources of radon emanation both from inside (radium contamination of any TPC or vessel material) and outside (radon diffusion from the air or emanation by the active getter or commercial recirculation pump).

Important to notice about radon as a background contributor in any noble liquid experiment is its nature of likely being spread uniformly in the whole active target, due to effects mentioned above. Not belonging to the class of surface contamination, the activity concentration can hardly be reduced by constraining the fiducial volume to inner parts and thereby profiting from the LXe self-shielding. Such background sources (radioactive krypton is the other main known contaminant) are called intrinsic and even in large future detectors not much will be gained if their concentration is not guaranteed at the lowest possible level.

So far we have not yet explained why radon actually adds to the potential radiation background for WIMP searches. From  $\alpha$  interactions, as it will be shown in Sec. 4.4.1, energy deposits are more than two orders of magnitude above the dark matter region of interest. And among the two remaining  $\beta$  decays, even one appears in close time-coincidence with another  $\alpha$  decay and therefore can easily be tagged as a spurious event. In fact there are only two potential candidates,  $^{212}\text{Pb}$  and  $^{214}\text{Pb}$ , one in each radon chain.

With 13% probability the  $\beta$  decay of  $^{212}\text{Pb}$  goes immediately to the ground state of  $^{212}\text{Bi}$  without sending an additional  $\gamma$  ray. The endpoint energy of  $E_{\beta,max} = 570\text{ keV}$  is far above the few keV region but the continuity of the spectrum down to zero kinetic energy creates some overlap with the WIMP recoil energy range. The analogue argumentation holds in case of  $^{214}\text{Pb}$  among the daughters of  $^{222}\text{Rn}$  with a branching ratio to the ground state of 9.2% and maximum  $\beta$  energy of 1019 keV. In all other cases featuring prompt  $\gamma$  ray emission at various energies, it is difficult to tell a priori whether the emitted photon will create at least a second scatter resolvable by the detector event vertex reconstruction. This depends much on the Compton and photo-absorption scattering lengths in LXe, both functions of the  $\gamma$  energy. Due to the complexity of combining various energy deposition spectra it is advantageous to calculate the energy overlap with the dark matter region of interest by means of Monte-Carlo simulations to estimate the number of expected background events. In the context of the XENON100 experiment such simulations were previously performed and published in [81] and we

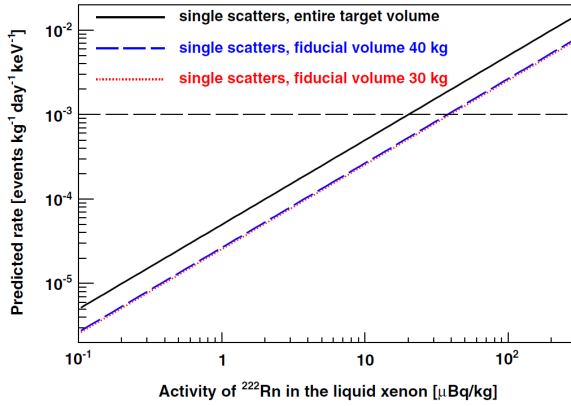


**Figure 4.2:** Predicted differential background rate induced by the  $^{222}\text{Rn}$  decay chain in the energy region below 100 keV deposited in single scatters (figure from [81] courtesy of XENON100). The event expectation, normalized per kg target mass, days of measurement and keV energy interval, is in linear relation to the  $^{222}\text{Rn}$  radio-activity concentration in a given fiducial volume.

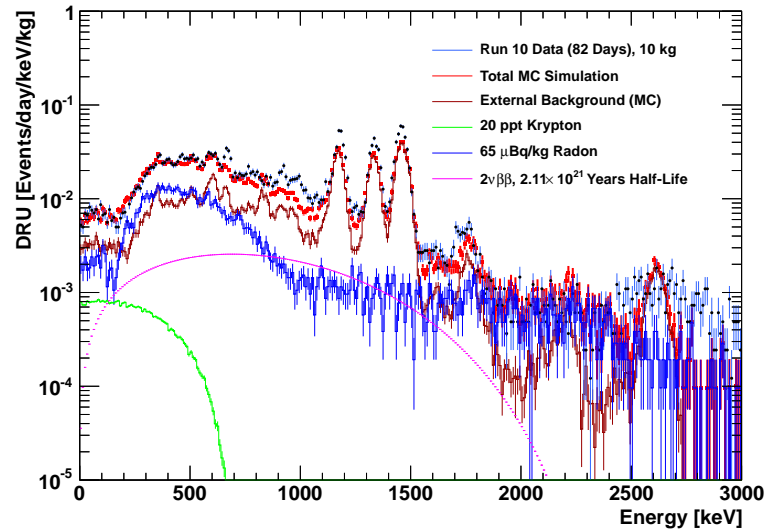
give the relevant outcome on the radon induced background expectation in Fig. 4.2.

In the mentioned analysis,  $^{222}\text{Rn}$  and all subsequent decays down to the long-lived  $^{210}\text{Pb}$  were processed in the particle simulation framework GEANT4 [65, 66] using a full description of the XENON100 detector geometry and an optimized low-energy physics lists ([81] and references therein). The radon was assumed homogeneously distributed within the active xenon volume (this assumption will be tested on data in Sec. 4.6.2) and the known S2 peak separation resolution (3 mm along the z-axis) was considered to discriminate single from multiple site interactions. Only events which effectively appear as a single scatter and have a summed energy deposit of less than 100 keV (low energy region of interest) are taken into account for the rate prediction. It is not written explicitly but independently confirmed in [82] that the plotted total rate is dominated by the  $^{214}\text{Pb}$  contribution. The outcome in Fig. 4.2 is normalized to standard units of the background index, given in DRU (differential rate per kg, day and keV recoil energy) and – as expected – is in linear relation to the assumed radio-activity concentration of  $^{222}\text{Rn}$  dissolved in the LXe target. The result is slightly dependent on the choice of the fiducial volume, as  $\gamma$  rays emitted in outer layers of the TPC have a better chance to escape the detector unrecognized and let the interaction appear more likely as single-sited.

The simulated contribution from radon (based on intrinsic activity measurements presented in Sec. 4.8) can be compared to other known sources of background in the XENON100 detector. Fig. 4.3 shows the result of a preliminary description of the measured differential background rate in a 10 kg inner fiducial volume for the most recent dark matter search run [42], provided by Kevin Lung. In order to match the observed spectrum (black histogram) by means of Monte-Carlo simulations (red spectral shape) of various radiation components, a significant contribution from radon decay is inferred (blue histogram). As it turns out by the central result of Sec. 4.8, radon has taken the role of the major intrinsic contaminant in the low-energy region relevant for the dark matter search. This results from the achievement of  $^{85}\text{Kr}$  purification from LXe in the latest reported science data run [42]. The radon contribution is still exceeded by external  $\gamma$  radiation background (dark red spectrum) whose impact will be significantly suppressed in future ton-scale detectors, however.

In the following we focus on achieving a proper understanding of the origin, time evolution and physical properties of the various components of radon, using experimental background data recorded during the XENON100 dark matter runs and detector commission phases. This shall not only give deeper insight about one important intrinsic background contaminant in the currently running experiment but can be also helpful for reducing the radon contribution in present and future noble liquid experiments.

**Figure 4.3:** Differential electromagnetic recoil spectrum for energies up to 3 MeV in the XENON100 experiment. Data (black histogram) is taken from a subset of the 225 live days measurement [42] after selection of single scatter recoils in the innermost 10 kg fiducial volume. Simulation of the total spectrum (light red) and classification according to different background origins is shown in parallel. Radon (blue histogram) contributes most among the intrinsic background sources in the relevant low energy region < 100 keV. Figure provided by Kevin Lung (courtesy of XENON100).



## 4.3 Data collection

No dedicated detector calibration with a known amount of radon gas fed into the TPC has been performed yet. Among the risks of such a measurement is the accumulation of the long-lived  $^{210}\text{Pb}$  which can potentially act as a background source during the dark matter runs. Other potential problems involve the actual production of a safe radon source and the leak-tight mounting to the xenon gas system, which must avoid any contamination with radioactive elements in air, such as  $^{85}\text{Kr}$ . However, during the commission phase before the first scientific run, a tiny leak in the xenon gas system caused a temporary ingress of air to the inner detector (first reported in [57]). What turned out unfortunate for the  $^{85}\text{Kr}$  level was in fact a lucky coincidence in terms of studying radon. In a short period after the incident roughly the same amount of radon decay events were collected as within the two combined science runs ( $\sim 325$  live days of data).

In this work, we will base our analyses on both the short time period of high radon concentration (10.4 live days in total), taken in late 2009, and data collected during the most recent dark matter run (225 live days), covering March 2011 until April 2012. We will use the former data to establish and train the dedicated analysis techniques and apply it later to the long-term data-taking.

## 4.4 Radon decay identification

First we will address the question how decays from the radon chain can be identified and correctly reconstructed from XENON100 data. As we have seen previously, one can classify the 5 constituents of each radon/thoron chain by the following attributes: Two  $\alpha$  disintegrations at distinct energies are followed by one pure  $\beta$  emitter, before finally one  $\beta$  and  $\alpha$  decay, separated by only  $0.3\ \mu\text{s}$  and  $164\ \mu\text{s}$  of half-life happens, respectively. The peak positions of  $\alpha$  lines are in principle unique and allow for event classification by energy. Pure  $\beta$  decays are complicated to identify since they imply no pronounced feature except for their accompanying  $\gamma$  lines. Eventually, the so-called BiPo coincidence of subsequent  $^{214}\text{Bi} \rightarrow ^{214}\text{Po}$  ( $^{212}\text{Bi} \rightarrow ^{212}\text{Po}$ ) decay provides a unique characteristic without need of any hard constraint on the reconstructed energies.

### 4.4.1 Alpha spectroscopy

Starting in our study with the most straightforward method to tag radon events, we first focus on pure  $\alpha$  decay reconstruction. According to Fig. 4.1 we expect energy depositions of a few MeV, far off the range which the XENON100 detector was designed for in first place. In the context of our experiment those regions are considered high energetic and require a modified set of data selection rules compared to the one introduced in Chapter 2 for elastic nuclear recoils. At the same time most cuts developed to remove electronic noise or define signal appearance are not needed because threshold effects do not play any prominent role at such high energies.

**Selection cuts** All  $\alpha$  decay events considered in the further analysis are selected according to only the following few rules (if not explicitly mentioned otherwise):

- **S1 PMT coincidence** The main S1 signal must be composed of at least two contributing PMTs, each above 0.3 PE threshold, within a 20 ns time coincidence window. This minimum coincidence requirement is supposed to clean our sample from obviously noise-triggered events (e.g. from PMT dark current).
- **S2 threshold** The largest S2 signal (sorted by integrated pulse area) must exceed the minimum threshold of 300 PE. With this requirement it is assured that the event has a valid S2 (important for correct vertex reconstruction) and does not happen in a region of incomplete charge collection (e.g. below the cathode mesh) or is triggered by spurious noise (e.g. delayed electron extraction from the liquid/gas interface). This condition will be removed when specifically studying detector regions which do not allow for drifting of the electrons (such as in between bottom PMTs and cathode mesh).
- **Misidentified additional S1** A proper event should fulfill the requirement of only one real S1 peak within the DAQ trace (otherwise another interaction happened independently in time, which is not expected for single decay  $\alpha$  emission). For dark matter search (Sec. 2.4) this condition was formulated such that any identified, second largest S1 must not involve more than 1 PMT in its trace (i.e. inverse of the S1 PMT coincidence). This cut turns out not sufficiently appropriate for such high light emission as is the case for  $\alpha$  events. A zoom into the S1 peak area of a typical summed waveform is shown in Fig. 4.4. The main S1 peak (labeled “S1sTot[0]”) caused by the  $\alpha$  particle consists of a very large number of photo-electrons ( $\sim 20\,000$  PE in this sample) within the short time of tens of nanoseconds. After those relatively huge pulses we observe the appearance of fluctuations in the PMT baseline shortly afterwards. However, sometimes the peak finder of the XENON100 data processor arbitrarily identifies those after-pulses as another S1 peak with more than one PMT involved. Since also the integration window (indicated by dashed vertical lines) is defined arbitrarily large, the total apparent peak area can grow as large as few hundred PE. Thus, we cannot simply apply the standard single S1 cut as it would falsely remove many valid  $\alpha$  decay events from our set.

Another observation is the occurrence of many single electron S2 signals after the major S1, most likely induced by photo-ionization of impurities with low ionization potential, dissolved in the LXe, or of the metallic grids. They appear in much larger number per waveform as in case of low S1 emission in other calibration or background studies. This also increases the chance for one of those peak structures (often forming a “forest” of pulses following the large peak) to be misidentified as another S1 signal. Also those events shall not be removed by the too strictly defined rule of the standard single S1 condition.

We show the spectrum of the *second* largest S1 peak (as identified by the data processor) in black line in Fig. 4.5 after having preselected high energetic largest S1 between 20 000 – 25 000 PE. The subset of events where this peak appears previous to the main S1 in time are presented in blue. Those events cannot be causally connected to the major signal. First we see that the majority of second S1 pulses has only a very small peak integral (included in the first bin of the spectrum) and in fact represents the well-known class of single-coincident PMT dark current signals. Then, ranging up to rather high S1, we see the distribution of the above mentioned fake signals. At a threshold of  $\sim 1600$  PE we find that practically all second signals appear *before* the main S1 and, thus, cannot be a consequence of S1 induced baseline noise. What we observe here is rather an upcoming population of true S1 signals. We will learn later that those arise from the time-coincident BiPo decays featuring two *real* interactions ( $\beta$ - $\alpha$ -decay) recorded within the same event window. We therefore pose our cut threshold at the indicated second S1 position of 1600 PE in order to keep as many valid pure  $\alpha$  events while at the same time distinguish from the class of BiPo events.

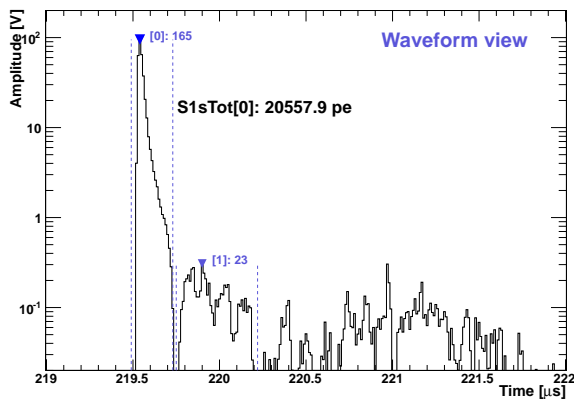


**Figure 4.4:** Zoom into the summed waveform of a typical  $\alpha$  decay event, recorded and processed by the XENON100 DAQ system. Largest (labeled “[0]”) and second largest S1 (“[1]”) were identified at recording time  $\sim 219.5$  and  $\sim 220 \mu\text{s}$ , respectively. Also given is the total peak integral of the largest peak and the integration window (marked by dashed vertical lines).

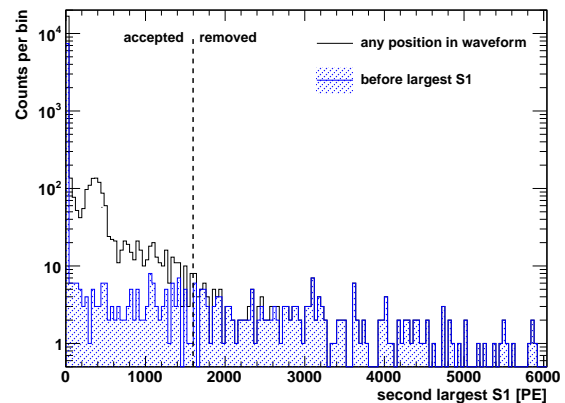


**Figure 4.5:** Spectrum of the second largest identified S1 peak (black histogram) after preselection of high-energetic main S1 ( $\alpha$  decays). Shown in blue is the subset of events in which the second S1 occurs previous to the main one. The dashed vertical line defines the cut threshold as discussed in text.

**S1 signal correction** We observe that the position dependent correction of the S1 signal – well-established for the usual energy space of interest of  $\mathcal{O}(100 \text{ keV})$  and below – does not yield a sufficient uniform correction of the S1 signal from  $\alpha$  decays. The effect can be seen in Fig. 4.6, where two distinct patterns in S1 (later attributed to  $\alpha$  lines of  $^{222}\text{Rn}$  and  $^{218}\text{Po}$ ) do not remain constant along the  $z$  axis. Similar non-uniformity is also observed for the corrected S1 as a function of the radial event position (not shown). In both cases, we have applied the common S1 correction map, which is defined on low-energetic, neutron-activated Xe lines [33]. The reason for the apparent deviation are two kinds of saturation effects: Firstly, the S1 signals from  $\alpha$  interactions are very large ( $\sim 20\,000$  PE on average) and occur within the typical integration window of few tens of ns. It sometimes causes the summed PMT readout to approach a saturation threshold. This explains why the standard correction causes a shift towards seemingly lower corrected S1 near the bottom of the TPC where the largest amount of

light is collected (remember that the majority of light is seen by the bottom array and the solid angle coverage becomes larger towards lower  $z$ ). Secondly, the inferred event position itself starts becoming less accurate because the  $S2$  light used for the vertex calculation becomes large enough to affect the position reconstruction algorithms, which are not sufficiently trained in this case.

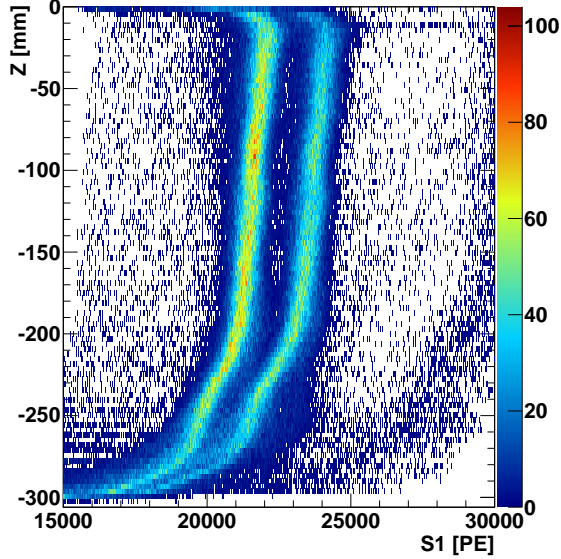


**Figure 4.6:**  $S1$  corrected by the standard map [33] (on the abscissa) as a function of reconstructed  $z$  position (ordinate) for very large  $S1$  range.

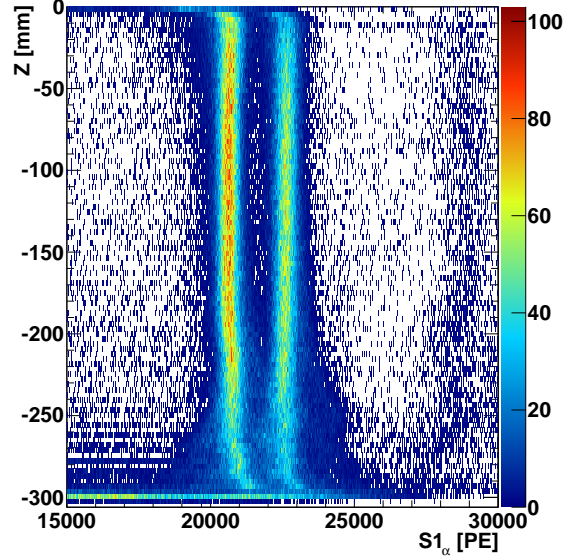


**Figure 4.7:**  $S1$  corrected by the dedicated alpha light map in 4.8 as function of  $z$  position. The response after correction is much more uniform in  $z$  and  $r$  (latter not shown).

In order to achieve a homogeneous  $S1$  response to  $\alpha$  decays within the entire active xenon volume we construct a distinct light response map, starting from the original *uncorrected*  $S1$  signals. Hereby, we benefit from the first dataset of high radon concentration, providing enough statistics within each bin to create a sufficiently high resolution map. The whole TPC is divided into  $31 \times 8 = 248$  bins on a 2-D lattice along radial and  $z$  position. The bin width along  $z$  is kept constant while a slightly decreasing bin size is chosen at larger radii to compensate for the quadratic increase in volume and to guarantee a comparable number of events in each bin. Further we fit the obtained high-energy spectrum of uncorrected  $S1$  in each bin by assuming two neighbouring Gaussian functions to describe the two present  $\alpha$  peaks. For two of these bins we draw the fitted  $S1$  distribution in Fig. 4.9. The upper plot shows a well separated double peak appearance in the center of the TPC. Towards rim regions (bottom figure) peak resolution becomes worse and the two Gaussian shapes begin overlapping. Still, the peak resolution remains sufficient for a determination of the maximum peak positions. Finally, we extract the two mean values from the Gaussian fits and take their (arithmetic) average. This observed  $S1$  mean value is fed into the corresponding bin of the spatial map. We repeat this evaluation for every  $(r,z)$  bin and eventually calculate the relative light yield by dividing by the average  $S1$ . The resulting relative correction map is shown in Fig. 4.8. The main features are not much deviating from the standard one (shown in Fig. 2.6 of Sec. 2.1.4): The absolute light yield varies by a factor of  $\sim 2$  between the uppermost and bottom region of the TPC, with the increased light amount at the bottom, where PMTs are immersed in the liquid phase and have a higher QE on average.

We use a bilinear interpolation (standard implementation for 2-D histograms in the data analysis framework ROOT [65, 66]) to approximate the correction factors for  $(r,z)$  positions anywhere between

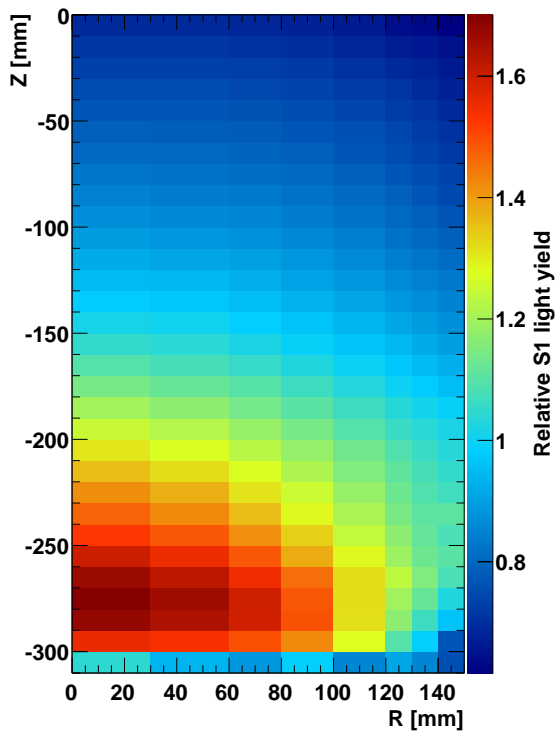


**Figure 4.8:** Spatial map of relative light yield from  $\alpha$  decay in the XENON100 TPC, divided into bins along radius  $r$  and  $z$ . For each bin the absolute observed S1 from the two main  $\alpha$  lines is divided by the global average. Light yield is highest near the bottom PMT array (except for the lowest bins which include events in the optical shadow of the grids).

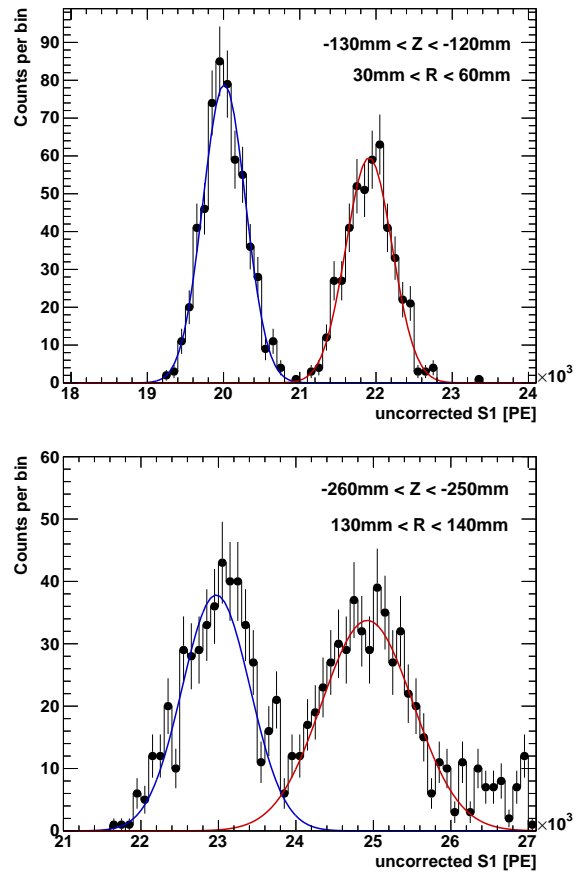


**Figure 4.9:** Gaussian fits to the observed (uncorrected) high energy S1 spectrum for two different detector regions near the centre (top figure) and edge (bottom figure) of the TPC. Using the average Gaussian means for each bin we construct the spatial S1 alpha correction map (Fig. 4.8).

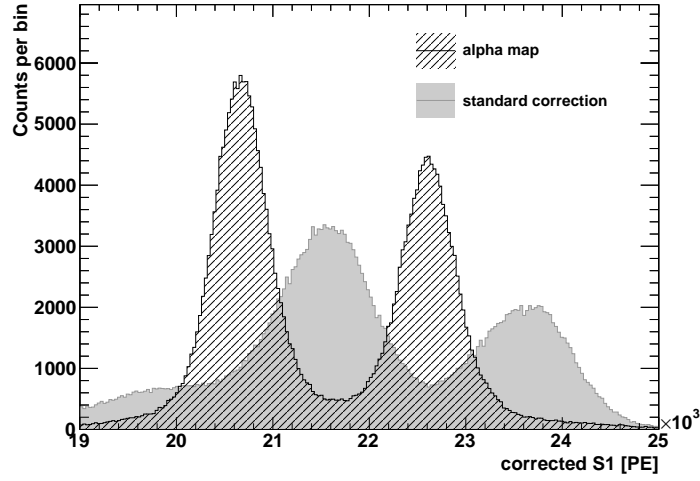


**Figure 4.10:** Improvement in S1 resolution using the newly defined S1 light correction map for high-energy  $\alpha$  decays (hatched black spectrum) compared to the standard correction (grey). The map allows for a global distinction between different  $\alpha$  energies and narrows the peak resolution by about a factor of 2 in full width at half maximum (FWHM). The two visible peaks arise from  $^{222}\text{Rn}$  (5.5 MeV) and  $^{218}\text{Po}$  (6.0 MeV).

the centres of the bins. Finally, the uncorrected (directly observed) S1 value at a given spatial position in  $(r,z)$  is divided by the corresponding spatial correction factor. When we apply the dedicated S1 alpha light map to the same sample of high energetic events as before, we find a much more uniform response shown in Fig. 4.7 (same improvement holds for the  $r$ -dependency, not shown) which allows to distinguish the two apparent components of the radon chain with much higher resolution inside the whole volume. Also visible in the figure is the onset of a third  $\alpha$  line at  $S1_{\alpha} \approx 29\,000$  PE from  $^{214}\text{Po}$  decay as discussed further in the next section.

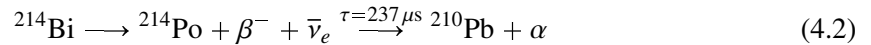
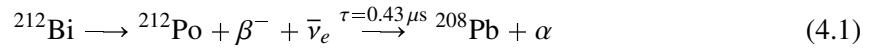
A 1-D projection on the corrected S1 for events between  $-290\text{ mm} < z < -10\text{ mm}$  in Fig. 4.10 illustrates the improvement in global resolution achieved by using the dedicated alpha light map. It allows for further selection and classification of  $\alpha$  events with different energies for the upcoming analyses. Events reconstructed at  $z \approx -300\text{ mm}$  most likely occur very close to or even on the surface of the cathode and screening meshes. The light yield is much influenced by the shadowing of these structures, so that we observe a very broad S1 signal spread and an artificial shift towards lower values even when corrected by the new light map. A detailed analysis of light and charge yield of alpha events will follow in Sec. 4.5.1.

#### 4.4.2 BiPo tagging and event reconstruction

Unlike pure  $\alpha$  emitters, the subsequent decays of bismuth and polonium can be uniquely identified using a time coincidence cut (known as BiPo coincidence). However, the actual reconstruction of those double-events (two-fold S1 and S2 signals) will require modified analysis techniques compared to the standard evaluation of XENON100 data, which was originally optimized for single event search. In the following, the selection of BiPo events is described in detail.

**Selection cuts** The following criteria are found suitable to almost uniquely select the time coincident decays in our study:

- **Two S1 signals** Within the recorded  $440\ \mu\text{s}$  DAQ window for every triggering event we require two distinctly identified S1 signals, each having at least two-fold PMT coincidence.
- **S1 thresholds** The larger of the two signals is attributed to the  $\alpha$  decay because its mean energy is far above the endpoint of the  $\beta$  spectrum and, as we will learn, the S1 light yield for  $\alpha$ 's is even higher than the one for  $\gamma$ 's and  $\beta$ 's. We will therefore use the notation  $S1_\alpha$  equivalently for the largest signal and require  $S1_\alpha > 200\ \text{PE}$  as minimum threshold. This cut is necessary to avoid noise misidentification occurring along with large light emission (see similar effect in  $\alpha$  event selection of Sec. 4.4.1). For the same reason we also ask  $S1_\beta > 100\ \text{PE}$ , where we have denoted the second largest S1 peak by  $S1_\beta$ . Concerning the  $\alpha$  it is extremely unlikely to fall below the set threshold except for events in the shadow of geometric structures, such as top and bottom grids or field shaping rings at the very edges.
- **Time coincidence** The defining condition for BiPo tagging is on the time coincidence of the two identified S1 peaks. Fortunately, the decay constants are largely separated for the two investigated radon chains, which allows for further classification:



In both cases  $S1_\beta$  has to appear prior to  $S1_\alpha$  along the recorded time axis within the same DAQ event window, thus we can put constraints of the assigned time of occurrence,  $T$ , by asking  $0.05\ \mu\text{s} < T(S1_\alpha) - T(S1_\beta) < 2\ \mu\text{s}$  to classify BiPo events from the  ${}^{220}\text{Rn}$  chain and  $T(S1_\alpha) - T(S1_\beta) > 2\ \mu\text{s}$  to tag the BiPo decay among the  ${}^{222}\text{Rn}$  products. A tiny overlap fraction cannot be avoided but the implied acceptance loss can easily be calculated in upcoming studies of the actual rates, using the radioactive decay law. The same is true for the lower time threshold of  $0.05\ \mu\text{s}$ , which is conservatively chosen to stay safely away from the minimum distance needed to identify two separate S1 peaks by the data processor.

Note that this set of constraints does not involve any condition placed on the S2. This turns out fortunate for upcoming studies at zero electric drift field (Sec. 4.6.5) – without any possibility to read out a charge signal. In fact, there are several possible scenarios for the occurrence of S2 peaks (when the drift field is on), which will play a role in the next paragraph.

**Event reconstruction** Having learnt how to make use of the time coincidence to identify potential BiPo decays, we focus now on how to correctly reconstruct the position and derive the correct signal strength for each ( $\beta/\alpha$ ) constituent. Thereby, we cannot rely carelessly on the corrected quantities given by the standard event processor because it automatically determines the S1 signal correction according to the primary vertex position derived from the largest S2 signal. In our study, it is not a priori clear whether the largest recorded S2 belongs to the  $\beta$  ( $S2_\beta$ ) or  $\alpha$  decay ( $S2_\alpha$ ) even though the underlying energy deposition is much higher in the latter case. The quenching arises from a much higher electron recombination rate around the very dense interaction core of  $\alpha$  particles and thus fewer escaping electrons can form the S2 afterwards. We will investigate the charge yield later in this

chapter. We notice further that the size of  $S2_\beta$  depends much on the actual  $\beta$  energy, which follows a continuous spectrum down to approximately zero.

Moreover, due to the finite size of the DAQ recording window, the S2 from the second ( $\alpha$ ) interaction may not be recorded at all if the decay of  $^{214}\text{Po}$  occurs after a comparably long lifetime (this problem is much less pronounced in the thoron chain because of the very short-lived  $^{212}\text{Po}$ ). Unlike the case in low background analyses the  $S1_\alpha$  (sometimes even  $S1_\beta$ ) is already large enough to exceed the hardware trigger threshold (for definition see Sec. 2.3). The S1 peak is then positioned in the centre of the event window, allowing only to look  $220\ \mu\text{s}$  backwards and forwards in time. Depending on the  $z$  position inside the detector (defines the electron drift time) and the time of decay, the  $S2_\alpha$  may or may not be observed in those remaining  $220\ \mu\text{s}$ .

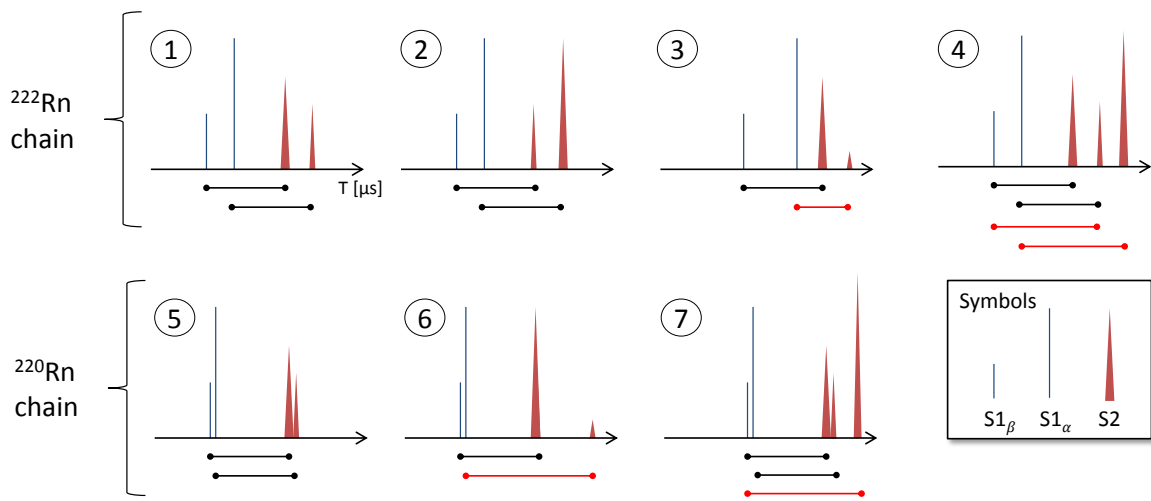


**Figure 4.11:** Scheme of possible topologies attributed to recorded BiPo events: (1) All signal information (S1 and S2) contained in the same waveform, matching occurrence in time, common S2 hierarchy; (2) Same as (1) but inverted S2 signal strength; (3) No matching in S1-S2 time distance, second identified S2 might be noise artifact; (4) Several major S2 peaks, two of which show time consistency, other may be from accompanying  $\gamma$  ray scattering; (5) Ideal candidate for BiPo from thoron chain: all information contained and matching time distance; (6) Only one regular S2 in trace (no time consistency with potential second S2 noise peak); (7) Several S2s, two of them in time consistency

Potential event topologies are illustrated in Fig. 4.11: Regarding the half-life of  $^{214}\text{Po}$  in the  $^{222}\text{Rn}$  chain only a fraction of events contains two appropriate S2s for the two corresponding S1 signals (Case (1) and (2)). In practice, we loop over all pair combinations between major S2 and  $S1_\alpha/S1_\beta$  peak positions in the waveform. Thereby the algorithm searches for matching time distances as an indicator of correct pair assignment. Note that the time ordering of  $S2_\beta$  and  $S2_\alpha$  is fixed: Since the two coincident decays happen at the same spatial position their drift length is equal and so is the time gap  $dT$  between connected S1 and S2 peaks. Due to finite resolution in the determination of any S2 peak position, we consider two time differences matching if they agree within  $1\ \mu\text{s}$  (corresponds to the order of the time resolution to determine the mean S2 peak position):  $|dT_1 - dT_2| < 1\ \mu\text{s}$ .

If this definition yields more than two coincidence pairs, we select those pairs carrying the largest S2 signals among all possible matches. In case the algorithm does not find two coincident pairs at all (3), it is very likely that the delayed  $S2_\alpha$  was not recorded in the waveform and thus there is no information about the  $\alpha$  charge signal available. The remaining largest S2 is then directly connected to  $S1_\beta$ . It is also possible that a  $\gamma$  ray is emitted simultaneously with the  $\beta$  and creates one or multiple additional S2 by Compton scattering (4). Again, we can apply the pairing algorithm to figure out the

proper assignments for  $\beta$  and  $\alpha$  interactions. However, the promptly generated S1 by the  $\gamma$  ray will inevitably add to  $S1_\beta$  and thereby adulterate the pure  $\beta$  spectrum.

We can apply the same methods for the BiPo reconstruction in the thoron chain (5,6,7). Unlike before, it is improbable to lose the second-in-time  $S2_\alpha$  by the limited DAQ event window because it should occur promptly after the  $S2_\beta$  (remember  $\tau = 0.43 \mu\text{s}$ ). On the contrary, it happens many times that the two S2 signal forms have too much overlap and are misinterpreted as one single peak. In this case (6), we can still infer the correct position information from the S2 but will end up with a skewed  $S2_\beta/S1_\beta$  ratio. Gamma emission and multiple real S2's (7) do equally arise. For all scenarios it is true that if no S2 above a given low-signal noise threshold is found we will assume that the event either happened at the surface of or in the region below the cathode mesh, where very limited or no charge extraction is achieved in the absence of an electrical drift field. As no valid drift time can be derived from the S2 in these cases, we deliberately assign to them the z position of the cathode. Finally, we present two real waveform examples in Fig. 4.12. One is featuring  $^{214}\text{BiPo}$  (top) and the other  $^{212}\text{BiPo}$  decay (bottom). In the first example (top) four major S2 peaks are identified but only two of them fulfill the filtering condition  $|dT_1 - dT_2| < 1 \mu\text{s}$ . The other S2 signals are supposedly caused by additional Compton scattering of an emitted  $\gamma$  (here, the emission must be in upward direction as the assigned drift time is shorter than from the actual decay vertex). In the lower picture the two S1 peaks appear very close-by (as expected given the small decay time) and so do their matching S2. Already at this distance there is significant overlap between the S2 signals and for even closer time-relations they will be recognized as a single one.

The next step after the peak assignment is the event reconstruction. We infer the spatial position in all three coordinates from the attributed  $S2_\beta$  (if an unique  $S2_\alpha$  is additionally found it is used for a consistency check as it is supposed to yield a very similar vertex position). Using the derived vertex we manually apply all position-dependent signal corrections by embedding parts of the XENON100 data processing code into our own analysis environment. Deviating from the standard analysis, we use our own high energy S1 light map from Sec. 4.4.1 to reconstruct the correct  $S1_\alpha$ .

We will apply both, the introduced set of S1 selection criteria and the manual peak assignment/signal correction, in all further related studies of BiPo events (if not explicitly mentioned otherwise).

**BiPo cut efficiency** Unlike in the reconstruction of pure  $\alpha$  events there is one experimental limitation in the tagging of BiPo coincidences. Since the XENON100 raw data processor was intentionally optimized for the identification of events including only one major S1 signal, the peak finding algorithm is not adjusted to spot narrow S1 pulses in the tail of the largest S2 peak. The reason is the regular observation of delayed, single electron S2 pulses arising after the main one as well as fluctuations in the recorded baseline. Noise spikes appearing in those signatures would then tend to be mis-identified as additional narrow S1 pulses.

The available time window for a  $S1_\alpha$  to appear in the same waveform is consequently limited by the drift time distance  $t_d$  between  $S1_\beta$  and  $S2_\beta$ , i.e. proportional to the z position of the initial  $\beta$  decay inside the TPC. Fortunately, we usually have this drift time information (if the event does not happen in region insensitive to drifting electrons) and we can calculate the BiPo tagging efficiency by cutting off the normalized exponential decay time distribution at the inferred drift time  $t_d$ :

$$\epsilon(t_d) = \frac{\int_0^{t_d} e^{-t/\tau} dt}{\int_0^\infty e^{-t/\tau} dt} = e^{-t_0/\tau} - e^{-t_d/\tau}. \quad (4.3)$$

The efficiency  $\epsilon(t_d)$  corresponds to the fraction of polonium decays occurring within the considered

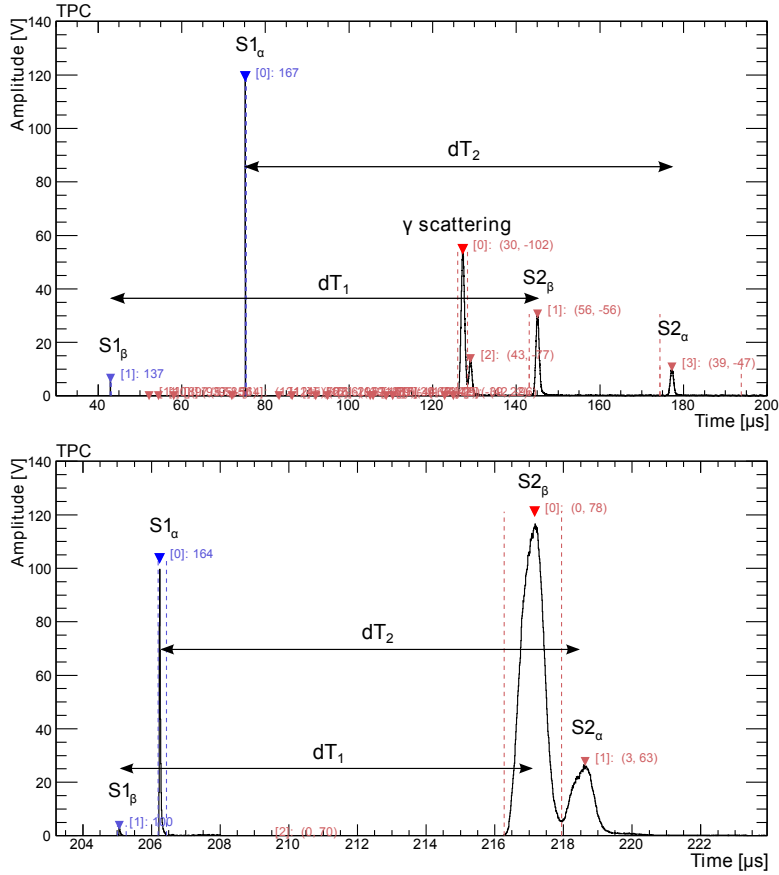


**Figure 4.12:** Two actual waveform examples of  $^{214}\text{BiPo}$  (top) and  $^{212}\text{BiPo}$  (bottom) events. In both cases we find two pairs of (S1,S2) which fulfill the time filtering requirement  $|dT_1 - dT_2| < 1 \mu\text{s}$ , allowing for correct peak assignment. For small time distances, as in  $^{212}\text{BiPo}$  decay, both S2 peaks already begin overlapping (bottom).

time interval  $[t_0, t_d]$ . In case of  $^{212}\text{BiPo}$  selection, the decay time constant  $\tau = 0.43 \mu\text{s}$  and the minimum time gap  $t_0$  between  $S1_\alpha$  and  $S1_\beta$  is set to  $0.05 \mu\text{s}$  – according to the previously defined selection rules. For  $^{214}\text{BiPo}$  the respective parameters are  $\tau = 237 \mu\text{s}$  and  $t_0 = 2 \mu\text{s}$ . In order to infer the correct counting number of  $^{214}\text{BiPo}$  we will divide the observed drift time distribution into a binned histogram and weigh each bin  $t_d^i$  by its respective correction factor of  $1/\epsilon(t_d^i)$ . This factor will exponentially grow from the bottom part (where the available appearance window is large) to the top part of the detector (where the remaining time gap is small).

Due to the fast disintegration time of  $^{212}\text{Po}$  the efficiency is essentially not affected by the available drift time  $t_d$ , except for events in the few mm top layer of the TPC. Instead, the upper integration limit  $t_d$  is fixed by the distinct upper cut-off of  $2 \mu\text{s}$ , defined to distinguish from  $^{214}\text{BiPo}$ , and  $\epsilon = e^{-0.05/0.43} - e^{-2.0/0.43} = 0.88$  is actually constant.

**BiPo decay time distributions** Measuring the different decay time distributions of  $^{212}\text{Po}/^{214}\text{Po}$  usually provides smoking gun evidence for the correct tagging of BiPo events. We focus on BiPo events selected from the long-term dataset as only there we find sufficient statistics for  $^{212}\text{BiPo}$  decays. We apply the previously defined criteria to identify events and plot the time difference  $t_{S1_\alpha} - t_{S1_\beta}$  between the  $S1_\alpha$  and  $S1_\beta$  signals in Fig. 4.13 (black data points). We expect this difference to follow

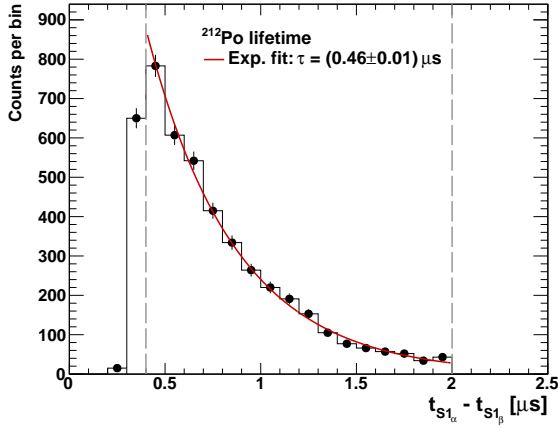


**Figure 4.13:** Exponential fit of the time gap distribution between  $S1_\alpha$  and  $S1_\beta$  signals for selected  $^{212}\text{BiPo}$  events, i.e. the decay time of  $^{212}\text{Po}$ . Vertical grey lines indicate the fitting region above solid peak separation threshold and predefined maximum time gap. The obtained mean lifetime of  $\tau = (0.46 \pm 0.01) \mu\text{s}$  deviates by 7% from the literature value – which can be explained by the fact that systematic effects in the event selection are not fully reflected by the error bar obtained from the fit.

the decay time distribution of  $^{212}\text{Po}$ . In fact, starting from  $\sim 0.5 \mu\text{s}$  the observed tail can be nicely fitted by an exponential function with mean lifetime of  $\tau = (0.46 \pm 0.01) \mu\text{s}$  calculated together with the error bar by the MINUIT routine of the ROOT data analysis toolkit [65, 66]. This value is only 7% larger than the one from literature ( $0.433 \pm 0.003 \mu\text{s}$ ) and possible explanations are small bias from the event selection (acceptance deficiencies) or event leakage from  $^{214}\text{BiPo}$  decay into the respective lifetime region. We observe that the tagging efficiency becomes significantly worse below  $t_{S1_\alpha} - t_{S1_\beta} \approx 0.4 \mu\text{s}$ . This points towards the inability of separating two distinct S1 peaks below that distance (remember that we found complications with comparably large baseline fluctuations in the tail of large S1 signals).

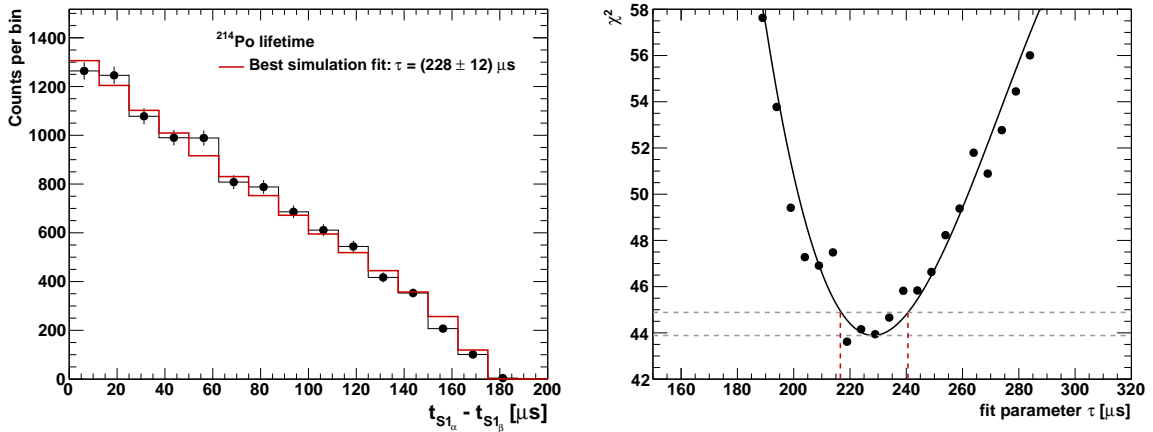


**Figure 4.14:** (Left) Measured and simulated lifetime distribution of  $^{214}\text{Po}$  decay for  $^{214}\text{BiPo}$  selected events, considering the known acceptance loss as function of electron drifttime. The time-difference between  $S1_\alpha$  and  $S1_\beta$  is drawn in black for data and red for the simulated result at minimum  $\chi^2$ . (Right)  $\chi^2$  distribution from the decay time simulation fit as a function of the fit parameter  $\tau$ . Around the (global) minimum the distribution is well-described by a third-order polynomial from which the  $1\text{-}\sigma$  confidence interval is determined by searching for the points where  $\Delta\chi^2 = 1$ . The extracted mean decay time of  $\tau = 228 \pm 12 \mu\text{s}$  is well consistent with the expected value of  $(237 \pm 3) \mu\text{s}$ .

The same analysis becomes considerably more complicated when turning towards the decay time distribution of  $^{214}\text{Po}$ . The reason has already been mentioned in the previous paragraph, where we stated that the probability of tagging one  $^{214}\text{BiPo}$  event depends on its vertex position since no S1 is recognized after the  $S2_\beta$  signal. Consequently, for each layer along the electron drift axis, only

those  $^{214}\text{Po}$  particles which decay within the available time window – set by the drift time  $t_d$  – can contribute to the overall observed spectrum. By this process the accumulative decay time spectrum will be notably distorted from a pure exponential shape. We try to account for this effect by means of a simulation: We start from the *measured* drift time distribution of  $^{214}\text{BiPo}$  selected events and divide it into a 100 bins histogram ranging from 0 to  $180\ \mu\text{s}$  (entire electron drift range). Further, the event number in each slice is corrected using the previously defined efficiency factor  $\epsilon(t_d)$  to infer the actual number of events expected at the particular  $t_d$ . For all events of each slice we randomly pick a decay time according to the pure exponential spectrum but leave the decay constant as a free parameter. We cut the resulting spectrum at the maximum available drift time  $t_d$ , repeat the same for all slices and finally add up the contributions in one histogram. Now the integral spectrum is compared to the measured one by scanning over a large range of assumed mean lifetime parameters  $\tau$ . We calculate the  $\chi^2$  (sum of quadratic divergences weighted by the statistical error of each data bin over all bins) and plot its distribution as a function of all scanned values of  $\tau$ . We determine a distinct  $\chi^2$  minimum at  $\tau = 228\ \mu\text{s}$  and extract the  $1\sigma$  uncertainty interval by selecting those lifetime values for which  $\Delta\chi^2 = 1$  (see Fig. 4.14). By this we extract a best fit value of  $\tau = (228 \pm 12)\ \mu\text{s}$ , consistent with  $(237 \pm 3)\ \mu\text{s}$  from literature. The spectral agreement for the best fit case with the measured time gap distribution is plotted in Fig. 4.14 (left).

In both cases we have thus derived first evidence that it is in fact BiPo decays which are tagged by the set of selection rules given at the beginning of this section and – even more – that the assignment to one of the two radon chains appears to be correct.

There is naturally little background contained in the selection of the BiPo time coincidence events. The only known candidate is the  $^{85}\text{Kr}$   $\beta$ - $\gamma$ -coincidence decay with  $\beta$  endpoint energy of 173 keV and  $1\ \mu\text{s}$  delayed  $\gamma$  emission at 514 keV. However, even in very rare cases that the energy signature was mistaken for a BiPo combination, the low concentration in LXe (order of parts per billion, ppt), long half-life (10.7 a) of  $^{85}\text{Kr}$ , and its tiny branching ratio (0.4%) for the delayed emission would still yield a negligible rate of typically few events per month compared to order of several tens of BiPo events per day under common background conditions.

**BiPo fractions in different datasets** As first application of the introduced event selection we determine the fraction of BiPo events arising from  $^{220}\text{Rn}$  and  $^{222}\text{Rn}$  and compare for the two mentioned datasets. During the air-spiked period (first dataset) we count in total  $\sim 35\ 000$  decays, of which only 3% are identified as  $^{212}\text{BiPo}$  and the remaining 97% are consistent with the longer  $^{214}\text{Po}$  half-life as part of the  $^{214}\text{BiPo}$ . During the long-term period of 225 live days of ultra-low background data we observe  $\approx 22\ 000$  BiPo candidates and a somewhat shifted partitioning of 25%  $^{212}\text{BiPo}$  and 75%  $^{214}\text{BiPo}$ . This difference in ratio is not unexpected since the former measurement is dominated by radon entering through the leaking gas system to the detector. The timescale for inward diffusion is supposedly much larger than the  $^{220}\text{Rn}$  decay time of  $\sim 1\ \text{m}$ , thus the thoron mainly disintegrates before reaching the inner detector volume. In the second dataset, the major radon source is emanation from all possible TPC materials, thus involves BiPos from both chains, depending on the radio-impurity concentration of  $^{228}\text{Th}$  and  $^{226}\text{Ra}$ , respectively. Of course, the available time for  $^{220}\text{Rn}$  to reach the sensitive detector after emanation is again limited. This may explain why we observe enrichment of  $^{214}\text{BiPo}$  also during regular operation.

## 4.5 Radon decay energy distributions

With the methods developed to identify and reconstruct different parts of the radon decay chains we can now apply them to study their released decay energy spectra. In this section we begin with the investigation of light and charge yield of  $\alpha$  decays and also want to check whether the spectra of  $\beta$  decay match our expectations. We base our evaluation mainly on the mentioned dataset of high radon concentration (refer to Sec. 4.3). The same analysis has been performed using accumulated data from the long term periods during the first and second dark matter run. We find almost complete qualitative agreement in our general observations and will highlight explicitly whenever they differ. Absolute counting rates, however, do significantly vary between those periods but will be evaluated and discussed in Sec. 4.7.

### 4.5.1 Light and charge yield for alpha decays

The light yield is defined as the mean number of S1 photoelectrons per units of expended energy. We already know that this number is dependent on the interacting particle, deposited energy and the spatial vertex position due to light collection inhomogeneity of the XENON100 TPC. For example, using various  $\gamma$  lines this quantity is regularly determined to construct the electromagnetic energy scale [33]. In order to achieve the same for the MeV energy regime we select events according to Sec. 4.4.1 and 4.4.2 to cut on single  $\alpha$  decays and those belonging to the BiPo coincidence, respectively. We further apply the alpha light correction before drawing the spatially averaged S1 spectra in Fig. 4.15. As mentioned before,  $^{212}\text{BiPo}$  is largely suppressed in the air-spiked dataset which is why we use the long-term period to evaluate the  $\alpha$  spectrum of  $^{212}\text{Po}$ . Moreover, it is necessary to put a requirement on the  $z$  vertex position because we will later see that the majority of BiPo events is located in the very bottom region of the detector where our light map resolution becomes worse and the peak shapes do not appear perfectly Gaussian. We will discuss those particularities in spatial distributions in one of the following sections.

We find two signal peaks with very large statistics in the top part of Fig. 4.15. Since we already know that  $^{222}\text{Rn}$  is the dominant contributor to the whole radon background we can assign those peaks to the absorption lines of the pure  $\alpha$  emitters  $^{222}\text{Rn}$  and  $^{218}\text{Po}$ . The other signals arise from the BiPo time coincidence and are identified by their different decay constants. Consistently, the  $\alpha$  from  $^{212}\text{Po}$  occurs at higher energy than from  $^{214}\text{Po}$ . We perform Gaussian fits to all observed  $\text{S1}_\alpha$  signals in order to extract information about the mean light yield and peak resolution. For the two major peaks it is necessary to assume a small constant pedestal underneath the double-gaussian shape. It is due to non-perfect position reconstruction because of incipient saturation effects on the relevant top PMT array. Consequently, the  $\text{S1}_\alpha$  signal correction becomes smeared beyond the otherwise achievable Gaussian resolution.

We provide a summary of the fit results in Tab. 4.1. The statistical error on the inferred average  $\text{S1}_\alpha$  is negligible due to very large counting numbers involved in the Gaussian peaks. From the standard deviation between the individual measurements we infer an additional systematic uncertainty of  $\sim 1\%$ , leading to an average light yield of  $(3.75 \pm 0.03)$  PE/keV for the 2009 measurement and  $(3.86 \pm 0.02)$  PE/keV during 2012. This means a 3% shift towards higher yields, observed at all peak positions. Between 2009 and 2012 this change was monitored on a very similar scale also for  $\gamma$  ray interactions and is likely to be explained by little changes in the liquid level of the TPC and, as a consequence, by a small change in the light reflection angles. For each individual dataset the mean light yield evaluated at different energies is almost equal and therefore consistent with a linear energy

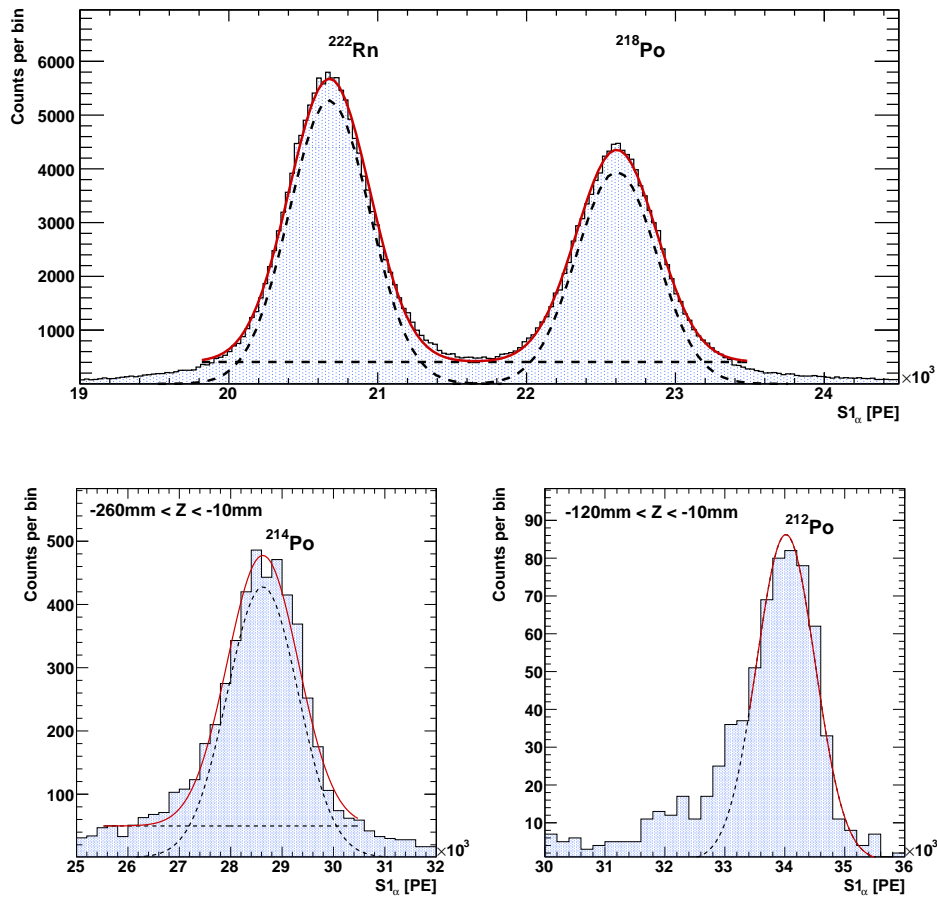


**Figure 4.15:** Spectra of  $\alpha$  decays in the active detector volume for different energy regions. The dedicated correction map is applied to compensate spatial light collection inhomogeneity. Top: Single  $\alpha$  decays of  $^{222}\text{Rn}$  and  $^{218}\text{Po}$  collected in the whole TPC. Bottom left: Decay of  $^{214}\text{Po}$  as part of BiPo coincidence; cut on  $z$  position applied to enhance peak resolution (details in text). Bottom right:  $\alpha$  spectrum as part of  $^{212}\text{BiPo}$  coincidence decay; cut on  $z$  position necessary to maintain proper resolution.

Decay isotope	Energy [MeV]	High radon concentration (2009)				225 live days (2011–2012)			
		$S1_\alpha$ [PE]	FWHM [PE]	Light yield [PE/keV]	FWHM/ $S1_\alpha$ [%]	$S1_\alpha$ [PE]	FWHM [PE]	Light yield [PE/keV]	FWHM/ $S1_\alpha$ [%]
$^{222}\text{Rn}$	5.49	20676	637	3.77	3.0	21196	756	3.86	3.6
$^{218}\text{Po}$	6.00	22605	636	3.77	2.8	23181	836	3.86	3.6
$^{214}\text{Po}$	7.69	28625	1625	3.72	5.6	29487	1440	3.83	4.8
$^{212}\text{Po}$	8.79		not evaluated			34018	1148	3.87	3.4

**Table 4.1:** Results of the  $S1$  peak analysis for  $\alpha$  decays. The light yield appears constant for all identified  $\alpha$  lines within the same run. A slight increase of 3% has been observed in the long-term data. Peak resolution is better than 5% for all cases. Statistics in the first dataset are not sufficient to perform the line fitting for  $^{212}\text{Po}$ .

scale for this type of particle interaction in LXe.

The light yield is roughly a factor 2.5 larger in comparison to  $\gamma$  interactions in the MeV range ( $\sim 1.5$  PE/keV for the  $^{60}\text{Co}$  lines in XENON100 [33]). Alpha particles are known to deposit their energy along dense ionization tracks of very limited range [55, 36] and therefore imply a high recombination probability of ionized electrons, leading to increased scintillation light emission (refer to Chapter 2.1.1). It thus explains the enhanced yield with respect to  $\gamma$  radiation. The large light amount implies also a very good relative energy resolution of only a few percent FWHM. Moreover, the reconstructed  $\alpha$  lines spectrum proves the validity of event class identification defined on  $\alpha$  decay energies.

We do not see any indication for the appearance of  $\alpha$  lines from  $^{220}\text{Rn}$  (6.28 MeV) and  $^{216}\text{Po}$  (6.78 MeV) – both parts of the thoron chain – in the dataset of high radon activity. It was already discussed that thoron gas is largely suppressed in this case. On the contrary, we would naively expect to see some indication for pure thoron lines in the 225 live days data since we have stated a significant fraction of succeeding  $^{212}\text{BiPo}$  decays. The absence will be understood by analyzing the spatial event distribution of various radon chain components and we will address this subject later in this chapter.

Next, we want to perform a similar study of the charge yield. The definition slightly differs from the light yield as it refers to the number of electron-ion pairs eventually produced per unit of deposited energy. At a finite drift field not all liberated electrons can escape recombination. Therefore, this quantity is affected by the applied electrical field strength and the ionization density caused by the incoming particle. On the contrary, the number does *not* depend on the detector geometry, provided that the loss of drifting electrons is appropriately compensated and the light emission per electron in the gaseous phase is known. The quantity obtained in such way can thus be used to compare with external measurements performed in different detectors. We restrict our analysis to the most prominent  $\alpha$  lines from  $^{222}\text{Rn}$  and  $^{218}\text{Po}$  for two main reasons: First, their mean S2 is still low enough to remain largely unaffected by S2 saturation effects and they provide highest statistics in the central regions of the XENON100 detector. Second, since we found the light yield independent of the actual energy deposition, we must expect a similar behavior for the electron yield assuming energy conservation in the sum of light and charge signal.

We use again the dataset from 2009 and further limit the fiducial volume to  $R < 100$  mm and  $-250$  mm  $< z < -200$  mm. Doing so we deliberately avoid detector regions where the S2 resolution is slightly worse and affected by saturation effects in the event location and signal correction. We also optimize peak separation as needed to distinguish the S2 populations from  $^{222}\text{Rn}$  and  $^{218}\text{Po}$ . While the S2 waveforms show large overlapping of their Gaussian shapes the resolution achieved in  $S1_\alpha$  is much enhanced, which can be seen in Fig. 4.16. By putting a simple condition on the corrected  $S1_\alpha$  it is possible to obtain very good peak separation of the two  $\alpha$  decays to proceed further with the projected S2 spectra from  $^{222}\text{Rn}$  ( $S1_\alpha < 21700$  PE) and  $^{218}\text{Po}$  ( $S1_\alpha > 21700$  PE). Both distributions can be well fitted by assuming a Gaussian shape (refer to Fig. 4.17) and we give their resulting means and FWHM in Tab. 4.2. We calculate the charge yield  $Q(E_d)$  at the nominal XENON100 drift field of  $E_d = 530$  V/cm as the ratio of mean observed S2 divided by the secondary scintillation gain  $L_q$  and the known  $\alpha$  energy  $E_\alpha$ :

$$Q = \frac{\langle S2 \rangle}{L_q E_\alpha}. \quad (4.4)$$

$L_q$  is constantly monitored in XENON100 by dedicated measurements of the secondary scintillation gain from the S2 distribution of single and few electrons extracted and accelerated in the gaseous phase (measurements not carried out by the author). The amplification factor is dependent on the

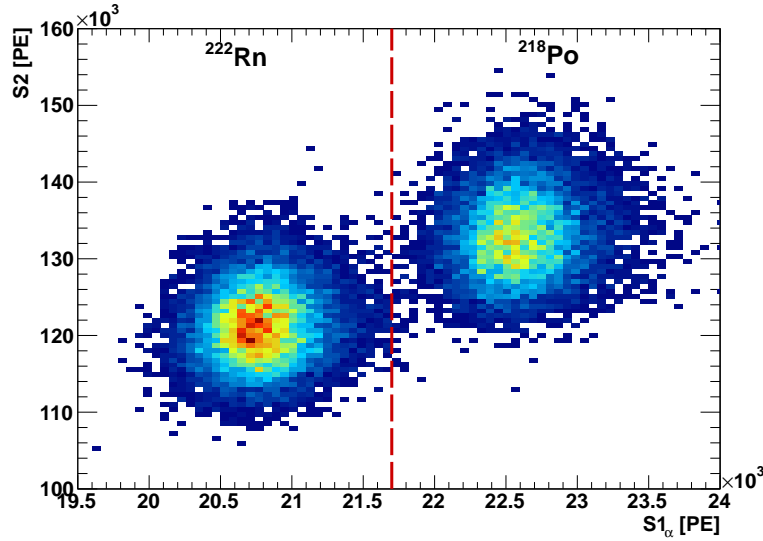


**Figure 4.16:** Combined distribution of secondary (S2) and primary (S1) scintillation light for  $^{222}\text{Rn}$  and  $^{218}\text{Po}$   $\alpha$  decays. Contrary to electron or  $\gamma$  absorption the resolution on the corrected  $S1_\alpha$  variable is significantly better than on the charge-proportional signal S2. We use a separation threshold at  $S1_\alpha = 21700$  PE (red dashed line) before fitting the individual 1-D projections on the S2 axis in Fig. 4.17.

partial pressure of the xenon gas and the size of the gap between liquid level and anode mesh. For the specific configuration of both around the time of this measurement, the mean scintillation gain per electron was determined as  $L_q = (17.9 \pm 0.1)$  PE/ $e^-$  [60].

Decay isotope	Energy [MeV]	Mean S2 [PE]	FWHM [PE]	FWHM/S2 [%]	$Q(E_d = 530 \text{ V/cm})$ [ $e^-/\text{keV}$ ]	$Q(E_d)/Q_0$ [%]
$^{222}\text{Rn}$	5.49	121340	10834	8.9	1.24	$1.93 \pm 0.04$
$^{218}\text{Po}$	6.00	133218	11877	8.9	1.24	$1.93 \pm 0.04$

**Table 4.2:** Evaluation of the absolute and relative charge yield of  $\alpha$  decays in LXe. S2 peak resolution is significantly worse than in  $S1_\alpha$  because less information carriers per unit of energy are collected at the nominal XENON100 drift field of 530 V/cm. Only 1.93% of electrons escape recombination assuming a W-value of  $(15.6 \pm 0.3)$  eV [83].

The quantity  $Q$ , evaluated at an applied finite drift field  $E_d$ , is commonly related to the (theoretical) number of electron-ion pairs per energy ( $Q_0$ ), obtained at infinite field strength, when all electrons escape recombination and the remaining number of pairs corresponds to the one originally created by the ionizing particle. It is the inverse of the so-called W-value, which is the amount of energy needed to produce one ionization pair. This value has been extrapolated in various measurements for several noble liquids, and was found to be  $W = (15.6 \pm 0.3)$  eV in LXe by [83].

With this number we expect  $Q_0 = (64.1 \pm 1.2)$   $e^-/\text{keV}$ . The absolute yield  $Q(E_d)$  is calculated and listed in Tab. 4.2, giving a consistent value of  $1.24 e^-/\text{keV}$  for both evaluated  $\alpha$  lines. Divided by  $Q_0$ , the results implies that only  $(1.93 \pm 0.04)\%$  of electrons are drifted away from the interaction core and can contribute to the charge proportional signal S2. This fraction of information carriers is lower than in the  $S1_\alpha$  channel, where we observe 3.75 photo-electrons per keV energy. Consequently, the peak resolution is considerably worse in S2 – opposed to other classes of ionizing particles. As mentioned

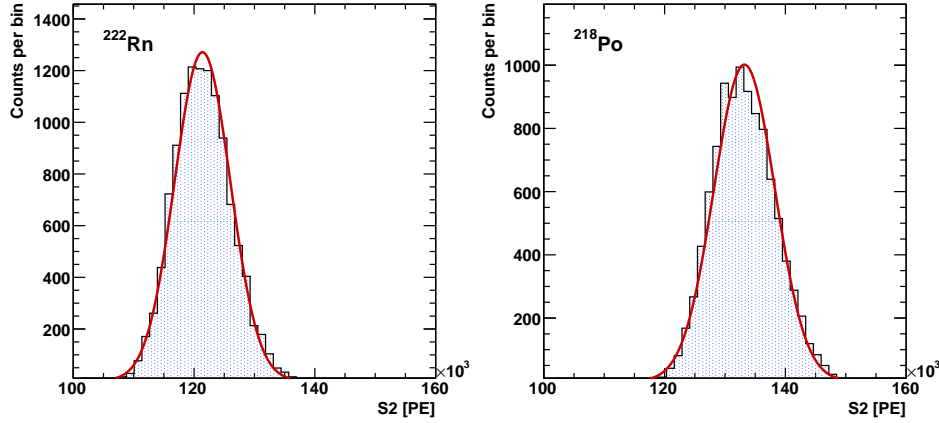


**Figure 4.17:** Gaussian fits to the projected S2 signals of  $^{222}\text{Rn}$  and  $^{218}\text{Po}$ . Without using peak separation in  $S1_\alpha$  (as indicated in the 2-D distribution of Fig. 4.16) both signal shapes would largely overlap. The fit results are collected in Tab. 4.2 and further used for the calculation of the relative charge yield of  $\alpha$  decays.

e.g. in [55], the reason for the suppressed charge yield is presumably due to the fact that  $\alpha$  particles lose their energy along very dense ionization tracks and electrons mostly remain in the vicinity of the ions. This enhances the probability for subsequent recombination supposed the external field is not strong enough to separate the pairs. The obtained ratio of  $Q/Q_0$  is in good agreement with dedicated calibration measurements performed much earlier in a parallel plate ionization chamber setup by [84]. In their work, they scan the mentioned ratio for 5.49 MeV  $^{241}\text{Am}$  and 5.31 MeV  $^{210}\text{Po}$   $\alpha$  decays over a wide range of applied drift fields and determine a value of  $Q/Q_0 \approx 1.9\%$  at  $E_d = 500 \text{ V/cm}$  in a LXe target.

## 4.5.2 Beta and alpha spectra from BiPo coincidence

We have previously studied the full absorption peaks arising from the largest S1 signal in BiPo selected waveforms and found their mean positions consistent with the linear energy scale set by pure  $\alpha$  decays. What we have not shown is the observation of a large tail of BiPo events below the full energy peak, appearing in the spectral projection of Fig. 4.18. The figure shows all events from the long-term dataset identified by  $^{214}\text{BiPo}$  criteria but we do not pose the time filter condition  $|dT_1 - dT_2| < 1 \mu\text{s}$  (see Sec. 4.4.2). By this, we want to ensure that the acceptance of BiPo decays is as high as possible to prepare interpretation of upcoming results from event counting. The distribution for  $^{212}\text{BiPo}$  looks very similar (but is not shown). When further information about the reconstructed z position is added one can see that the vast majority of  $S1_\alpha$  downward fluctuating events has a vertex location below  $z < -300 \text{ mm}$ , i.e. very close to or even on the surface of the cathode grid. Scintillation light absorption by the structure material is most likely the reason for the observed reduction of collected  $S1_\alpha$ . More interesting, there is an additional event population ranging up a few cm above the mesh but with similar  $S1_\alpha$  suppression. We suppose that these events are in fact sitting near the cathode as well, but are mis-reconstructed by the BiPo algorithm due to a simple reason: Prompt  $\gamma$  rays emitted by the Bi decay can be directed upwards and interact in the lower TPC volume. Because of the high charge yield from  $\gamma$  absorption, the created S2 signals are likely to be larger than the ones belonging to the  $\alpha$  deposition and they are sometimes picked up arbitrarily to define the position vertex. If we instead

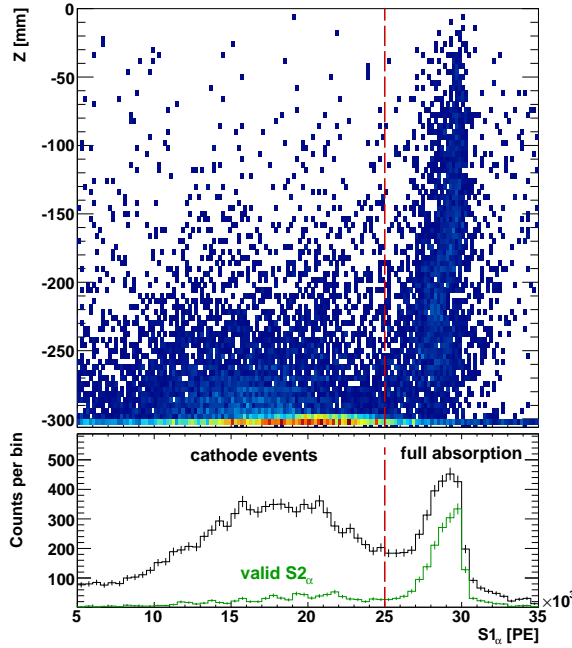


**Figure 4.18:** Correlation between the  $S1_\alpha$  signal – as part of time coincident  $^{214}\text{BiPo}$  decay – and the assigned  $z$  position inside the TPC. Event clustering near the cathode position ( $z \approx -306$  mm) suggests that most of the decaying  $^{214}\text{Po}$  sticks to the electrical grid. The light collection for those events is significantly reduced due to scintillation light absorption by the mesh wires. Parts of the events are seemingly located in a few cm layer above the cathode but most likely mis-reconstructed (refer to text for details). Events stretched along the entire  $z$  axis contribute most to the full absorption  $\alpha$  peak. If we apply the requirement of consistent drift times for  $\beta$  and  $\alpha$  signals (valid  $S2_\alpha$ ), mainly the full absorption peak is reconstructed as expected (green histogram).

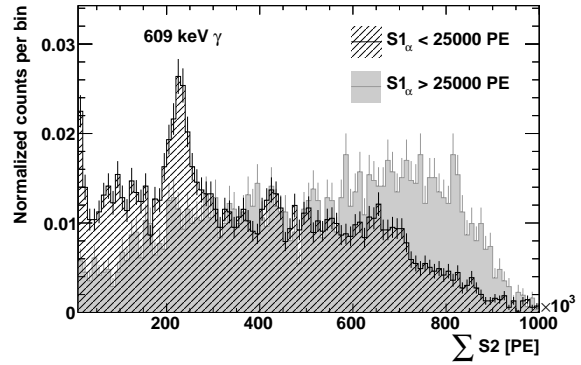


**Figure 4.19:** Sum over all major  $S2$  signals within the waveform of selected  $^{214}\text{BiPo}$  events, divided into two parts: The grey filled spectrum contains all those events which appear in the  $S1_\alpha$  full absorption peak (above red dashed line in Fig. 4.18) and have an approximately flat distribution in their summed  $S2$  signals. The black hatched spectrum refers to all events below the  $S1_\alpha$  threshold and shows a significant resonance at the  $S2$  from a  $\approx 609$  keV  $\gamma$ , which is the most dominant line in the decay of  $^{214}\text{Bi}$ . It can explain why events occurring at the cathode are mis-reconstructed up to a few cm above.

restrict our sample to events having consistent drift times for  $\beta$  and  $\alpha$  signals,  $|dT_1 - dT_2| < 1 \mu\text{s}$ , one recovers mainly the full absorption part and a tail of events truly occurring at the cathode level (green spectrum in Fig. 4.18, bottom).

Among several possible  $\gamma$  lines, we mention only the most dominant ones at 609 keV (with 46% probability), 1120 keV (15%) and 1765 keV (15%). Those energies imply typical absorption lengths of a few cm in LXe. Since they are prompt signals they interfere with  $\beta$  emission and they may deposit only a fraction of their full energy before leaving the detector, which is both why we don't see their characteristic features in proportional  $S1$  energy. However, we can collect additional information by summing over all  $S2$  signals in the BiPo waveform and split the sample into events from the lower  $S1_\alpha$  part ( $S1_\alpha < 25\,000$  PE, red dashed line in Fig. 4.18) and above ( $S1_\alpha > 25\,000$  PE). In the latter case we reconstruct a featureless  $S2$  spectrum as expected if the largest contributions arise from the emitted  $\beta$  particle which is used to correctly define the position of the BiPo decay. Only under the former condition we find evidence for a line-shaped excess at around 225 000 PE. This is only few percent below the mean  $S2$  value from the 661 keV  $^{137}\text{Cs}$  calibration line (refer to Fig. 24 in [33]) and of similar width, which justifies to assign this peak to the most prominent  $\gamma$  energy of 609 keV in

$^{214}\text{Bi}$  decay. There is at least indication for one or even two more line features related to the higher energy  $\gamma$  emissions. All findings add further evidence to the hypothesis of mis-reconstructed BiPo decays because of upscattering  $\gamma$  rays. We conclude that the true  $z$  distribution is split into two parts: One fraction is quite uniformly stretched through the length of the detector, the other, much larger fraction, is concentrated to the cathode position.

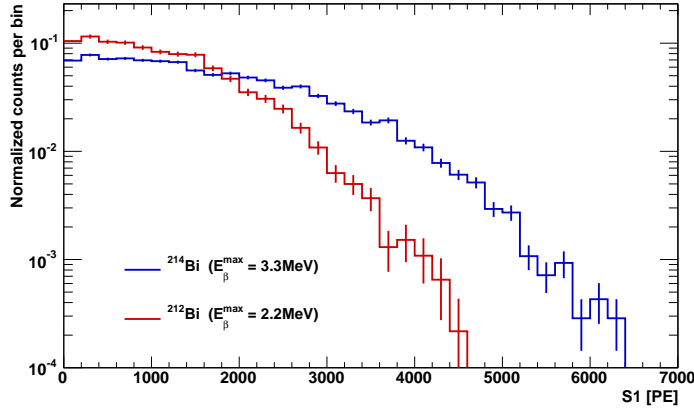


**Figure 4.20:** S1 spectra of the two  $\beta$  decays of  $^{212}\text{BiPo}/^{214}\text{BiPo}$ , identified by the time coincidence method. The spectra are normalized to their respective integral number and resemble the typical shape of  $\beta$  emission with different endpoint energies  $E_{\beta}^{\max}$  for  $^{212}\text{Bi}$  and  $^{214}\text{Bi}$ . It adds further confirmation that the chain assignment is done correctly by the introduced selection criteria.

So far we have mostly neglected the second energy information from BiPo events, which is the spectrum of the smaller of the two S1 involved. Fig. 4.20 shows the reconstructed spectra from  $^{212}\text{BiPo}$  and  $^{214}\text{BiPo}$  as a function of their S1 (light efficiency corrected by the standard XENON100 map). We cannot convert the distribution into real energy space because such a conversion has not been calibrated in XENON100 and is difficult to achieve anyway for a continuous spectrum spanning a wide range of energy (as opposed to fixed  $\gamma$  calibration lines). However, one can recognize the typical shape of  $\beta$  emission spectra, which level off towards low energies and have a defined endpoint energy corresponding to the decay Q-value. We must consider that spectra from both,  $^{212}\text{Bi}$  and  $^{214}\text{Bi}$ , comprise the sum over various  $\beta$  emission branches, each with different endpoint energy. Their highest endpoints, however, are set by 2.2 MeV and 3.3 MeV for  $^{212}\text{Bi}$  and  $^{214}\text{Bi}$ , respectively. The ratio of 3.3 MeV/2.2 MeV  $\approx$  1.5 between the two endpoints is fairly consistent with the observed one of  $\sim 6400 \text{ PE}/4600 \text{ PE} = 1.4$  and suggests a largely constant light yield of  $\beta$  particles in the MeV range. These findings provide further proof of the correct tagging and assignment by the introduced BiPo selection criteria.

## 4.6 Spatial distributions

In the following we turn the focus on the spatial distributions of various radon chain components. From this we want to draw conclusions about the dynamics of (potentially charged) radon daughters in a noble liquid environment. This will also be helpful for the interpretation of the absolute activity concentrations measured later in this chapter and become finally important when we will look back at some open questions on the energy spectra introduced before.

### 4.6.1 Position reconstruction

We use the position information provided by the XENON100 raw data processor for each recorded event (Sec. 4.3). Best radial resolution is obtained with the neural network (NN) reconstruction algorithm commonly used for the evaluation of low-energy data. Nevertheless, we observe a fraction of events clustering around certain radii which match the pattern of PMT rings on the top array. This indicates that the (x,y) positioning – determined from the S2 signal distribution of the top light sensors – runs into a saturation regime because all available algorithms were designed for and trained on low-energetic  $\gamma$  ray lines. In our case, however, this does not have a large effect on the interpretation of upcoming observations.

### 4.6.2 Spatial distribution of alpha decays

We begin our investigation with the comparison of the spatial distribution of pure  $\alpha$  emitters inside the XENON100 TPC. We select events according to the introduced criteria in Sec. 4.4.1. For the corrected  $S1_\alpha$  variable we put an eased condition of  $15\,000\text{ PE} < S1_\alpha < 30\,000\text{ PE}$  because we also want to include events close to the TPC walls or sticking to the grids' surfaces, where edges and meshes absorb a significant fraction of the originally emitted number of scintillation photons. We divide the whole TPC into equal bins along  $z$  and  $r^2$  and normalize the bin contents by the integral event number, thus obtaining a spatial density plot in Fig. 4.21 for the high radon concentration data (left) and long-term study (right).

Stripes appearing at certain radial position are due to a deficiency of the positioning algorithm. It can occur when the amount of S2 light created in the upper gas gap is such large that some of the detecting PMTs become saturated. This is not an issue for the energy region relevant for the dark matter search but can arise in background studies of high energetic events, as  $\alpha$  decays for example. The saturation pattern also reveals the bending of field lines in the lower  $z$  region at large radii, which is accounted for by the dedicated position correction mentioned in Chapter 2.1.4. Apart from these artificial features, the spatial density appears very homogeneous up to the TPC walls in case of the first dataset (left Fig. 4.21), where large amounts of  $^{222}\text{Rn}$  were known to enter from the gas system to the detector. A spiked concentration is observed at the position of the cathode grid. We will later find that the presence of the electrical drift field has some impact on the spatial distribution and in this case it could be that positively charged  $^{222}\text{Rn}$  or  $^{218}\text{Po}$  ions are drifted towards the (negative) cathode (the presence of positive decay products is often observed after  $\alpha$  emission because some shell electrons may be stripped off from the recoiling atom [85]). The analogous picture looks different in case of the 225 live days of low background data (part of Fig. 4.21). While the inner part ( $r < 145\text{ mm}$ ) is also evenly populated with  $\alpha$  decays, there is a sharp rise in event density towards the PTFE walls surrounding the TPC. Unfortunately, the  $S1_\alpha$  resolution is not good enough in this area ( $r > 145\text{ mm}$ ) to tell apart  $\alpha$  sources by their energy but we rather see a broadly smeared  $S1_\alpha$  distribution between

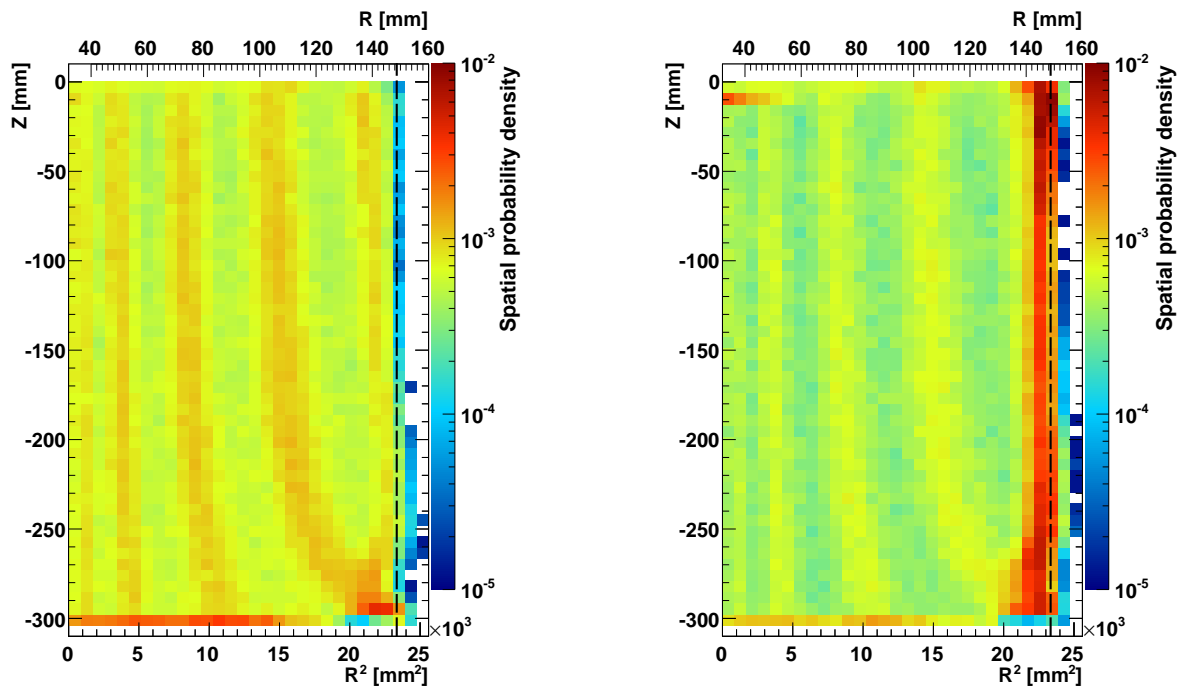


**Figure 4.21:** Comparison of integral normalized  $\alpha$  event distributions. (Left) Dataset of high radon concentration (10.4 live days from 2009). Apart from radial clustering (stripes along  $z$  axis, for explanation refer to text) we find very homogeneous spread up to the corners of the TPC but significant excess of events at the cathode grid position. (Right) The same distribution for 225 live days of data, taken in 2011/2012. Except similar stripe structures, the overall distribution for  $r < 145$  mm appears homogeneous. We observe a strong increase of events close to the TPC walls ( $r > 145$  mm).

15 000 and 25 000 PE. This range could also cover  $\alpha$  decays initiated by the emanation of thoron: In this process  $^{220}\text{Rn}$  is ejected from the PTFE walls into the first few micron layers of the LXe phase because of the  $\mathcal{O}(100\text{ keV})$  recoil energy transferred by  $\alpha$  emission in opposite direction of the decaying  $^{224}\text{Ra}$  nucleus which was originally situated at the surface. Since it is short-lived (and so is the decay product  $^{216}\text{Po}$ ) it has not enough time to move far away from the boundary before undergoing another decay. On the contrary,  $^{222}\text{Rn}$  lives for several days on average, which provides enough time to become evenly distributed in the bulk of the TPC via diffusion or convection.

Another contribution could come from surface contamination of the long-lived  $^{210}\text{Pb}$  ( $T_{1/2} = 22.3\text{ a}$ ), which may have accumulated during the years of detector construction and commissioning or was already abundant in traces in the original PTFE material. One of its subsequent decay products,  $^{210}\text{Po}$ , also emits  $\alpha$  particles in the same energy range (5.3 MeV).

We conclude that under regular conditions of background data at least a large part of the  $\alpha$  emitters arise from radon emanation off the porous PTFE material. In case of large radon amounts leaking through the recirculation gas system, however, the relative contribution from the edges is subdominant and the radon is most likely to enter to the liquid phase via gas condensation on the cold finger.

### 4.6.3 Spatial distribution of BiPo decays

The study of BiPo event distribution is of particular interest because it adds information about the dynamics of decaying isotopes from both radon chains within a LXe volume in the presence of an

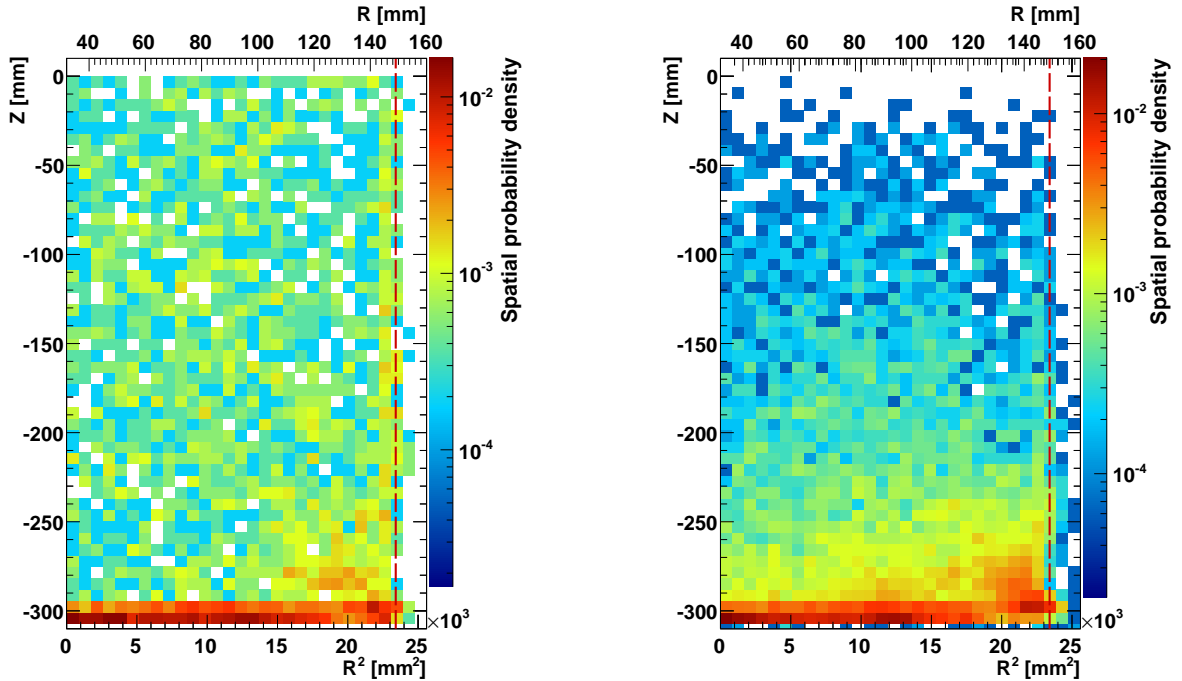


**Figure 4.22:** Comparison of event position distributions inside the TPC during the second long-term dark matter run – normalized to the integral number of counts. (Left) Disintegration of  $^{212}\text{BiPo}$ . In the inner volume a uniform spread of events is found. Around the cathode position ( $z \approx -306$  mm) a sudden rise in rate appears. (Right) The same distribution shown for  $^{214}\text{BiPo}$  decays. The exponential increase in observed rate from top to bottom is explained by the fact that the tagging efficiency depends on the particular electron drift length and is not yet corrected for in this plot (refer to Sec. 4.4.2). Very similarly, the vast majority of BiPo events is located close to the cathode position. The red dashed line indicates the physical boundary of the TPC.

electrical field. We have seen that the dispersion of the first two isotopes,  $^{222}\text{Rn}$  and  $^{218}\text{Po}$ , is almost homogeneous when neglecting a few mm in radius at the outermost edges. This is not surprising given the relatively long decay time of  $^{222}\text{Rn}$ , which allows for uniform penetration of the whole volume. On the other hand,  $^{218}\text{Po}$  lives only for about 3 min on average, which is too short to move away considerably by diffusion. Going further down along the chain, the following decays of  $^{214}\text{Pb}$  (pure  $\beta$  decay,  $\tau = 26.8$  m) and  $^{214}\text{Bi}$  ( $\tau = 19.9$  m) have both decay times of many minutes and, more importantly, are pure  $\beta$  emitters likely to remain positively charged after disintegration. Within the thoron chain the corresponding time gap between the two  $\alpha$  decays and the  $^{212}\text{BiPo}$  is even enhanced by several hours lifetime of the  $^{212}\text{Pb}$ .

In Fig. 4.22 we present the reconstructed event positions for the two time coincidence pairs,  $^{212}\text{BiPo}$  (left) and  $^{214}\text{BiPo}$  (right). The underlying data is accumulated during the long-term run but does not appear different in the high concentration period, as was checked for the  $^{214}\text{BiPo}$  selection. Note that the shown spatial dispersion of  $^{214}\text{BiPo}$  is not yet corrected for the drift-time dependent tagging efficiency (Sec. 4.4.2), which explains the exponential increase from top to bottom of the TPC. It is apparent that both distributions are significantly spiked around the cathode position inside the TPC but remain relatively flat in radial direction. This suggests an obvious downward shift along the axis of the electrical field and accumulation on the cathode surface. The available time for this displacement is thereby limited by the many minutes (hours) lifetime in between the  $\alpha$  and BiPo events.

We want to interpret this observation by first discussing two different mechanisms: ion drift and diffusion. Both are balanced by the mobility of heavy ions dissolved in liquefied xenon. In first

place, the mobility  $\mu$  is defined as the proportional constant mediating the ion drift velocity  $v_d$  and the strength of the external electrical field  $E$ , enforcing the motion via  $v_d = \mu E$ .

To our knowledge there is only a limited number of external studies on the electrical mobility of very heavy ions in LXe. A few years ago Wamba et al. [86] have performed such dedicated measurements for  $^{226}\text{Th}^+$  ions and found a mobility  $\mu = 0.24 \pm 0.01(\text{stat.}) \pm 0.01(\text{sys.}) \text{ cm}^2 \text{ kV}^{-1} \text{ s}^{-1}$  at somewhat lower liquid xenon temperature and pressure ( $T = 163 \text{ K}$ ,  $p = 0.9 \text{ bar}$ ) than applied in XENON100. Earlier studies by Walters and Mitchel [87] yielded a deviating result of  $\mu = (0.133 \pm 0.004) \text{ cm}^2 \text{ kV}^{-1} \text{ s}^{-1}$  for  $^{208}\text{Tl}^+$  ions, which suggests that the mass number of the heavy ion does play some role (find a discussion about potential reasons in [87] and references therein). Therefore, we will refer to the latter value as we consider the  $^{208}\text{Tl}$  closer to our isotopes of interest.

Let us first turn to the hypothesis of diffusion providing an explanation for the movement of radon decay daughters and observed accumulation at the cathode. It would provide a relevant mechanism only if neutralization of the decay products  $^{212}\text{Bi}/^{214}\text{Bi}$  happened promptly after  $\beta$  emission of the polonium parent isotope. The available time scale for equal diffusion in all directions is then limited by the bismuth lifetime. We calculate the diffusion constant  $D$  via the Einstein relation [88]  $D = (\mu/q) k_B T = 2.1 \times 10^{-10} \text{ m}^2 \text{ s}^{-1}$ , where  $q$  equals the elementary charge,  $k_B$  the Boltzmann constant and  $T = 181 \text{ K}$  corresponds to the LXe temperature in our experimental setup. The mean displacement from the original point of decay (diffusion length  $L$ ) in three spatial dimensions is proportional to the square root of time,  $L = \sqrt{6Dt}$ , but yields less than 10 mm distance even when inserting many hours lifetime, as is the case for  $^{212}\text{Bi}$ . We conclude that this type of motion cannot dominantly describe the high concentration accumulation at the very bottom of the TPC because an average distance of half the TPC length ( $\sim 15 \text{ cm}$ ) would have to be overcome. Additionally, as there is no preferred direction in the diffusion process one would expect to observe enhanced BiPo activity also at the radial boundaries, which does not seem to be the case.

In [87] a conservative lower bound on the lifetime ( $\tau > 5 \text{ s}$ ) of positive Tl ions before neutralizing in liquid xenon environment is additionally derived. It is also argued why the actual value is likely to be even much larger (ranging up to 1 m survival time) than indicated by the lower limit. It is important to note that they also applied active removal of gaseous impurities to reduce their concentration to the level of few parts per billion (ppb), as similarly achieved in XENON100 [33]. Therefore, the second option assumes that the disintegration products of  $^{212}\text{Po}/^{214}\text{Po}$  remain positively charged after the electron emission. In this case, the produced ions are able to drift downwards at typical speed of  $v_d = \mu E = 0.07 \text{ cm/s}$  if inserting  $E = 530 \text{ V/cm}$  for the XENON100 electric field strength. Thereby, they have to overcome the average distance of about 15 cm before reaching the cathode position (making the well-motivated assumption that  $^{212}\text{Pb}/^{214}\text{Pb}$  are uniformly dispersed – as are their parental isotopes). We continue with a closer investigation of this model in the next section.

#### 4.6.4 Modeling $^{212}\text{Bi}^+$ ion drift

We try to reproduce the measured distribution of  $^{212}\text{BiPo}$  with a simple, 1-parametric model in order to extract a value of the lifetime of  $^{212}\text{Bi}^+$  ions (i.e. the average time of staying charged in pure LXe environment), necessary to cause the observed event accumulation. We refrain from using  $^{214}\text{BiPo}$  data (which would be available with larger statistics) because of two reasons: We learnt before that the reconstructed event positions are disturbed by accompanying  $\gamma$  emission and observe this effect much less pronounced for  $^{212}\text{BiPo}$  where most of the  $\beta$  decays end already in the ground state. Secondly, we do not have to worry about the tagging efficiency loss as a function of  $z$  position.

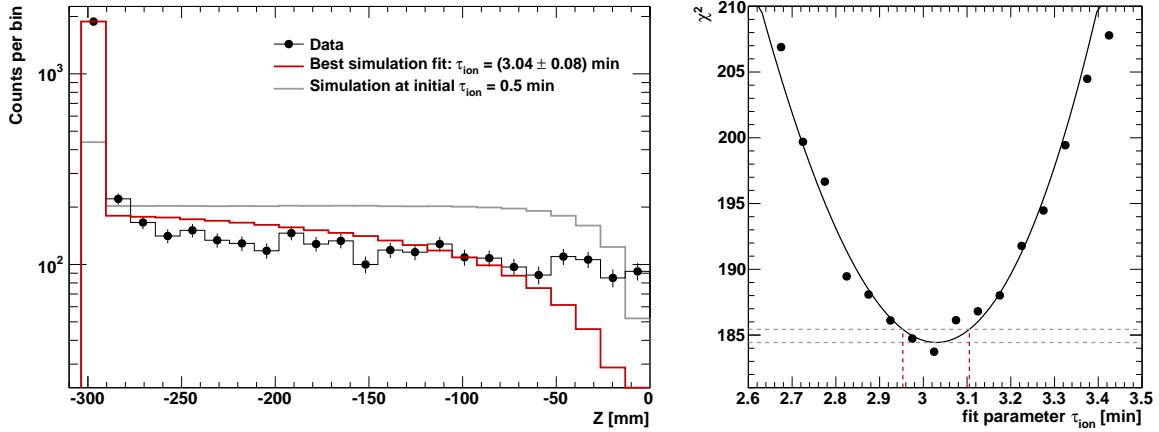


**Figure 4.23:** (Left) Measured (black points) and simulated (red) distribution of  $^{212}\text{BiPo}$  events along the detector  $z$  axis. For comparison the simulated position histogram for a fixed value of the ion lifetime ( $\tau_{ion} = 0.5$  min) is additionally shown in gray. The best fit reproduces very well the accumulation at the cathode position within the 1-parametric model but gives poor agreement in the top region of the detector. (Right)  $\chi^2$ -distribution for the varying model parameter  $\tau_{ion}$ . A global minimum is found at  $3.04 \pm 0.08$  min, with the  $1\text{-}\sigma$  error extracted from those points that correspond to  $\Delta\chi^2 = 1$  with respect to the minimum value of the parabolic fit.

The attenuation for drifting ions is supposed to follow a typical absorption law (analogously to drifting electrons, Sec. 2.1.3)

$$N(z) = N_0 e^{-\frac{z(t)}{\lambda_{ion}}} = N_0 e^{-\frac{v_d t}{\lambda_{ion}}} = N_0 e^{-\frac{t}{\tau_{ion}}}, \quad (4.5)$$

where the mean distance  $\lambda_{ion}$  is connected to the survival drift time  $\tau_{ion}$  according to  $\tau_{ion} = \lambda_{ion}/v_d$  and the drift velocity  $v_d$  is known for  $^{208}\text{Tl}^+$  from [87]. By means of a simulation we want to extract the lifetime parameter  $\tau_{ion}$ : First, we pick a uniform random position  $z_0$  along the vertical dimension of the TPC at the time of  $^{212}\text{Pb}$  decay and assume that all decay products are in fact positively charged. Moving downwards along the field lines there are two relevant time scales which determine the finally measured  $z$  position of the subsequent  $^{212}\text{BiPo}$  event: the known  $^{212}\text{Bi}$  radioactive decay time  $\tau = 87.3$  min and the unknown ion lifetime, which is treated as a free parameter. For each event both are randomly drawn (following their exponential distribution) and the smaller is taken to define the available drift time  $t_d$ . The updated spatial position is calculated by  $z = z_0 - v_d t_d$  and filled into a histogram, finally normalized to the recorded event number in data. For candidates reaching the cathode position we require them to stick to the grid surface and do not drift further. We implement this algorithm as part of a parameter scan over  $\tau_{ion}$ , comparing each outcoming  $z$  spectrum to the measured one of  $^{212}\text{BiPo}$  tagged events from the long-term run. The best fit result is given in Fig. 4.23, together with the corresponding  $\chi^2$  distribution. We find a global  $\chi^2$  minimum at  $\tau_{ion} = (3.04 \pm 0.08)$  min and construct the  $1\sigma$  error bounds by searching for those two neighbouring points where the  $\Delta\chi^2$  has increased by one. The simulated  $z$  distribution does well reproduce the event accumulation at the bottom grid but fails in describing the measurement at the very top. This indicates that there remains a certain fraction of  $^{212}\text{Bi}$  atoms which stay at their initial position because of immediate neutralization after  $^{212}\text{Po}$  decay. Depending on the  $\beta$  energy of every individual decay it is conceivable that ion-electron recombination occurs if the electron cannot travel far enough in LXe. Adding a constant fraction of uncharged particles to the simulation model leads to a better minimum  $\chi^2$  and increases the inferred  $\tau_{ion}$  by up to 4 min. Another argument why the quoted error must be taken with care is the fact that we might not observe all BiPo events occurring at the cathode position. Indeed, we will

discuss later in more detail the overall deficit of tagged BiPo events with respect to the  $\alpha$  rate from the parent radon isotopes. It indicates that some fraction of the time-coincident decays remains unseen.

Finally, one could argue that there is another possible systematic effect unregarded by the current model description. Besides diffusion and electric field motion there might also be convection patterns responsible for spatial dispersion. Coherent movement could be induced by temperature gradients caused by heat influx (from the cryostat walls but most likely from the bottom PMTs) and simultaneous cooling by the active condensing of recirculated xenon gas (re-entering the liquid phase from the top). However, we can rely on our observation of spatial uniformity in the distribution of  $^{222}\text{Rn}$  and  $^{218}\text{Po}$  to conclude at least that the convective effects should not apparently dominate the dynamics of dissolved radon daughters. Yet, we want to mention that the existence of a strong directed motion towards the TPC bottom (top) would imply  $\tau_{ion}$  to become smaller (larger) in reality than suggested by the fit result.

Believing in the predominance of electric ion drift our inferred result points towards the suggestion made by Walters and Mitchel that the ion lifetime in purified LXe is in fact much greater than set by their lower bound, ranging up the order of several minutes.

### 4.6.5 BiPo at zero drift field

In order to probe our hypothesis that ion drift provides a valid explanation for the non-uniform BiPo distribution, we evaluate available data from a detector commission phase, where the electric drift field was switched off for an integral amount of 3.9 live days in 2012. The hardware event trigger threshold – by default designed to have  $> 99\%$  efficiency for  $S2 > 150$  PE – does not need to be changed as it is easily exceeded by the huge S1 signals from  $\alpha$  decay as part of the BiPo coincidence. In fact we observe that already the second largest S1 (from  $\beta$  deposit) is sufficiently large to be marked as the triggering peak within the waveforms in almost 100% of all tagged BiPo events.

Without electrical field, no electrons can be drifted to create the S2 signal and thus, no event localization is possible in first place. Accordingly, the S1 signals cannot be corrected by the light collection efficiency map and energy resolution becomes poor. Fortunately, all BiPo selection criteria are based on the S1 pulses without need for position corrected quantities. Consequently, the same data cuts as before can be used to identify the time-coincidence topology. Without S2 peaks in the recorded waveforms there is even no position dependent tagging efficiency to be considered (compare to Sec. 4.4.2). This becomes first obvious in the lifetime distribution of  $^{214}\text{Pb}$  decay. In Sec. 4.4.2 it was necessary to account for the acceptance loss in a dedicated simulation in order to extract the expected average decay time. Using zero field data, the lifetime distribution directly follows an exponential shape with  $\tau = (250 \pm 50) \mu\text{s}$  in agreement with the literature value but large fit error due to limited statistics in this dataset.

Even without precise vertex determination we can compute the asymmetry between the S1 light detected by the top and bottom PMT array in order to obtain a rough idea about the vertical event position:

$$A_{S1} \equiv \frac{S1_{\text{top}} - S1_{\text{bottom}}}{S1_{\text{top}} + S1_{\text{bottom}}} . \quad (4.6)$$

by definition,  $A_{S1} \in [-1, 1]$  and yields lower values for events near the bottom PMTs and higher values for those closer to the top. An approximate calibration of the asymmetry parameter is obtained by drawing its correlation for  $\alpha$  events (Fig. 4.24) and BiPo decays (Fig. 4.25) as a function of the (known)  $z$  distribution in regular data, for which the electric field is applied.

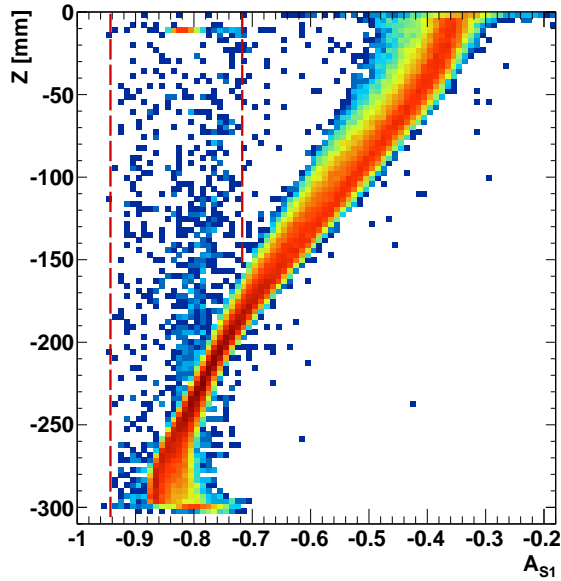


**Figure 4.24:** Correlation between S1 light asymmetry and vertical  $z$  position for  $\alpha$  decays inside the TPC at finite drift field (logarithmic color axis represents event densities). Red vertical lines are to draw attention towards a population with constant  $A_{S1}$  but far-ranging  $z$  positions. Those are most likely decaying in the charge insensitive region below the cathode grid but are picked up in time correlation with a random S2 noise peak.

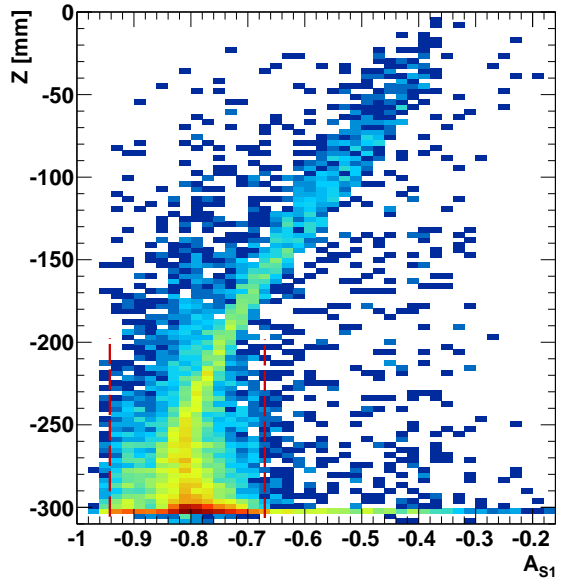


**Figure 4.25:** Same correlation as shown in the left picture between asymmetry and vertical position of reconstructed  $BiPo$  events at finite drift field. The majority of events occurs at the cathode position where the asymmetry has a very broad spread. Again, misidentified positioning causes a population towards higher  $z$  but equal  $A_{S1}$ .

Note that  $A_{S1}$  stays negative even for events close to the liquid/gas interface, which is not unexpected because the bulk amount of S1 light is always to be seen by the bottom PMTs due to the large internal reflection of VUV light at the LXe surface. While a precise mapping from  $z$  position to the asymmetry parameter is not possible we do observe that cathode events are typically spread around  $-0.95 < A_{S1} < -0.70$  (indicated by red vertical lines in the figures). We know this because it affects the vast majority of  $BiPo$  events known to happen at the grid if the  $E$ -field is applied and because we observe a similar spread for  $\alpha$  events without physical S2. The latter appear uniformly along  $z$  only since they get connected to some unrelated (or photo-ionization) S2 which randomly appears in the waveform. The fact that the asymmetry stays constant is a good indicator for fake positioning and suggests the event to happen just below the cathode where charge collection is absent or incomplete. This knowledge becomes important when discussing the  $BiPo$  locations at zero field where  $A_{S1}$  is the only available position estimator.

A comparison of the asymmetry parameter distributions for three different event selections is shown in Fig. 4.26. The black spectrum is a projection on  $A_{S1}$  over all  $z$  positions above  $z \approx -300$  mm of Fig. 4.24 and is considered our test sample of  $\alpha$  decays, which we know to be evenly distributed along the vertical axis even when  $E = 530$  V/cm. As opposed to the  $\alpha$  distribution the green histogram contains the same quantity for  $BiPo$ 's at the same finite  $E$ -field, where we know that almost all of them occur near the cathode. Our main interest is now on the blue spectrum of  $BiPo$  tagged events in the zero field dataset (for which  $A_{S1}$  is the only spatial information available). All histograms are normalized to the integral number of events in each class. Comparing to the others it is obvious that the measured  $BiPo$  distribution at  $E = 0$  V/cm resembles much better the one of homogeneously

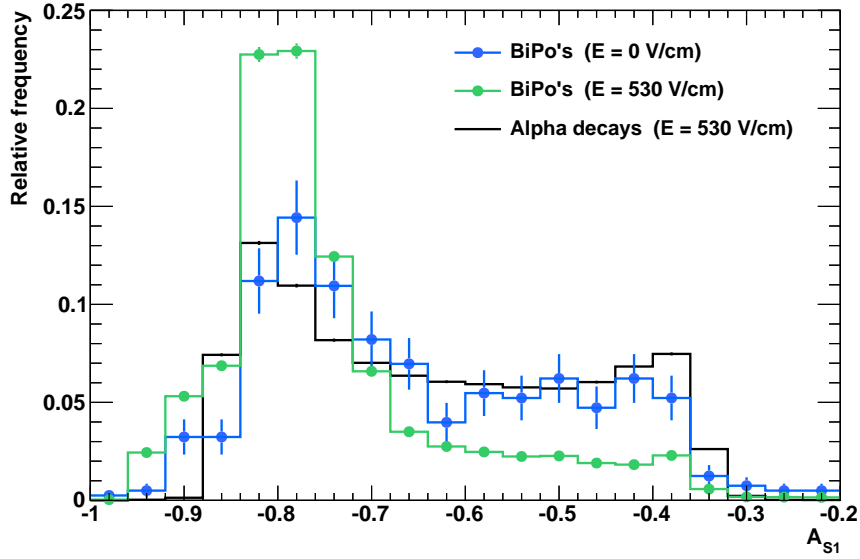


**Figure 4.26:** Normalized spectral comparison of the  $A_{S1}$  parameter between BiPo selections at two different electric field configurations and homogeneously dispersed  $\alpha$  decays. The uniform control sample is much better matched if the electric field is off, indicating that that BiPo events only accumulate at the cathode position if the grid is applied to an electric potential.

dispersed  $\alpha$  decays ( $\chi^2 = 67$  for 20 bins) than the spiked BiPo concentration at non-zero field ( $\chi^2 = 7740$ ). We interpret this result as further evidence of the drift hypothesis. In one case BiPo events seem far more evenly distributed than in the other because only when an extraction field is applied the produced ions will be dragged away from their initial decay position. Other effects mentioned, like diffusion or convection, should accordingly play a sub-dominant role.

#### 4.6.6 Summary of spatial distributions

We summarize our various attempts at understanding the entire picture of spatial dispersion of different components of the radon/thoron chain. Significant effects are observed mostly along the vertical TPC axis while radial distributions appear mostly flat (except for ring patterns due to position reconstruction saturation in the  $(x,y)$  plane). The  $z$  dependency of event localization for all detectable components is shown in Fig. 4.27 for data accumulated from the long-term analysis. The black spectrum is obtained when selecting a wide range of  $\alpha$  energies between  $15\,000\text{ PE} < S1_\alpha < 30\,000\text{ PE}$  and therefore particularly contains also those decays occurring near or on the cathode grid, where the detected  $S1_\alpha$  is suppressed and the light correction map is inefficient. Away from the very bottom it corresponds practically to the sum of the individual contributions of the two major  $\alpha$  peaks from  $^{222}\text{Rn}$  and  $^{218}\text{Po}$ , provided by the blue and red histograms. The two  $\alpha$  components are selected and separated according to  $S1_\alpha$  intervals defined such that 99.5% of each gaussian integral is accepted (refer to Fig. 4.15). Since the electro-negative purity was far better in the second major dark matter run than at the time of high radon concentration, the detected  $S2$  signals are generally larger and radial position saturation becomes slightly worse. In the same amount radial resolution becomes somewhat decreased, the  $S1_\alpha$  resolution, achieved with the position dependent alpha light correction map, deteriorates. This explains why the  $\alpha$  peak separation for  $z < -260\text{ mm}$  is not as good as in the 2009 data

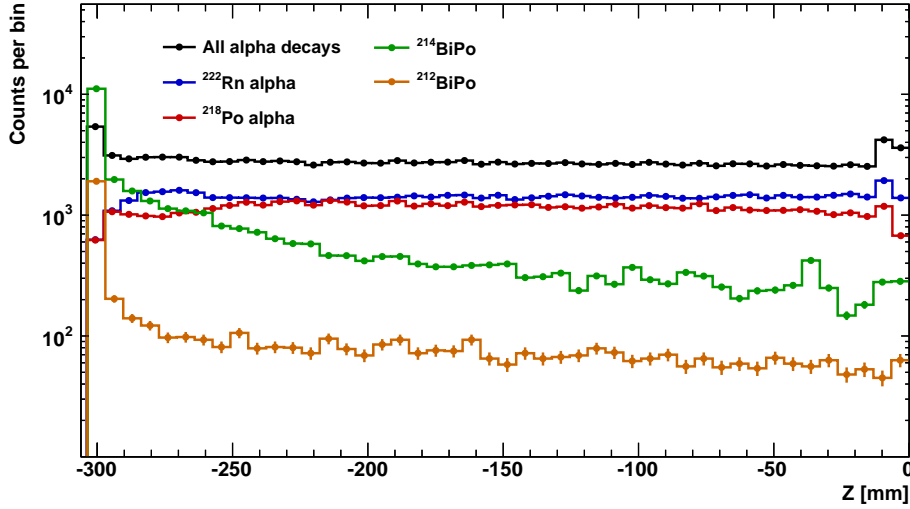


**Figure 4.27:** Z position distribution of different radon chain components as measured and reconstructed during the 225 live days dark matter run.  $\alpha$  decays are uniformly spread in first place with some accumulation at the cathode position. On the contrary, obvious spiking at the bottom grid mesh is observed for BiPo's from both radon decay chains.

and why the spatial concentrations seem a little anti-correlated at the TPC bottom, while their sum (black histogram) remains perfectly flat. For the very first bin (cathode position) the peak separation fails entirely because the  $S1_\alpha$  correction is insufficient in this low  $z$  region (it explains why the sum of the individual peak contribution does not match the combined  $\alpha$  event number defined over a broad  $S1_\alpha$  interval). Apart from the cathode position ( $z \approx -306$  mm) another spike at  $z \approx -10$  mm becomes visible. By looking at the asymmetry parameter  $A_{S1}$  we find clear evidence that those events in reality happen below the charge sensitive region underneath the cathode – without possibility to drift ionization charges. The  $S2$  is then created by photo-ionization of metallic structures close to the liquid surface by the VUV scintillation light. Thereby emitted photo-electrons only have to overcome a short drift distance before reaching the liquid level. Since a huge amount of  $S1$  light is created due to  $\alpha$  decay the chances for producing those electrons is much enhanced compared to the usual, small light signals. In any case, we remark that excess events in this bin in fact belong to the cathode position.

The distributions from the two BiPo candidates have already been discussed in detail in the previous sub-section and are shown for completeness. For the first time, we plot the  $^{214}\text{BiPo}$  distribution after having applied the position dependent efficiency function, as given in 4.4.2. The fact that the green spectrum from  $^{214}\text{BiPo}$  appears to increase slowly below  $z < -250$  mm was already shown to be caused by mistaken  $\gamma$  scatters while the  $^{214}\text{Bi}$  decay in fact happens close to the cathode. This effect is much suppressed for  $^{212}\text{BiPo}$  (orange histogram) due to smaller  $\gamma$  emission probability.

## 4.7 Radon rate evolution

Since the level of internal radon concentration in the XENON100 detector directly affects the background rate for dark matter search, it becomes important to establish a reliable counting monitor for  $\alpha$  and BiPo events. In this way even tiny air leaks to the gas system can be traced by watching for a sudden rate increase as happened during the detector commission phase in late 2009 and shown in Fig. 4.28.

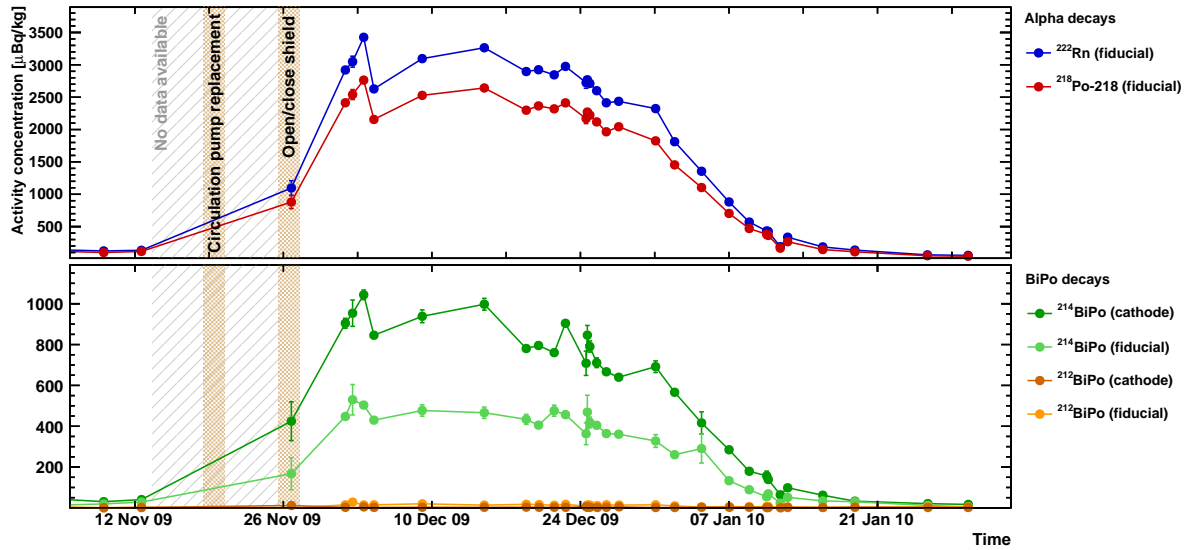


**Figure 4.28:** Evolution of the activity concentration for various radon chain components as a function of time during the period of external air intrusion. Shortly after detector maintenance (involving replacement of the circulation pump and opening/closing of the external shield) a leak allows for infiltration of ambient air and causes a significant rise in all components but  $^{212}\text{BiPo}$ .

In this figure and further discussion we refer to radon concentration, defined as the observed count rate within a given fiducial detector volume and thus normalized to the corresponding LXe mass, in units of  $\mu\text{Bq/kg}$ . This notation is advantageous when later translating into an expected background index for the dark matter search window (in principle this quantity is also suitable for comparison with other liquid noble gas detectors because it is independent of the target size and material). To count events, we apply the earlier introduced tagging criteria for  $\alpha$  and BiPo decays. The latter are corrected for their  $z$  dependent acceptance loss and therefore understood as corrected concentration rates. Since we have learnt that BiPo events tend to cluster at the cathode position (i.e. are depleted in the inner part of the TPC) we divide their total concentration into separate contributions from the cathode and fiducial volume.

**Radon increase through air leak** We begin our evaluation of internal radon concentration for the detector commission phase in late 2009. As indicated in Fig. 4.28, there is a significant rise in the radon level by more than one order of magnitude shortly after performing maintenance work and handling of the xenon purification loop (including replacement of a recirculation pump and temporary opening of the passive shield). It appears that a tiny air connection established to the environmental air, now transporting amounts of natural radon into the inner detector vessel through the gas recirculation lines. The exact moment of the incident is difficult to trace because during that time only a limited number of datasets were processed and made available until the time of writing. When the problem was finally noticed the pump was sealed with a bag and constantly flushed with pure nitrogen. This helped to reduce the radon level even slightly below the initial value before the incident occurred. It is worth noting from the plot that the  $^{212}\text{BiPo}$  rate from the thoron chain was not affected at all by the air influx. This validates our presumption that  $^{220}\text{Rn}$  is too short-lived to arrive in the active volume through the external gas system.

We want to infer a rough estimate of the integral air volume entering to the detector and compare this value to the expected amount from an independent analysis of the noble gas krypton concentration

measured by rare gas mass spectrometry from a xenon sample drawn during the subsequent dark matter run (100 live-days). This dedicated krypton analysis is performed by and reported in the work of [64]. We calculate the total number  $N_{Rn}$  of  $^{222}\text{Rn}$  decays from the blue curve in Fig. 4.28 from the moment of opening/closing the detector shield (refer to Fig. 4.28). At that time, there is the first indication of sudden rate increase in available data. The upper time intergration bound is set at the end of the observed rate excess in late January 2010. During this time period we count an intergral amount of  $N_{Rn} = 1.44 \times 10^6$  radon decays. The result contains scaling to the total LXe mass of 161 kg in the detector. Important to remark that this calculation relies on the assumption that  $^{222}\text{Rn}$  is evenly distributed not only inside the 62 kg LXe TPC (where we have confirmed homogeneity through measurement) but also in the surrounding total volume. The number can be translated into an equivalent activity  $A_{Rn}^0$ , entering the system all at once and given infinite time for radioactive decay:

$$A_{Rn}^0 = \frac{1}{\tau_{Rn}} \cdot N_{Rn} = 3.0 \text{ Bq} . \quad (4.7)$$

In the real case of long-term infiltration, the condition of infinite time is valid by good approximation when comparing the decay of  $^{222}\text{Rn}$  to the duration of the excess rate period ( $\sim 1$  month). To convert this activity into a leak volume one needs to know the radon concentration in ambient air. For the XENON100 experimental site, this quantity is constantly probed with a commercial RAD7 radon monitor (manufactured by Durridge Company) installed outside the detector shield. The rate shows typically large seasonal fluctuations (for example caused by changing water level in the rock cavern) but can sometimes even change by 20% on a daily basis – depending on the air ventilation in this part of the underground laboratory. For the time period of interest we determine an average radon concentration of  $c_{Rn} = 300 \pm 6 \text{ Bq/m}^3$ . This implies an air volume of  $V_{air} = A_{Rn}^0/c_{Rn} = (10.0 \pm 0.2) \text{ l}$ , which has diluted into the detector system. While the quoted error is solely given by the uncertainty in average radon content in air, there is a further systematic uncertainty by the assumption of homogeneity in the  $\sim 99 \text{ kg}$  veto volume without experimental proof. The facts that both volumina, inside and outside of the TPC, are connected and, after all, the entire amount of LXe is circulated within few days, provides good reason for the hypothesis. Nevertheless, in the extreme case that  $^{222}\text{Rn}$  is only present in the PTFE surrounded TPC (62 kg target mass), the estimated leaking volume shrinks to  $\sim 3.9 \text{ l}$ . The same value inferred from measurements of the (natural) krypton concentration in the LXe, is found to be  $\sim 8 \text{ l}$  (preliminary result to be published in [64]), after applying reasonable assumptions on the krypton gas concentration in ambient air, and in good agreement with the mean volume obtained from the amount of radon when presuming an even distribution in the entire LXe volume.

It is clear that with the infiltration of  $^{222}\text{Rn}$  a contamination with the long-lived  $^{210}\text{Pb}$  isotope will slowly build up on the timescale of decades. However, in all later analyses of the radon background there is no indication for an  $\alpha$  line arising from the equilibrium decay of  $^{210}\text{Po}$ . This supports the hypothesis that the heavy lead metal plates out at the cold TPC surfaces and decays such close to the walls that the energy resolution is not sufficient to disentangle from other  $\alpha$  decays. Among the emanation of short-lived  $^{220}\text{Rn}$  this can contribute to the observed increase of  $\alpha$  rate at large radii (Fig. 4.21). In any way, it does not represent an observable background component in the inner part of the TPC volume which is relevant for dark matter searches.

**Long-term radon evolution** Fig. 4.29 shows the time evolution of radon concentration in the various chain components during the time of the 225 live days dark matter search run in 2011/2012 [42]. Over the duration of more than one year the rates are constant within local fluctuations of  $< 30\%$  around the mean. As we will discuss in the next section, these fluctuations are partly correlated with the ambient air radon concentration outside the detector shield, pointing towards a tiny leak rate into

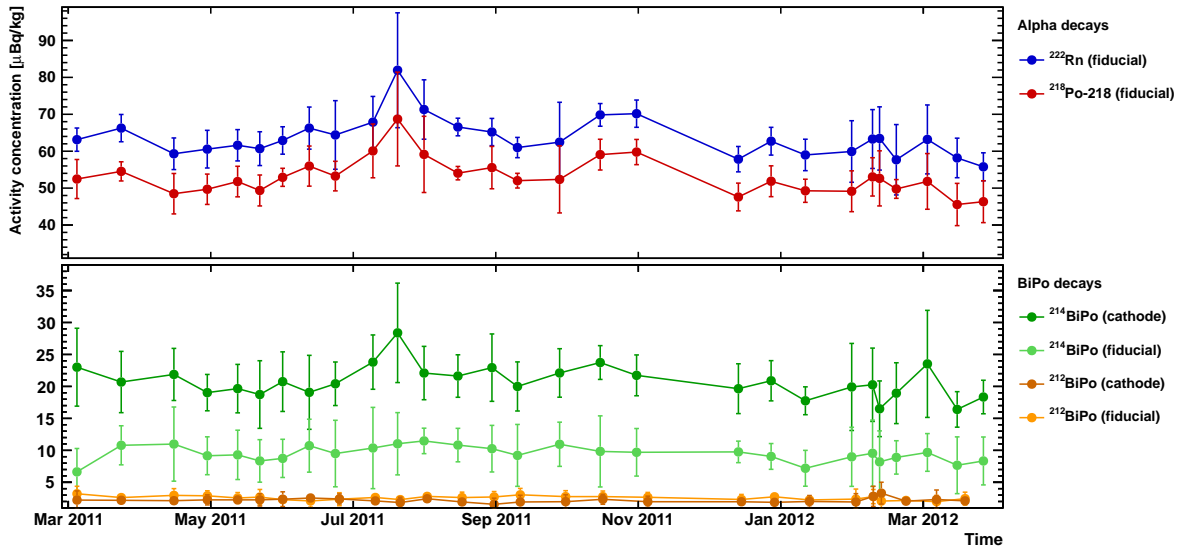


**Figure 4.29:** Time evolution of the activity concentration for various radon chain components during the 225 live days period of dark matter search. All rates appear relatively constant in time. The contribution from BiPo's is split into cathode and fiducial volumes to show that its abundance is largely depleted in the inner parts. Each point shown represents the average of ten single datasets and the size of the related error is given by the standard deviation of the individual measurements within the binned sample. It therefore includes both statistical and systematic fluctuations occurring on the timescale of the applied binning.

the gas system on top of a larger contribution from radon emanation off internal detector materials. The amount of  $^{212}\text{BiPo}$  is largely suppressed compared to the components of the other radon chain and approximately at the same level as in data from late 2009. Therefore we conclude that the abundance of  $^{220}\text{Rn}$  is entirely caused by emanation through inner components, such as PTFE, PMTs or the steel cryostat. Even more constant in time, but with slightly differing average rates, we monitor the evolution during the published 11 and 100 live days dark matter analyses, reported in [67, 47]. We will continue with the discussion of the different periods in Sec. 4.8.

**Ratios of chain components** It is an apparent feature in all monitored radon data that the measured concentration decreases among the radon chain components, showing highest rates in the original radon decay and lowest in BiPo events. In Fig. 4.30 we present the ratios of  $^{218}\text{Po}/^{222}\text{Rn}$

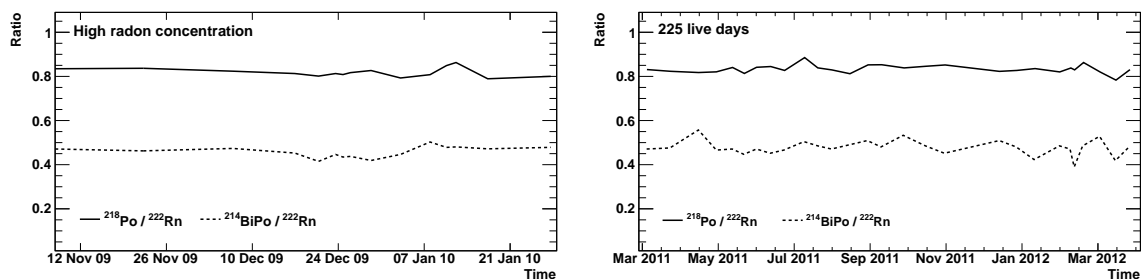


**Figure 4.30:** Rate comparison of  $^{218}\text{Po}$  and  $^{214}\text{BiPo}$  (cathode and fiducial volume contributions summed) relative to their parent isotope  $^{222}\text{Rn}$  for the two time periods of high (left) and low (right) radon concentration. The ratios are almost equal between both runs and are constant with time.

and  $^{214}\text{BiPo}/^{222}\text{Rn}$ , with the summed BiPo contributions from cathode and fiducial volume. They are almost equal between the two datasets of very high and low radon concentration and appear constant over time. The largest gap of  $\sim 50\%$  is observed between the pure  $\alpha$  and BiPo decays but fits to our previous findings of charged  $\text{Bi}^+$  ions accumulating at the cathode mesh. Sitting on the surface of a metallic grid it is very likely that the emitted  $\beta/\alpha$  energy from the subsequent BiPo decay is deposited in the material and not detectable at all. The same effect could explain the measured deficit in  $^{218}\text{Po}$  concentration. It is well conceivable (and experimentally known from radon monitor detectors, e.g. in [85]) that a large fraction of  $^{218}\text{Po}$  remains positively charged after decay of its parent isotope  $^{222}\text{Rn}$ . The sign and charge number depends on how many atomic shell electrons are stripped-off by the recoiling nucleus and how strong is the recombination rate of ion-electron pairs afterwards. From the low charge yield of  $\alpha$  decays (see Sec. 4.4.1) we know that neutralization probability is large but in this case we need only  $\sim 15\%$  of ionized daughters drifting to the cathode to explain the mismatch in the two  $\alpha$  emitters. This hypothesis is supported by the increase of tagged  $\alpha$  number at the cathode position, already shown in Fig. 4.27. Since energy resolution for cathode events is too poor to tell the two  $\alpha$  lines apart, it is easy to imagine (but hard to prove) an excess of drifted  $^{218}\text{Po}$  ions at this place.

**Correlation with ambient air  $^{222}\text{Rn}$  concentration** Looking at the time evolution of internal radon activity during the 225 live days background run (Fig. 4.29) we observe rate fluctuations beyond statistical counting errors. This raises the question of what could provide a possible explanation for the systematic variations. A straightforward idea is to search for potential correlations with the external concentration of  $^{222}\text{Rn}$  in the ambient air at the experimental site, constantly monitored with the already mentioned RAD7 monitor. Then – in case of air leaking into the gas system – the activity concentration in the inner LXe volume can become coupled to the radon density in the external laboratory. We propose the following model function  $c_{\text{Rn}}^{\text{in}}(t)$  to test the correlation hypothesis:

$$c_{\text{Rn}}^{\text{in}}(t) = c_0 + f \cdot c_{\text{Rn}}^{\text{ext}}(t - \Delta t). \quad (4.8)$$

According to this ansatz, the internal radon concentration (calculated in units of  $\mu\text{Bq/kg}$ ) can be described by the sum of a time-independent component  $c_0$ , supposedly from internal radon emanation off the complete cryostat/detector system, and a fraction  $f$  of the external radon concentration  $c_{\text{Rn}}^{\text{ext}}(t)$  (given in  $\text{Bq/m}^3$ ), entering to the system by inward diffusion of outside air and observed to be a function of time. We additionally allow for a time shift  $\Delta t$  which defines the delay of the detector response to outside variations (and encodes the air diffusion time through a potential mini-leak/porous material). Thereby, we have to make the underlying assumption that radon becomes quickly dissolved in the LXe after entering the inner system compared to the timescale set by  $\Delta t$ . Both the evolution of the externally measured  $^{222}\text{Rn}$  level and the best fit to all internal  $^{222}\text{Rn}$  activity concentration data points, recorded during the 225 live days, are shown in Fig. 4.31 and the implied fit parameters given in Tab. 4.3.

The internal data are binned according to the recorded datasets taken in the 225 live days run, thereby averaging rates over  $\sim 1$  day. Related errors for each individual dataset are solely statistical ( $\sqrt{N}$ ). The external radon level is originally stored to database every  $\sim 1$  h but for our purpose forced into a daily binning (averaging over 24 points) to provide similar resolution as in the internal measurement. The fit function interpolates linearly between two neighbouring points. The  $\chi^2$  minimization is realized by the MINUIT algorithm used in the ROOT analysis toolkit [65, 66] and parameter errors are extracted such that they imply a change in  $\Delta\chi^2 = 1$  compared to the minimum value. For comparison we fit the same data, assuming the hypothesis of a constant activity concentration over time.

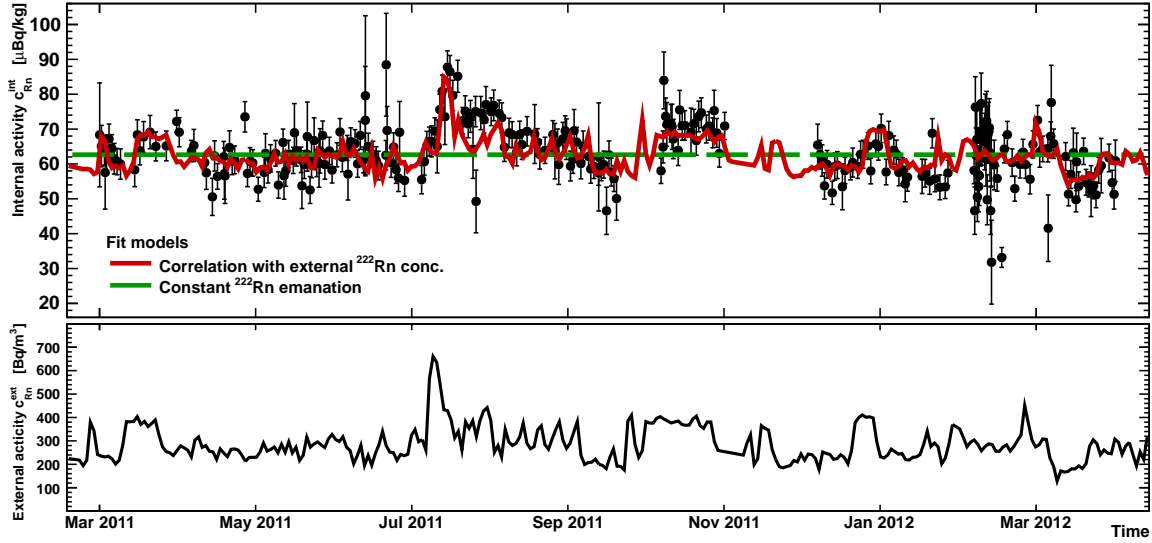


**Figure 4.31:** Test of hypothetical time-correlation of the internal  $^{222}\text{Rn}$  activity (black data points, upper frame) with the outside radon decay concentration (black line, lower frame) in the ambient air at the XENON100 detector site. The best fit of the model function  $c_{\text{Rn}}^{\text{int}}$  is represented by the red line, while a constant fit to data is shown in green for comparison.

Model	Fit parameters				
	$c_0$ [ $\mu\text{Bq/kg}$ ]	$f$ [ $\text{ml/kg}$ ]	$\Delta t$ [d]	$\chi^2/\text{NDF}$	p-value
Time correlation with external $^{222}\text{Rn}$	$45 \pm 1$	$0.060 \pm 0.003$	$4.5 \pm 0.1$	496/277	$10^{-14}$
Only internal $^{222}\text{Rn}$ emanation	$63 \pm 1$	–	–	770/279	$10^{-47}$

**Table 4.3:** Estimated fit parameters of the two model functions applied to the inner measured  $^{222}\text{Rn}$  concentration of Fig. 4.31.

The individual minimal  $\chi^2$  and the respective p-value<sup>2</sup>, taken as a measure for the goodness of fit, are both such that the underlying hypotheses are rejected at very high confidence and thus neither of them provides a complete model description. However, the improvement of the time-correlated fit with respect to the constant one is obvious and thus favouring the supposed time-dependency. It is evident that a complex process like the emanation of radon from a large integrated system (XENON100 detector plus purification loop) cannot entirely be described over one year with only three parameters. It is likely that additional radon sources, for example coupled to duty cycles of the hot getter, are neglected by our model. Yet, it can nicely connect both general trends and spikes appearing in external and internal data. From the fit parameters, we infer a large pedestal  $c_0 = (45 \pm 1) \mu\text{Bq/kg}$  of unrelated radon concentration. In the next section, we will find that this values matches very well the total level of  $^{222}\text{Rn}$  during the earlier 100 live days period. During this period, the observed radon level shows much less variation over time and we can thus conclude that the rate excess in the 225 live days is in fact caused by a tiny connection to the outside air which must have been created in the commission phase between the two runs. It further tells us that the total  $^{222}\text{Rn}$  emanation equilibrium rate of the XENON100 detector system is at the order of  $c_0 \cdot 161 \text{ kg} \approx 7 \text{ mBq}$  under the assumption that  $^{222}\text{Rn}$  is evenly spread not only in the observable TPC but also in the total 161 kg target mass volume. Under

<sup>2</sup>The p-value yields the probability that any remaining discrepancy between data and model are only due to statistical fluctuations of the data and is calculated from the complementary cumulative chisquare distribution function.

the same supposition, we extract an equilibrium amount of  $f \cdot e^{\Delta t/\tau_{Rn}} \cdot 161 \text{ kg} \approx 22 \text{ ml}$  of air entering to the purification loop within an average time of  $\Delta t \approx 4.5 \text{ d}$ . Thereby, we have already corrected for the loss of radon concentration by radioactive decay ( $\tau_{Rn} = 5.5 \text{ d}$ ) during the time  $\Delta t$  it takes for the air to diffuse through the outside connection. If the leak is previous to the hot getter purification most of the electronegative impurities (mostly from outgassing/leaking  $\text{O}_2$ ) will be removed from the circulated gas before re-entering the detector and explains why the lifetime of drifting electrons remains unaffected.

## 4.8 Impact of radon on low energy background

After studying various properties we come back to one of the important initial questions of how does the presence of the radio-active noble gas radon impact the background rate in the energy region of interest for dark matter searches. As it is nicely described in [82] and can be learnt from the multi-component fit to the spectral shape of the electromagnetic background spectrum in XENON100 [81], the  $\beta$  decay of  $^{214}\text{Pb}$  marks the only relevant contributor among the various radon chain components. All other parts,  $\alpha$  decays and BiPo events, can either be discriminated by their high energy or obvious time-coincidence, while the low energy continuum of the  $^{214}\text{Pb}$   $\beta$  spectrum will add to the electromagnetic recoil background in the WIMP search region.

In the introduction to this chapter (Sec. 4.2) we have already mentioned MC simulations to convert a given internal radon activity concentration  $A_{Rn}$  into expected differential background rate  $R_{Rn}$  in the low energy range of  $0 - 100 \text{ keV}$ . From those simulations, summarized in Fig. 4.2 in [81], one finds that the relation is linear and can be described as

$$R_{Rn} = 0.029 \times \left( \frac{A_{Rn}}{\mu\text{Bq kg}^{-1}} \right) \text{ mDRU} , \quad (4.9)$$

where the differential rate unit is defined as  $1 \text{ DRU} = 1 \text{ d}^{-1} \text{ kg}^{-1} \text{ keV}^{-1}$ .

What remains to discuss is which value of  $A_{Rn}$  from the different radon chain components should be inserted because the simulation does not take into account the measured reduction of subsequent decay daughter concentrations in the active volume. Since the present analysis is not able to directly observe the  $^{214}\text{Pb}$   $\beta$  decay we only know for sure that the background relevant activity concentration in the inner part of the TPC must be in between the quantities measured for  $^{218}\text{Po}$  and  $^{214}\text{BiPo}$ . To be conservative in the predicted rate we will further use the measured  $^{218}\text{Po}$  activity for the above conversion relation. However, we will take into account the observation of  $\sim 15\%$  event rate reduction after the  $^{222}\text{Rn} \rightarrow ^{218}\text{Po}$  decay to estimate a lower systematic uncertainty on the background prediction, thereby assuming that the product from  $^{218}\text{Po} \rightarrow ^{214}\text{Pb}$   $\alpha$  decay shows the same rate decrease.

Results are summarized in Tab. 4.4. Between the different runs we find significant differences in the overall average radon levels, which are likely to explain by slightly varying air diffusion rates into the gas system (caused e.g. by exchange of pump equipments, sealings, o-rings, etc.). The different levels linearly translate into the expected single scatter background rate in the low energy window according to Eq. (4.9). To draw meaningful conclusions, one has to compare the radon induced background level to the contributions from internal  $^{85}\text{Kr}$  contamination and external  $\gamma$  radiation.

The krypton content in XENON100 can be determined by (at least) two independent techniques. One is the on-line determination in the recorded XENON100 data, using a  $\beta$ - $\gamma$  time coincidence method [89]. The other is rare gas mass-spectrometry (RGMS) of the natural krypton concentration contained in a xenon sample drawn from the detector and measured off-line after transportation from the underground laboratory to MPIK, Heidelberg (refer to work of [64]). The latter technique is very

Time period	Mean activity concentration [ $\mu\text{Bq/kg}$ ]			Predicted background $R_{Rn}$ [mDRU]
	$^{222}\text{Rn}$	$^{218}\text{Po}$	$^{214}\text{BiPo}$ (total)	
11 live days (2009)	$138 \pm 3$	$111 \pm 3$	$61 \pm 2$	$3.2^{+0.1(\text{stat.})}_{-0.5(\text{sys.})}$
100 live days (2010)	$45 \pm 1$	$41 \pm 1$	$19.0 \pm 0.6$	$1.18^{+0.03(\text{stat.})}_{-0.18(\text{sys.})}$
225 live days (2011/2012)	$63 \pm 1$	$52 \pm 1$	$30.6 \pm 0.3$	$1.51^{+0.03(\text{stat.})}_{-0.23(\text{sys.})}$

**Table 4.4:** Mean activity concentrations of different radon chain components and predicted background contribution in the 0–100 keV energy range for the three major science runs of XENON100, reported in [67, 47, 42]. The concentrations of  $^{222}\text{Rn}$  and  $^{218}\text{Po}$  refer to an inner cylindrical volume of  $-260 \text{ mm} < z < -10 \text{ mm}$  and  $r < 145 \text{ mm}$ . BiPo decays are only restricted by a  $r < 145 \text{ mm}$  radial selection, thus including the cathode concentrations. Errors given for the measured average are merely statistical. The predicted background is calculated from the  $^{218}\text{Po}$  concentration as discussed in text. The upper uncertainty of the rate prediction is inferred from the statistical fluctuations of the measured concentrations. The lower bound is estimated by assuming a similar  $\sim 15\%$  signal reduction in the inner fiducial volume as observed after  $\alpha$  decay of  $^{222}\text{Rn} \rightarrow ^{218}\text{Po}$ .

challenging because only tiny traces at the level of parts per trillion (ppt) have to be identified in a macroscopic xenon gas volume. Translation to direct counts inside the detector finally relies on the isotopic abundance of radioactive  $^{85}\text{Kr}$  in natural krypton of the ambient air. A  $^{85}\text{Kr}/^{nat}\text{Kr}$  ratio of  $2 \times 10^{-11}$  [90] is assumed in the conversion done by [64].

For the 225 live days an ultra-pure total background index of  $R_{Tot} = 5.3 \pm 0.6$  mDRU is measured inside the selected 34 kg fiducial volume after all event quality cuts (except particle discrimination) and reported in [42] for the dark matter region of interest. The RGMS measurement found a  $^{nat}\text{Kr}$  concentration in LXe of  $(19 \pm 4)$  ppt, consistent with  $(18 \pm 8)$  ppt from the delayed coincidence method [42]. Combining this concentration with results from the electromagnetic background MC simulation [81] the differential rate  $R_{Kr}$  of single scatter background events in the energy region 0 – 100 keV scales with the krypton level concentration  $A_{Kr}$  as follows:

$$R_{Kr} = 0.039 \times \left( \frac{A_{Kr}}{\text{ppt}} \right) \text{ mDRU} . \quad (4.10)$$

This implies a  $^{85}\text{Kr}$  background contribution of  $(0.74 \pm 0.16)$  mDRU in the 225 live days period. Subtracting both internal background levels of radon and krypton from the total one, there remains a discrepancy of

$$\Delta R = R_{Tot} - R_{Rn} - R_{Kr} = 3.1^{+0.7}_{-0.6} \text{ mDRU} , \quad (4.11)$$

with the error asymmetry caused by  $\Delta R_{Rn}$ . The remaining rate comes from the contribution of the external  $\gamma$  ray background from radio-impurities in the construction materials. All single detector components were screened for radioactivity before mounting into the cryostat [63] and the individual impurity concentrations of all detectable radionuclides fixed in the detector simulation. As a result, a total background from all outside materials (detector + shield) of 3.2 mDRU and 1.8 mDRU was derived in [81] for a 40 kg and 30 kg fiducial volume respectively. First order linear interpolation between the two volumes yields 2.4 mDRU for the considered 34 kg fiducial cut, which is in agreement within uncertainties to the rate discrepancy  $\Delta R$  calculated above (also mind that the simulation itself and the activity concentration of the various materials imply a non-negligible error not quoted in the final results of [81]).

This combined result remarks a noteworthy achievement in the characterization of the XENON100 background relevant for the dark matter search. With three major components, intrinsic radon (deter-

mined in the present work), krypton and external radiation, derived from actual measurements of the single detector pieces, the whole observed electromagnetic background in the relevant WIMP region of interest can be sufficiently described.

## 4.9 Summary of radon analysis

Radon has long been considered a minor threat when most attention was paid to the removal of  $^{85}\text{Kr}$  – the other major intrinsic source of radioactive contamination in noble liquid dark matter detectors. However, with advancing progress in the krypton purification using cryogenic distillation [91] radon has become the leading internal source of background in the low energy search window as just shown in the previous section. For the next generation of ton-scale target mass detectors which aim at a much more powerful reduction of the external background from  $\gamma$  radiation, the importance of internally dispersed contaminants will even gain because their contribution does not necessarily scale inversely with the fiducial mass. Even stronger measures must be taken against radon emanating from the innermost construction materials and components in the circulation/purification gas system (for example by carefully screening and selecting the individual detector components to obtain lowest possible concentration in primordial elements). In parallel, techniques for in-situ removal of the radon concentration have to be brought forward.

We have analyzed and presented various properties with the goal of better understanding the evolution of radon and its decay products. The results have impact on the current interpretation of data from the XENON100 detector and can help as a guideline during the construction of future LXe detectors.

We have shown for XENON100 that it is possible to distinguish different constituents of the radon/thoron decay chains by applying alpha-spectroscopic and time-coincidence methods. The correctness of the latter technique is finally proven by reconstructing the respective decay-time and  $\alpha$  energy spectra of  $^{212}\text{BiPo}/^{214}\text{BiPo}$ .

Using both methods, we were able to calculate charge and light yields for various  $\alpha$  decays and found consistency with earlier measurements done with small xenon sample detectors. Due to their dense interaction core  $\alpha$  decays are followed by a high recombination probability of ion-electron pairs which leads to an increased light yield of  $\sim 3.8$  PE/keV but diminished charge yield of  $\sim 1.2$   $e^-$ /keV (at 530 V/cm drift field) with respect to other types of radiation. This general effect was already mentioned in previous works, e.g. in [55, 36].

About the origin of radon we conclude that  $^{222}\text{Rn}$  emanates mainly from the inner detector materials and dissolves homogeneously in the liquid phase but can also enter the detector system through air leak diffusion as shown for both the period of high internal concentration and during the long-term measurements of 2011/2012. Unaffected by the latter phenomenon is the level of  $^{220}\text{Rn}$  because it will almost entirely disintegrate given its short half-life and does not reach the sensitive LXe volume. Yet, the  $^{212}\text{BiPo}$  tagging method does prove the abundance of products from the thoron chain, however no direct evidence for  $^{220}\text{Rn}/^{216}\text{Po}$  is seen in the  $\alpha$  spectrum. This allows for the interpretation of  $^{220}\text{Rn}$  solely emanating from the internal TPC or cryostat materials. Afterwards, it decays too fast to dilute into regions with sufficient  $S1_\alpha$  resolution ( $r < 145$  mm). The observed increase of unresolvable  $\alpha$  events near the TPC boundaries ( $145$  mm  $< r < 153$  mm) gives further support to this hypothesis.

It is further confirmed that homogeneous distribution of radon (daughters) is only provided for the pure  $\alpha$  emitters. From the reconstructed position distribution for BiPo events and comparison with zero drift field configuration there is evidence that ion drift of  $^{212/214}\text{Bi}^+$  is responsible for the accumulation at the electric field cathode. Present data favour single charged ion lifetimes of several minutes to explain the shift and are in agreement with earlier bounds achieved in much smaller dedicated LXe

chambers [87]. The eventual BiPo rate in the inner fiducial volume is thus significantly reduced resulting in a “self-cleaning” effect of the applied  $E$ -field and can also provide explanation for the complete absence of the long-lived  $^{210}\text{Pb}$  (and its decay products) in the observable TPC. The information is also important for the modeling of radon-induced background using Monte-Carlo-simulations. Any of their outcome scale with the measured activity concentration but using the number of BiPo events would adulterate the prediction. Instead one must rather insert the determined concentration of  $^{218}\text{Po}$  because it provides a closer estimate to the number of  $^{214}\text{Pb}$   $\beta$  decays relevant for the low energy background in the potential WIMP benchmark region.

Combining the obtained prediction of radon-induced event rate with independent measurements of the  $^{85}\text{Kr}$  contamination [64] and the simulated contribution of  $\gamma$  radiation [81] we have shown to be able to describe the background composition during the 225 live-days run. This provides indirect proof that no additional major source of background has been neglected in the latest dark matter search of XENON100.



# Light and Charge From Nuclear Recoils

Among the advantages of a two-phase detector is the power to distinguish between recoils off the nucleus and interactions with the atomic shell electrons of the target material. The former are mainly induced by uncharged, heavy particles like neutrons or potential WIMPs, the latter are mostly produced by background radiation. The ratio of produced charge carriers (electrons) and scintillation photons depends thus on the underlying scattering processes and allows for particle type identification, which is essential for the interpretation of dark matter searches.

In this chapter we aim at a complete reproduction of the detector signal response to  $^{241}\text{AmBe}$  neutron calibration<sup>1</sup>. This allows for a comparison between simulated and measured nuclear recoil distributions of the detection observables S1 and S2. By achieving very satisfactory agreement while inserting the independently determined neutron source strength we will finally provide proof of the consistency and robustness of the applied energy scale and estimated signal acceptance assumed and reported in previous WIMP searches of XENON100 [47, 42].

In order to achieve this goal, the charge yield for nuclear recoils and their light yield with respect to ordinary radiation – both a function of recoil energy – are of particular interest since they determine the above mentioned, characteristic response to heavy neutral particles which scatter elastically off xenon atoms. Equally important, they are necessary to construct the energy scale for nuclear recoils, and consequently, for any potential WIMP interaction.

We begin with an introductory presentation of how energy deposits translate into photons and electrons in liquid xenon. Afterwards we perform an indirect measurement of the charge yield function  $Q_y$  and relative scintillation efficiency  $\mathcal{L}_{eff}$ , using data from neutron calibration and comparing it to a Monte-Carlo simulation of the XENON100 detector. Having done so, we proceed with the analysis of the combined S1-S2 signature of nuclear recoils. Finally, we conclude by discussing implications on the response to potential WIMP signals.

## 5.1 Nuclear recoil energy scale

As straightforward as energy calibration appears for ionizing radiation (Sec. 2.4.3) as complicated it becomes for massive, neutral particles. The reason why complexity increases is mainly due to the fact that only a fraction of the total energy is expended into electronic excitation.

Starting from the initial process, an incoming neutral particle would first scatter elastically off a xenon nucleus, thereby transferring part of its kinetic energy. Next, the energy deposit is turned into kinetic motion of the recoiling atom, which itself can either scatter elastically or inelastically with neighbouring atoms. But only in case of inelastic scattering excitation or ionization of shell electrons it causes a detectable signal. The major amount of energy is spread into a cascade of elastic scatters. The resulting atomic motion is dispersed into heat and no more accessible for detection in a LXe-type experiment. It is important to note that the energy dissipation mediated by the recoiling atoms or

---

<sup>1</sup>Parts of the author's work presented in this chapter are submitted for a XENON100 journal publication, also available as electronic pre-print [92].

ions is entirely decoupled from the initial nuclear recoil. Consequently, the observed S1-S2 signature remains the same for all heavy neutral particles, i.e. regardless whether the original hit was induced by a neutron or potential WIMP.

The effect described has been known as *nuclear quenching* for many decades. First theoretical calculations of energy partition into electronic and atomic excitation for low-energetic atom collisions were presented by Lindhard [93, 94] and hold for a large variety of detector media. Large integral expressions over electronic and nuclear stopping power functions of cascading atomic tracks result effectively in one energy dependent quenching factor  $L$  that defines the fraction of energy deposited in electronic excitation.

More recent calculations by Hitachi [95, 96] introduce a further mechanism to explain why the light production could even be more reduced than predicted by Lindhard originally. The process is now known as *biexcitonic quenching* and includes the possibility that at high excitation densities (apparent in heavy ion tracks induced by nuclear recoils) in the collision of two xenon excimers only one scintillation photon is finally released.

At any rate, constructing an energy directly from this quenching factor is intricate since one would need to measure the absolute amount of photons  $N_{S1}$  and ionization electrons  $N_q$  formed in the interaction. To evade this problem an alternative way is to express the signal reduction via an effective quenching factor,  $\mathcal{L}_{eff}$ . Historically from single-phase detectors, this quantity was defined only considering the primary scintillation light S1. Neglecting for a moment any drift field dependency therein, the amount of S1 light per unit energy at a given nuclear recoil energy  $E_{nr}$  is compared to the amount created by a  $\gamma$  ray absorption at a fixed energy  $\hat{E}$ :

$$\mathcal{L}_{eff}(E_{nr}) = \frac{S1^{NR}(E_{nr})/E_{nr}}{S1^{ER}(\hat{E})/\hat{E}}. \quad (5.1)$$

The denominator is nothing but the light yield for electronic recoils,  $L_y = S1^{ER}(\hat{E})/\hat{E}$ , and can be determined experimentally. Commonly, one chooses the 122 keV  $\gamma$  line from  $^{57}\text{Co}$  as a reference. Note, that  $L_y$  depends specifically on the experimental setup and the efficiency to detect scintillation photons. So far  $\mathcal{L}_{eff}$  was introduced only at zero electric field. At finite field, the number of recombining electrons will be different though and therefore affect the amount of light produced in nuclear and electronic interactions in separate ways. To compensate for this, one introduces two correction factors,  $S_e$  and  $S_n$ , which shift the field dependency from zero to finite value for electronic and nuclear recoils, respectively. For the drift field of 0.53 kV/cm applied in the XENON100 experiment, one has measured  $S_e = 0.58$  [55] and  $S_n = 0.95$  [97] and the average light yield at 122 keV determined as  $L_y = (2.28 \pm 0.04)$  PE/keV for the 225 live days dark matter search reported in [42]. With the newly defined quantities we can write

$$\mathcal{L}_{eff}(E_{nr}) = \frac{S1^{NR}(E_{nr})}{L_y \cdot E_{nr}} \cdot \frac{S_e}{S_n}. \quad (5.2)$$

Various measurements to determine  $\mathcal{L}_{eff}$  as function of nuclear recoil energy have been carried out in the past. A direct determination, for example, can be achieved by scanning the S1 response to a range of neutron energies in a fixed target experiment. This requires a monochromatic neutron source and a setup capable of accurately measuring scattering angles. The advantage of these measurements is that they can be carried out externally, using a dedicated xenon chamber with high light yield. Recent direct measurements of  $\mathcal{L}_{eff}$  are shown in Fig. 5.1. Small scattering angles necessary for small  $E_{nr}$  and threshold effects pose a challenge and limit the current sensitivity down to  $\approx 3$  keV recoil energy [98, 99].

Once  $\mathcal{L}_{eff}$  is known, solving Eq. (5.2) for  $E_{nr}$  automatically provides an energy scale for nuclear recoils based on S1 in any LXe detector, characterized only by its average light yield  $L_y$ :

$$E_{nr} = \frac{S1}{\mathcal{L}_{eff}(E_{nr}) \cdot L_y} \cdot \frac{S_e}{S_n}. \quad (5.3)$$

Similar to Lindhard's idea of introducing a general suppression factor  $L$ ,  $\mathcal{L}_{eff}$  in Eq. 5.3 compensates for the fact that only a fraction of the nuclear recoil energy is turned into the accessible signal channel S1. One often writes  $E_{nr}$  in units of keVnr to indicate that the energy was not entirely measured but rather reconstructed from the S1 signal. The obvious advantage of  $\mathcal{L}_{eff}$  over  $L$  is that it defines a scale from the detectable S1 rather than the emitted number of photon in the LXe, which is difficult to infer and introduces further systematic uncertainty.

In the last few paragraphs we have only made use of S1 as an energy estimator. However, we don't want to neglect that we can as well relate the charge signal S2 to the recoil energy, even directly without need of any reference point. Therefore, one defines the charge yield  $Q_y$  for nuclear recoils as the number of escaping electrons  $N_q$  per unit of deposited energy  $E_{nr}$ ,

$$Q_y(E_{nr}) = \frac{N_q}{E_{nr}} = \frac{S2}{g_{S2} \cdot E_{nr}}. \quad (5.4)$$

Therein, we have made use of the relation in Eq. (2.12) to translate from the number of free electrons  $N_q$  (at drifttime  $dt = 0$ ) to the equivalent corrected S2 signal. The mean secondary amplification gain factor  $g_{S2}$  was measured to be  $(19.5 \pm 0.1)$  PE/e<sup>-</sup> with a  $1\sigma$  Gaussian single electron S2 width of  $\Delta g_{S2} = 6.7$  PE/e<sup>-</sup> in the XENON100 detector during the time period which is relevant for the later considered <sup>241</sup>AmBe neutron calibration in 2011 [60]. Besides the energy,  $Q_y$  depends also on the applied electrical field which affects the recombination rate and thus the number of escaping electrons. In [55] it was shown, however, that the variation appears only at the few percent level over a range of 0 – 5 kV/cm field strengths.

If  $Q_y$  was accurately known, solving Eq. (5.4) for  $E_{nr}$  would provide an energy scale with improved resolution due to the secondary amplification of the number of information carriers  $N_q$  via proportional scintillation:

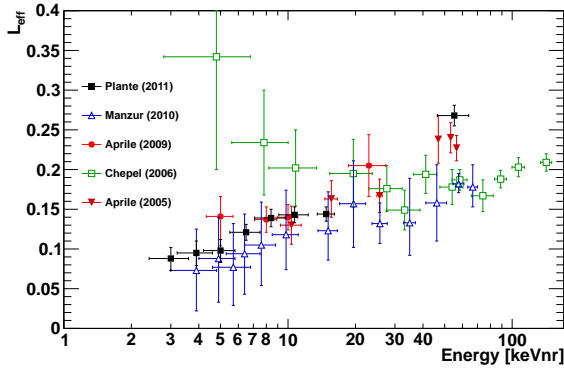
$$E_{nr} = \frac{S2}{g_{S2} \cdot Q_y(E_{nr})}. \quad (5.5)$$

Furthermore, the energy scale would be less prone to Poissonian fluctuations which govern the S1 signal at low recoil energies when only a few photo-electrons are detected.

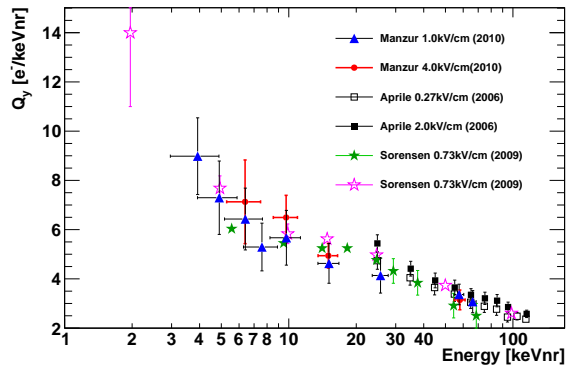
In principle,  $Q_y$  can be determined in the same way as  $\mathcal{L}_{eff}$  by measuring the charge yield for fixed recoil energies in a dedicated setup. In contrast to single phase detection chambers that can measure only S1, a two-phase TPC and the requirement of efficient electron drifting adds further complexity to those experiments. To date, only a few direct measurements of  $Q_y$  have been conducted and especially data at low recoil energies become very sparse.

Fig. 5.1 and 5.2 show a summary of available data for  $\mathcal{L}_{eff}$  and  $Q_y$ , respectively. The most recent measurements by Plante et al. [98] and Manzur et al. [99] have tremendously improved the accuracy down to very low recoil energies and agree in a moderately falling  $\mathcal{L}_{eff}$  as a function of decreasing energy.

On the contrary, only one direct measurement of  $Q_y$  down to very low recoil energies has been performed by Manzur et al. [99]. Their result features an increase of  $Q_y$  with decreasing recoil energy below  $\sim 10$  keVnr. As we will see in a final comparison at the end of this chapter (Fig. 5.38), this is somewhat in contradiction to the findings of indirect measurements presented later in this work and also conducted by the ZEPLIN-III and XENON10 experiments.



**Figure 5.1:** Relative scintillation yield  $\mathcal{L}_{eff}$  as a function of nuclear recoil energy determined by direct measurements. Symbols correspond to Plante et al. [98] (■); Manzur et al. [99] (▲); Aprile et al. [100] [97] (●, ▼) and Chepel [101] (□).



**Figure 5.2:** Charge yield function  $Q_y$  for nuclear recoils measured by direct and indirect methods at various electric fields. Data points taken from Manzur et al. [99] (●, ▲); Aprile et al. [55] (□, ■) and two separate approaches by Sorensen [102] (★).

## 5.2 Neutron calibration data

We have seen before that the signal quenching after nuclear scattering is entirely determined by the kinematics of the recoiling xenon atom and does not encode any information about the primarily incoming particle apart from being massive and uncharged. Therefore, we can expect that any potential WIMP interaction causes the same signal response as neutrons do, even if the WIMP mass and velocity distribution are far different. Consequently, neutron irradiation provides the ideal means of defining the nuclear recoil energy scale and particle discrimination as there is no better calibration source of neutral particles handily available.

### 5.2.1 Neutron source

For the purpose of neutron generation a broad-band  $^{241}\text{AmBe}$  source is inserted into the passive shield via the regular source pipe and positioned close to the inner LXe vessel. The source is encased in a cylindrical steel capsule of 17.6 mm length and 6.4 mm outer diameter. The kinetic energy spectrum of the neutrons released ranges from 0.5 – 12 MeV, peaked at around 4 MeV. This implies a roughly exponentially falling spectrum of energy deposits in LXe between  $\sim 0 - 250$  keV, depending on the kinetic energy and the scattering angle of the neutron. A lead brick between the source and the cryostat prevents the low-energetic  $\gamma$  rays of the  $^{241}\text{Am}$  decay from entering the xenon target.

The only information about the nominal  $^{241}\text{Am}$  source activity of  $(3.7 \pm 0.5)$  MBq was provided by the certificate of the manufacturing company *Eckert & Ziegler*. They refer to a commonly used conversion factor of  $2.2 \times 10^6$  neutrons per 37 GBq  $^{241}\text{Am}$  activity without further reference. This yield implies an integral neutron rate of  $(220 \pm 33)$  1/s for the neutron source deployed in XENON100.

In the progress of matching the Monte-Carlo generated neutron events to data it was always found a considerable excess of events in the simulation when imposing the above mentioned rate. We investigated intensely possible explanations for the obvious discrepancy and performed thereby many cross-checks of the existing data processing techniques and also of the neutron simulation itself. However, no obvious reasons for the disagreement could be identified. This finally led to the decision – initiated by the author of the present work – to have the neutron source strength measured directly

and independently in a dedicated detector setup at the Physikalisch-Technische Bundesanstalt (PTB), Braunschweig, in summer 2012. The source was placed inside a paraffin box at a defined distance from a Bonner sphere spectrometer [103] ( $^3\text{He}$ -filled proportional neutron counter) and its strength measured by comparison with a calibrated standard [104]. The neutron yield was determined to be  $(160 \pm 4) \text{ 1/s}$  [92, 104] – significantly different from the first estimate based on the  $^{214}\text{Am}$   $\gamma$  activity and, more importantly, solving the problem of rate excess. The author was further told that the apparent mismatch to the naive conversion is conceivable given that the quoted factor may depend on the actual source geometry and the manufacturing process [105]. Additional studies performed by the PTB measurement also confirmed that the neutrons are emitted isotropically from the source centre and thus no deviations from the actual positioning during the calibration runs in XENON100 are expected. We will use you this important result for fixing the absolute scale in upcoming data/simulation comparisons.

### 5.2.2 Data acquisition

Restricted by the rules of LNGS, neutron calibration is usually allowed once per year for a maximum live time of 3 days. Since 2009 three dedicated measurements have been carried out, only a few days before or after a new science run was started. In all cases, the electron drift field was set to common operation value of 0.53 kV/cm and the anode voltage at 4.5 kV (in 2010) and 4.4 kV (in 2011/2012). The 2011 and 2012 data were recorded with improved hardware trigger conditions (see Sec. 2.3) and allow for a lowered recoil energy threshold. In addition, the much improved electronegative impurity concentration in 2011 enabled the electron lifetime to be almost a factor of two better than in 2010. A significantly increased PMT dark count rate accidentally occurring during the 2012 neutron calibration makes a direct merging with the other data complicated. These arguments combined, and the fact that already one set of measurement provides enough statistics, explain why we always refer to the 2011 calibration run in all upcoming studies. The run contains 13 sequential datasets taken at standard detector conditions applying 4.4 kV anode voltage to achieve S2 amplification. The accumulative live time is 94555 s (26.3 h) after correcting for small dead-time loss due to the hardware trigger hold-off. The measurements themselves were not carried out by the author but regular shifters on site. Data is preprocessed, stored and made accessible in the same way as for dark matter runs.

### 5.2.3 Event selection

Since neutron recoils share the same properties with those of potential WIMPs it is no surprise that most of the selection criteria applied for dark matter searches, as introduced in chapter 2.4, were tailored for and tested on neutron calibration data. In this chapter we cannot only profit from these well-established data cuts but even turn the argument by proving consistency of their calculated acceptance loss when aiming at the reproduction of the absolute neutron event rate. For completeness, we briefly state the event criteria in the following paragraphs but refer to chapter 2.4 for detailed description of the individual cuts.

The quality cuts based on the single largest S1 width and pulse-shape entropy information are applied although their effect on only a few hours of measuring time is negligible since they were originally designed to remove only a few events out of tens of days of continuous detector operation. Furthermore, events have to pass the developed noise suppression filters which help to remove events triggered by electronic artifacts, large baseline fluctuations and single PMT dark current. The

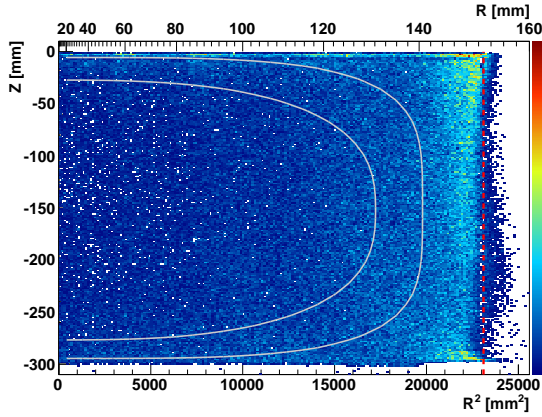


**Figure 5.3:** Spatial density distribution of single-fold scattering neutrons. The light and dark gray lines confine a 48 kg (Run 8) and 34 kg (Run 10) fiducial volume, respectively. The vertical red dashed line marks the radial border of the TPC.

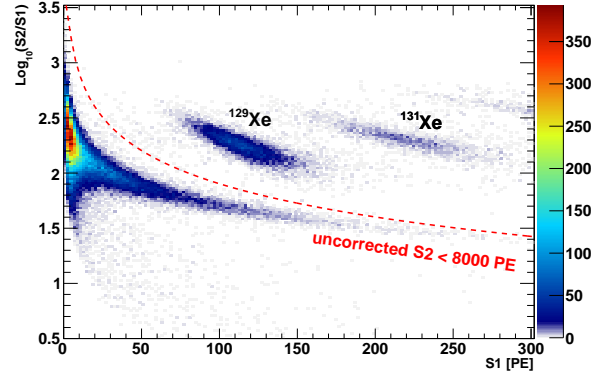


**Figure 5.4:** Nuclear recoil band and activated xenon lines. Separation of elastic neutron recoils from inelastic scatters with a simple cut on uncorrected  $S2 < 8000$  PE (indicated by the red dashed line).

amount of the latter is specifically reduced by placing the two-fold S1 coincidence condition.

An S2 threshold cut of 150 PE is applied to guarantee  $> 99\%$  hardware-trigger probability. Moreover, the width of the S2 signal shape must satisfy the energy and drift-time dependent criterion to discard events in the gaseous xenon.

Only one single S1 peak (above 0.35 PE noise threshold per contributing PMT) can be allowed in the waveform to represent a clean sample and exclude pile-up events or delayed signals from prompt de-excitation after inelastic neutron scattering.

This requirement must not be mixed up with the further condition of applying the single scatter cut by defining an upper threshold on the second largest S2. In fact, the selection of single site events is crucial for the following analysis of nuclear recoils since in multiple interactions the S1 would consist of the sum over all prompt scintillation signals sent from different scatter positions. Consequently, this would render any deconvolution of the individual contributions impossible and distort the calculation of  $\mathcal{L}_{eff}$  as a quantity defined per single recoil.

By applying a fiducial volume cut we further restrict the analysis to the inner part of the TPC. The motivation is two-fold: Firstly, we constrain all further analysis to a part of the detector where any type of edge effects such as incomplete charge collection, strong light yield variations and imperfect position reconstruction can be excluded. Secondly, we can connect the outcome of our analysis immediately to the most recent 225 live days WIMP search in which – due to optimization of the dark matter discovery potential – an inner 34 kg super-elliptical volume was chosen. Even with this conservative choice (if it was for the first argument only, the volume could easily be extended to 48 kg) the remaining statistics of neutron events is large enough for all later purpose, as the neutron penetration in LXe is much less suppressed compared to  $\gamma$  rays. This feature is highlighted in Fig. 5.3. Grey border lines indicate the boundaries of a 48 kg (light) and 34 kg (dark) volume on top of all available single-site neutron events recorded inside the TPC.

Finally, we want to restrict our studies to elastic neutron scatters. In case of inelastic interactions, a fraction of the kinetic neutron energy deposition is transferred into nuclear excitation of the xenon. The energy is released by characteristic  $\gamma$  emission in the few tens to hundreds of keV range, depending on the particular excitation isotope. Making use of the increased charge yield and low escape probability of these ejected  $\gamma$  rays, we can identify such events easily by their size of the S2 as pre-

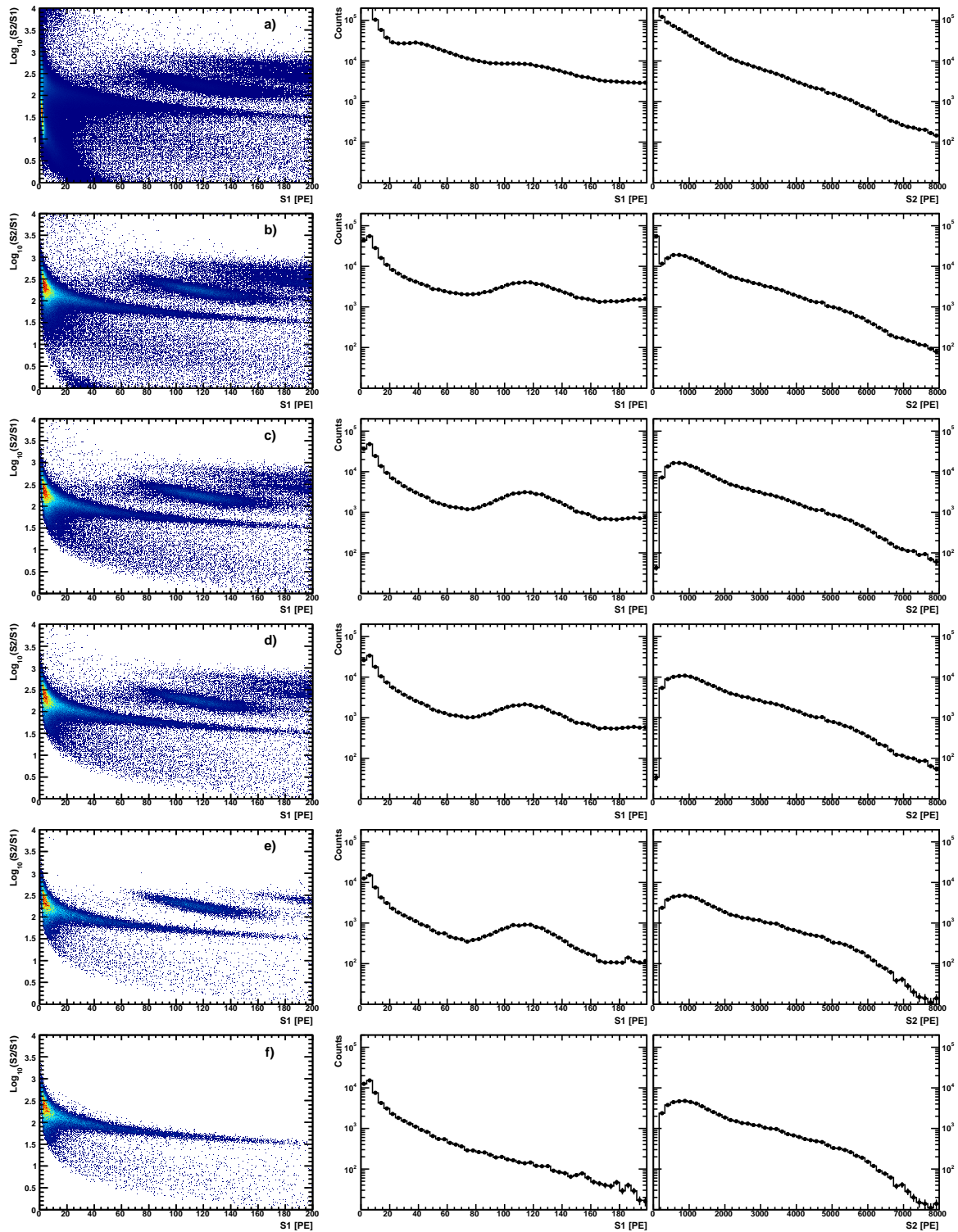


**Figure 5.5:** Different stages of nuclear recoil event selection presented in discrimination space,  $S1$  and  $S2$  (columns 1–3, respectively). From top to bottom the following criteria are applied in successive order: (a) no cuts; (b) noise suppression and waveform quality; (c)  $S1$  coincidence,  $S2$  threshold,  $S2$  width and single  $S1$  peak requirements; (d) single scatter selection; (e) 34kg fiducial volume cut (as shown in Fig. 5.3); (f) after selecting only elastic neutron scatters

sented in Fig. 5.4. The inelastic  $\gamma$  lines arising from  $^{129}\text{Xe}$  and  $^{131}\text{Xe}$  can be removed from the recoil sample by asking for the uncorrected S2 to be smaller than 8000 PE, indicated by the red dashed separation line.

In Fig. 5.5 we summarize the various stages of nuclear recoil event selection as done for the neutron calibration data. Starting with no cuts at all (a) we show the impact on the event sample after successively applying the discussed event quality criteria (b – e). In the final stage we are left with a pure sample of nuclear recoil interactions that will provide the data basis for later comparison with simulated spectra.

## 5.3 Monte-Carlo simulation of neutron calibration

Having prepared a clean sample of neutron calibration data we aim now at a complete simulation of the observed S1 and S2 signal distribution in the XENON100 detector by means of Monte-Carlo techniques. Our approach is split into two parts: Firstly, we collect datasets of simulated neutron events, generated by the particle simulation framework GEANT4 [65, 66] and provided to collaboration members [62]. The output of the GEANT4 simulations contains information about the spatial position, type of interaction and energy deposit for every single step of a particular neutron track and secondary particles, such as  $\gamma$  rays from inelastic scattering. It does *not* provide any information about the physical observables S1 and S2, which are needed to perform a comparison with measured data. To calculate those by taking into account the processes of signal generation and entire detector response to nuclear recoils is subject of the second part of the simulation, which is the author's own contribution. The second step is technically decoupled from the GEANT4 processing to minimize computational time and simplify embedding into fitting algorithms as later used to determine  $Q_y$  and  $\mathcal{L}_{eff}$ . We continue with providing more details on both, GEANT4 and custom-made parts, of the Monte-Carlo signal simulation.

### 5.3.1 Neutron track simulation with GEANT4

The XENON100 collaboration has adapted the simulation toolkit GEANT4<sup>2</sup> to the real detector setup and shield geometry as well as the specific requirements of low energy physics processes, as presented in the study of the electronic recoil background in [81]. For further reading, a complete description of the model, containing a summary of all used materials, is given in [62].

The cutaway model in Fig. 5.6, adopted from [81], provides a short summary of the design implementation. Beginning with the external shields, layers of lead, polyethylene (acting as outer neutron shield) and copper surround the cryostat and parts of the electronic cable feedtroughs as well as the gas inlet/outlet pipes. The inner detector is modelled with even greater detail, containing for example every single PMT, the PTFE panels and field shaping rings enclosing the TPC, electric meshes, liquid/gaseous xenon volumes and the external calibration source pipe, by which the neutron source is fed into the radiation shield. Its eventual location (label (5) in Fig. 5.6) is surrounded by a lead brick next to the cryostat vessel, approximately at the center of the TPC vertical dimension. The lead brick is needed to protect the detector from the  $\gamma$  activity of the  $^{241}\text{AmBe}$  source during calibration but hardly presents any barrier for the neutron flux.

Starting at the source position, neutrons are generated and sent isotropically in every direction. Their initial kinetic energy distribution is drawn from the ISO 8529-1 (2001) [106] differential emis-

---

<sup>2</sup>Version 4.9.3p02 is used for the present study

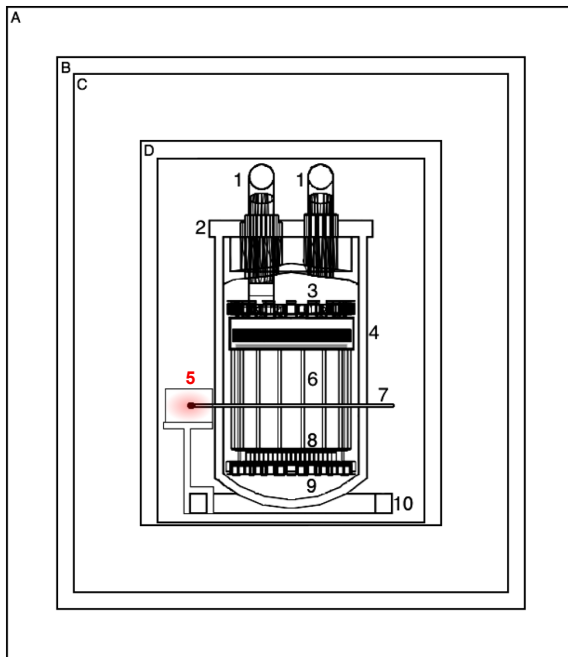


**Figure 5.6:** GEANT4 implementation of the XENON100 detector and shield geometry, courtesy of the XENON collaboration [81]: A - outer lead layer, B - inner lead layer, C - polyethylene shield, D - copper shield; 1 - pipes to the PMT feedtroughs and pumping ports, 2 - stainless steel cryostat, 3 - top PMT arrays in TPC and veto, 4 - top PMT array in the TPC gas phase, 5 -  $^{241}\text{AmBe}$  neutron source position surrounded by lead brick, 6 - TPC wall (PTFE panels), 7 - copper pipe for calibration wire, 8 - bottom PMT array in the TPC, 9 - bottom PMT array in the veto, 10 - support bars for the cryostat.

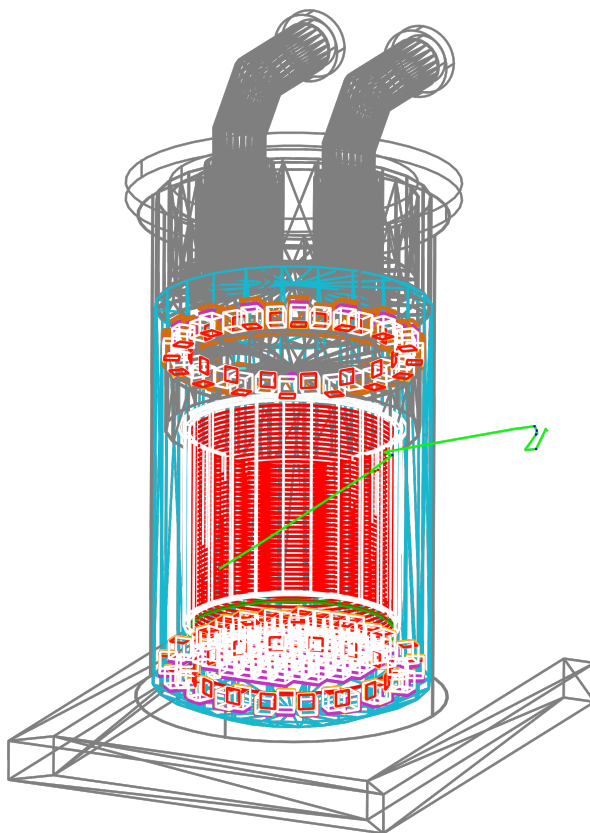


**Figure 5.7:** Simulated neutron track from  $^{241}\text{AmBe}$  source position to the LXe target. Only selected layers in the innermost part of the GEANT4 model are drawn for simplicity. Every neutron hit along the track inside the active volume are recorded and stored to disk for subsequent processing.

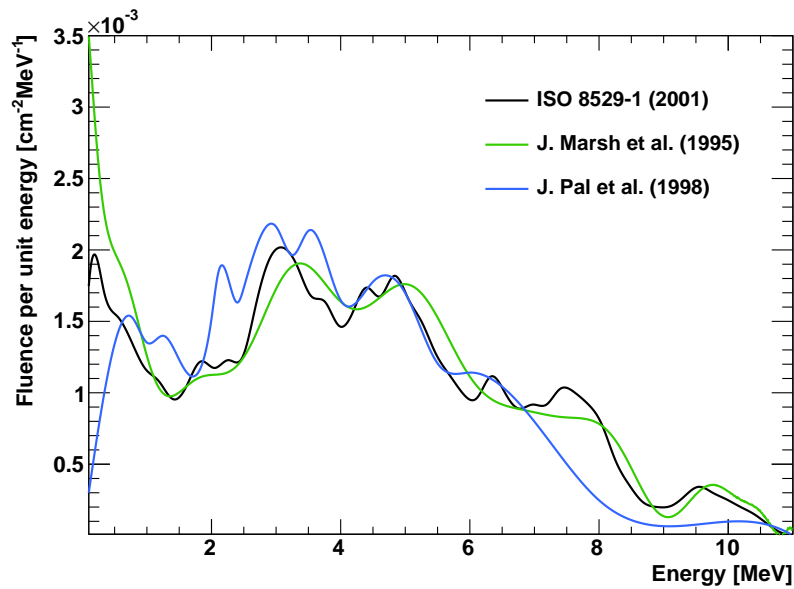


**Figure 5.8:** Comparison of  $^{241}\text{AmBe}$  neutron emission spectra as a function of kinetic neutron energy measured by Marsh et al. (green), Pal et al. (blue) and presented in ISO 8529-1 (2001) [106] (black). We tested all choices as input to the GEANT4 neutron simulation and checked their impact on the registered recoil energy inside the active detector volume.

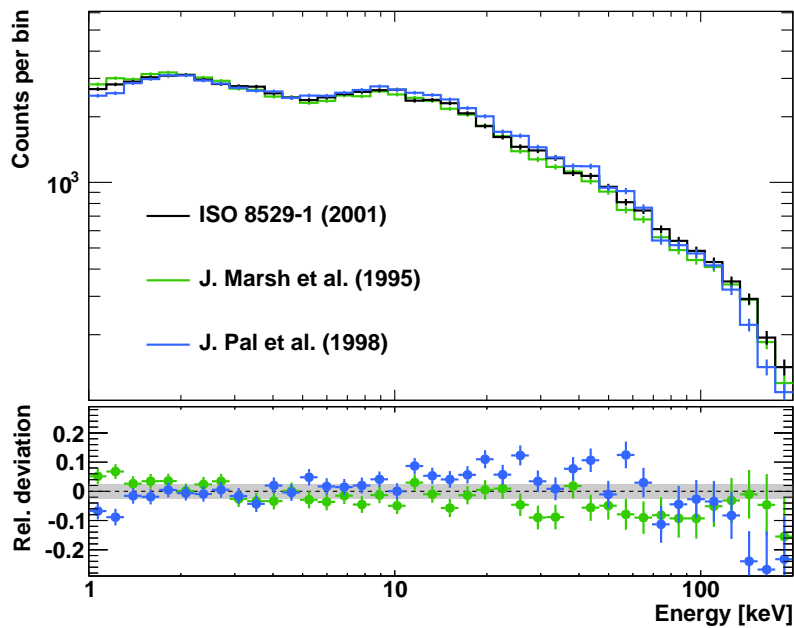


**Figure 5.9:** Simulated nuclear recoil energy deposition for single scatter neutron events inside the active LXe detector volume, comparing different  $^{241}\text{AmBe}$  input spectra to the simulation, as selected from Fig. 5.8. Relative deviations with respect to using ISO 8529-1 in the bottom plot are found to be on  $< 5\%$  percent level on average and do not exceed much the 2.5% systematic uncertainty of the source strength (light gray band).

sion spectrum of  $^{241}\text{AmBe}$ . We note that there are some alternative data available and remark that precise measurements are complicated to achieve since it requires a profound knowledge of the threshold and energy-dependent efficiency of the spectrometer. However, in a dedicated comparison of using different available input spectra to generate the initial neutron energy distribution (Fig. 5.8) we find relative deviations  $< 5\%$  on average among the resulting simulated nuclear recoil spectra in the relevant recoil energy region between  $\sim 1 - 200$  keV (Fig. 5.9). The somewhat increasing deficit towards large recoil energies can possibly be explained by the earlier cut-off in the spectral data from Pal et al. compared to the other measurements by Marsh et al. and provided in ISO 8529-1 (see Fig. 5.8).

After initialization, any neutron is iterated stepwise from the source until it eventually stays at rest (i.e. its kinetic energy drops below  $O(0.1$  keV) or escapes the world volume). In Fig. 5.7 we display a single neutron track (green path) as it penetrates the inner part of the detector model. In any step, the probability for a neutron to undergo an elastic or inelastic reaction is internally calculated using the ENDF/B-VI/VII library [107], which contains up-to-date cross-section tables for all xenon isotopes and all other used materials. Interactions happening along the track are called *hits* and store information about type, spatial position and change in energy/momentum of the particle. The collection of all hits is named *event* and saved in the final output tree. If secondary particles (e.g.  $\gamma$  rays from excited xenon nuclei) are created, they are put on an internal *stack* and are likewise simulated until they become absorbed or fall below some relevant threshold. After the simulation of a given number of neutrons, the outcoming events are subject to further processing. In particular, energy deposits less than  $10\ \mu\text{m}$  apart from each other are summed up and hits within one event are ordered according to their  $z$  coordinate. Furthermore, energy depositions are sorted according to whether they arise from electronic or nuclear recoils. This information will become necessary in the second part of the signal response simulation. To minimize the statistical error of the final output,  $2 \times 10^7$  emitted neutrons are tracked by the GEANT4 part and passed to the next simulation stage to compute S1 and S2.

### 5.3.2 Simulation of observable S1 and S2

So far we have only taken an intermediate step in order to compare simulated neutron events to actual data because the outcome of the GEANT4 delivers only the absolute energy transfer (given in units of keV) from neutrons to recoiling xenon nuclei. Yet, what is missing is a model of how this energy converts into the experimental observables S1 and S2 and how to take detection resolution and acceptances correctly into account. Eventually, we aim at producing a simulation output which resembles the one from real data processing as close as possible.

A simplified flow chart in Fig. 5.10 displays the concept of signal convolution and implementation of detector response. Starting from the output tree of the preceding GEANT4 simulation of neutron tracks, the program iterates all events successively, as there is no physical interference between any two neutron tracks. As mentioned earlier, each event consists of a collection of hits which contain all relevant information about the energy transfer and interaction position.

Already the first step of the algorithm contains the core functions of the entire conversion process. Given the energy deposit  $E_{nr}$  for an elastic nuclear recoil we can calculate the expected average number of S1 photoelectrons by means of Eq. (5.3). The obtained S1 represents the corrected signal in data after applying the spatial correction map  $\mathcal{M}_{\text{S1}}(x, y, z)$  (refer to Sec. 2.1.4). However, since the fluctuation of this quantity is determined by the number of actually observed photoelectrons, we explicitly compute the uncorrected value by multiplying the inverse map  $\mathcal{M}_{\text{S1}}^{-1}$  with the simulated signal and call it ucS1.

In order to estimate the statistical spread of ucS1 we assume a Poisson distribution, using the pa-



parameterization given in Eq. (2.8). Afterwards, the obtained integer number is smeared by the average measured single photo-electron resolution of the PMTs according to Eq. (2.9). Since in data all the S1 light is recorded within one S1 peak only, we add up all individual S1 contributions from all present hits.

Parameter Name	Symbol	Used in Eq.	Unit	Value
Average S1 light yield at 122 keV $\gamma$ -line	$L_y$	(5.3)	PE/keV	2.28
Average single PE PMT resolution	$\Delta_{PMT}$	(2.9)	PE/PE	0.5
Electric field suppression for ER	$S_e$	(5.3)	1	0.58
Electric field suppression for NR	$S_n$	(5.3)	1	0.95
Single $e^-$ gas amplification	$g_{S2}$	(5.4, 2.13)	PE/ $e^-$	19.5
Gaussian spread of $e^-$ amp.	$\Delta g_{S2}$	(2.13)	PE/ $e^-$	6.7
Electron lifetime	$\tau$	(2.10)	$\mu s$	356
Measured $^{241}\text{Am}$ neutron source strength	$R$		$s^{-1}$	160
Accumulated $^{241}\text{Am}$ live time	$T$		h	26.3

**Table 5.1:** Collection of fixed input parameters in the S1/S2 signal simulation. All quantities, except  $S_e$ ,  $S_n$  and  $R$ , are directly measured with the XENON100 detector. Related errors are considered sub-dominant for the purpose of signal generation by the simulation compared to uncertainties in  $\mathcal{L}_{eff}$  and  $Q_y$ .

For modeling the S2 signal, the number of produced escape electrons  $N_q = Q_y(E_{nr})E_{nr}$  is calculated first by using the definition of the  $Q_y$  charge yield function. Statistical fluctuations of this quantity are governed by recombination processes. Studies on the decomposition of the nuclear recoil band width in the work of [53] suggest that the spread in the recombination probability  $r$  is nearly consistent with a binomial distribution. Lacking explicit information in our approach about  $r$  as a function of recoil energy, we approximate the fluctuation by assuming an only one-parametric Poissonian probability function, evaluated for mean  $N_q$ . In the succeeding step we apply the electron-lifetime suppression of drifting electrons (Eq. 2.10) before modeling the secondary amplification in the gaseous phase with a Gaussian smearing (Eq. 2.13). In this way, we produce mean and spread of an uncorrected S2 signal, which we call ucS2. A summary of all numerical quantities provided to the simulation and kept fixed in the calculation of S1 and S2 as described above is listed in Table 5.1.

In the continuing step we model the detector capability of distinguishing two nearby recoil locations along the drift axis  $z$  needed for the identification of multiply scattering events. The separation of two adjacent S2 peaks by the data processor depends on the width and distance in drift time of the two individual Gaussian S2 waveforms, as shown for actual neutron data in Fig. 5.11. In this plot we apply only minimal bias selection rules and allow deliberately for multiple neutron scatters. Going towards larger drift lengths (lower  $z$ ) we discover that the roll-off position from a constant plateau in the minimally resolvable distance between two neighbouring S2 peaks slightly increases. In case of perfect resolution one would expect a uniform behavior of that threshold down to zero peak separation distance. The observed effect can instead be explained by the overlap of two neighbouring S2 peaks, which appear as one below some distance threshold. Note that this distance threshold is consistent on average with the reported  $\sim 3$  mm resolution in  $z$  direction of the XENON100 detector [33]. The shift of the roll-off position as a function of  $z$  is caused by the rising S2 peak width as the electron clouds dilute along their way to the surface. In fact, when relating the absolute distance to the average S2 signal width of the neighbouring peaks the dependency disappears and we find a uniform roll-off position at  $\sim 2 \times \text{FWHM}$  of the individual S2 shapes (Fig. 5.12). In our simulation we mimic

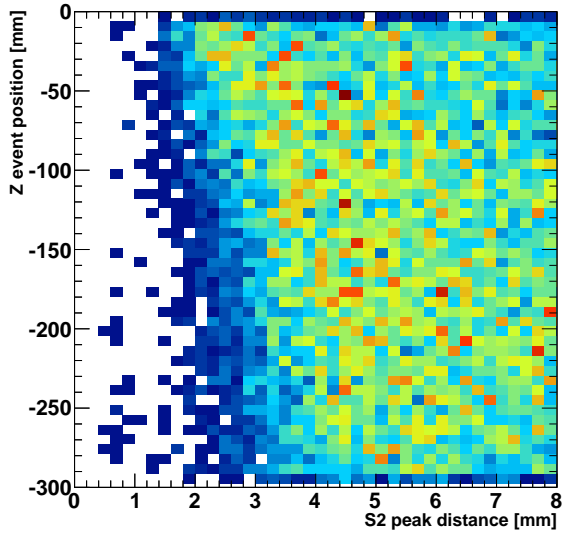


**Figure 5.11:** Distance of neighbouring S2 peaks along the drift axis  $z$ . The roll-off distance increases as a function of interaction depth due to enlarging of S2 peak widths.

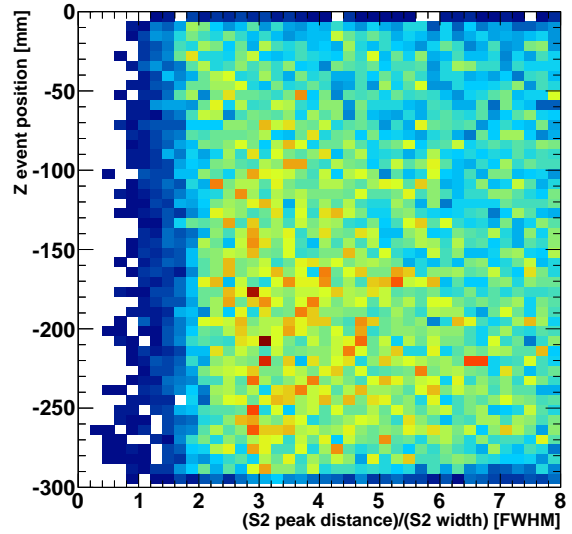


**Figure 5.12:** S2 Peak distance normalized to their measured S2 width. A constant roll-off at  $\approx 2 \times FWHM$  is found along the  $Z$  axis.

the detector peak resolution power, using an existing parametrization of the S2 width as a function of drift length, as determined in the context of data quality cut development (Sec. 2.4). Hits are collected into hit clusters containing all simulated neutron scatters that cannot be resolved because their distance is smaller than twice their FWHM (3 mm on average). For a given cluster the single hit ucS2 contributions are summed and an updated, central scatter position is calculated. Like in the real experiment the individual hit clusters are subsequently ordered by their ucS2 size.

Having accumulated only uncorrected values it is necessary to apply the same spatial-dependent corrections to the total ucS1 and individual ucS2 signals as done in data. With the updated position information this is performed by applying  $M_{S1}(x, y, z)$ , defined in Sec. 2.1.4, and considering the exponential electron lifetime correction according to Eq. (2.17), respectively.

Eventually we must account for the detection acceptance loss induced by those data selection criteria which we do not reproduce in the simulation. This concerns all listed data quality conditions except the S2 threshold, single scatter and fiducial volume requirements, which are already defined on available information in the simulation. To account for the remaining cuts, we rely on the already existing acceptance calculations presented in the context of the 225 live days dark matter search [42]. From the overall acceptance function we remove the contributions from those few quality conditions which are either not applied in neutron data or directly modelled by the calibration simulation itself. Those few changes only cause a slight deviation from the published curve. The remaining acceptance as a function of S1 is plotted in Fig. 5.13. Starting at roughly 90 % from high S1 values the acceptance decreases only moderately until dropping considerably faster below  $\sim 8$  PE. At this point detector threshold effects, like the two-fold S1 coincidence or the S2 threshold, start becoming dominant. Below 1 PE the function becomes essentially zero.

Practically, we use the random generator class TRandom3, part of the ROOT data analysis toolkit [65, 66], to draw floating numbers uniform in  $[0, 1]$  and approve a given event if the random value is smaller than the acceptance function evaluated at the generated S1. Only in that case the event – including all converted signal and original energy deposit information – is directed to the final output tree, other-

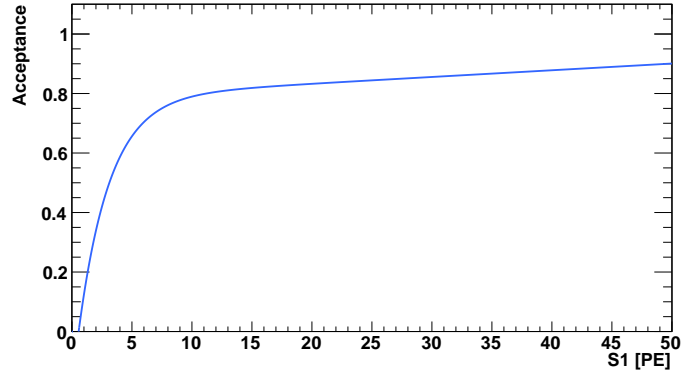


**Figure 5.13:** Nuclear recoil cut acceptance as function of S1. All individual contributions from the event selection criteria applied to the latest dark matter search [42] (except S2 threshold, single scatter and event discrimination) are combined in the blue curve.

wise discarded. The format of the output tree thereby resembles the structure of the real data trees.

Finally, at the end of this section we want to make a brief detour. As pointed out in the preceding paragraphs the present method does not treat the production of scintillation photons and ionization charge from first principles, but rather makes use of the effective conversion from recoil energy by means of the energy-dependent functions  $\mathcal{L}_{eff}$  and  $Q_y$ . The main advantage of this effective approach is that its implications can be tested against available data from direct measurements without need of theoretical model assumptions, such as it is the case for calculating the nuclear recoil quenching via Lindhard's function  $L$  [94].

Nevertheless we want to mention the alternative approach, as recently brought forward by the authors of the GEANT4 based toolkit NEST (Noble Element Simulation Technique). It relies on direct computation of the number of excitons and escaping electrons after applying Lindhard's theory of nuclear recoil quenching to account for the fact that only part of the total energy release is turned into accessible signals. As pointed out in [108] and references therein, the suppression of energy transfer can be described by the formula

$$E_{nr}L(E_{nr}) = (N_{ex} + N_i)W, \quad (5.6)$$

where  $E_{nr}$  denotes the recoil energy,  $L$  the energy dependent, effective Lindhard factor and  $W$  the average energy to produce either one exciton ( $N_{ex}$ ) or one ionization electron ( $N_i$ ). While the value of the effective work function  $W$  could be determined experimentally [53], theoretic parameter assumptions enter the characterization of both, the shape of the Lindhard function  $L$  and the ratio of  $N_{ex}/N_i$ , with the latter resulting as a property of the interacting particle type and track geometry. Since simultaneous measurements of light and charge response to known nuclear recoil energies have not yet been achieved, there is no directly measured data of  $L$  available to compare with the theoretical prediction.

## 5.4 Fitting simulation to data

Using the introduced model, we are now capable of performing a comparison to the measured detector response of nuclear recoils. Thereby we have to make the important choice of which parameterization of the conversion functions  $Q_y$  and  $\mathcal{L}_{eff}$  we want to use in order to generate S1 and S2 signals.

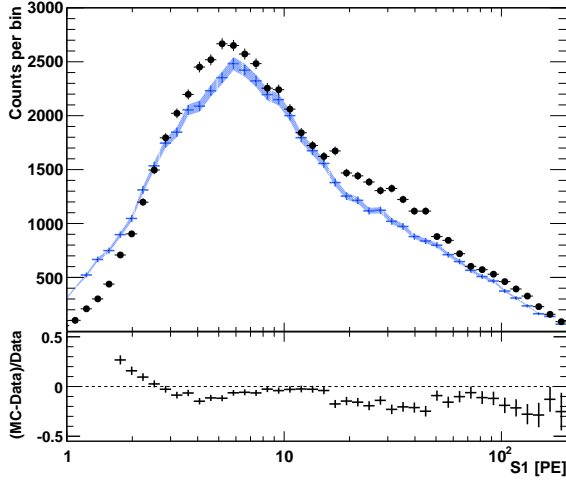


**Figure 5.14:** Data/MC comparison of the S1 spectrum using the global fit  $\mathcal{L}_{eff}$  from [47]. Spectral disagreement between MC (blue points with shaded uncertainty area from the source strength) and data (black points) is most obvious in the range of lowest and central S1.

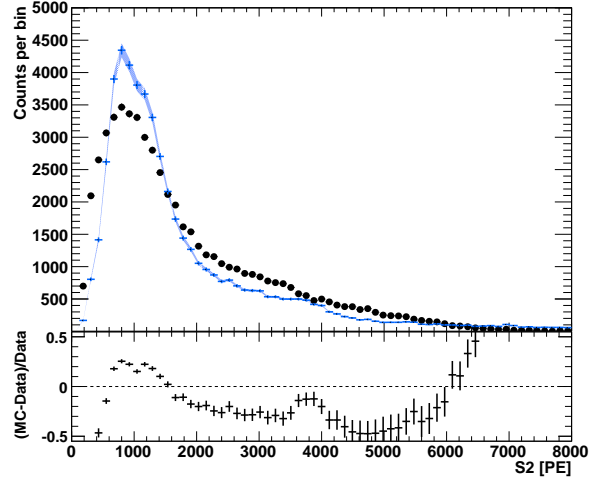


**Figure 5.15:** Data/MC comparison of the S2 spectrum using an interpolation of Manzur  $Q_y$  data points from [99] measured at 1 kV/cm drift field strength. Obvious spectral mismatch throughout the entire S2 range is found.

Naively, we rely on already measured values and begin our analysis using the global weighted best fit through all available  $\mathcal{L}_{eff}$  data points as first presented in [47] (plotted in Fig. 5.18) and  $Q_y$  determined in [99] for an electrical drift field of 1.0 kV/cm and depicted in Fig. 5.2. Like in all following analyses we apply equivalent selection criteria to simulation and data, in particular 34 kg fiducial volume, single scatter requirement and S2 threshold  $> 150$  PE. Note that especially for the single scatter cut we apply the same definition as found appropriate in data (see chapter 2.4), i.e. we ask for the second largest S2 peak to be smaller than  $\sim 70$  PE. To account for the acceptance loss due to the remaining cuts we apply the S1 dependent acceptance function as shown in 5.13. We always print MC generated spectra in blue data points and indicate the systematic uncertainty on the absolute source yield with a blue shaded band. Real neutron data is displayed in black points, carrying the statistical error of event number per bin. Fixing the number of simulated neutrons to  $2 \times 10^7$  and knowing the  $^{241}\text{AmBe}$  source strength to be  $(160 \pm 4)$  n/s we scale all MC spectra such that they match the measured live time of presented neutron calibration.

As one can extract from Fig. 5.14 and 5.15 the level of agreement is not yet satisfying – especially for the S2 – when using the aforementioned  $\mathcal{L}_{eff}$  and  $Q_y$  input. Local discrepancies in the spectral shape reach 20% or even more, depending on the recoil energy. As these appear in both signal channels over a wide energy range, they cannot only be caused by a simple mistake in one of the global parameters, like for example the S2 gain factor  $g_{S2}$  or the average S1 light yield  $L_y$ . Hence we conclude that the remaining mismatch must be due to a non optimal choice of  $\mathcal{L}_{eff}$  and  $Q_y$  as they are both functions of recoil energy and therefore affect the differential shape of S1 and S2.

Given that  $\mathcal{L}_{eff}$  has recently been measured with greater accuracy down to very low recoil energies than  $Q_y$  (refer to Fig. 5.1, 5.2 and references therein) we propose the following approach to improve the spectral matching between MC and data, and – at the same time – obtain an indirect measurement of both quantities as a function of recoil energy:

Firstly, we embed our presented simulation into a  $\chi^2$ -fit of the generated S2 spectrum to data and allow  $Q_y$  to vary as a free input parameter until the best matching is established. Thereby, we hold the global fit  $\mathcal{L}_{eff}$  representation of [47] fixed during the fitting process but keep track of how different

parameterizations affect the outcome on  $Q_y$  in a detailed study of systematic uncertainties. In the same way, we take further potential sources of error from the choice of the S1 acceptance function into account. Secondly – having gained a decent description of the S2 – we can use the result to inversely fit the S1 spectrum by varying  $\mathcal{L}_{eff}$  in the same way as  $Q_y$  before to also reach optimal matching of the S1. In the end, we can combine our improved understanding to compute the agreement in the 2-D discrimination space and gain important insight about the matching of inter-correlation of both functions.

### 5.4.1 Fitting S2 and determining $Q_y$

In this first step we want to investigate which choice of  $Q_y$  enables optimal matching of the simulated S2 spectrum to data and study the error bounds on the obtained function by varying otherwise fixed parameters in a reasonable manner. The problem can be formulated and solved by the well-known technique of  $\chi^2$  minimization. Given a set of  $n$  discrete data points  $(x_i, y_i)$ ,  $i \in \{1, \dots, n\}$ , and a physics model  $f(x; p_1, \dots, p_m)$  described by  $m$  parameters  $\mathbf{p} = (p_1, \dots, p_m)$  the general goal is to find a local minimizer  $\mathbf{p}^{min}$  of the quadratic sum

$$\mathcal{S}(\mathbf{p}) = \sum_{i=1}^n (y_i - f(x_i; \mathbf{p}))^2. \quad (5.7)$$

In our context  $y_i$  and  $f(x_i; \mathbf{p})$  translate into the measured and simulated S2 spectrum, respectively, both of which divided into  $n$  bins. The model outcome  $f(x_i; \mathbf{p})$  is numerically computed using the entire signal generation algorithm introduced in section 5.3.2. Out of all parameters  $\mathbf{p}$  which enter the model building of S2,  $Q_y$  has naturally the largest impact and will therefore represent the subset of free parameters to be varied in the fitting process, while other, much weaker determinants, like  $\mathcal{L}_{eff}$  or  $g_{S2}$ , remain fixed.

Since there is no analytical parameterization of  $Q_y$  as a function of recoil energy it would theoretically imply an infinite number of parameters  $\mathbf{p}$  to enter in the numerical optimization of (5.7), which would render the method impossible to handle. We therefore follow a technique that was previously applied in similar studies by [102, 109], which use a spline interpolation of  $Q_y$  between only few pivot points, thereby drastically reducing the degrees of freedom to the number of nodes. The spline puts constraints on the continuity and differentiability at the pivot positions but, apart from this, allows for the pivot values to float independently. In our case we apply a modification of the well-known cubic spline construction: the so called *Akima* spline interpolation [110]. It provides better stability towards the outlying points and significantly reduces oscillatory behaviour in between neighbouring nodes, as sometimes caused by the standard third order polynomial technique.

An open source C++ realization of the Levenberg-Marquardt (LM) algorithm, provided by [111], is used in the technical implementation of the fit routine. The LM algorithm has become a standard method of solving non-linear least-square problems and combines the advantages of the well-known steepest descent and Gauss-Newton approach [111]. Starting from an initial set of parameters  $\mathbf{p}^{init}$ , at any step  $j$  the algorithm computes a descent direction  $\Delta \mathbf{p}^j$  and step width  $h$  such that  $\mathcal{S}$  will decrease at the updated position:

$$\mathcal{S}(\mathbf{p}^j + h \Delta \mathbf{p}^j) < \mathcal{S}(\mathbf{p}^j). \quad (5.8)$$

Note that for any intermediate step  $j$  we call the entire signal conversion for  $O(10^7)$  emitted neutrons, evaluated at the current parameter choice  $\mathbf{p}^j$ , in order to provide enough statistics to updated calculation of  $\mathcal{S}$ . This task would not be feasible in reasonable computation time without having decoupled

the GEANT4 part of the simulation from the S1/S2 generation.

The iteration terminates when either  $\chi^2$  or the vector norm  $\|h \Delta \mathbf{p}\|$  has fallen below some critical threshold. The latter case particularly means that a local – not necessarily global – minimum in  $\mathbf{p}$  was found and represents the most frequent termination condition in our application, which is not surprising given the large dimensional parameter space covered. We will later check that our result is robust against variations of the initial parameter choice  $\mathbf{p}^{init}$  and hence make sure that within a reasonably large part of the parameter space the local minimum is absolute.

We implement the  $Q_y$  interpolation with 8 spline points at 0.5, 3, 8, 15, 25, 40, 100 and 250 keVnr, providing a higher pivot density at lower energies where by far the majority of neutron recoil energies is expected (refer to spectrum in Fig. 5.9) and direct measurements show broader uncertainties than at high energies (see Fig. 5.2). We further assume a constant value of  $3.5 \text{ e}^-/\text{keVnr}$  as the initial condition set for any of the spline values  $p_1, \dots, p_m$ . We point out that the lowest spline point at 0.5 keVnr is chosen below the obvious detection threshold but is motivated by the need of providing an unbiased way to extrapolate down to practically zero recoil energy. By this, we prevent any hard cut on the simulated energy scale in keVnr. However, the point is not meant to be of equal importance as the other pivots and – as we will prove later – has negligible impact on the outgoing shape of the S2 spectrum.

The S2 spectra from both MC and data are equally divided into 65 bins, covering the whole observed range of recoils in the elastic scattering neutron band (see Fig. 5.5 f). This choice makes sure that the statistical error for every bin is negligible even in the high energy tail but also provides reasonable resolution of the low energy part, where the sensitivity of the spectral shape towards changes in  $Q_y$  is expected to be largest.

Due to the random nature of the underlying MC simulation, the final fit and its terminal  $\chi^2$  is observed to slightly vary if not all random seeds are kept constant. It was also observed that – depending on these random variations – the algorithm is sometimes forced to stop at unsatisfying high  $\chi^2$  and it is obvious that the fit has not converged in such cases. Therefore, and in order to include the statistical uncertainty of the the neutron simulation, we repeat every fit result later presented at least 100 times for varying random seeds. Thereby, those results which do not represent a decent agreement between data and MC are discarded based on the observed excess above a reasonably fixed  $\chi^2$  threshold.

**Determine central  $Q_y$**  We first perform the fit using the best available knowledge of the fixed input parameters  $\mathcal{L}_{eff}$  and S1 cut acceptance. As mentioned before, we describe  $\mathcal{L}_{eff}$  by the global fit through all direct measurements as given in [47] and fix the acceptance curve to the central one in Fig. 5.13. All remaining inputs to the simulation correspond to those listed in Table 5.1. We present the best fit result on the spectral S2 matching in Fig. 5.16. Black points describe the distribution of data and are to be compared to the blue spectrum generated by simulation as the outcome of  $\chi^2$  minimization. In grey colour we include how the numerically obtained S2 distribution looks like at the beginning of the fitting process when initiated with a constant  $Q_y$  of  $3.5 \text{ e}^-/\text{keVnr}$ . The reduced  $\chi^2$ ,

$$\chi_{red}^2 := \frac{1}{NDF} \sum_{i=1}^N \frac{(y_i - f(x_i; p_1, \dots, p_m))^2}{\sigma_{y_i}^2} = \frac{1}{N - m - 1} \sum_{i=1}^N \frac{(y_i - f(x_i; p_1, \dots, p_m))^2}{\sqrt{y_i^2}}, \quad (5.9)$$

which relates the quadratic deviations to the statistical error  $\sqrt{y_i}$  for every data bin and the number of degrees of freedom  $NDF = N - m - 1$  underlying the fit, drops significantly from  $28\,000/56 = 500$  to  $210/56 = 3.75$  after the algorithm has terminated. Using  $\chi^2$  and  $NDF$  we can also express the goodness of the fit model in terms of the p-value. It corresponds to the probability that any remaining

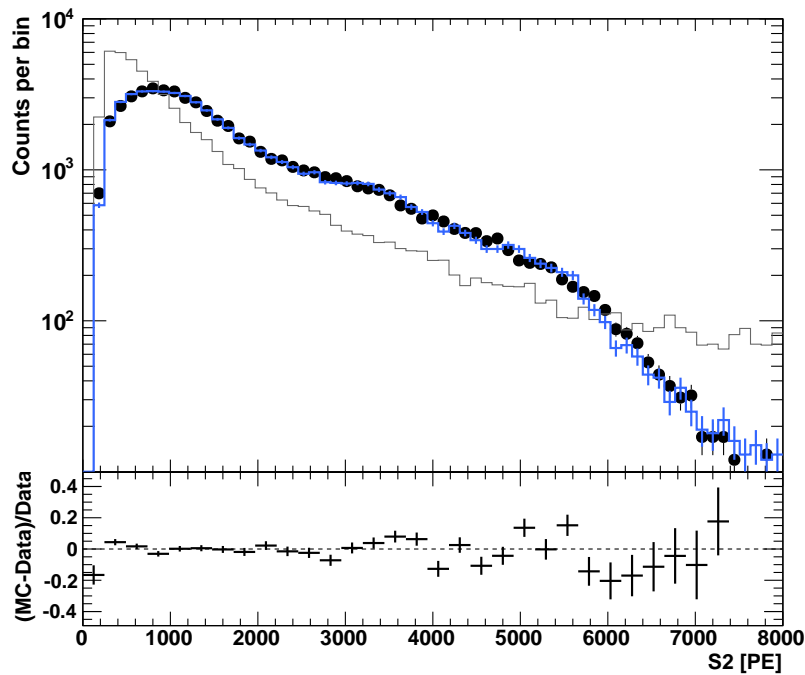


**Figure 5.16:** Best fit of the simulated S2 spectrum (blue line) to data (black points). Very satisfying agreement with average relative deviations less than 10% is found up to the very high energetic tails of the S2 distribution. The best matching case implies  $Q_y$  as shown in Fig. 5.17. The gray spectrum corresponds to a flat  $Q_y$  as injected in the initial step of the fitting routine.

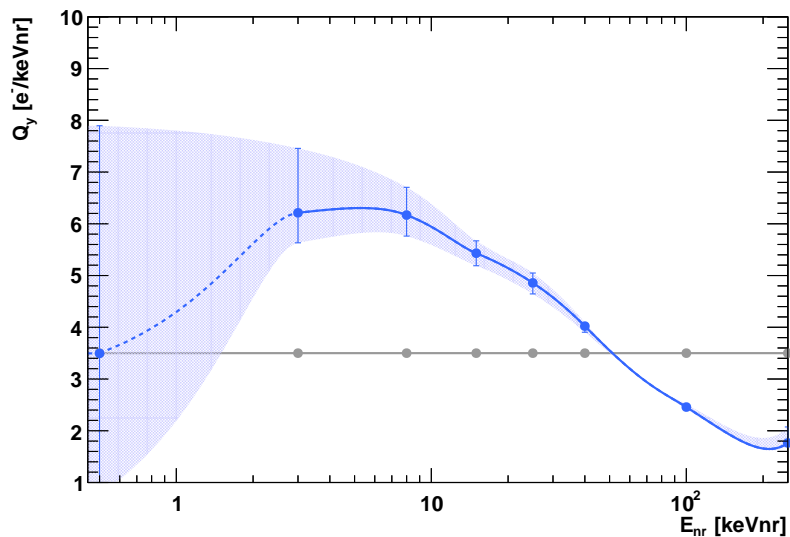


**Figure 5.17:** Best fit  $Q_y$  providing a solution to the least-square minimization problem. The blue central line represents the spline interpolation through the 8 pivot points varied by the fit process. Systematic variations of other input parameters imply deviating best-fit solutions of  $Q_y$ , indicated by the blue shaded uncertainty area (details in text). Shown in grey is the initial choice of spline points used to start the spectral optimization.

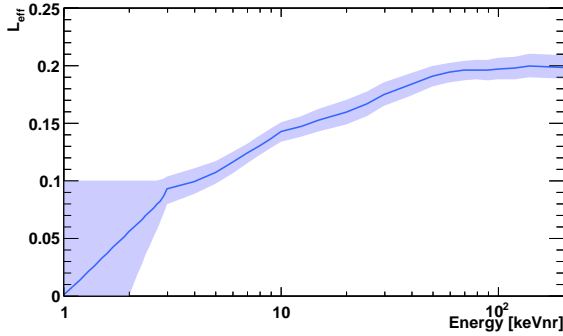


**Figure 5.18:** Global fit  $\mathcal{L}_{eff}$  and  $\pm 1\sigma$  uncertainty region adopted from [47]. The central curve (blue line) and upper/lower error bounds are injected to the simulation in order to study the impact on the resulting best-fit  $Q_y$ .

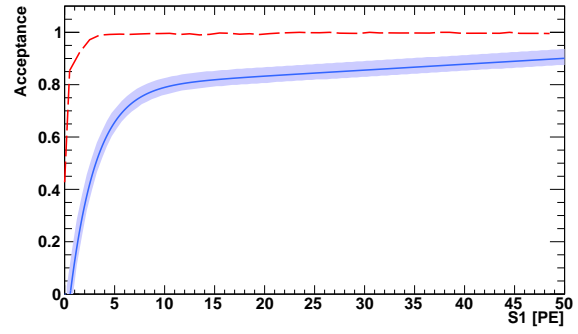


**Figure 5.19:** Nuclear recoil cut acceptance as a function of S1. All individual contributions of the neutron event selection (except S2 threshold, single scatter and event discrimination) are combined in the blue central curve. The light blue uncertainty band represents a conservative error assumption ( $\pm 10\%$ ) used in the determination of systematic effects on  $Q_y$ . The red dashed line shows the effect of the applied S2 threshold ( $S2 > 150$  PE) in the simulation, converted into a function of S1. Figure adopted from [92].

deviation between data and model is only due to Gaussian fluctuation of the data points and thus a high p-value renders the model likely to be true. Note that even  $\chi_{red}^2 = 3.75$  implies a very poor significance (small p-value) of the obtained fit in Fig. 5.16. The reason is that only the statistical error of the measurement is thereby taken into account in the denominator of Eq. (5.9). We will see soon, however, that any outcome of our nuclear recoil simulation also depends to some extent on other parameters like  $\mathcal{L}_{eff}$  and the assumed acceptance loss as function of S1, both adding systematic dependencies on the level of few percent. This statement is underlined by the fact that  $\chi_{red}^2 \approx 1$  and  $p \approx 0.3$  by only taking into account a conservative systematic error estimate of 10% in the calculation of the goodness of fit.

Underneath the spectral comparison we present the spline interpolation through the minimizing set  $\mathbf{p}^{min}$  of pivot points, which represents the central result from the S2 matching. As expected the result has considerably moved from the initial (flat) choice of parameters and approaches a result near the direct  $Q_y$  measurements.

**Uncertainty estimate** Having obtained the central curve of  $Q_y$  if fixing other parameters to best known values we test the stability of the fit result against systematic variations of them. The first to mention is the impact of the chosen  $\mathcal{L}_{eff}$ . It can be probed by inserting the  $\pm 1\sigma$  bounds of the global  $\mathcal{L}_{eff}$  parameterization from [47] (indicated by blue uncertainty region in Fig. 5.18) to the fitting routine instead of the the central curve. Although the generated S2 spectrum is in principle decoupled from the light quenching, some effect is expected to be present at low recoil energies where  $\mathcal{L}_{eff}$  controls the number of events passing the general cut acceptance as a function of S1 (central blue function in Fig. 5.19). It turns out that using the lower  $1\sigma$  contour of  $\mathcal{L}_{eff}$  implies a somewhat decreased charge yield around threshold because the S1 light corresponding to a given recoil energy appears diminished and therewith the probability of the event falling into the signal acceptance region. This causes a slight shift in the underlying energy distribution of finally accepted events towards higher recoil energies. To compensate this effect and maintain the spectral matching in S2 the algorithm needs to favour lower  $Q_y$  values. As expected, the effect on varying  $\mathcal{L}_{eff}$  almost

vanishes for recoil energies larger than 15 keVnr as detection acceptances become constant in S1 and thresholds play no major role. The same argumentation holds in opposite direction and we find that using the upper contour of  $\mathcal{L}_{eff}$  implies re-arrangement in  $Q_y$  towards higher yields.

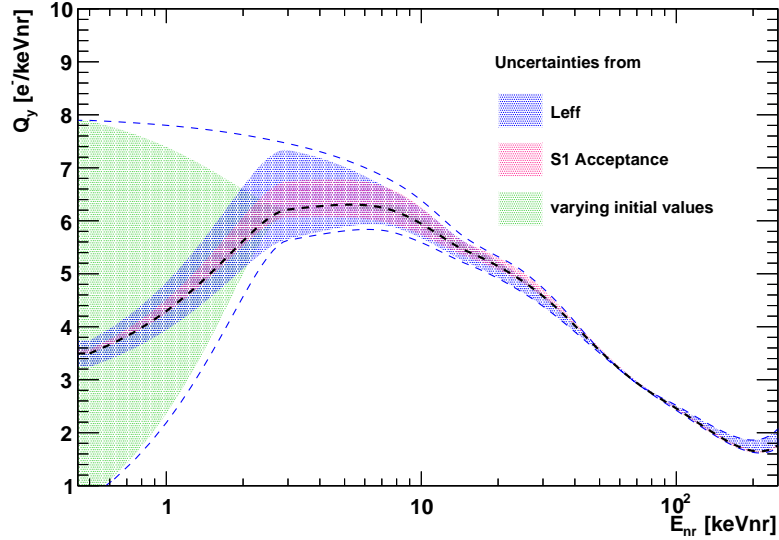


**Figure 5.20:** Decomposition of main sources of systematic uncertainties to the extracted best fit  $Q_y$  (black dashed line). The quadratic sum of all contributions is indicated by the blue dashed line.

A very similar effect is observed by any direct shift of the assumed S1 cut acceptance. Since a precise determination of systematic errors coming with each individual selection criterion is very subtle and has not been exhaustively analyzed in the context of dark matter searches in XENON100, we study potential impact on our indirect  $Q_y$  measurement by conservatively allowing for a  $\pm 10\%$  variation of the acceptance (blue shaded uncertainty region in Fig. 5.19). Again, we find that a lower detection efficiency implies a decrease in  $Q_y$  and vice versa, around low nuclear recoil energies. The effect becomes very small for central and high energies where the acceptance function becomes essentially flat.

Further systematic uncertainties inherent to the present method come with the position of pivot points and their initial values  $p_1, \dots, p_8$ . We have tested the impact of several different combinations but always come to the conclusion that only the initial choice of the very lowest pivot point at 0.5 keVnr impacts the resulting  $Q_y$  at that particular energy. We observe that the  $Q_y$  value at this pivot position always sticks close to the initial choice during the entire fitting routine. This does not arise unexpectedly, as the generated S2 spectrum is hardly influenced by the extrapolation of  $Q_y$  below the known detection threshold at  $\approx 3$  keVnr. Eventually we only provided the lowest pivot point for an unbiased completion of the whole energy range but conclude that it does not affect the spectral matching in the accessible S2 range.

Continuing the study of systematic effects we also realize that there is essentially no impact on the spectral matching when changing from the source strength to an integral normalization of the simulated neutron number. In the latter case, when leaving the normalization as a free fit parameter, the best matching requires a neutron emission rate of  $\sim 159$  n/s – well within the experimentally measured rate of  $(160 \pm 4)$  n/s.

For each of the mentioned uncertainty origins we evaluate separately the deviation from the initially

obtained central  $Q_y$  value at every pivot position and finally sum the single contributions in quadrature. The total outcome is represented by the light blue uncertainty band included in Fig. 5.17 and the decomposition of the various contributions shown in Fig. 5.20. The error band is not completely symmetric around the central curve as the above mentioned effects are not necessarily linear but in parts controlled by the interplay of  $\mathcal{L}_{eff}$  and S1 acceptance. The relative error grows with decreasing recoil energy for reasons discussed above. The large uncertainty on the lowest pivot point reflects once more that this value effectively floats freely and that the present method is not sensitive to energy regions below 3 keVnr where the detection threshold of the XENON100 detector is reached. The slight uncertainty increase for the uppermost pivot point can be understood from the lack of statistics in the very high S2 tails where the  $\chi^2$  technique becomes less sensitive towards variations in  $Q_y$ . Compared to these findings, systematic uncertainties inherent to the other fixed parameters listed in Tab. 5.1 are considered sub-dominant since they are associated with relative errors of  $< 3\%$ .

### 5.4.2 Fitting S1 and determining $\mathcal{L}_{eff}$

Using the previously extracted shape of the charge yield  $Q_y$  to update our signal response framework allows us to turn the same developed routine into a fit of the measured S1 light distribution. Thereby we can similarly extract an updated  $\mathcal{L}_{eff}$  from the data/MC comparison. Due to the correlation of  $\mathcal{L}_{eff}$  and  $Q_y$  near the detection threshold we must underline that any result on  $\mathcal{L}_{eff}$  will be limited in its precision by at least the uncertainty of the global parameterization in Fig. 5.18, which already entered the determination of  $Q_y$ .

We choose the same number and position of pivot points for the Akima spline as in the previous paragraph. Already having reliable information about the shape of the light quenching function, we sample the initial values  $\mathbf{p}^{init}$  from the existing global fit of  $\mathcal{L}_{eff}$  from Fig. 5.18. Data and MC spectra are divided into 50 bins between 1 and 200 PE with logarithmically increasing width to compensate for the steep spectral decline towards larger S1 and to give further weight to lower energies where maximum sensitivity is needed. It is assured that the outcome is only marginally different from using a linear binning. In the allowed fit range we have excluded S1 below 2 PE. No reasonable matching can be gained in this extremely low tail of the light distribution, regardless of how  $\mathcal{L}_{eff}$  is extrapolated or even cut to zero. It is well known that this area is at the very edge of the understood signal acceptance with less than only 2 PE being recorded and many kinds of subtle (hardware) threshold effects setting in. All other parameters and inputs to the simulation remain unchanged but we take the central  $Q_y$  from Fig. 5.17 to calculate the S2 in parallel. Again, we repeat the fit many times and pose a cut on the resulting  $\chi^2$  to discard failed attempts of the fit routine.

The best spectral agreement is shown in Fig. 5.21 and the inferred minimum solution of  $\mathcal{L}_{eff}$  presented underneath. Above  $\sim 2$  PE good overall agreement, with average deviations of less than 5–10% between data and MC, is achieved. The implied minimizing solution of  $\mathcal{L}_{eff}$  is largely consistent with the presumed knowledge from direct  $\mathcal{L}_{eff}$  determinations and lies within the  $2\sigma$  uncertainty of the standard parameterization except for the spline point at 25 keVnr. The deviation originates from improved matching of the measured S1 spectrum between 20 – 50 PE compared to using the initial  $\mathcal{L}_{eff}$  definition. The extracted  $\mathcal{L}_{eff}$  does not achieve improved accuracy compared to the existing global parameterization through all available direct measurements because of its discussed intercorrelation with  $Q_y$ . The dependency could eventually be resolved in a combined 2-D fit of the whole nuclear recoil band by simultaneously varying  $\mathcal{L}_{eff}$  and  $Q_y$ . Such minimization would depend on a large number of free parameters and possibly require a further optimized computational implementation.

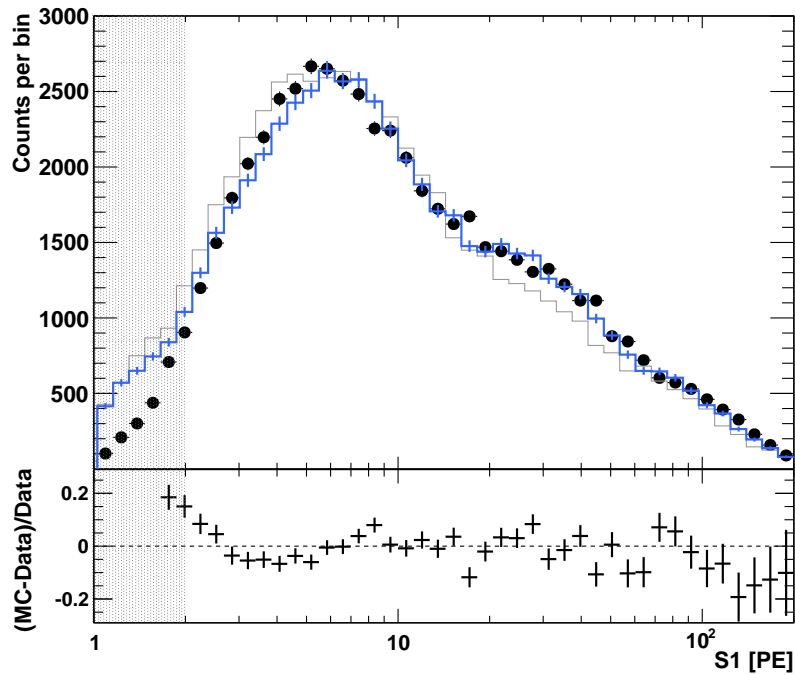


**Figure 5.21:** Best fit of the simulated S1 spectrum (blue line) to data (black points). Good agreement with average relative deviations less than 10% is found for S1 above 2 PE. Excluded from the fit range are signals below 2 PE (grey shaded region). The best matching case implies  $\mathcal{L}_{eff}$  as shown in Fig. 5.22. The gray spectrum is obtained with the  $\mathcal{L}_{eff}$  from the global fit through all available experimental data, as given in [47] and used as initial choice for the fit.

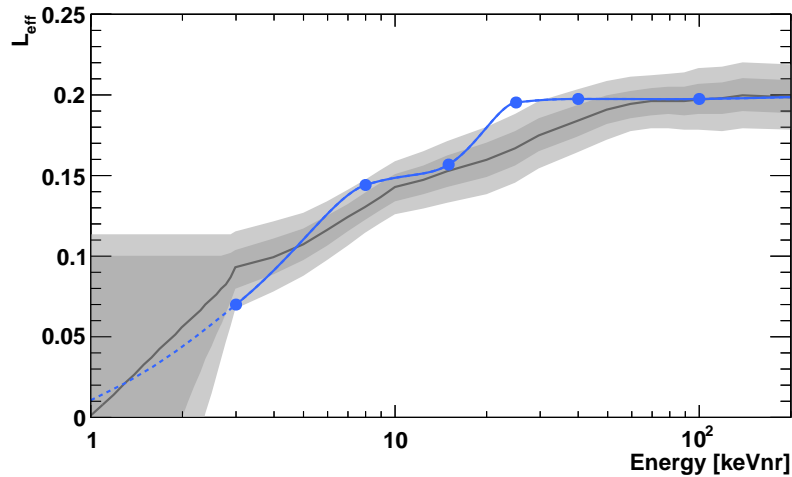


**Figure 5.22:** Best fit  $\mathcal{L}_{eff}$  providing a solution to the least-square minimization problem. The blue central line represents the spline interpolation through the 8 pivot points varied by the fit process and is obtained using the previously updated result on  $Q_y$  for the generation of S2. Also shown by the grey solid line is the initial choice of  $\mathcal{L}_{eff}$  inserted to start the spectral optimization. The grey shaded regions reflect the 1 and  $2\sigma$  uncertainty on the global  $\mathcal{L}_{eff}$  parameterization from [47].

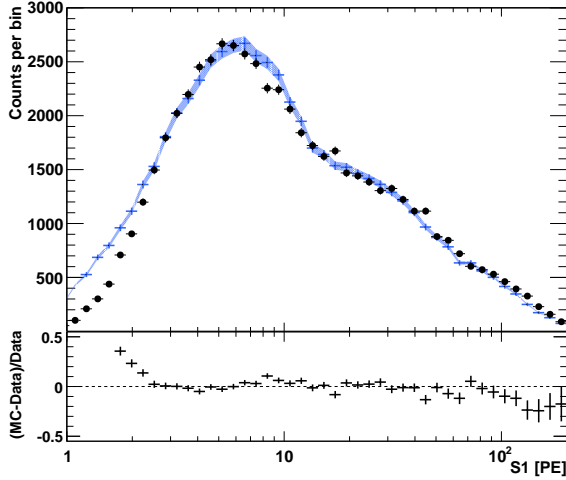


**Figure 5.23:** Data/MC comparison of the S1 spectrum using the best fit results of  $\mathcal{L}_{eff}$  and  $Q_y$  as input to the simulation.

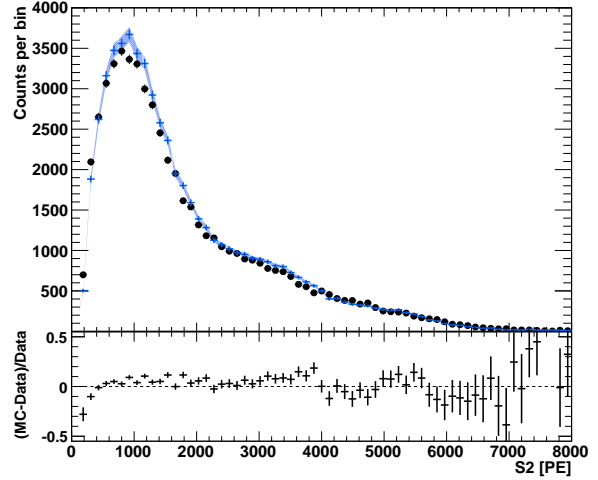


**Figure 5.24:** Data/MC comparison of the S2 spectrum using the best fit results of  $Q_y$  and  $\mathcal{L}_{eff}$  as input to the simulation.

### 5.4.3 Data matching using combined best fit $\mathcal{L}_{eff}$ and $Q_y$

We insert both central curves of  $\mathcal{L}_{eff}$  and  $Q_y$  – yielded by the previous 1-D spectral fitting of S1 and S2, respectively – to our simulation framework in order to check the spectral matching with both functions applied simultaneously. All other input parameters, listed in Tab. 5.1 remain unchanged, and the same event selection criteria (including the 34 kg fiducial volume) are applied as before. The number of simulated neutrons is again fixed by the product of externally measured neutron yield and the calibration live time.

The observed matching – plotted in Fig. 5.23 and 5.24 – is evident, both in spectral shape and absolute rate and appears considerably improved with respect to Fig. 5.14 and 5.15. The obtained residuals are mostly within the known 2.5% uncertainty on the measured neutron yield (marked by blue error band) for almost the entire observable range and above 2 PE in S1. As stated before, below this threshold no absolute agreement is found, even when setting  $\mathcal{L}_{eff}$  to zero below 3 keVnr recoil energy. Note that no more than  $\sim 60,000$  single scatter neutrons end up in the defined acceptance region after all cuts considered and  $\sim 1.5 \times 10^7$  particles iterated throughout the simulation, starting from the initial source position.

Using the output of our simulation we can as well compare the spatial density of selected neutron events with the measurement, as plotted in Fig. 5.25. We show both distributions, data and MC, first without any partial volume cut. We find overall good agreement on the absolute scale, except for a population at large radius and high  $z$ , more pronounced in the MC than data. Also not reproduced by the simulation (by definition) is the worsening of position reconstruction capability seen close to the boundaries of the TPC. Inside the 34 kg fiducial volume (marked by the red line), there is a convincing agreement along both the radial and  $z$  position (refer to Fig. 5.26), adding much to the validity of neutron propagation and correct assumptions on the elastic scattering length used by the GEANT4 simulation.

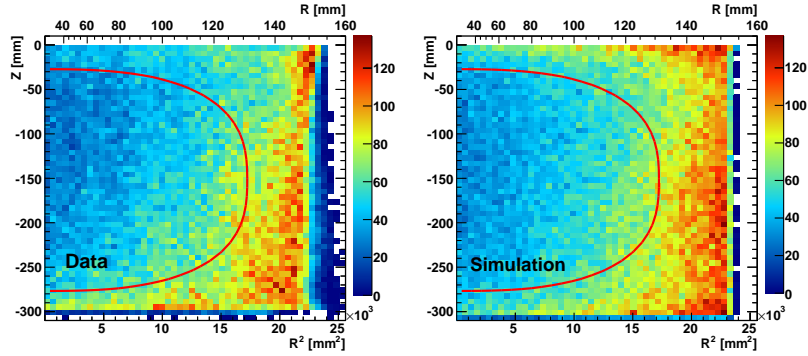


**Figure 5.25:** Spatial distribution of single-scatter neutron events from data (left) and simulation (right). The 34 kg super-elliptical fiducial volume, applied to all analyses presented in this chapter, is marked by the red contour. With exception of the upper edge region, very satisfying agreement between data and MC on absolute scale is reached up to the very boundaries of the TPC, where limitations from the XENON100 position reconstruction set in.

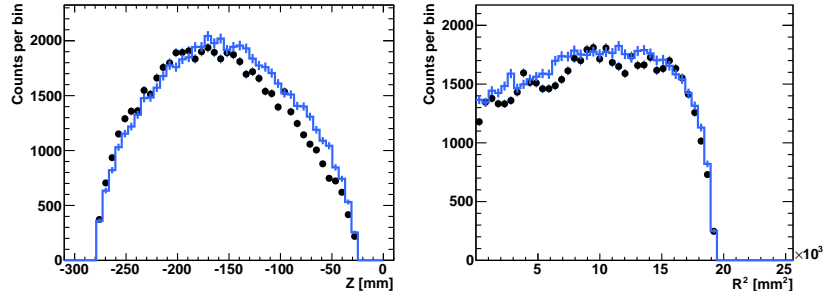


**Figure 5.26:** Projections of the spatial distribution along Z (left) and  $R^2$  (right) for events only within the 34 kg fiducial cut. In this detector region, where all previous analyses are based on, the agreement between data (black points) and simulation (blue line) is convincing, given the quoted uncertainty of the absolute neutron rate.

## 5.5 Reproducing combined S1/S2 nuclear recoil distributions

In the next step we want to use our solid understanding from individual signal matching of the scintillation and ionization channel in order to reproduce the combined S1/S2 response to nuclear recoils in the XENON100 detector within the present simulation framework. This appears particularly important as any result on dark matter searches in XENON100 is presented in the so-called particle discrimination space where electronic interactions (mainly from radiative backgrounds) and nuclear recoils (as induced by neutrons or potential WIMPs) form distinct populations (refer to Sec. 2.4.2).

The previously described simulation remains unchanged except that the best fit parameterizations of  $\mathcal{L}_{eff}$  and  $Q_y$  (central blue curves in Figures 5.22 and 5.17) are now used as input to the signal generation. Finally selected events obey the same aforementioned S2 threshold and single scattering criteria as applied on data. They are further restricted to the 34 kg inner fiducial volume. Similarly, the S1 cut acceptance loss is taken into account according to the measured parameterization in Fig. 5.13. The amount of simulated neutrons is again scaled to match the measured  $^{241}\text{Am}$  neutron strength.

**Light-charge correlation** We evaluate first the observed correlation between charge and light channels, as presented in Fig. 5.27. The plot shows the combined distribution of S1 and S2 for selected single scatter nuclear recoils obtained from data (top) and simulation (bottom). The peculiar flattening of the distribution profile is caused by the combination of increasing  $\mathcal{L}_{eff}$  and simultaneously falling  $Q_y$  with recoil energy. The measured population is well reproduced by the Monte-Carlo result as supported by the good agreement of median and  $\pm 1\sigma$ -quantiles of the projected S2 distribution for slices of 5 PE in S1 (Fig. 5.28). Observed remaining discrepancies are subject of later investigation but we note at this point that the S2 generated by MC slightly overestimates values from the measurement.

**Nuclear recoil bands** Next we focus on the event distributions forming the typical recoil type discrimination space of  $\log_{10}(S2/S1)$  vs. S1. The ratio of the charge-proportional and light signal is not constant along S1 due to the individual, non-linear response of both channels to nuclear recoils. In addition the “banana”-like shape is enhanced by the combination of two distinct statistical processes governing the fluctuations of S1 and S2 at low energies, as discussed later in this chapter. Again, the overall agreement of the general band shape between simulation and data is striking. It provides solid proof that the signal description obtained from 1-D fitting sufficiently encodes the inter-dependency between S1 and S2. Similar to the S2 vs. S1 population studied before, minor deviations turn out in the reproduction of the width of the recoil band (refer to Fig. 5.30 and Fig. 5.31).

There are two possible interpretations of the slight mismatch in the width of the 2-D dimensional band structure. To explain the effect, we draw projections on  $\log_{10}(S2/S1)$  for several slices in S1 in Fig. 5.31, ranging from lowest to higher recoil energies. In all cases the mean and the upper tails, which resemble a proper Gaussian shape, are very well reproduced. For the lower tails, however, the simulation does not fully reflect the non-gaussianity observed in data. This effect is the most pronounced for small S1, where Poissonian fluctuations of the observed number of photo-electrons become dominant. In our simulation model, we assume an average mean over all contributing PMTs without accounting for the individual responses in quantum-efficiency and, more important, single PE gain. Implementing this would also require a full simulation of light propagation through the XENON100 geometry and undermine the idea of a smart distinction between the GEANT4 and the detector response simulation, which made efficient data-MC fitting in Sections 5.4.1 and 5.4.2 possible in the first place. A second argument can be found in the imperfect reproduction of events with incomplete charge collection. Some fraction of incoming neutrons will scatter in a detector region from where no electrons are drifted to the anode because the electrical field is absent or skewed. Nevertheless, the direct scintillation light is likely to be recorded and will just add to the S1 whenever the neutron undergoes another scattering inside the active volume. Those events may look like ideal single site interactions but in fact carry the sum of two prompt S1 signals. Consequently, the ratio of S2/S1 will be shifted towards a smaller value and, particularly for low energetic recoils, lead to a distortion of the population. The largest insensitive area is between the cathode grid and the bottom PMT arrays. While any missing charge effect from there is in principal modelled in the detector response simulation there are other origins (e.g. in the space between PMTs or around the fixation of the grid meshes in the edges of the lower TPC) that are not considered and add to the askew tails in the mentioned ratio. The event class is even apparent enough to form a visible side-band of constantly low S2 over a wide range of S1, as can be seen in Fig. 5.27, but is only reproduced in parts by the simulation. All in all we remark that the present deviations are small, acting only very mildly on the median and  $1\sigma$  quantiles of the 2-D distributions and, therefore, have secondary impact for the central result, which is the indirect determination of the energy dependency of  $Q_y$  and  $\mathcal{L}_{eff}$ . Key to fully reproducing the response up to higher order will be to consider every individual PMT response

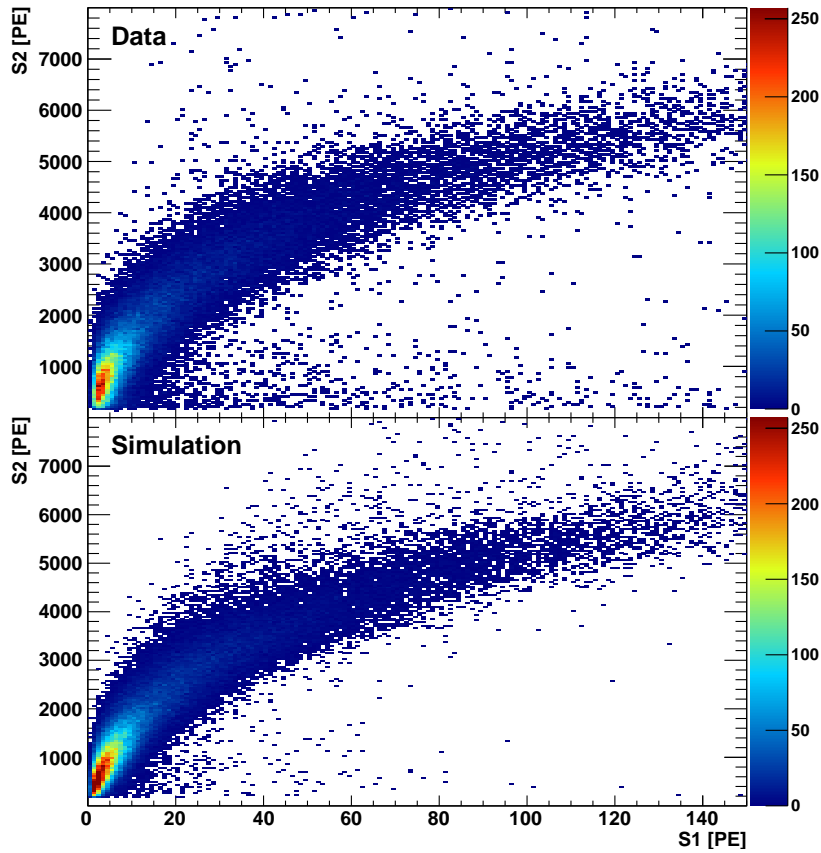


**Figure 5.27:** Measured (top) and simulated (bottom) S1-S2 signal correlation for single neutron scatters. The color axis represents absolute number of events per S1-S2 bin.

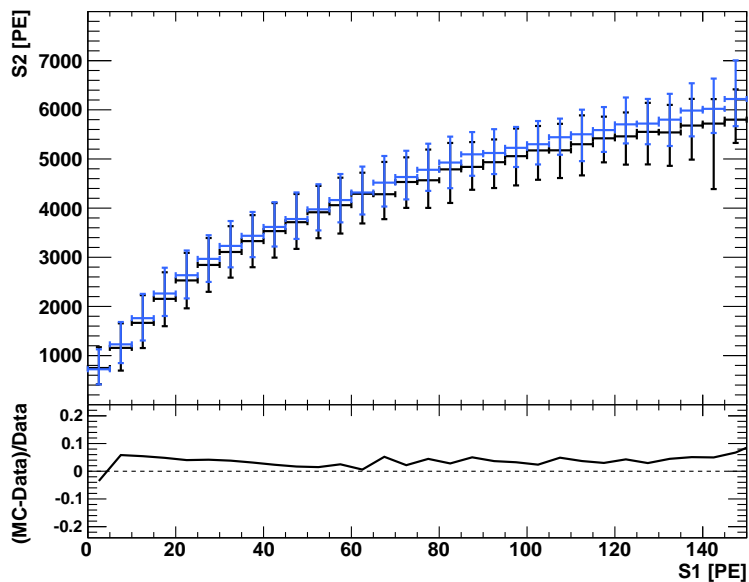


**Figure 5.28:** Comparison of the band-shaped S1-S2 signal correlation in data (black) and simulation (blue). For every bin in S1 (units of 5 PE) medians and  $\pm 1\sigma$ -quantiles of the projected S2 distribution are drawn. The overall agreement is at the level of 5% up to very high S1. The bending slope is caused by the non-linearity of  $\mathcal{L}_{eff}$  and  $Q_y$  as a function of recoil energy.

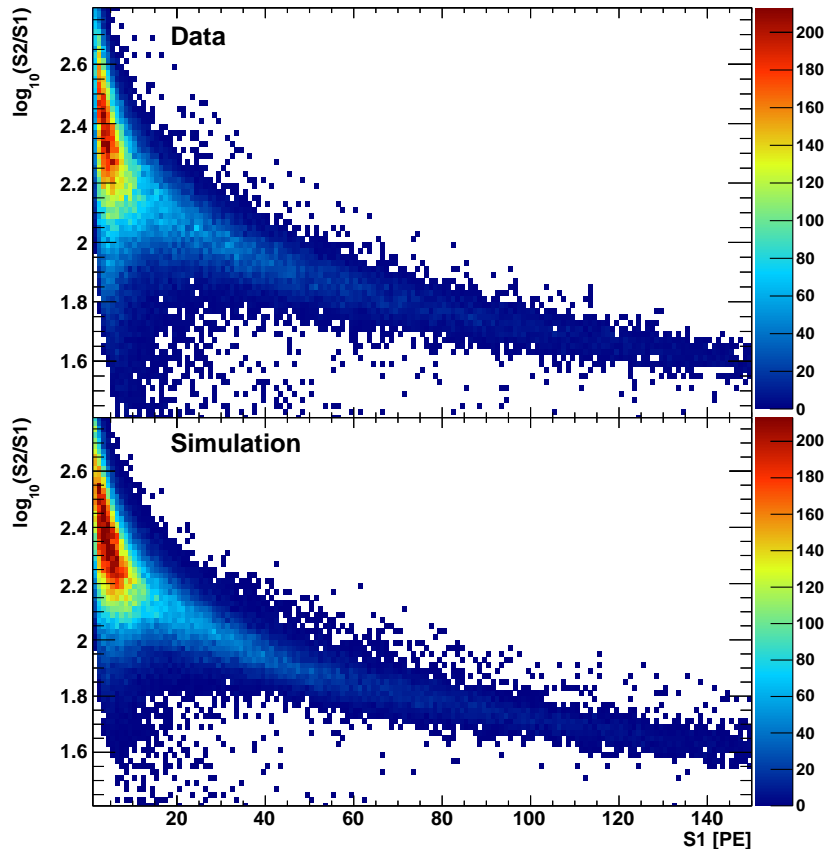


**Figure 5.29:** Measured (top) and simulated (bottom) nuclear recoil bands from single scattering neutrons. The color axis represents absolute number of events per bin.

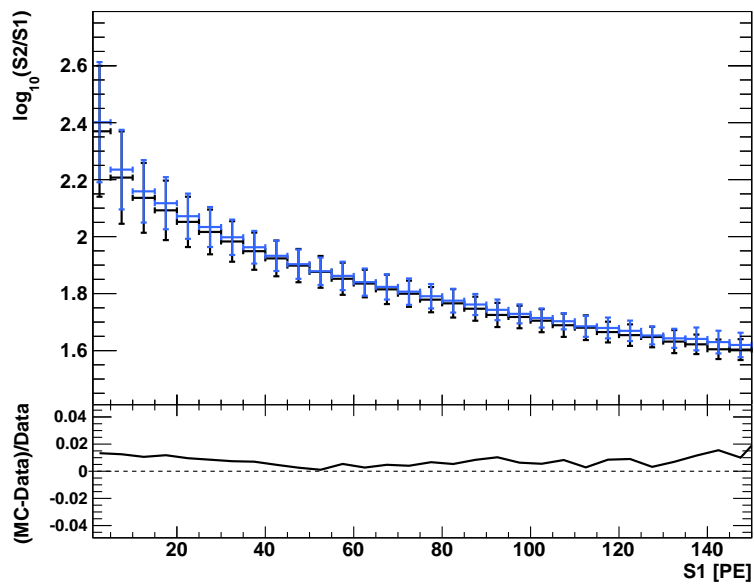


**Figure 5.30:** Comparison of the nuclear recoil band shapes of data (black) and simulation (blue). For every bin in  $S1$  (units of 5 PE) medians and  $\pm 1\sigma$ -quantiles of the projected distribution in the discrimination parameter  $\log_{10}(S2/S1)$  are drawn. The overall agreement on the logarithmic scale is at the level of 1% up to very high  $S1$ .

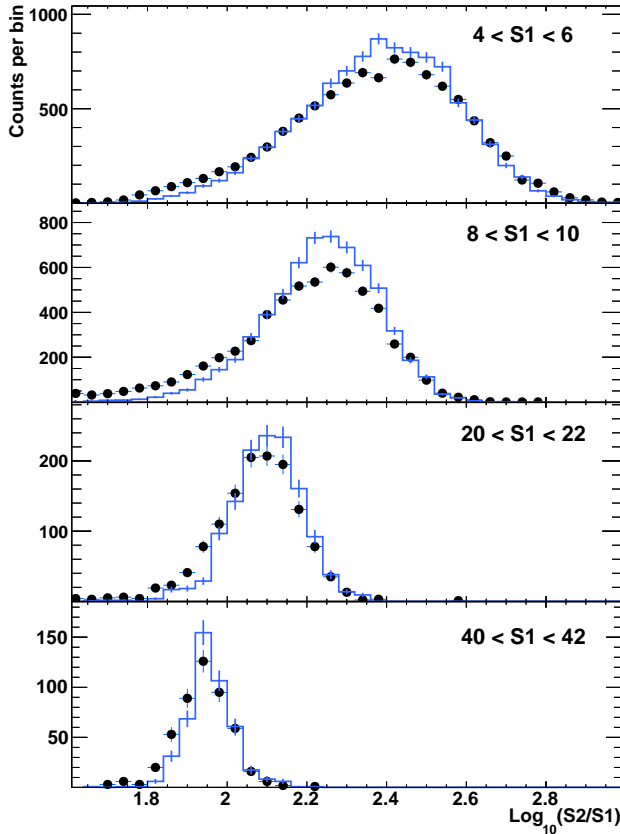


**Figure 5.31:** 1-D projections of the nuclear recoil band for several slices of S1. Measured spectra in  $\log_{10}(S2/S1)$  (black data points) are compared to predicted ones from simulation (blue histograms). Non-gaussian tails towards smaller  $\log_{10}(S2/S1)$  appear increased at low recoil energies and possible origins are discussed in text.

function and complete treatment of geometric effects, such as incomplete charge collection.

**Band decomposition** We close our examinations of this section by further studying the formation of the band structure for nuclear recoils. With data provided by the output of the simulation we can classify events by their initial energy deposit and draw their position in  $\log_{10}(S2/S1)$  vs. S1 space. For two specific energy ranges, one near detection threshold ( $6.5 \pm 0.2$  keVnr) and another well above ( $30 \pm 0.5$  keVnr), the outcome is shown in Fig. 5.32 (left). We also give their projected S1 and S2 distribution in Fig. 5.33.

Events selected by their low energy deposit (marked blue in Fig. 5.32) are widely spread along the discrimination axis, which can be explained by relatively large upward fluctuations in S1. Not only is this caused by the slight asymmetry of a Poisson distributed random variable – present for small mean values – but also by the progress of a quickly rising detection acceptance as a function of S1. Both arguments combined effectively shift the centre of the population towards larger S1 values (compare grey and blue histograms in Fig. 5.33 to see the effect of switching on/off the finite acceptance probability).

In contrast, for events far away from the threshold, at around 30 keVnr (marked green), the detector acceptance is flat and both S1 and S2 are well approximated by Gaussian fluctuations. This leads to a flattening and narrowing of the observed band structure. Still, the absolute uncertainty on the energy estimator S1 remains comparably large due to finite light collection in XENON100 and only moderate increase of  $\mathcal{L}_{eff}$  with growing energy transfer.

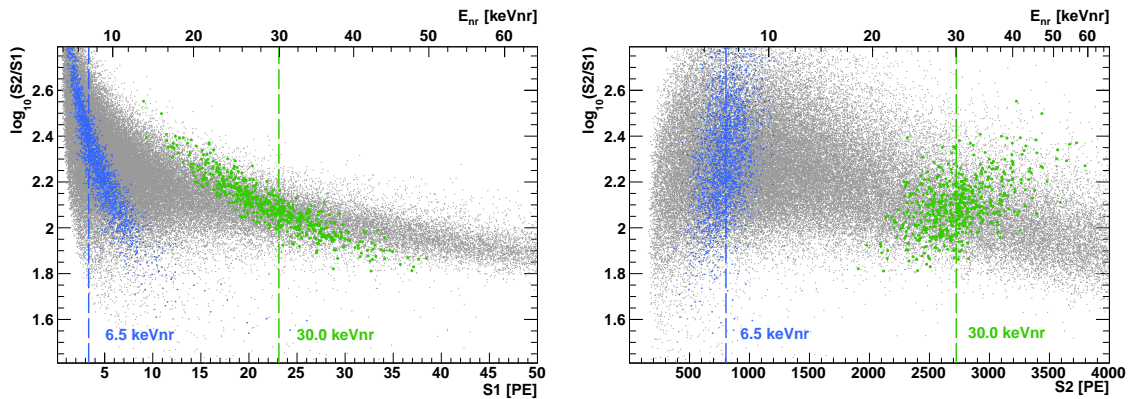


**Figure 5.32:** Left: Nuclear recoil band (grey) as a function of S1 from the detector response simulation. Highlighted are events with fixed recoil energy at  $(6.5 \pm 0.2)$  keVnr (blue) and  $(30 \pm 0.5)$  keVnr (green). The energy scale (top axis) is calculated using the central fit of  $\mathcal{L}_{eff}$  from Sec. 5.4.2. Right: Nuclear recoil band (grey) as a function of S2. The energy scale (top axis) is calculated using the central fit of  $Q_y$  from Sec. 5.4.1.

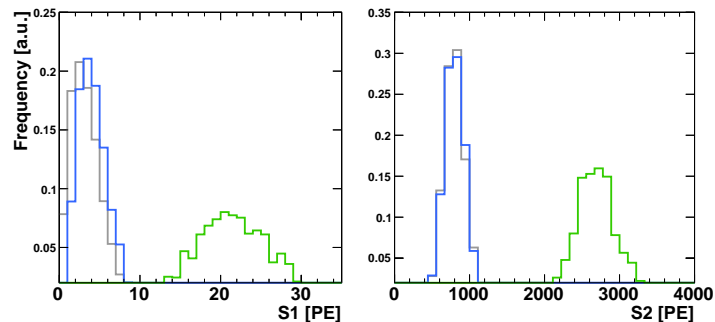


**Figure 5.33:** Left: Projected and integral normalized S1 distribution for event selections with constraint nuclear recoil energies of  $(6.5 \pm 0.2)$  keVnr (blue) and  $(30 \pm 0.5)$  keVnr (green). Right: Corresponding S2 distribution for event selections with constraint nuclear recoil energies. Both: Result with 100% S1 acceptance (assuming no detection threshold) is shown in light grey.

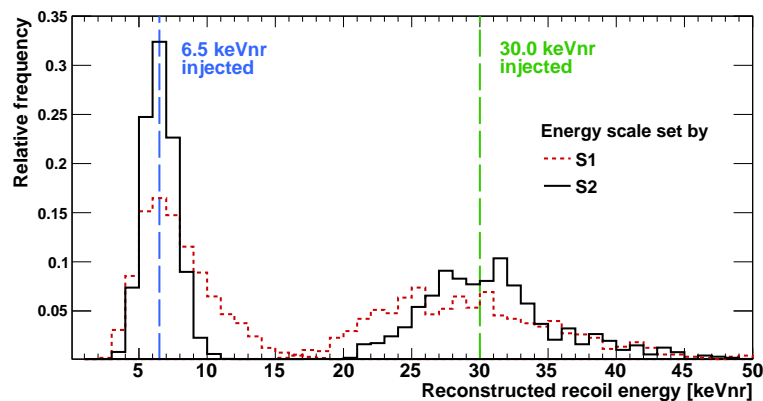


**Figure 5.34:** Comparison of two energy scales defined by either S1 and  $\mathcal{L}_{eff}$  (red dashed) or S2 and  $Q_y$  (solid black). Recoils of energies restricted at  $(6.5 \pm 0.2)$  keVnr (blue vertical line) and  $(30 \pm 0.5)$  keVnr (green) are injected to the detector simulation and their reconstructed distributions after processing and smearing shown. Improvement becomes obvious particularly at low energy.

**Comparison of energy scales** A better resolution can be accomplished if the energy scale is determined by S2 and  $Q_y$  according to Eq. (5.5). The improvement can be judged by directly comparing the energy resolution with the one achieved by the common translation via Eq. (5.3), when using S1 and  $\mathcal{L}_{eff}$ . The difference is shown by the comparison of simulated results for single scatter neutron interactions from distinct energy injections at  $(6.5 \pm 0.2)$  keVnr and  $(30 \pm 0.5)$  keVnr. After their processing and signal smearing we reconstruct the original energy either from the outgoing S1 or S2 in Fig. 5.34. In the latter case, the peak structures appear narrower and better Gaussian-shaped, thus providing an increased resolution. This is particularly true for lowest recoil energies, where the S2 signal is much less prone to Poisson fluctuations and has a considerably smaller relative counting error from the number of information carriers (ionization electrons instead of scintillation photons). The same features are also inherent to Fig. 5.32 (right), in which the usual discrimination parameter is drawn against the energy calculated from S2 to be compared to the left plot of the same figure. Note that the energy scale (top axis) is equal in both pictures.

Not only with the improved understanding of  $Q_y$  in this work but also with more direct measurements to come, S2 may soon replace the traditional role of the currently used energy estimator S1 in order to benefit of enhanced energy resolution.

## 5.6 Simulation of WIMP recoils

Having concluded with the analysis and reproduction of the detector response to neutron calibration we want to apply our improved understanding to the simulation of possible dark matter interactions in the XENON100 detector. Thereby, we benefit from the fact that the expected signature of nuclear recoils at a given energy deposit is the same, regardless whether a WIMP or a neutron scatters off the target. What is different, however, is their underlying energy recoil spectrum. Therefore, we need to briefly revise the theory of interaction between dark matter and particles, as already introduced in Chapter 1.5.

**Dark matter rate spectrum** We restrict our study to the same dark matter model of non-relativistic, spin-independent WIMP-nucleon interaction as usually preferred in direct search publications and thus, compatible with the presented XENON100 results in [42]. Since it is our goal to inject dark matter particles into the simulation, we have to first generate a set of events following the expected differential (i.e. recoil energy-dependent) interaction rate spectrum, parameterized by the assumed WIMP mass  $m_\chi$  and SI cross-section  $\sigma_{\chi N}^{SI}$ . In our case, the predicted spectrum is given by Eq. (1.10) and yields the number of WIMP recoils per units of keV, kg and day.

We insert common assumptions on the astrophysical parameters, as already introduced in Sec. 1.5. These consider the dark matter density profile to follow the one of an isothermal sphere and assume its local value (i.e. at the place of our Solar system within the Galactic halo) to be  $\rho_\chi = 0.3 \text{ GeV/cm}^3$  (e.g. in [20]). The model further applies a Galactic escape velocity of  $v_{esc} = 544 \text{ km/s}$  [22] (particles at higher speed are no longer bound by the gravitational potential of our Galaxy) and a local circular velocity of  $v_0 = 220 \text{ km/s}$  [21] around the Galactic centre. Mind that deviations from those parameters, as well as the proposed functional shape of the proposed dark matter velocity distribution (here assumed to follow the widely used Maxwellian), directly affect the inferred value of the interaction cross-section from experiments. Similar is true on the particle physics side, where we assume equal coupling of WIMPs to protons and neutrons and compensate nucleon coherence effects according to the common nuclear form factor parameterization of [25].

With these input parameters the spectral rate is essentially fixed but we must still choose a specific WIMP mass and spin-independent WIMP-nucleon cross-section. We decide to study two test cases:

- $m_\chi = 8 \text{ GeV}/c^2$  and  $\sigma_{\chi N}^{SI} = 3.0 \times 10^{-41} \text{ cm}^2$ . Low WIMP mass scenario with SI cross-section at the lower border of the discovery region favoured by the CoGeNT experiment [40].
- $m_\chi = 25 \text{ GeV}/c^2$  and  $\sigma_{\chi N}^{SI} = 1.6 \times 10^{-42} \text{ cm}^2$ . At this WIMP mass the XENON100 sensitivity is almost maximal and the cross-section is near the favoured signal region of the CRESST-II claim [32].

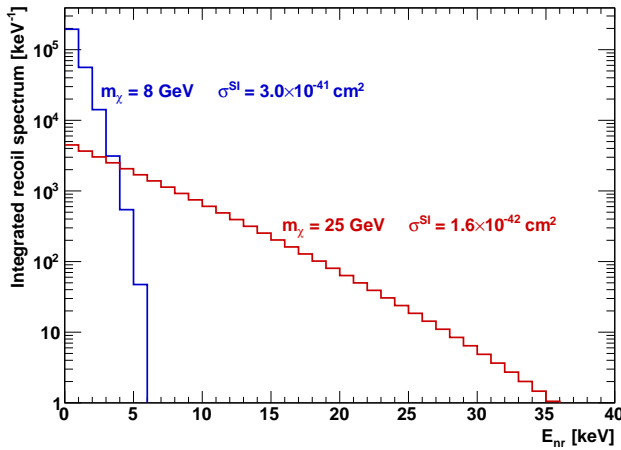


**Figure 5.35:** Recoil energy spectra calculated for WIMP scattering off xenon nuclei according to Eq. 1.10, integrated by the exposure of the most recent XENON100 dark matter search (224.6 live days  $\times$  34 kg) [42]. Two scenarios are shown, covering interactions of a  $8 \text{ GeV}/c^2$  (blue) and  $25 \text{ GeV}/c^2$  (red) WIMPs with corresponding  $\sigma_{\chi N}^{SI}$  in the region of recent discovery claims by the CoGeNT [40] and CRESST [32] experiments.

The calculated spectra are shown in Fig. 5.35. For the numerical implementation of the expected rate equation (1.10) we used the internal “Xephyr” computation package, developed in the XENON100 collaboration. The binning is of 1 keV intervals, i.e. the differential function provided by the WIMP rate equation is integrated over the range of each bin unit. For absolute normalization, the spectrum is scaled to match the live time and active mass volume of the most recently published XENON100 scientific run (224.6 live days  $\times$  34 kg). As expected, the recoil spectrum is steeply falling in case of the light mass WIMP, with its endpoint hitting the typical S1 inferred energy threshold around 6 keV. For the second scenario, the integral rate is much reduced, due to the factor  $\sim 10$  reduced cross-section, but reaches to far higher recoil energies because of the greater WIMP mass.

**Convolution with detector response** From the obtained spectrum we generate a set of single scattering nuclear recoil events, using the same data format as in the neutron study. Recoil energies are assigned according to the respective spectrum in Fig. 5.35. The spatial hit positions are randomly attributed, thereby making sure that the 34 kg super-elliptical fiducial volume is uniformly filled.

To generate the detector response, the prepared set of WIMP events is injected to and processed by the previously introduced signal conversion simulation in the same way as it was done for neutron data. We use the central  $Q_y$  from the best fit determination in Sec. 5.4.1 but decide to take the common  $\mathcal{L}_{eff}$  parameterization from [47] to be consistent in the inferred S1 energy scale with the most recent dark matter analysis from XENON100, with which we eventually want to compare the WIMP interpretation. As stated in Sec. 5.4.2, the outcome of the fitted  $\mathcal{L}_{eff}$  is largely consistent within the error bounds of standard description and we have also checked that conclusions remain unchanged, independent of the two alternatives. We take our previous S1 nuclear recoil acceptance function from 5.13 into account and apply the S2 threshold cut. Both combined yield essentially the same acceptance curve as used in the published dark matter search (Fig. 1 in [42]).

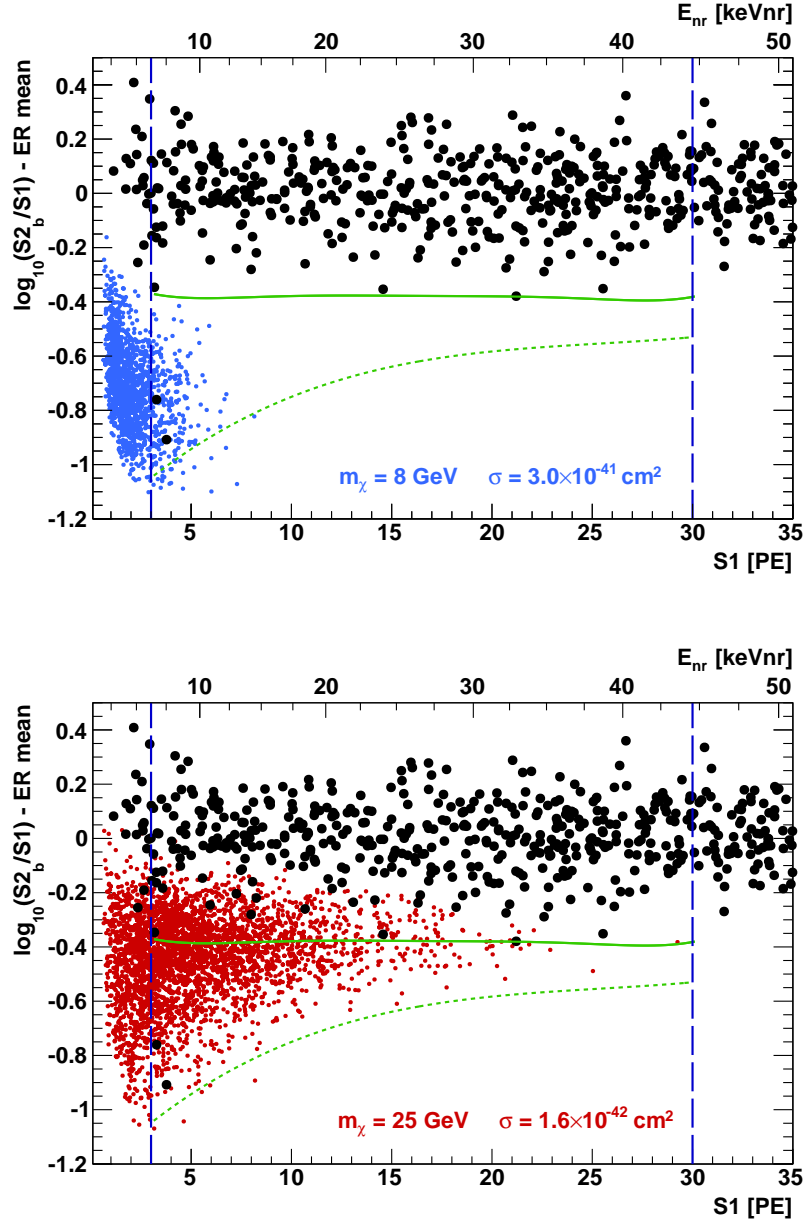


**Figure 5.36:** Simulated event signatures for the two considered WIMP model assumptions of  $m_\chi = 8 \text{ GeV}/c^2$  (top, blue points) and  $m_\chi = 25 \text{ GeV}/c^2$  (bottom, red points), both matching the exposure of the latest 225 live days XENON100 dark matter run. The predictions are presented in the flattened discrimination space and overlapped by the measured XENON100 data after unblinding. Blue dashed lines mark the range of the predefined benchmark region between 3 – 30 PE in S1. The solid green line represents the 99.75% background rejection level and dashed green gives the lower bound defined by the lower  $3\sigma$  contour from neutron calibration.

**Simulated WIMP prediction** To allow for a direct comparison with the published results from XENON100 we finally map the obtained pairs of convoluted S1 and S2 into the flattened parameter space of signal discrimination, where the position along  $\log_{10}(S2_b/S1)$  is subtracted by the mean of the electronic background band as a function of S1 (refer to Sec. 2.4.2). Note that only the S2 light detected by the bottom PMT array is used. The mean ratio of bottom/total S2 can be directly inferred from XENON100 data and was recently determined to be  $S2_{\text{bottom}}/S2_{\text{total}} = 0.41$ , with percent-level accuracy on the mean value (result from internal XENON100 study). The generated (total) S2 is multiplied by this factor before mapping it into the final discrimination space.

The final result of the WIMP prediction is shown in Fig. 5.36. For the two dark matter scenarios we draw the resulting distribution in flattened discrimination space (blue points) after having simulated signal convolution and detection acceptance for an exposure compatible with the most recent XENON100 dark matter run (data after unblinding shown in black). Also indicated is the predefined benchmark region, optimized for the maximum-gap analysis used to cross-check the XENON100 result from the profile likelihood method. It spans between 3 – 30 PE in S1 (blue vertical lines) and covers the region above the lower  $3\sigma$  contour of  $^{241}\text{AmBe}$  neutron population and below 99.75% background rejection level in the discrimination parameter (dashed and solid green borders).

For the low mass region, we discover that upwards fluctuations of the S1 enable a sizable amount of events to enter the benchmark region although the majority of underlying recoil energies is below the inferred (true) recoil energy threshold at  $\sim 6.8 \text{ keVnr}$  (refer to Fig. 5.35). The distribution is generally elongated along the discrimination axis, as we have already observed to be the case for low energetic neutron recoils (see Fig. 5.32). Obviously the centre of the population is shifted towards lower values in  $\log_{10}(S2/S1)$  than suggested by the bulk of the neutron band. This effect is explained by the combination of the steeply falling recoil spectrum for the low mass WIMP model and the sudden increase of the event acceptance as a function of S1 near the detection threshold. Statistical fluctuations in S1 are dominated by Poissonian statistics and introduce an asymmetry such that it is more likely to find events passing the S1 based detection threshold than falling below. At the same time, the S2 is less prone to upward fluctuations and therefore the mean ratio between S2 and S1 is affected by the asymmetric spread in S1.

The picture changes drastically when focusing on the higher WIMP mass scenario. Here, the bulk of the distribution follows very much the shape of the broad-band  $^{241}\text{AmBe}$  calibration and the majority of events exceeds the detection threshold.

Finally, we study both scenarios in a more quantitative way. While it is easy to count the number of predicted events in the benchmark region we must also take care of quoting a reasonable error on this number. As we have learnt so far, there are many sources of systematic uncertainties inherent to the simulation model. The most dominant for our purpose are the errors on  $\mathcal{L}_{\text{eff}}$  and  $Q_y$  because they mainly define the end-up position in the discrimination space. Therefore, for each WIMP mass scenario, we repeat the procedure applied above but assume both optimistic and conservative combinations of the two functions. In the optimistic case (high charge and light yields), we insert the upper  $1\sigma$  uncertainty contour of the global  $\mathcal{L}_{\text{eff}}$  characterization given in Fig. 5.22 and the upper error bound of the  $Q_y$  derivation given in Fig. 5.17. Likewise we use the lower error contours for both  $\mathcal{L}_{\text{eff}}$  and  $Q_y$  in the conservative case.

We find the number of expected WIMP events in the benchmark region to be  $217^{+343}_{-44}$  and  $1378^{+46}_{-37}$  for the  $m_\chi = 8 \text{ GeV}/c^2$  and  $m_\chi = 25 \text{ GeV}/c^2$  scenario, respectively, with the upper (lower) error derived from the optimistic (conservative) combined choice of  $\mathcal{L}_{\text{eff}}$  and  $Q_y$ . The observation of the low mass signal is evident even when making conservative assumptions on the light quenching and charge yield functions. The error bars on the quoted number is however not symmetric. This is

caused by an asymmetry of events fluctuating above and below the predefined S1 threshold, even enhanced by the exponential falling shape of the recoil energy spectrum (Fig. 5.35): With more events at lower energies scattering upwards than vice versa, the net effect appears as an excess of events above threshold. This explains why the result is more robust in the conservative than optimistic case. For the high mass WIMP all threshold effects become negligible and also the systematic uncertainty on  $\mathcal{L}_{eff}$  and  $Q_y$  shrinks considerably for now relevant energies. Consequently, the systematic uncertainty induced by the different choices is not much larger than the statistical counting error any more.

The predicted WIMP signatures are obviously incompatible with the observation of only 2 signal candidates in the benchmark region of the latest 225 live days dark matter search of XENON100. Consistently, the published limit placed on the spin-independent WIMP-nucleon cross-section [42] excludes the investigated WIMP parameter regions of this case study.

## 5.7 Summary of the nuclear recoil response study

We have presented our efforts in understanding the XENON100 detector response to elastic nuclear recoil interactions by intensely studying and modeling the calibration with a  $^{241}\text{AmBe}$  neutron source. We created a stand-alone simulation framework, which is suited for translating the mere energy outcome of GEANT4 based neutron tracking into the experimental observables S1 and S2 – thereby including proper signal smearing, detector resolution and cut acceptance – and finally providing the output in a equivalent format as real data. In comparison with calibration measurements, we have shown to be able to match both the absolute rate and the observed S1/S2 spectral shapes from elastic, single-fold neutron scattering. The absolute matching is even more striking considering that a total number of  $\mathcal{O}(10^7)$  generated neutrons after all simulation stages is reduced to a mere  $\sim 60,000$  events in the final acceptance region within the inner 34 kg fiducial volume.

By fitting simulated S1 and S2 spectra to data, two elementary and general properties of LXe as a target material for nuclear recoils,  $\mathcal{L}_{eff}$  and  $Q_y$  respectively, have been indirectly determined. In case of  $Q_y$  the extracted result adds new stringent information to the limited list of existing measurements and is the only one applied at the nominal electrical drift field of the XENON100 experiment over a wide range of recoil energies. The present method is sensitive down to low recoil energies of  $\sim 3\text{ keVnr}$ . The systematic error on the best fit result has been carefully investigated and quantified by testing the impact and robustness under variation of other crucial input parameters to the simulation. Within the quoted uncertainties it is largely consistent with existing data (particularly compared to a similar indirect method applied by Horn et al. for the ZEPLIN-III experiment [109]) but suggests a slightly different behavior at lowest energies with respect to direct measurements by Manzur et al. (refer to Fig. 5.38). All previous measurements were performed at slightly different electrical drift field strength, which  $Q_y$  is supposed to be only weakly dependent on [55].

Very satisfactory matching of the S1 spectrum could be achieved with only moderate variation of  $\mathcal{L}_{eff}$  from the global fit curve through existing (direct) measurements (Fig. 5.37). Our solution suggests that the quenching function remains flat down to  $\sim 25\text{ keVnr}$  – which is somewhat lower than suggested by the global parameterization of [47] – before monotonically decreasing. Below 3 keVnr recoil energy, the present method is not sensitive as no significant impact on the simulated S1 spectrum is observed.

We found further that very sufficient agreement in the combined, two-dimensional correlation between S1 and S2 is obtained, when inserting the best fit results of  $\mathcal{L}_{eff}$  and  $Q_y$  to the signal simulation. Mean and first order quantiles are well reproduced, which provides further consistency of the energy dependency extracted individually for both functions before. We discussed potential origins of the

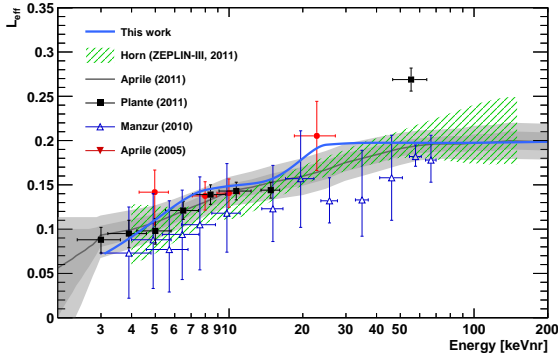


**Figure 5.37:**  $\mathcal{L}_{eff}$  result in comparison with other measurements performed in data/MC comparison by Horn et al. (ZEPLIN-III) [109] and fixed neutron energy setups by Plante et al. [98], Manzur et al. [99] and Aprile [97]. The global fit through all direct measurements from [47] (Aprile et al.) is shown with grey  $1, 2\sigma$  uncertainty bands.

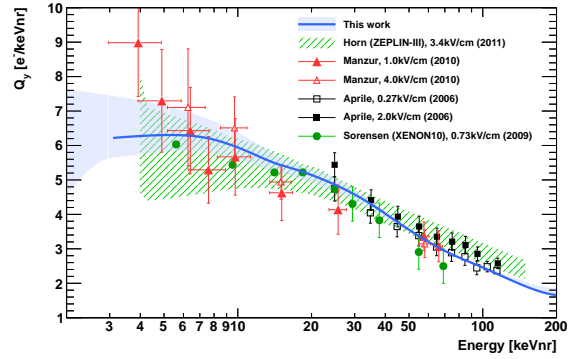


**Figure 5.38:**  $Q_y$  result in comparison with previous measurements performed with a fixed neutron beam setup by Manzur et al. [99], indirect MC matching by Horn (ZEPLIN-III) [109], Sorensen (XENON10) and indirect determination by Aprile [55].

observed discrepancy in the reproduction of the lower tails of the S2 distribution.

The absolute spectral matching further implies the important conclusion that the S1 signal acceptance assumed in the latest reported XENON100 dark matter searches [47, 42] has been correctly derived and applied.

Having shown the overall good agreement between simulated and measured nuclear recoil response for neutrons, we used our developed framework to inject signals as potentially arising from elastic, spin-independent WIMP-nuclei interactions in the XENON100 detector. As toy models, we chose two different scenarios in assumed WIMP mass and interaction cross-section, for which recent dark matter signals were claimed by the CoGeNT [40] and CRESST [32] experiments. For both cases it can be confirmed that the XENON100 detector with its latest reported exposure of 225 live days would have been capable of observing a positive signal if dark matter existed and – as equally important – its interaction was sufficiently described by the standard assumptions on astrophysical parameters and properties of WIMP-nucleon scattering.

---

# Summary and Outlook

Within three years of operation the XENON100 experiment has reached the designed sensitivity for the search on spin-independent WIMP-nucleon interaction and made the liquid xenon detection principle become the most advanced at the time of writing. The demonstration of efficient background suppression as well as the proof of stability and reliability of the applied technology has already caused many people – among the XENON collaboration – to think ahead towards a new generation of large-scale noble liquid detectors. Research and development for a novel experiment, XENON1T, employing a total liquid xenon mass of  $\sim 3$  tons, of which about 1 ton is supposed to act as inner ultra-pure fiducial target, are ongoing and proceeding fast. Construction works of the planned surrounding water tank for moderation of ambient neutrons, and additionally instrumented as a Water-Cerenkov muon veto, are scheduled to begin in Summer 2013. It will be followed by the assembly of the inner cryogenic vessel and the time projection chamber that contains the liquid xenon. The first detector commission phase is aimed to take place in 2015.

The new experiment is foreseen to probe the spin-independent WIMP-nucleon cross-section parameter space down to maximum sensitivity of  $\sim 1 \times 10^{-47} \text{ cm}^2$ , which requires to lower the final background level to roughly 1 event per year and ton, which is about 100 times less than in the current XENON100 experiment. Besides many technical challenges to be overcome, a tremendous effort at selecting radio-pure construction materials and purifying the xenon from intrinsic radioactive sources must be made to achieve this goal.

In the present work we have studied and emphasized the role of radon as a crucial intrinsic background contributor. Provided the currently achieved krypton purification capability and even enhanced external radiation suppression it is likely that radon will become the dominant background component. It is therefore planned to apply active means of “on-line” radon removal – in parallel to the regular xenon recirculation – to reduce the remaining amount of the emanating radioactive gas inside the closed detector system [64]. Beforehand, it will be crucial to screen and select all essential parts of the inner cryogenic system for their amount of radon release even before mounting the detector.

In the second part of this thesis we could prove a decent understanding of the XENON100 detector response to nuclear recoil interactions, as mediated by neutrons and, supposedly, hypothetical WIMPs. The achieved absolute and spectral agreement between measured neutron data and a complete detector signal simulation strengthen the argument of large xenon TPCs to correctly reconstruct the number and energy distribution of incoming neutral particles. In case of a future WIMP discovery this will help to add confidence in the correct signal interpretation by using LXe as a detection material. Furthermore, the indirect determination of the charge yield  $Q_y$  can also contribute to establish an improved nuclear recoil energy scale, based on both S1 and S2.

---

# Bibliography

- [1] F. Zwicky, “Die Rotverschiebung von extragalaktischen Nebeln,” *Helvetica Physica Acta* **6** (1933) 110–127.
- [2] V. C. Rubin, N. Thonnard, and W. K. Ford, Jr., “Extended rotation curves of high-luminosity spiral galaxies. IV - Systematic dynamical properties, SA through SC,” *Astrophys. J.* **225** (1978) L107–L111.
- [3] K. G. Begeman, A. H. Broeils, and R. H. Sanders, “Extended rotation curves of spiral galaxies - Dark haloes and modified dynamics,” *Monthly Notices of the Royal Astronomical Society* **249** (1991) 523–537.
- [4] M. Milgrom, “A modification of the Newtonian dynamics as a possible alternative to the hidden mass hypothesis,” *Astrophys. J.* **270** (1983) 365–370.
- [5] A. Einstein, “Über den Einfluß der Schwerkraft auf die Ausbreitung des Lichtes,” *Annalen der Physik* **340** no. 10, (1911) 898–908.
- [6] F. Zwicky, “Nebulae as Gravitational Lenses,” *Phys. Rev.* **51** (1937) 290.
- [7] P. Ade *et al.*, “Planck 2013 results. XVI. Cosmological parameters,” [arXiv:1303.5076](https://arxiv.org/abs/1303.5076).
- [8] C. Bennett *et al.*, “Four year COBE DMR cosmic microwave background observations: Maps and basic results,” *Astrophys.J.* **464** (1996) L1–L4, [arXiv:astro-ph/9601067](https://arxiv.org/abs/astro-ph/9601067).
- [9] E. Komatsu *et al.* (WMAP Collaboration), “Seven-Year Wilkinson Microwave Anisotropy Probe (WMAP) Observations: Cosmological Interpretation,” *Astrophys. J. Suppl.* **192** (2011) .
- [10] V. Springel *et al.*, “Simulations of the formation, evolution and clustering of galaxies and quasars,” *Nature* **435** (2005) 629–636.
- [11] J. Diemand, M. Kuhlen, and P. Madau, “Formation and evolution of galaxy dark matter halos and their substructure,” *Astrophys.J.* **667** (2007) 859–877, [arXiv:astro-ph/0703337](https://arxiv.org/abs/astro-ph/0703337).
- [12] G. Gelmini and P. Gondolo, “Dark matter production mechanisms,” in *Particle Dark Matter*, G. Bertone, ed., ch. 7. Cambridge University Press, 2010.
- [13] G. Jungman, M. Kamionkowski, and K. Griest, “Supersymmetric dark matter,” *Phys.Rept.* **267** (1996) 195–373, [arXiv:hep-ph/9506380](https://arxiv.org/abs/hep-ph/9506380).
- [14] G. Steigman and M. S. Turner, “Cosmological constraints on the properties of weakly interacting massive particles,” *Nuclear Physics B* **253** (1985) 375 – 386.
- [15] G. Bertone, *Particle Dark Matter. Observations, Models and Searches*. Cambridge University Press, 2010.

- 
- [16] ATLAS Collaboration, “Search for dark matter candidates and large extra dimensions in events with a photon and missing transverse momentum in  $pp$  collision data at  $\sqrt{s} = 7$  TeV with the ATLAS detector,” *Phys.Rev.Lett.* **110** (2013) 011802, arXiv:1209.4625.
- [17] CMS Collaboration, “Search for Dark Matter and Large Extra Dimensions in  $pp$  Collisions Yielding a Photon and Missing Transverse Energy,” *Phys. Rev. Lett.* **108** (2012) 261803.
- [18] C. Weniger, “A tentative gamma-ray line from Dark Matter annihilation at the Fermi Large Area Telescope,” *Journal of Cosmology and Astroparticle Physics* **8** (2012) 7, arXiv:1204.2797.
- [19] D. G. Cerdeño and A. M. Green, “Direct detection of wimps,” in *Particle Dark Matter*, G. Bertone, ed., ch. 17. Cambridge University Press, 2010.
- [20] L. M. Widrow, B. Pym, and J. Dubinski, “Dynamical Blueprints for Galaxies,” *Astrophys.J.* **679** (2008) 1239–1259, arXiv:0801.3414.
- [21] M. C. Smith, G. Ruchti, A. Helmi, R. Wyse, J. Fulbright, *et al.*, “The RAVE Survey: Constraining the Local Galactic Escape Speed,” *Mon.Not.Roy.Astron.Soc.* **379** (2007) 755–772, arXiv:astro-ph/0611671.
- [22] F. Kerr and D. Lynden-Bell, “Review of galactic constants,” *Mon. Not. Roy. Astron. Soc.* **221** (1986) 1023.
- [23] C. McCabe, “The Astrophysical Uncertainties Of Dark Matter Direct Detection Experiments,” *Phys.Rev.* **D82** (2010) 023530, arXiv:1005.0579.
- [24] J. Engel, “Nuclear form-factors for the scattering of weakly interacting massive particles,” *Phys. Lett.* **B264** (1991) .
- [25] J. Lewin and P. Smith, “Review of mathematics, numerical factors, and corrections for dark matter experiments based on elastic nuclear recoil,” *Astroparticle Physics* **6** no. 1, (1996) 87 – 112.
- [26] J. Kopp, T. Schwetz, and J. Zupan, “Global interpretation of direct Dark Matter searches after CDMS-II results,” *Journal of Cosmology and Astroparticle Physics* **2010** no. 02, (2010) 014.
- [27] F. Kahlhöfer, “Sensitivity of Liquid Xenon Detectors for Low Mass Dark Matter (Diplomarbeit Universität Heidelberg),” 2010.
- [28] G. Plante, *The XENON100 Dark Matter Experiment: Design, Construction, Calibration and 2010 Search Results with Improved Measurement of the Scintillation Response of Liquid Xenon to Low-Energy Nuclear Recoils*. PhD thesis, Columbia University, 2012.
- [29] Z. Ahmed *et al.* (CDMS Collaboration), “Search for Weakly Interacting Massive Particles with the First Five-Tower Data from the Cryogenic Dark Matter Search at the Soudan Underground Laboratory,” *Phys.Rev.Lett.* **102** (2009) 011301, arXiv:0802.3530.
- [30] E. Armengaud *et al.*, “Final results of the EDELWEISS-II WIMP search using a 4-kg array of cryogenic germanium detectors with interleaved electrodes,” *Phys. Lett.* **B702** (2011) 329–335, arXiv:1103.4070.

- [31] M. Bravin, M. Bruckmayer, T. Frank, S. Giordano, M. Loidl, *et al.*, “Simultaneous measurement of phonons and scintillation light for active background rejection in the CRESST experiment,” *Nuclear Instruments and Methods A* **444** (2000) 323–326.
- [32] G. Angloher *et al.* (CRESST Collaboration), “Results from 730 kg days of the CRESST-II Dark Matter Search,” *Eur.Phys.J.* **C72** (2012) 1971, arXiv:1109.0702.
- [33] E. Aprile *et al.* (XENON100 Collaboration), “The XENON100 dark matter experiment,” *Astroparticle physics* **35** no. 9, (2012) 573–590.
- [34] V. Lebedenko, H. Araujo, E. Barnes, A. Bewick, R. Cashmore, *et al.*, “Result from the First Science Run of the ZEPLIN-III Dark Matter Search Experiment,” *Phys.Rev.* **D80** (2009) 052010, arXiv:0812.1150.
- [35] D. S. Akerib *et al.* (LUX Collaboration), “The Large Underground Xenon (LUX) experiment,” *Nuclear Instruments and Methods A* **704** (2013) 111–126, arXiv:1211.3788.
- [36] E. Aprile, “Liquid xenon detectors for particle physics and astrophysics,” *Reviews of modern physics* **82** no. 3, (2010) 2053–2097.
- [37] P. Benetti, R. Acciarri, F. Adamo, B. Baibussinov, M. Baldo-Ceolin, *et al.*, “First results from a Dark Matter search with liquid Argon at 87 K in the Gran Sasso Underground Laboratory,” *Astropart.Phys.* **28** (2008) 495–507, arXiv:astro-ph/0701286.
- [38] D. Akimov *et al.*, “Light Yield in DarkSide-10: a Prototype Two-phase Liquid Argon TPC for Dark Matter Searches,” arXiv:1204.6218.
- [39] R. Bernabei *et al.*, “First results from DAMA/LIBRA and the combined results with DAMA/NaI,” *Eur.Phys.J.* **C56** (2008) 333–355, arXiv:0804.2741.
- [40] C. Aalseth *et al.*, “Search for an Annual Modulation in a P-type Point Contact Germanium Dark Matter Detector,” *Phys.Rev.Lett.* **107** (2011) 141301, arXiv:1106.0650.
- [41] Z. Ahmed *et al.* (CDMS Collaboration), “Results from a Low-Energy Analysis of the CDMS II Germanium Data,” *Phys.Rev.Lett.* **106** (2011) 131302, arXiv:1011.2482.
- [42] E. Aprile *et al.* (XENON100 Collaboration), “Dark matter results from 225 live days of xenon100 data,” *Phys. Rev. Lett.* **109** (2012) 181301.
- [43] S. Archambault *et al.*, “Constraints on Low-Mass WIMP Interactions on  $^{19}\text{F}$  from PICASSO,” *Phys.Lett.* **B711** (2012) 153–161, arXiv:1202.1240.
- [44] E. Behnke *et al.*, “First Dark Matter Search Results from a 4-kg  $\text{CF}_3\text{I}$  Bubble Chamber Operated in a Deep Underground Site,” *Phys.Rev.* **D86** (2012) 052001, arXiv:1204.3094.
- [45] A. S. Barabash and A. I. Bolozdynya, “How to detect the dark matter of the galaxy if it is made up of weakly interacting neutral particles with masses 1-10  $\text{GeV}/c^2$ ,” *JETP Lett.* **49** (1989) 356.
- [46] J. Angle *et al.*, “First Results from the XENON10 Dark Matter Experiment at the Gran Sasso National Laboratory,” *Phys.Rev.Lett.* **100** (2008) 021303, arXiv:0706.0039.

- 
- [47] E. Aprile et al. (XENON100 Collaboration), “Dark Matter Results from 100 Live Days of XENON100 Data,” *Phys. Rev. Lett.* **107** (2011) 131302.
- [48] U. Asaf and I. T. Steinberger, “Photoconductivity and electron transport parameters in liquid and solid xenon,” *Phys. Rev. B* **10** (1974) 4464–4468.
- [49] R. Reininger, U. Asaf, I. T. Steinberger, P. Laporte, and V. Saile, “Free electrons and excitons in fluid krypton,” *Phys. Rev.* **B26** (1982) 6294–6296.
- [50] S. Kubota, M. Hishida, and J. Raun, “Evidence for a Triplet State of the Self-Trapped Exciton States in Liquid Argon, Krypton and Xenon,” *J. Phys. C* **11** (1978) 2645.
- [51] J. Jortner et al., “Localized Excitations in Condensed Ne, Ar, Kr, and Xe,” *The Journal of chemical physics* **42** no. 12, (1965) 4250.
- [52] A. Hitachi *et al.*, “Effect of Ionization Density on the Time Dependence of Luminescence from Liquid Argon and Xenon,” *Phys. Rev. B* **27** (1983) 5279.
- [53] C. E. Dahl, *The physics of background discrimination in liquid xenon, and first results from XENON10 in the hunt for WIMP dark matter*. PhD thesis, Princeton University, 2009.
- [54] T. Doke, A. Hitachi, S. Kubota, A. Nakamoto, and T. Takahashi, “Estimation of Fano factors in liquid argon, krypton, xenon and xenon-doped liquid argon,” *Nuclear Instruments and Methods* **134** (1976) 353–357.
- [55] E. Aprile, C. Dahl, L. DeViveiros, R. Gaitskell, K. Giboni, *et al.*, “Simultaneous measurement of ionization and scintillation from nuclear recoils in liquid xenon as target for a dark matter experiment,” *Phys.Rev.Lett.* **97** (2006) 081302, arXiv:astro-ph/0601552.
- [56] J. Angle *et al.*, “A search for light dark matter in XENON10 data,” *Phys.Rev.Lett.* **107** (2011) 051301, arXiv:1104.3088.
- [57] E. Aprile et al. (XENON100 Collaboration), “Analysis of the XENON100 Dark Matter Search Data,” arXiv:1207.3458.
- [58] A. Lansiaert et al., “Development research on a highly luminous condensed xenon scintillator,” *Nuclear instruments and methods* **135** no. 1, (1976) 47.
- [59] A. Bolozdynya, “Two-phase emission detectors and their applications,” *Nuclear Instruments and Methods A* **422** (1999) 314 – 320.
- [60] E. Aprile et al. (XENON100 Collaboration) *To be published* .
- [61] Y. Mei, *Direct Dark Matter Search with the XENON100 Experiment*. PhD thesis, Rice University, 2011.
- [62] A. Kish, *Dark Matter Search with the XENON100 Experiment*. PhD thesis, University of Zurich, 2011. <http://opac.nebis.ch/ediss/20121322.pdf>.
- [63] E. Aprile et al. (XENON100 Collaboration), “Material screening and selection for XENON100,” *Astroparticle Physics* **35** no. 2, (2011) 43 – 49.
- [64] S. Lindemann, *In preparation*. PhD thesis, Universität Heidelberg, 2013.

- [65] S. Agostinelli *et al.*, “Geant4 – a simulation toolkit,” *Nuclear Instruments and Methods A* **506** no. 3, (2003) 250 – 303.
- [66] J. Allison *et al.*, “Geant4 developments and applications,” *Nuclear Science, IEEE Transactions on* **53** no. 1, (2006) 270 –278.
- [67] E. Aprile *et al.* (XENON100 Collaboration), “First dark matter results from the XENON100 experiment,” *Phys. Rev. Lett.* **105** no. 13, (2010) 131302.
- [68] E. Aprile, R. Budnik, B. Choi, H. Contreras, K.-L. Giboni, *et al.*, “Measurement of the Scintillation Yield of Low-Energy Electrons in Liquid Xenon,” arXiv:1209.3658.
- [69] E. Aprile *et al.* (XENON100 Collaboration), “Likelihood Approach to the First Dark Matter Results from XENON100,” *Phys.Rev.* **D84** (2011) 052003, arXiv:1103.0303.
- [70] S. Yellin, “Finding an upper limit in the presence of an unknown background,” *Phys.Rev.* **D66** no. 3, (2002) 032005, arXiv:physics/0203002.
- [71] E. Aprile *et al.*, “The neutron background of the XENON100 dark matter search experiment,” *To be published* .
- [72] E. Aprile *et al.* (XENON100 Collaboration), “Limits on spin-dependent WIMP-nucleon cross sections from 225 live days of data,” arXiv:1301.6620.
- [73] E. Aprile *et al.* (XENON100 Collaboration), “Implications on Inelastic Dark Matter from 100 Live Days of XENON100 Data,” *Phys.Rev.* **D84** (2011) 061101, arXiv:1104.3121.
- [74] K. Lim, *XENON100 Dark Matter Search: Scintillation Response of Liquid Xenon to Electronic Recoils*. PhD thesis, Columbia University, 2012.
- [75] J. Angle *et al.*, “Constraints on inelastic dark matter from XENON10,” *Phys.Rev.* **D80** (2009) 115005, arXiv:0910.3698.
- [76] S. S. Wilks, “The large-sample distribution of the likelihood ratio for testing composite hypotheses,” *Ann. Math. Statist.* **9** no. 1, (1938) 60–62.
- [77] Laboratoire National Henri Becquerel, “Recommended Data of Radionuclides.” [http://www.nucleide.org/DDEP\\_WG/DDEPdata.htm](http://www.nucleide.org/DDEP_WG/DDEPdata.htm), updated 16th January 2013.
- [78] K.-H. Ackermann *et al.* (GERDA Collaboration), “The GERDA experiment for the search of  $0\nu\beta\beta$  decay in  $^{76}\text{Ge}$ ,” arXiv:1212.4067.
- [79] W. Rau and G. Heusser, “Rn emanation measurements at extremely low activities,” *Applied Radiation and Isotopes* **53** no. 1-2, (2000) 371–375.
- [80] G. Zuzel,  $^{226}\text{Ra}$  in the nylon scintillator vessel as a background source in the solar neutrino experiment BOREXINO. PhD thesis, Jagellonian University, Krakow, Poland, 2002.
- [81] E. Aprile *et al.* (XENON100 Collaboration), “Study of the electromagnetic background in the XENON100 experiment,” *Phys.Rev.* **D83** (2011) 082001, arXiv:1101.3866.
- [82] S. Br unner, “Study of radon adsorption on activated carbon for a purification system in XENON1T (Diplomarbeit Universit t Graz),” 2013.

- [83] T. Takahashi, S. Konno, T. Hamada, M. Miyajima, S. Kubota, A. Nakamoto, A. Hitachi, E. Shibamura, and T. Doke, "Average energy expended per ion pair in liquid xenon," *Phys. Rev. A* **12** (1975) 1771–1775.
- [84] E. Aprile, R. Mukherjee, and M. Suzuki, "Ionization of liquid xenon by  $^{241}\text{Am}$  and  $^{210}\text{Po}$  alpha particles," *Nuclear Instruments and Methods A* **307** no. 1, (1991) 119 – 125.
- [85] J. Kiko, "Detector for  $^{222}\text{Rn}$  measurements in air at the  $1\text{ mBq/m}^3$  level," *Nuclear Instruments and Methods A* **460** (2001) 272–277.
- [86] K. Wamba *et al.*, "Mobility of thorium ions in liquid xenon," *Nuclear Instruments and Methods A* **555** (2005) 205–210.
- [87] A. J. Walters and L. W. Mitchell, "Mobility and lifetime of  $^{208}\text{Tl}$  ions in liquid xenon," *Journal of Physics D* **36** no. 11, (2003) 1323.
- [88] A. Einstein, "Über die von der molekularkinetischen Theorie der Wärme geforderte Bewegung von in ruhenden Flüssigkeiten suspendierten Teilchen," *Annalen der Physik* **322** no. 8, (1905) 549–560.
- [89] G. Alimonti *et al.*, "Science and technology of Borexino: a real-time detector for low energy solar neutrinos," *Astroparticle Physics* **16** no. 3, (2002) 205 – 234.
- [90] X. Du, K. Bailey, Z.-T. Lu, P. Mueller, T. P. O'Connor, and L. Young, "An atom trap system for practical kr-81-dating," *Review of Scientific Instruments* **75** (2004) 3224.
- [91] K. Abe *et al.* (XMASS Collaboration), "Distillation of liquid xenon to remove krypton," *Astroparticle Physics* **31** no. 4, (2009) 290 – 296.
- [92] E. Aprile *et al.* (XENON100 Collaboration), "Response of the XENON100 Dark Matter Detector to Nuclear Recoils," [arXiv:1304.1427](https://arxiv.org/abs/1304.1427).
- [93] J. Lindhard and M. Scharff, "Energy dissipation by ions in the kev region," *Phys. Rev.* **124** (1961) 128–130.
- [94] J. Lindhard *et al.*, "Integral equations governing radiation effects," *Mat. Fys. Medd. Dan. Vid. Selsk.* **33** (1963) .
- [95] A. Hitachi, "Properties of liquid xenon scintillation for dark matter searches," *Astroparticle physics* **24** no. 3, (2005) 247–256.
- [96] A. Hitachi, T. Doke, and A. Mozumder, "Luminescence quenching in liquid argon under charged-particle impact: Relative scintillation yield at different linear energy transfers," *Phys. Rev. B* **46** (1992) 11463–11470.
- [97] E. Aprile, L. Giboni, K. P. Majewski, K. Ni, M. Yamashita, R. Hasty, A. Manzur, and D. N. McKinsey, "Scintillation response of liquid xenon to low energy nuclear recoils," *Phys. Rev. D* **72** (2005) 072006.
- [98] G. Plante, E. Aprile, R. Budnik, B. Choi, K.-L. Giboni, L. W. Goetzke, R. F. Lang, K. E. Lim, and A. J. Melgarejo Fernandez, "New measurement of the scintillation efficiency of low-energy nuclear recoils in liquid xenon," *Phys. Rev. C* **84** (2011) 045805.

- [99] A. Manzur, A. Curioni, L. Kastens, D. N. McKinsey, K. Ni, and T. Wongjirad, “Scintillation efficiency and ionization yield of liquid xenon for monoenergetic nuclear recoils down to 4 keV,” *Phys. Rev. C* **81** (2010) 025808.
- [100] E. Aprile, L. Baudis, B. Choi, K. L. Giboni, K. Lim, A. Manalaysay, M. E. Monzani, G. Plante, R. Santorelli, and M. Yamashita, “New measurement of the relative scintillation efficiency of xenon nuclear recoils below 10 keV,” *Phys. Rev.* **C79** (2009) 045807.
- [101] V. Chepel *Astroparticle physics* **26** no. 58, (2006) .
- [102] P. Sorensen, “The scintillation and ionization yield of liquid xenon for nuclear recoils,” *Nuclear Instruments and Methods A* **601** no. 3, (2009) 339–346.
- [103] B. Wiegel and A. Alevra, “NEMUS - The PTB Neutron Multisphere Spectrometer: Bonner Spheres and More,” *Nuclear Instruments and Methods A* **476** (2002) 36–41.
- [104] B. Wiegel and H. Schuhmacher, “Messung der Quellstärke einer  $^{241}\text{AmBe}$  Neutronenquelle, die als Kalibrierquelle bei dem XENON100 Dark Matter Experiment verwendet wird.” Internal PTB Report, 2013.
- [105] B. Wiegel. Private communication.
- [106] International Standards ISO/DIS 8529-1, 2000.
- [107] “ENDF/B-VI Summary Document, BNL-NCS-17541 (ENDF-201),” tech. rep., National Nuclear Data Center, Brookhaven National Laboratory, Upton, NY, USA, 1991.
- [108] M. Szydagis, N. Barry, K. Kazkaz, J. Mock, D. Stolp, *et al.*, “NEST: A Comprehensive Model for Scintillation Yield in Liquid Xenon,” *JINST* **6** (2011) P10002, arXiv:1106.1613.
- [109] M. Horn, “Nuclear recoil scintillation and ionisation yields in liquid xenon from ZEPLIN-III data,” *Physics letters. B* **705** no. 5, (2011) 471.
- [110] H. Akima, “A new method of interpolation and smooth curve fitting based on local procedures,” *J. ACM* **17** no. 4, (1970) 589–602.
- [111] M. Lourakis, “levmar: Levenberg-marquardt nonlinear least squares algorithms in C/C++.” <http://www.ics.forth.gr/~lourakis/levmar/>, updated 2011.

---

# Danksagung

Es gilt so vielen Menschen dankzusagen, die bewusst oder unbewusst zu der Entstehung dieser Arbeit beigetragen haben, dass es mir nicht einfach fällt, einen Anfang zu finden (ein Ende noch weniger). Ohne Zweifel sind meine Erstbetreuer Prof. Wolfgang Hampel und Prof. Manfred Lindner hervorzuheben, die mir die Möglichkeit gegeben haben, an einem ungemein spannenden Experiment am Puls der Forschung mitzuwirken. Bedanken möchte ich mich auch bei Prof. André Schöning, der sich bereit erklärt hat, die Zweitbegutachtung der Arbeit zu übernehmen.

Ich fahre fort mit denen, die mir bei der alltäglichen Arbeit am nächsten waren. Es sind alle Mitglieder der Forschungsgruppe "Astroteilchenphysik" am Max-Planck-Institut für Kernphysik, die mir jederzeit auf einzigartige Weise mit Rat und Tat zur Seite standen. Ohne Garantie auf Vollständigkeit seien insbesondere Dr. Hardy Simgen, Dr. Jochen Schreiner und Dr. Gerd Heusser genannt. In besonderem Maße danke ich Sebastian Lindemann für die gemeinsame Zeit als Doktorand. In den Höhen des Heidelberger Instituts aber vor allem in den Tiefen des Gran Sasso wäre sie nicht dieselbe gewesen und ohne ihn wären viele Fragen in dieser Arbeit unbeantwortet geblieben. Gleicher Dank gilt Stefan Brünner, der mir außerdem Einblicke in die österreichische Lebensart gewährte. Aber auch die erfolgreiche und jederzeit angenehme Zusammenarbeit mit den weiteren Kollegen der Gruppe möchte ich herausstellen. Darunter sind Dr. Florian Kaether für wertvolle Diskussionen und Lehrstunden über Statistik, Julia Haser sowie Dominik Stolzenburg, Janina Hakenmüller und Dr. Werner Maneschg bei der unterhaltsamen Errichtung des neuen Germanium-Spektrometers.

Hinaus in die Welt geht weiterer Dank an die gesamte XENON100 Forschungsgemeinschaft. Ich habe sie als einen tatsächlich außergewöhnlich motivierten Haufen von Wissenschaftlern kennengelernt, die mir ungemein Vieles beigebracht haben und ohne deren Hingabe für das Experiment kein Anlass für meine Arbeit bestanden hätte. Von allen zu nennenden Namen möchte ich die herausheben, die mich in ganz besonderem Maße eingelernt und unterstützt haben: Prof. Marc Schumann, Dr. Teresa Marrodán Undagoitia, Prof. Rafael Lang, Dr. Alfredo Ferella und viele weitere aus der XENON100 "Datenanalyse-Mannschaft". Für hilfreiche Diskussionen und Zusammenarbeit bedanke ich mich außerdem namentlich bei Fei Gao, Dr. Paul Scovell, Dr. Alexander Kish, Dr. Guillaume Plante und Dr. Antonio Melgarejo Fernandez. Nicht zuletzt für einen erinnerungswürdigen Aufenthalt an ihrem Institut in der Stadt der Städte bedanke ich mich bei Prof. Elena Aprile. Ein ebenso aufrichtiges Dankeschön gilt der PTB und insbesondere Dr. Burkhard Wiegel für die Messung der AmBe Neutronenquellstärke.

Aber was wären die Jahre in Heidelberg gewesen ohne meinen Freundeskreis! Für wunderbare Augenblicke und ebenso wertvolle Hilfe beim Korrigieren danke ich insbesondere Fabian Zimmer, Konrad Schade, Tobias Hofmann, Marco Meißner und Tobias Harion.

Meinen Eltern Margit und Friedwalt, und meiner Schwester Sandra gilt grenzenloser Dank für all die Unterstützung und Aufmunterung während der vergangenen Jahre. Die Höhen und Tiefen des Doktorandenlebens musste schließlich Deborah Kram ertragen. Du bist mein Glück und meine Liebe!